

# Nondestructive Evaluation of Concrete Bridge Decks with Overlays

PUBLICATION NO. FHWA-HRT-21-023

MARCH 2021



U.S. Department of Transportation  
**Federal Highway Administration**

Research, Development, and Technology  
Turner-Fairbank Highway Research Center  
6300 Georgetown Pike  
McLean, VA 22101-2296

## FOREWORD

This report documents the results of an investigation to identify effective and promising nondestructive evaluation (NDE) techniques to detect and characterize deterioration in concrete bridge decks with overlays. The results of the study on which this report is based will provide bridge owners with a practical protocol and information to identify NDE technologies to assess the performance of different types of overlays.

Cheryl Allen Richter, Ph.D., P.E.  
Director, Office of Infrastructure  
Research and Development

### Notice

This document is disseminated under the sponsorship of the U.S. Department of Transportation (USDOT) in the interest of information exchange. The U.S. Government assumes no liability for the use of the information contained in this document.

The U.S. Government does not endorse products or manufacturers. Trademarks or manufacturers' names appear in this report only because they are considered essential to the objective of the document.

### Quality Assurance Statement

The Federal Highway Administration (FHWA) provides high-quality information to serve Government, industry, and the public in a manner that promotes public understanding. Standards and policies are used to ensure and maximize the quality, objectivity, utility, and integrity of its information. FHWA periodically reviews quality issues and adjusts its programs and processes to ensure continuous quality improvement.

## TECHNICAL REPORT DOCUMENTATION PAGE

1. Report No. FHWA-HRT-21-023	2. Government Accession No.	3. Recipient's Catalog No.	
4. Title and Subtitle Nondestructive Evaluation of Concrete Bridge Decks with Overlays		5. Report Date March 2021	
		6. Performing Organization Code 1YX01	
7. Author(s) Shibin Lin, Hoda Azari (HRDI-20; ORCID: 0000-0002-7340-0035), Dewei Meng, and Sadeh Shams		8. Performing Organization Report No.	
9. Performing Organization Name and Address Engineering & Software Consultants, Inc. 14123 Robert Paris Court Chantilly, VA 20151		10. Work Unit No.	
		11. Contract or Grant No. DTHF61-D-14-00011	
12. Sponsoring Agency Name and Address Office of Infrastructure Research and Development Federal Highway Administration 6300 Georgetown Pike McLean, VA 22101		13. Type of Report and Period Covered Final Report; October 2016–April 2019	
		14. Sponsoring Agency Code HRDI-20	
15. Supplementary Notes The Contracting Officer's Representative was Hoda Azari (HRDI-20; ORCID: 0000-0002-7340-0035).			
16. Abstract Concrete bridge deck overlays have been used in the United States since 1960 to extend the service life of deteriorated concrete bridge decks and improve reliability. Concrete bridge decks with overlays suffer various types of deterioration, so it is necessary to identify and assess the effectiveness of different nondestructive evaluation (NDE) technologies in the laboratory under controlled conditions and in the field under actual conditions. This report provides an overview of seven types of widely used overlays: asphalt with a liquid membrane, asphalt with a fabric membrane, asphalt without a membrane, silica fume-modified concrete, latex-modified concrete (LMC), epoxy polymer concrete, and polyester polymer concrete. This report identifies and ranks available and promising NDE technologies to assess the performance of different types of overlays and concrete bridge decks. This report describes laboratory validation on overlays for nine commonly used NDE technologies. The nine NDE technologies are: sounding, ultrasonic surface waves (USW), impact echo (IE), ultrasonic tomography (UT), impulse response (IR), ground-penetrating radar (GPR), electrical resistivity (ER), half-cell potential (HCP), and infrared thermography (IRT). This report details the results of laboratory tests validating the NDE technologies for the seven different types of overlays. Field validation using the RABIT™ bridge deck assessment tool and manual testing equipment was also performed. Results from the study on which this report is based indicated that GPR was the most effective method for detecting defects in underlying concrete specimens through both bonded and debonded overlays; however, GPR could not detect overlay debonding. Results also showed that USW, IE, and UT were effective stress-wave-based methods for detecting defects under bonded overlays but not asphalt overlays. Researchers found that asphalt overlays at low temperatures (i.e., 32°F or below) improved the applicability of IE. Sounding and IR were effective methods for detecting overlay debonding but could not detect defects under bonded overlays. HCP measured the potential difference between areas with and without active corrosion but could only detect active corrosion on LMC and polyester overlays due to the electric insulation of the other overlay materials. Researchers also found that IRT was an effective method for detecting overlay debonding and shallow defects under some overlays. Results concluded that ER was the least effective method due to the resistivity of overlays.			
17. Key Words Concrete bridge decks, overlays, nondestructive evaluation		18. Distribution Statement No restrictions. This document is available to the public through the National Technical Information Service, Springfield, VA 22161. <a href="http://www.ntis.gov">http://www.ntis.gov</a>	
19. Security Classif. (of this report) Unclassified	20. Security Classif. (of this page) Unclassified	21. No. of Pages 240	22. Price N/A

## SI\* (MODERN METRIC) CONVERSION FACTORS

### APPROXIMATE CONVERSIONS TO SI UNITS

Symbol	When You Know	Multiply By	To Find	Symbol
<b>LENGTH</b>				
in	inches	25.4	millimeters	mm
ft	feet	0.305	meters	m
yd	yards	0.914	meters	m
mi	miles	1.61	kilometers	km
<b>AREA</b>				
in <sup>2</sup>	square inches	645.2	square millimeters	mm <sup>2</sup>
ft <sup>2</sup>	square feet	0.093	square meters	m <sup>2</sup>
yd <sup>2</sup>	square yard	0.836	square meters	m <sup>2</sup>
ac	acres	0.405	hectares	ha
mi <sup>2</sup>	square miles	2.59	square kilometers	km <sup>2</sup>
<b>VOLUME</b>				
fl oz	fluid ounces	29.57	milliliters	mL
gal	gallons	3.785	liters	L
ft <sup>3</sup>	cubic feet	0.028	cubic meters	m <sup>3</sup>
yd <sup>3</sup>	cubic yards	0.765	cubic meters	m <sup>3</sup>
NOTE: volumes greater than 1,000 L shall be shown in m <sup>3</sup>				
<b>MASS</b>				
oz	ounces	28.35	grams	g
lb	pounds	0.454	kilograms	kg
T	short tons (2,000 lb)	0.907	megagrams (or "metric ton")	Mg (or "t")
<b>TEMPERATURE (exact degrees)</b>				
°F	Fahrenheit	5 (F-32)/9 or (F-32)/1.8	Celsius	°C
<b>ILLUMINATION</b>				
fc	foot-candles	10.76	lux	lx
fl	foot-Lamberts	3.426	candela/m <sup>2</sup>	cd/m <sup>2</sup>
<b>FORCE and PRESSURE or STRESS</b>				
lbf	poundforce	4.45	newtons	N
lbf/in <sup>2</sup>	poundforce per square inch	6.89	kilopascals	kPa
<b>APPROXIMATE CONVERSIONS FROM SI UNITS</b>				
Symbol	When You Know	Multiply By	To Find	Symbol
<b>LENGTH</b>				
mm	millimeters	0.039	inches	in
m	meters	3.28	feet	ft
m	meters	1.09	yards	yd
km	kilometers	0.621	miles	mi
<b>AREA</b>				
mm <sup>2</sup>	square millimeters	0.0016	square inches	in <sup>2</sup>
m <sup>2</sup>	square meters	10.764	square feet	ft <sup>2</sup>
m <sup>2</sup>	square meters	1.195	square yards	yd <sup>2</sup>
ha	hectares	2.47	acres	ac
km <sup>2</sup>	square kilometers	0.386	square miles	mi <sup>2</sup>
<b>VOLUME</b>				
mL	milliliters	0.034	fluid ounces	fl oz
L	liters	0.264	gallons	gal
m <sup>3</sup>	cubic meters	35.314	cubic feet	ft <sup>3</sup>
m <sup>3</sup>	cubic meters	1.307	cubic yards	yd <sup>3</sup>
<b>MASS</b>				
g	grams	0.035	ounces	oz
kg	kilograms	2.202	pounds	lb
Mg (or "t")	megagrams (or "metric ton")	1.103	short tons (2,000 lb)	T
<b>TEMPERATURE (exact degrees)</b>				
°C	Celsius	1.8C+32	Fahrenheit	°F
<b>ILLUMINATION</b>				
lx	lux	0.0929	foot-candles	fc
cd/m <sup>2</sup>	candela/m <sup>2</sup>	0.2919	foot-Lamberts	fl
<b>FORCE and PRESSURE or STRESS</b>				
N	newtons	2.225	poundforce	lbf
kPa	kilopascals	0.145	poundforce per square inch	lbf/in <sup>2</sup>

\*SI is the symbol for International System of Units. Appropriate rounding should be made to comply with Section 4 of ASTM E380. (Revised March 2003)

## TABLE OF CONTENTS

<b>CHAPTER 1. INTRODUCTION</b> .....	<b>1</b>
<b>CHAPTER 2. OVERVIEW OF SEVEN TYPES OF OVERLAYS</b> .....	<b>3</b>
<b>Asphalt With a Liquid or Fabric Membrane</b> .....	<b>3</b>
<b>Asphalt Without a Membrane</b> .....	<b>4</b>
<b>Portland Cement and Silica Fume-Modified Concrete</b> .....	<b>4</b>
<b>LMC</b> .....	<b>4</b>
<b>EPC</b> .....	<b>5</b>
<b>PPC</b> .....	<b>5</b>
<b>CHAPTER 3. OVERVIEW OF NDE TECHNOLOGIES</b> .....	<b>7</b>
<b>Introduction</b> .....	<b>7</b>
<b>IRT</b> .....	<b>7</b>
<b>GPR</b> .....	<b>9</b>
<b>IE</b> .....	<b>11</b>
<b>USW</b> .....	<b>12</b>
<b>ER</b> .....	<b>14</b>
<b>HCP</b> .....	<b>15</b>
<b>UT-MIRA</b> .....	<b>17</b>
<b>IR</b> .....	<b>19</b>
<b>Sounding</b> .....	<b>20</b>
<b>Rank of NDE Technologies for the Overlay Study</b> .....	<b>21</b>
<b>CHAPTER 4. DESIGNING SMALL-SCALE SPECIMENS</b> .....	<b>25</b>
<b>Small-Scale Specimen Design</b> .....	<b>25</b>
<b>Boundary Effect Analysis</b> .....	<b>26</b>
Cases 1 and 2.....	28
Cases 3 and 4.....	31
<b>Heat-Transfer Analysis</b> .....	<b>35</b>
<b>CHAPTER 5. CONSTRUCTING THE SMALL-SCALE SPECIMENS</b> .....	<b>43</b>
<b>Creating Artificial Defects</b> .....	<b>43</b>
Delaminations.....	43
Honeycombing.....	44
Voids.....	46
Vertical Cracks.....	46
Precorroded Rebar.....	48
<b>Assembling and Constructing the Specimens</b> .....	<b>50</b>
<b>Accelerated Corrosion for Precorroded Rebar</b> .....	<b>51</b>
<b>CHAPTER 6. NDE TESTS OF LABORATORY SPECIMENS</b> .....	<b>53</b>
<b>CHAPTER 7. NDE RESULTS OF SPECIMENS WITHOUT OVERLAYS</b> .....	<b>59</b>
<b>Sounding</b> .....	<b>59</b>
<b>USW Method</b> .....	<b>63</b>
<b>IE Method</b> .....	<b>68</b>
<b>UT Method</b> .....	<b>72</b>

IR Method.....	90
GPR Method.....	94
ER Method.....	110
HCP Method.....	115
IRT Method.....	120
Summary.....	129
<b>CHAPTER 8. CONSTRUCTION OF OVERLAYS.....</b>	<b>133</b>
Epoxy Polymer Overlay .....	134
Latex and Silica Fume-Modified Concrete Overlays .....	136
Polyester Polymer Overlay.....	137
Asphalt Overlay .....	138
<b>CHAPTER 9. NDE RESULTS OF SPECIMENS WITH OVERLAYS.....</b>	<b>143</b>
Sounding Condition Maps.....	143
USW Condition Maps.....	147
IE Condition Maps.....	152
UT C- and B-Scans.....	157
IR Condition Maps .....	177
GPR C-Scans, B-Scans, and Deterioration Maps .....	181
ER Condition Maps .....	197
HCP Condition Maps .....	199
IRT Condition Maps.....	203
<b>CHAPTER 10. SUMMARY.....</b>	<b>211</b>
<b>CHAPTER 11. FIELD VALIDATION.....</b>	<b>219</b>
Clara Barton Parkway Cantilever Structure.....	219
Arlington Memorial Bridge .....	222
<b>REFERENCES.....</b>	<b>227</b>

## LIST OF FIGURES

Figure 1. Illustration. Structure of an asphalt overlay with a liquid membrane. ....	3
Figure 2. Equation. Stefan–Boltzmann law. ....	7
Figure 3. Illustration. Heat flow of a concrete bridge deck with delamination. ....	8
Figure 4. Photo. IRT of a concrete slab (measured at 1:00 p.m.). ....	8
Figure 5. Equation. $R$ at an interface. <sup>(34)</sup> .....	9
Figure 6. Illustration. GPR scanning of a reinforced concrete bridge deck and the B-scan results. ....	10
Figure 7. Graph. Deterioration map of a concrete bridge deck. ....	10
Figure 8. Photo. IE testing system. ....	11
Figure 9. Illustration. Schematic of an IE test. ....	12
Figure 10. Photo. PSPA. ....	13
Figure 11. Graph. Modulus map of a concrete bridge deck. ....	14
Figure 12. Photo. Wenner probe. ....	14
Figure 13. Equation. Resistivity. <sup>(40)</sup> .....	15
Figure 14. Graph. Corrosion rate map of a concrete bridge deck. ....	15
Figure 15. Photo. HCP testing equipment. ....	16
Figure 16. Graph. Contour map of active corrosion for a concrete bridge deck. <sup>(32)</sup> .....	16
Figure 17. Photo. Top view of a UT-MIRA tomographer. ....	17
Figure 18. Photo. Bottom view of a UT-MIRA tomographer. ....	18
Figure 19. Illustration. Ultrasonic pulse–echo. ....	18
Figure 20. Graph. UT-MIRA B-scan from a test location. ....	18
Figure 21. Graph. 3D UT-MIRA scan of a concrete bridge deck. ....	19
Figure 22. Photo. IR testing. ....	20
Figure 23. Photo. Sounding with a hammer. ....	20
Figure 24. Illustration. Design of the small-scale specimens with artificial defects. ....	26
Figure 25. Illustration. FE model with delamination 12 inches from the left edge for cases 1 and 2. ....	27
Figure 26. Illustration. FE model with delamination 6 inches from the left edge for cases 3 and 4. ....	27
Figure 27. Equation. Point load function. ....	27
Figure 28. Graph. Time histories of accelerations received for case 1. ....	28
Figure 29. Graph. Time histories of accelerations received for case 2. ....	29
Figure 30. Graph. Data from receiver No. 16 from an IE test. ....	29
Figure 31. Graph. Frequency spectrum of data from receiver No. 16 from an IE test. ....	30
Figure 32. Graph. Data from receivers Nos. 16 and 20 from a USW test. ....	30
Figure 33. Graph. Phase differences between receivers Nos. 16 and 20 from a USW test. ....	31
Figure 34. Graph. Time histories of accelerations received for case 3. ....	32
Figure 35. Graph. Time histories of accelerations received for case 4. ....	32
Figure 36. Graph. Data from receiver No. 12 from an IE test. ....	33
Figure 37. Graph. Frequency spectrum of data from receiver No. 12 from an IE test. ....	33
Figure 38. Graph. Data from receivers Nos. 12 and 16 from a USW test. ....	34
Figure 39. Graph. Phase differences between receivers Nos. 12 and 16 from a USW test. ....	34
Figure 40. Illustration. Geometry of a concrete slab with defects for heat-transfer analysis. ....	36

Figure 41. Plots. Temperatures at different times in the cooling period for shallow delaminations. ....	37
Figure 42. Graph. Temperature change at shallow delamination defect points for 2-inch-deep delamination without an overlay. ....	38
Figure 43. Graph. Temperature change at shallow delamination defect points for 2-inch-deep delamination with an asphalt overlay and no waterproof membrane. ....	40
Figure 44. Graph. Temperature change at deep delamination defect points for 6-inch-deep delamination without an overlay. ....	42
Figure 45. Photos. Artificial delamination. ....	44
Figure 46. Photos. Artificial honeycombing. ....	45
Figure 47. Photos. Artificial void. ....	46
Figure 48. Photos. Artificial vertical crack. ....	47
Figure 49. Illustration. Accelerated corrosion setup. ....	48
Figure 50. Photos. Precorroded rebar with accelerated corrosion. ....	49
Figure 51. Photos. Installed artificial defects and construction of specimens. ....	50
Figure 52. Illustration. Accelerated corrosion setup. ....	52
Figure 53. Photo. Accelerated corrosion of precorroded rebar. ....	52
Figure 54. Photos. Active corrosion and cracking after 1 week of accelerated corrosion. ....	52
Figure 55. Photos. NDE tests of specimens without overlays. ....	56
Figure 56. Photos. Temperature chamber. ....	57
Figure 57. Graphs. NDE condition maps with sounding. ....	63
Figure 58. Graphs. NDE condition maps with USW. ....	67
Figure 59. Graphs. NDE condition maps with IE. ....	72
Figure 60. Graphs. NDE C-scans with UT-MIRA. ....	77
Figure 61. Graphs. NDE B-scans with UT-MIRA. ....	81
Figure 62. Graphs. NDE C-scans with UT-EyeCon. ....	85
Figure 63. Graphs. NDE B-scans with UT-EyeCon. ....	89
Figure 64. Graphs. NDE condition maps with IR. ....	94
Figure 65. Graphs. NDE B-scan and condition map of specimen S1 with GPR before accelerated corrosion. ....	96
Figure 66. Graphs. NDE C-scans with GPR after accelerated corrosion. ....	101
Figure 67. Graphs. NDE B-scans with GPR after accelerated corrosion. ....	105
Figure 68. Graphs. NDE condition maps with GPR after accelerated corrosion. ....	109
Figure 69. Graph. NDE condition map of specimen S1 with ER before accelerated corrosion. ....	110
Figure 70. Graphs. NDE condition maps with ER after accelerated corrosion. ....	114
Figure 71. Graph. NDE condition map of specimen S1 with HCP before accelerated corrosion. ....	115
Figure 72. Graphs. NDE condition maps with HCP after accelerated corrosion. ....	119
Figure 73. Graphs. NDE IRT (temperature at 3:00 p.m.). ....	124
Figure 74. Graphs. NDE IRT (temperature difference 11:00 a.m. to 3:00 p.m.). ....	128
Figure 75. Photos. Concrete surface preparation for overlays. ....	134
Figure 76. Photos. Constructing an epoxy polymer overlay. ....	135
Figure 77. Photos. Constructing latex and silica fume-modified concrete overlays. ....	136
Figure 78. Photos. Constructing a polyester polymer overlay. ....	137
Figure 79. Photo. Latex and silica fume overlays after construction. ....	138

Figure 80. Photos. Samples of liquid and sheet membranes.....	138
Figure 81. Photos. Installing a liquid membrane and parchment paper for debonding. ....	139
Figure 82. Photos. Installation of sheet membrane and parchment paper for debonding. ....	140
Figure 83. Photo. Parchement paper installation for debonding on an asphalt overlay with no waterproof membrane. ....	140
Figure 84. Photos. Constructing asphalt overlays on three specimens. ....	141
Figure 85. Graphs. NDE condition maps from the sounding method. ....	146
Figure 86. Graphs. NDE condition maps of four specimens for the USW method.....	149
Figure 87. Graph. Modulus versus temperature with the USW method on specimen S7A. ....	150
Figure 88. Graphs. NDE condition maps of three specimens with the USW method.....	151
Figure 89. Graphs. NDE condition maps of four specimens with the IE method. ....	154
Figure 90. Graphs. Dominant frequency versus temperature using the IE method on specimen S7A.....	155
Figure 91. Graphs. NDE condition maps of three specimens with the IE method. ....	156
Figure 92. Graphs. NDE C-scans four specimens with UT-MIRA. ....	159
Figure 93. Graphs. NDE B-scans in bonded area of four specimens with UT-MIRA. ....	161
Figure 94. Graphs. NDE B-scans in debonded area of four specimens with UT-MIRA. ....	163
Figure 95. Graphs. NDE C-scans of four specimens with UT-EyeCon. ....	165
Figure 96. Graphs. NDE B-scans in bonded area of four specimens with UT-EyeCon.....	167
Figure 97. Graphs. NDE B-scans in debonded area of four specimens with UT-EyeCon. ....	169
Figure 98. Graphs. NDE B-scans of the debonded and intact areas of specimen S7A. ....	172
Figure 99. Graphs. NDE C-scans of three specimens with UT-MIRA. ....	174
Figure 100. Graphs. NDE B-scans in bonded area of three specimens with UT-MIRA.....	175
Figure 101. Graphs. NDE B-scans in debonded area of three specimens with UT-MIRA. ....	177
Figure 102. Graphs. NDE condition maps with IR.....	181
Figure 103. Graphs. NDE C-scans with the GPR method.....	185
Figure 104. Graphs. NDE B-scans in bonded areas with the GPR method.....	189
Figure 105. Graphs. NDE B-scans in debonded areas with the GPR method. ....	193
Figure 106. Graphs. NDE condition maps with the GPR method. ....	197
Figure 107. Graphs. NDE condition maps with the ER method.....	198
Figure 108. Graphs. NDE condition maps with HCP.....	202
Figure 109. Graphs. NDE using the IRT method (temperature at 3:00 p.m.). ....	206
Figure 110. Graphs. NDE using the IRT method (temperature difference from 3:00 to 11:00 a.m.).....	210
Figure 111. Photo. Test section of the Clara Barton Parkway cantilever structure. ....	219
Figure 112. Photo. RABIT.....	220
Figure 113. Graph. NDE condition map with the USW method.....	220
Figure 114. Graph. NDE condition map with the IE method. ....	221
Figure 115. Graph. NDE condition map with the GPR method. ....	221
Figure 116. Graph. NDE condition map with the ER method.....	222
Figure 117. Graph. NDE condition map with the USW method.....	223
Figure 118. Graph. NDE condition map with the IE method. ....	223
Figure 119. Graphs. NDE B-scans of the debonded and intact areas. ....	225

## LIST OF TABLES

Table 1. $\epsilon_r$ for various materials.....	9
Table 2. Relationship between resistivity and corrosion rate. ....	15
Table 3. Analysis matrix of NDE technologies. ....	22
Table 4. Ranking of NDE technologies for each defect based on accuracy. ....	23
Table 5. Properties of the materials used in the heat-transfer analysis. ....	35
Table 6. Depth of defects after assembly.....	51
Table 7. Equipment, test spacing, and parameters for nine NDE technologies.....	53
Table 8. Applicability of NDE technologies for detecting defects in concrete bridge deck specimens without overlays. ....	131
Table 9. Specimens and their respective overlays. ....	133
Table 10. NDE technologies for concrete bridge decks with epoxy overlays (S1E).....	213
Table 11. NDE technologies for concrete bridge decks with LMC overlays (S3L).....	214
Table 12. NDE technologies for concrete bridge decks with sheet membrane asphalt overlays (S4AS). ....	215
Table 13. NDE technologies for concrete bridge decks with liquid membrane asphalt overlays (S5AL). ....	215
Table 14. NDE technologies for concrete bridge decks with silica fume-modified overlays (S6S).....	216
Table 15. NDE technologies for concrete bridge decks with asphalt without waterproof membrane overlays (S7A).....	217
Table 16. NDE technologies for concrete bridge decks with PPC overlays (S8P). ....	218

## LIST OF ABBREVIATIONS AND SYMBOLS

### Abbreviations

2D	two-dimensional
3D	three-dimensional
AASHTO	American Association of State Highway and Transportation Officials
DC	direct current
DOT	department of transportation
EM	electromagnetic
EPC	epoxy polymer concrete
ER	electrical resistivity
FE	finite element
GPR	ground-penetrating radar
HCP	half-cell potential
IE	impact echo
IR	impulse response
IRT	infrared thermography
LMC	latex-modified concrete
NDE	nondestructive evaluation
PCC	portland cement concrete
PPC	polyester polymer concrete
PSPA	portable seismic property analyzer
RABIT	robotics-assisted bridge inspection tool
RC	reinforced concrete
SAFT	synthetic aperture focusing technique
SDOF	single-degree-of-freedom
SH	shear horizontal
USW	ultrasonic surface waves
UT	ultrasonic tomography

### Symbols

$c_t$	contact duration of impact
$F(t)$	impact function
$F_{amp}$	amplitude of the impact force
$Q$	infrared radiation
$R$	reflection strength
$T$	surface temperature
$t$	time
$\varepsilon$	emissivity
$\varepsilon_r$	dielectric constant
$\rho$	resistivity
$\sigma$	Stefan–Boltzmann constant



## CHAPTER 1. INTRODUCTION

Concrete bridge deck overlays have been used in the United States since 1960 to extend the service life of deteriorated concrete bridge decks and improve rideability. Concrete bridge decks with overlays deteriorate in different ways, including debonding, which is the most common defect.<sup>(1-3)</sup> Even if an overlay appears intact, the underlying concrete bridge deck may have hidden deterioration (e.g., rebar corrosion and delamination). Since the underlying concrete bridge deck is inaccessible, it is necessary to identify deteriorated areas through an overlay using nondestructive evaluation (NDE) technologies.

Various NDE technologies have been used to assess concrete bridge decks with overlays.<sup>(1-12)</sup> However, there have been no systematic studies on the applicability of various NDE technologies for evaluating concrete bridge decks with different types of overlays. Sounding has been used to locate debonding on portland cement concrete (PCC)-based overlays, but its ability to detect debonding on other types of overlays and delamination in underlying concrete bridge decks through bonded overlays has not been thoroughly examined.<sup>(1,2)</sup> The ultrasonic surface waves (USW) method has been used to detect overlay debonding and measure modulus, but the capability of USW to detect defects in underlying concrete bridge decks through bonded overlays has not been evaluated.<sup>(2-4)</sup> Although impact echo (IE) can detect overlay debonding and delamination in underlying bridge decks through bonded overlays, its applicable temperature range for asphalt overlays is yet undetermined.<sup>(2,5-8)</sup> Ultrasonic tomography (UT) and electrical resistivity (ER) have been used for detecting defects in bare decks, but their applicability for concrete bridge decks with different types of overlays has not been studied.<sup>(9)</sup> Impulse response (IR) has been used to detect debonding on PCC-based overlays, but its performance has not been examined for detecting debonding on other types of overlays or delamination in underlying concrete bridge decks through bonded overlays.<sup>(2,3,5)</sup> Half-cell potential (HCP) has been used to evaluate the ability of latex-modified concrete (LMC) and silica fume-modified concrete overlays to slow down rebar active corrosion, but their performance for other overlays has not been investigated.<sup>(1)</sup> Ground-penetrating radar (GPR) has been used to image delamination in concrete bridge decks with overlays, but its applicability to map the corrosive environment in underlying concrete bridge decks with various overlays has not been studied.<sup>(10,11)</sup> Although infrared thermography (IRT) could evaluate the overlay bonding condition, its applicability for detecting delamination in underlying concrete bridge decks through bonded overlays has not been examined.<sup>(10,12)</sup> Thus, many questions regarding the use of NDE technologies for concrete bridge decks with overlays remain unanswered.

This study focused on validating the applicability of nine commonly used NDE technologies to assess the condition of concrete bridge decks with seven types of overlays in the laboratory under controlled conditions and in the field under actual conditions. The nine NDE technologies are sounding, USW, IE, UT, IR, GPR, ER, HCP, and IRT. The seven overlays are epoxy polymer concrete (EPC), LMC, silica fume-modified concrete, polyester polymer concrete (PPC), asphalt with a liquid membrane, asphalt with a sheet membrane, and asphalt without a membrane. Field validation using the RABIT™ bridge deck assessment tool and manual testing equipment was performed. The results from the study on which this report is based complemented an extensive literature review summarized in table 3.



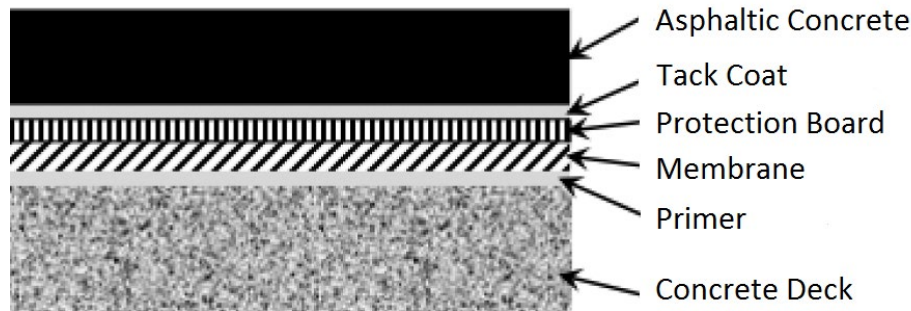
## CHAPTER 2. OVERVIEW OF SEVEN TYPES OF OVERLAYS

Concrete bridge deck overlays can protect the underlying concrete substrate, restore ride quality, provide added cover as protection for embedded reinforcement, and modify existing roadway vertical alignment or deck drainage. This study focused on seven types of overlays: asphalt with a liquid membrane, asphalt with a fabric membrane, asphalt without a membrane, PCC, LMC, EPC, and PPC. Overviews of these seven types of overlays are presented in the following sections. (The overviews for the liquid and fabric membranes are combined in a single section.)

### ASPHALT WITH A LIQUID OR FABRIC MEMBRANE

Asphalt overlays with waterproof membranes are widely used in the United States and other countries.<sup>(13,14)</sup> Out of 52 State departments of transportation (DOTs), 28 have used asphalt overlays with waterproof membranes.<sup>(15)</sup> Asphalt overlays with waterproof membranes consist of a primer, liquid or preformed sheet membrane, tack coat, and surface-wearing asphalt concrete. Depending on the manufacturer, the materials used for the liquid membrane can be rubberized asphalt, two-component polymer, polyurethane, methyl methacrylate, rubber polymer, polymer-modified asphalt, or rubberized bitumen. The materials for preformed sheet membranes are described by different manufacturers as rubberized asphalt, bituminous membrane, polymer-modified asphalt, modified bitumen, polymeric membrane, or bitumen and polymers.

The structure of an asphalt overlay with a waterproof membrane (liquid or preformed sheet) is shown in figure 1.



Source: FHWA.

**Figure 1. Illustration. Structure of an asphalt overlay with a liquid membrane.**

Following specifications from American Association of State Highway and Transportation Officials (AASHTO) and State DOTs, installations of asphalt overlays with waterproof membranes usually include the following steps:<sup>(16,17)</sup>

1. Surface preparation—the concrete bridge deck surface should be free of protrusions and rough edges. All contamination should be removed from the concrete bridge deck with abrasive blasting. The concrete bridge deck surface should be cleaned with brooms, vacuuming, or compressed air to remove all loose material. Cracks on the concrete bridge deck surface should be repaired.

2. Primer application—primer is used to enhance the bond between the concrete bridge deck and the membrane and is required by AASHTO and State DOT specifications or the manufacturer. The concrete bridge deck surface must be dry before applying primer.
3. Membrane application—a liquid membrane can be applied either hot or cold using spray equipment or rollers and squeegees based on manufacturer requirements. If a reinforcing fabric is used with a liquid membrane, one layer of liquid is sprayed before the fabric is placed and a second layer of liquid is sprayed on top of the placed fabric. A preformed sheet membrane either includes a self-adhesive backing or is bonded to the concrete bridge deck.
4. Tack coat application—a tack coat can be required by the manufacturer before an asphalt overlay is installed to enhance the bond between the membrane and overlay.
5. Protection board application—a protection board can be used to protect and waterproof a concrete bridge deck.
6. Asphalt concrete overlay installation—there should be enough time for the membrane to cure before the first layer of overlay is installed. To avoid potential damage, a membrane should not be exposed longer than the maximum time required by the manufacturer.

## **ASPHALT WITHOUT A MEMBRANE**

Asphalt concrete overlays without a waterproof membrane are usually not recommended for concrete bridge decks. When used, asphalt concrete overlays without a waterproof membrane are usually installed with a paving machine and compacted with a roller to provide a minimum compacted thickness of 1.5 inches. Necessary patching must be completed, and a tack coat can be applied prior to installation.<sup>(18)</sup> Out of 52 State DOTs, 37 have used asphalt concrete overlays without a waterproof membrane.<sup>(15)</sup>

## **PORTLAND CEMENT AND SILICA FUME-MODIFIED CONCRETE**

PCC-based overlays typically use the same concrete mixture as the concrete bridge deck and may or may not have reinforcement.<sup>(19–21)</sup> PCC-based overlays typically add supplementary cementitious materials, such as silica fume—a byproduct from the production of silicon or ferro-silicon alloys—and latex, to reduce permeability to moisture and chlorides. Typically, silica fume contains at least 85 percent amorphous silicon dioxide, allowing the silica fume to refine the pore structure of the cement paste and produce a denser matrix. However, the supplementary cementitious materials can cause shrinkage and cracking. The main advantage of PCC-based overlays is that their mechanical and thermal properties are similar to those of the concrete bridge deck. Out of 52 State DOTs, 25 have used PCC-based overlays.<sup>(15)</sup>

## **LMC**

LMC combines latex particles into PCC to replace a portion of the mix water.<sup>(22–24)</sup> LMC increases flexibility, decreases permeability, and increases resistance to chemicals but is prone to shrinkage and cracking. LMC has been a common overlay for concrete bridge decks over the last

decade. LMC can be installed and cured within 56 hr of lane closure.<sup>(18)</sup> Based on field data, the service life of LMC ranges from 22 to 26 yr.<sup>(18)</sup>

Installing LMC requires specialized equipment and contractor experience because it is sensitive to weather conditions. The curing process of LMC differs from normal concrete in that LMC should be covered with saturated burlap immediately after casting. The burlap should stay in place for the first 48 hr, followed by air curing for another 48 hr. Two standard specifications for LMC are available: American Concrete Institute 548.4-93, *Standard Specification for Latex-Modified Concrete (LMC) Overlays*;<sup>(26)</sup> and West Virginia Division of Highways Supplemental Specifications Section 679, *Overlaying of Portland Cement Concrete Bridge Decks*.<sup>(26)</sup> Out of 52 State DOTs, 36 have used LMC overlays.<sup>(15)</sup>

## **EPC**

EPC is formed by polymerizing a monomer and aggregate mixture.<sup>(7)</sup> The epoxy binder is a two-part system composed of the epoxy resin and a hardener/catalyst agent. EPC overlays are typically used as a preventative measure on concrete bridge decks with little to no damage. EPC overlays reduce permeability to moisture and chlorides and increase skid resistance. EPC overlays are formulated to cure rapidly and generally require less labor and specialized equipment than a rigid overlay. EPC overlays are effective when the thickness of the patches is <0.8 inch.<sup>(18)</sup> Depending on the traffic volume, the service life of EPC varies from 7 to 30 yr.<sup>(18)</sup> EPC overlays, also called multiple-layer overlays or broom-and-seed overlays, are installed by distributing a layer of epoxy polymer binder on the prepared concrete bridge deck surface with brooms, squeegees, or spray bars and then broadcasting gap-graded aggregates over the epoxy layer by hand, shovel, or automated spreading device. Two or three layers of epoxy and aggregate are typically used. Excess aggregate is blown off after each layer cures for 2 to 3 hr. Out of 52 State DOTs, 32 have used EPC overlays.<sup>(15)</sup> EPC shrinks more than the materials used to construct concrete bridge decks. Shrinkage can be reduced by proportioning mixtures to minimize the cement and water and maximize the aggregate content.<sup>(18)</sup>

## **PPC**

PPC is similar to EPC. PPC is a two-part system composed of a polyester resin and a hardener/initiator agent.<sup>(8)</sup> The initiator (e.g., organic peroxide) controls the rate of curing, and the resin is the principal ingredient that determines the chemical properties of the binder. The advantages of PPC overlays include rapid strength development (i.e., PPC only requires a 2-hr cure after placement), small water permeability, excellent freeze–thaw cycling resistance, high temperature resistance, and saturated water-vapor pressure resistance. PPC overlays are generally designed to be between 0.5 and 1 inch thick, depending on underlying surface conditions, and can also have iron ore coke added to increase conductivity for cathodic protection or to act as a heating element for deicing. The service life of PPC overlays varies from 15 to 20 yr and depends on the mixture and surface preparation, both of which are critical.<sup>(9,30)</sup> Out of 52 State DOTs, 16 have used PPC overlays.



## CHAPTER 3. OVERVIEW OF NDE TECHNOLOGIES

### INTRODUCTION

Both overlays and concrete bridge decks deteriorate over time. An overlay can debond or delaminate from the underlying concrete bridge deck and allow the permeation of moisture and chlorides, further exacerbating deterioration. If repairs are not made, debonded or delaminated overlay regions can deteriorate into open spalls and compromise the structural integrity of the concrete bridge deck. Destructive testing methods, such as coring, are costly, time consuming, and subjective depending upon where the cores were taken. NDE technologies are necessary to efficiently and accurately locate deteriorated areas in need of repair. Conventional NDE technologies, such as hammer sounding and chain dragging, are effective at inspecting overlay debonding and delamination but only marginally effective at assessing subsurface defects without removing an overlay. Researchers conducted a literature review and identified the following nine NDE technologies with the potential to detect and characterize deterioration in both overlays and concrete bridge decks:

- IRT.
- GPR.
- IE.
- USW.
- ER.
- HCP.
- UT.
- IR.
- Sounding.

### IRT

IRT has been used to detect subsurface defects, such as voids and delaminations, in concrete roadways and bridge structures. IRT uses cameras to measure the infrared radiation ( $Q$ ) (wavelength ranging from 0.7 to 14.0  $\mu\text{m}$ ) emitted by a structure, which is related to its surface temperature ( $T$ ) by the Stefan–Boltzmann law shown in figure 2.

$$Q = \varepsilon\sigma T^4$$

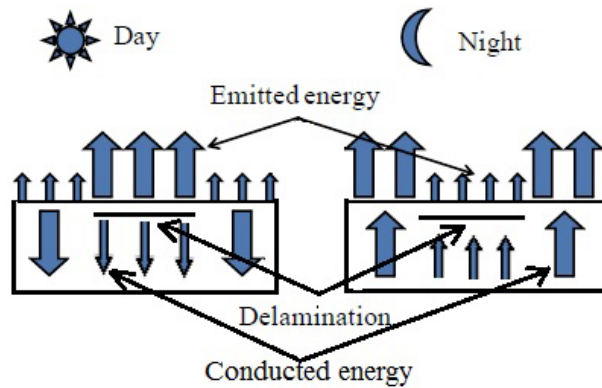
**Figure 2. Equation. Stefan–Boltzmann law.**

Where:

$\varepsilon$  = emissivity of the object.

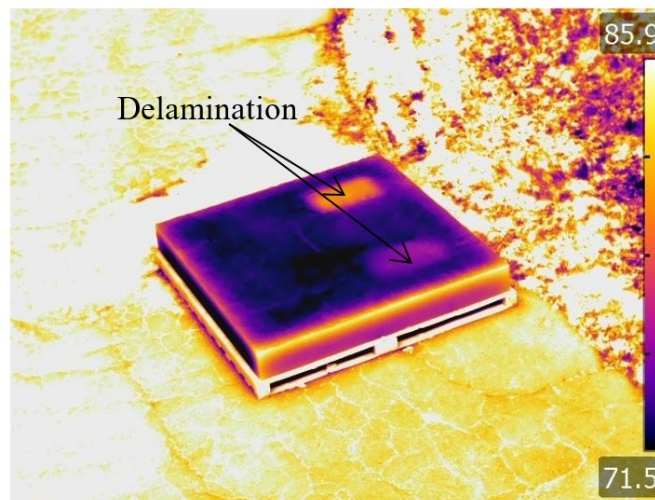
$\sigma$  = Stefan–Boltzmann constant ( $5.67 \times 10^{-8} \text{Wm}^{-2}\text{K}^{-4}$ ).

Anomalies, such as voids and delaminations, cause variations in material properties, such as thermal conductivity and capacity, resulting in different heating and cooling behaviors than the surrounding material, as shown in figure 3. Delaminated areas heat up and cool down more quickly than the surrounding concrete. In figure 4, areas with subsurface anomalies show higher temperatures than intact areas during the daytime (i.e., warming period).



Source: FHWA.

**Figure 3. Illustration. Heat flow of a concrete bridge deck with delamination.**



Source: FHWA.

**Figure 4. Photo. IRT of a concrete slab (measured at 1:00 p.m.).**

Even when following ASTM D4788-03, *Standard Test Method for Detecting Delaminations in Bridge Decks Using Infrared Thermography*, IRT has limitations.<sup>(31)</sup> Measurements are heavily dependent on weather conditions, surface anomalies, and boundary conditions. Deep flaws are difficult to detect, and the exact depth of flaws cannot be measured.

IRT may only reveal debonding on an overlay and fail to detect rebar-level delamination.<sup>(23,33)</sup> Despite the depth limitations, IRT is effective at detecting subsurface defects on concrete bridge decks.<sup>(21,22)</sup>

## GPR

GPR uses a ground-coupled antenna to transmit electromagnetic (EM) waves into a concrete bridge deck to provide a two-dimensional (2D) cross-sectional view of a concrete bridge deck. The EM waves reflect back to the surface when the dielectric constant ( $\epsilon_r$ ) of materials in the concrete bridge deck vary (i.e., when anomalies are detected). The  $\epsilon_r$  for different materials is shown in table 1. The strength of the reflection ( $R$ ) at an interface is related to the  $\epsilon_r$  of the materials and is calculated using the equation in figure 5, where a negative value indicates a phase change.<sup>(24,34)</sup> Part of the EM wave energy is reflected back to the receiver while the remainder continues penetrating the interface and is reflected back to the receiver from other interfaces until it is diminished. EM waves with a lower frequency can penetrate deeper than waves with a higher frequency but will have a lower resolution.

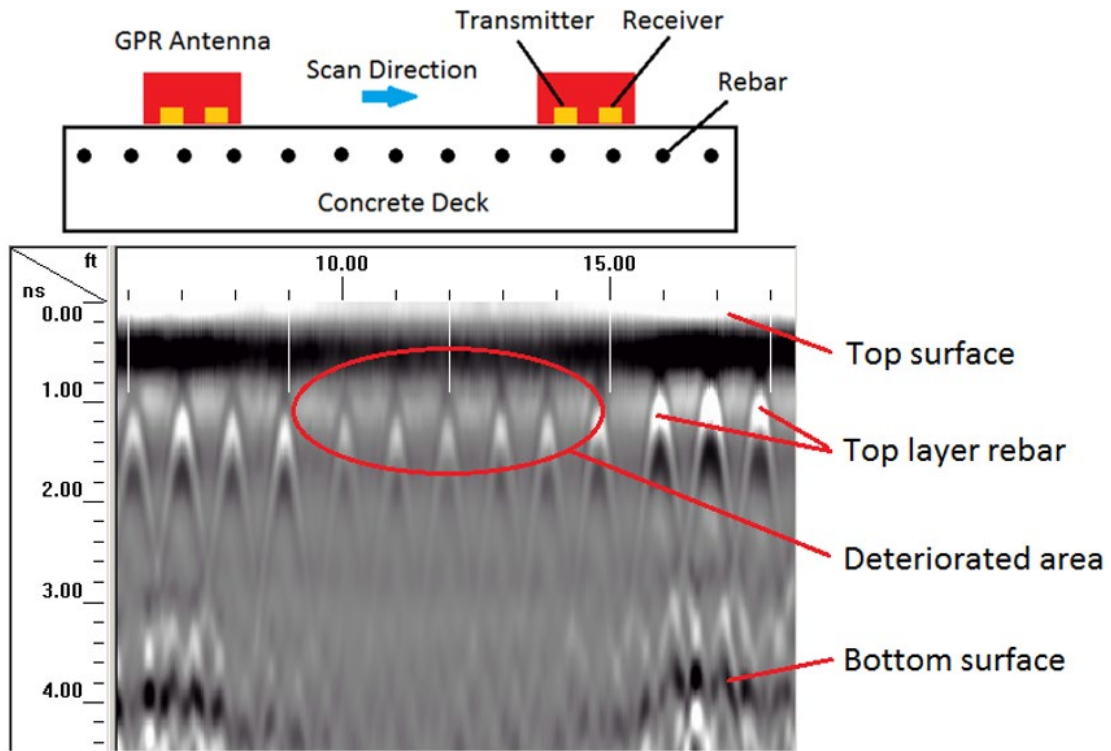
$$R = \frac{\sqrt{\epsilon_{r1}} - \sqrt{\epsilon_{r2}}}{\sqrt{\epsilon_{r1}} + \sqrt{\epsilon_{r2}}}$$

**Figure 5. Equation.  $R$  at an interface.**<sup>(34)</sup>

**Table 1.  $\epsilon_r$  for various materials.**

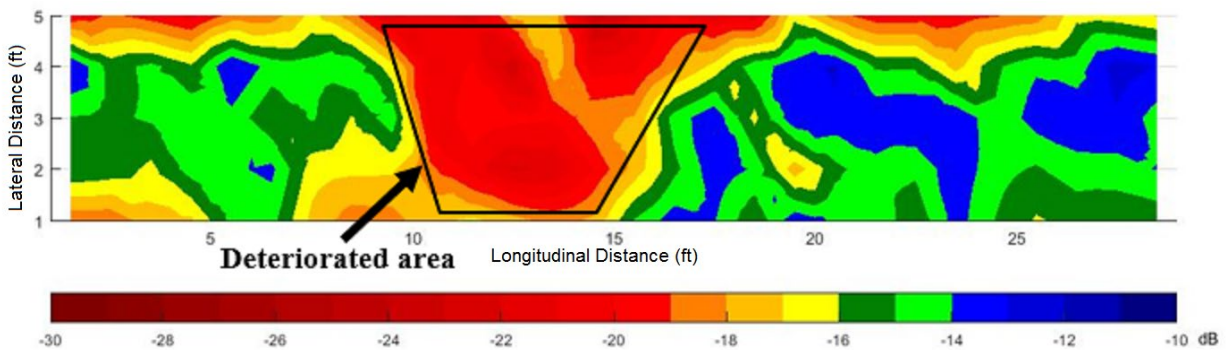
<b>Material</b>	<b><math>\epsilon_r</math></b>
Air	1.0
Water	81.0
Asphalt	4.0–8.0
Concrete	8.0–10.0
Insulation board	2.0–2.5

Corrosive concrete environments are usually high in free chloride ions that attenuate EM waves, which is why condition assessments of concrete bridge decks using GPR are based on evaluating the attenuation of EM waves at the uppermost rebar level. GPR scanning of a reinforced concrete bridge deck and the B-scan results are shown in figure 6. While A-scans are waveforms acquired at each scan point, B-scans offer a 2D cross-sectional view of the concrete bridge deck. GPR data are collected along equally spaced profile lines perpendicular to the direction of the uppermost rebar level of the concrete bridge deck.<sup>(35)</sup> A contour map of deterioration can be drawn based on the EM wave reflection at each rebar location. An example deterioration map for a concrete bridge deck is shown in figure 7.



Source: FHWA.

**Figure 6. Illustration. GPR scanning of a reinforced concrete bridge deck and the B-scan results.**



Source: FHWA.

**Figure 7. Graph. Deterioration map of a concrete bridge deck.**

Since the  $\epsilon_r$  of water and air are different from that of concrete, GPR can detect subsurface delamination. GPR has been reported as the only viable NDE method for evaluating the condition of concrete bridge decks with asphalt overlays.<sup>(36)</sup>

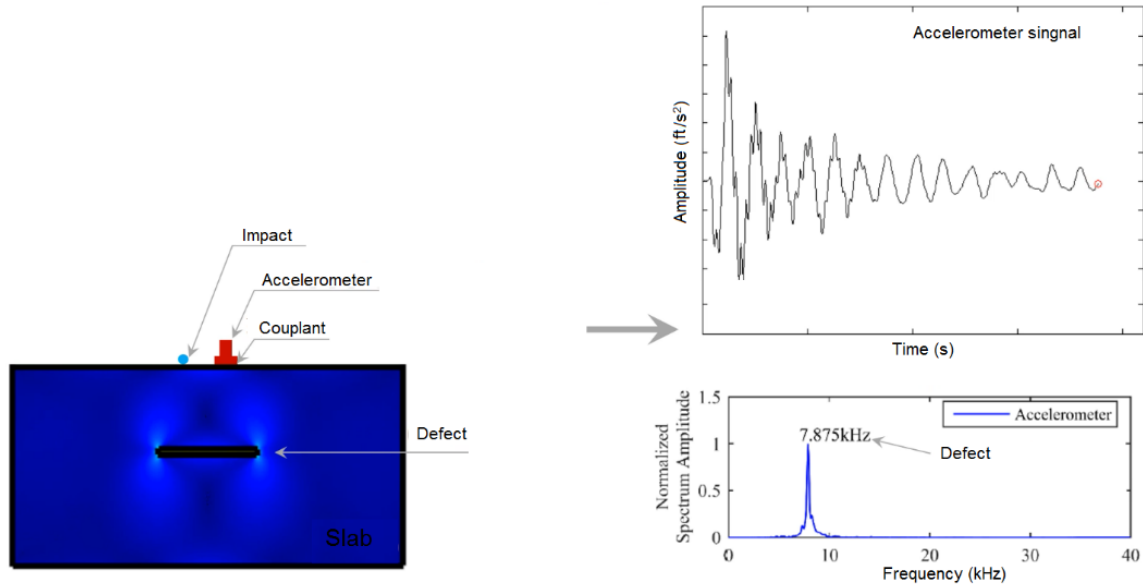
## IE

The IE method uses multiple stress wave reflections to detect defects in concrete bridge decks by striking the concrete bridge deck with an appropriate transient impact and measuring the surface motion at a selected location. Figure 8 shows a custom-built pneumatic acoustic array with eight impact–receiver pairs for IE tests. Figure 9 shows a schematic diagram of an IE test where the concrete bridge deck surface is struck by a transient impact, which can be wire-mounted steel spheres, solenoid-type impactors, or automated projectile sources, and the surface motion is measured by a physically coupled accelerometer or an air-coupled microphone. The frequency spectrum of the surface motion can be used to identify the peak frequency, which represents the transient resonances caused by multiple reflections of stress waves between the top of the slab surface and the reflector (e.g., delamination, slab bottom surface). The reflector is defined as the interface between two media with a relatively large acoustic impedance difference, such as concrete–air interface for delaminations and voids.



Source: FHWA.

**Figure 8. Photo. IE testing system.**



Source: FHWA.

**Figure 9. Illustration. Schematic of an IE test.**

An intact area has the dominant frequency corresponding to the bottom of the concrete bridge deck. A delaminated area introduces a shift of the dominant frequency because the stress waves are reflected at a shallower depth. The appearance of the dominant frequency in the spectrum depends on the continuity and dimension of the delamination. An initial delamination has stress wave reflections from the delamination and the concrete bridge deck bottom and can be identified through the presence of multiple dominant frequencies. A completely developed delamination is characterized by a single dominant frequency, which is identified as the thickness-mode frequency for a small and deep reflector or the flexural-mode frequency for a large and shallow reflector. The flexural-mode frequency usually falls in the audible frequency range.

IE has been used to detect debonding on concrete bridge decks with PPC overlays and delaminations within concrete bridge decks beneath asphalt overlays.<sup>(37–39)</sup> IE can detect small, deep defects but is less effective on decks with asphalt concrete overlays at high temperatures due to significant energy dissipation.<sup>(39)</sup>

## USW

USW are stress waves that travel along the free surface of a solid medium carrying about two-thirds of the total energy of the wave and contain the geometrical and mechanical information of the medium. Through the dispersion phenomenon of surface waves (i.e., phase velocity as a function of frequency or wavelength) in horizontally layered systems, the USW method obtains the thickness and elastic modulus of each layer. Detecting subsurface defects in concrete bridge decks with USW requires high-frequency surface waves with their penetration depths within the thickness of the concrete bridge deck. The high-frequency surface waves become nondispersive in decks—the phase velocity does not vary with frequency. This phase

velocity is used to calculate the elastic modulus with the assumed density and Poisson's ratio of the concrete bridge deck.

A USW test consists of the following three steps:

1. Stress waves are generated from an impact source and detected by a pair of receivers.
2. The dispersion curve is extracted from the wave motions with the spectral analysis of surface waves method.
3. The modulus is obtained with the phase velocity from the dispersion curve, assumed density, and Poisson's ratio of the concrete bridge deck.

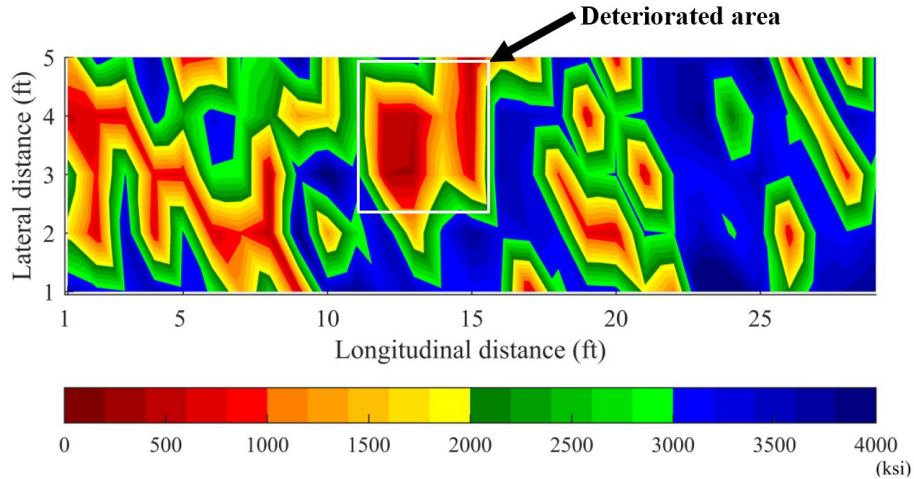
In real-world applications, the phase velocities of high-frequency surface waves in different concrete bridge decks inevitably show different extents of variations. An average velocity is used to calculate the concrete modulus. A significant variation of the phase velocity is an indication of a defect (e.g., delamination, void). A portable seismic property analyzer (PSPA) (figure 10) is a USW device that can be used to generate a modulus map to assess concrete bridge decks (figure 11).

The USW method has been used to monitor overlay stiffness and detect debonding in overlays.<sup>(37)</sup> When debonding occurs, low-frequency wave transmissions are lost, and it becomes time consuming and labor intensive to detect the quality of concrete bridge decks one location at a time.



Source: FHWA.

**Figure 10. Photo. PSPA.**

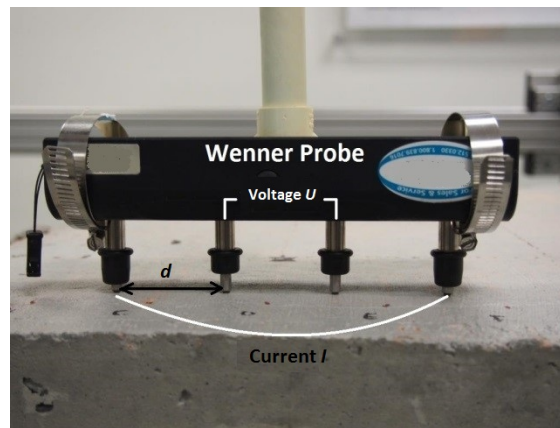


Source: FHWA.

**Figure 11. Graph. Modulus map of a concrete bridge deck.**

## ER

The ER method detects concrete's susceptibility to corrosion by characterizing its corrosive environment. The most common electrode layout in civil engineering applications is the Wenner probe shown in figure 12. Resistivity is calculated based on the current applied between the outer electrodes and the potential measured between the two inner electrodes according to the equation in figure 13. Water and chlorides decrease the ER of the concrete. The resistivity is on the order of 100 to 1,000  $\Omega\text{m}$  for fully saturated concrete and  $10^6 \Omega\text{m}$  for oven-dried concrete. The relationship between ER and the normally observed corrosion rate of reinforced concrete (RC) is given in table 2.<sup>(40)</sup>



Source: FHWA.

$U$  = potential in volts;  $d$  = distance between electrodes;  
 $I$  = current.

**Figure 12. Photo. Wenner probe.**

$$\rho = 2\pi d \frac{U}{I}$$

**Figure 13. Equation. Resistivity.**<sup>(40)</sup>

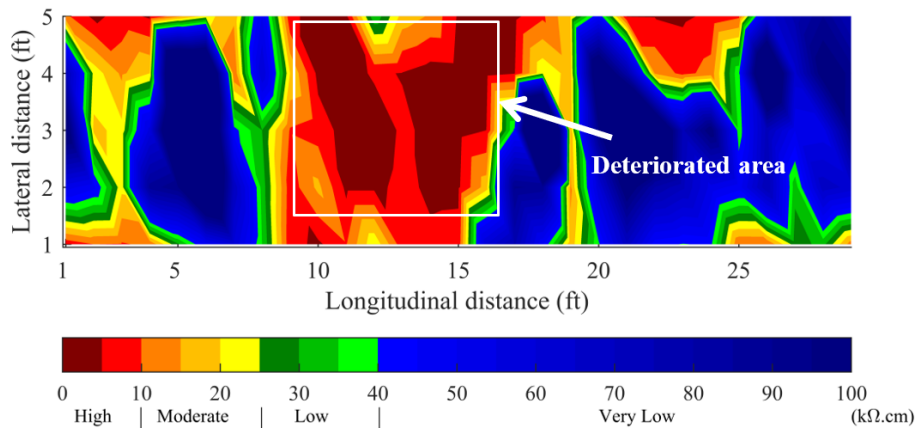
Where:

- $d$  = distance between electrodes.
- $\rho$  = resistivity.
- $U$  = potential in volts.
- $I$  = current.

**Table 2. Relationship between resistivity and corrosion rate.**

Resistivity (kΩcm)	Corrosion Rate
<5	Very high
5–10	High
10–20	Moderate
>20	Low

The electrodes need galvanic coupling to the concrete, and the surface of a test object must be wetted. Usually, ER data collected from a grid on the bridge deck can be used to create a contour map. One example is shown in figure 14. The ER method cannot work on concrete decks with electrically isolating coatings or overlays, such as asphalt overlays on bridge decks.



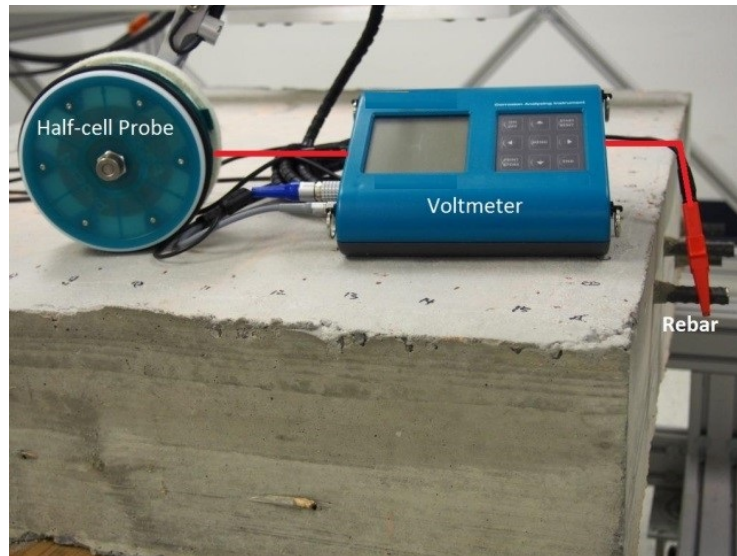
Source: FHWA.

**Figure 14. Graph. Corrosion rate map of a concrete bridge deck.**

## HCP

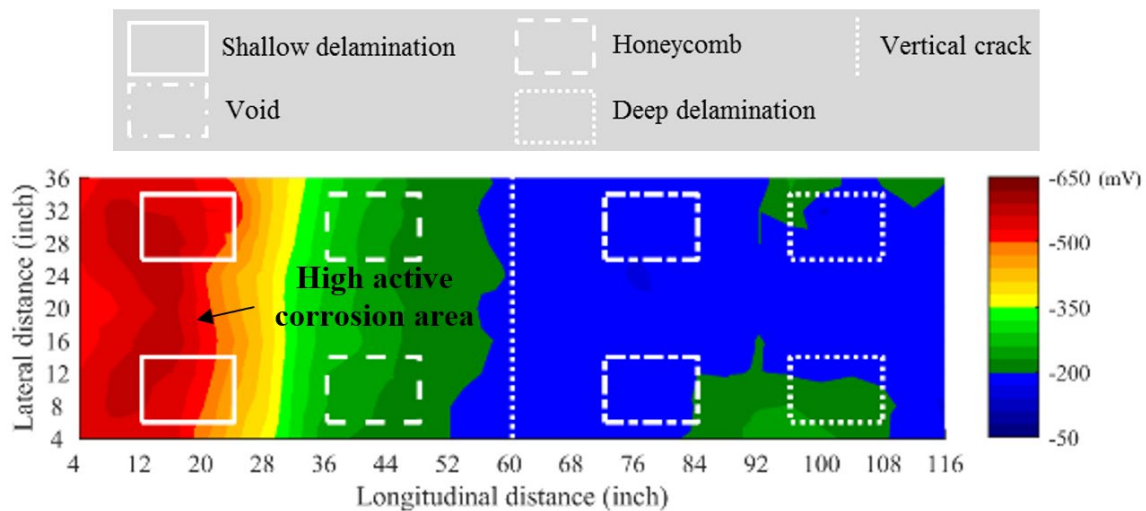
HCP is an electrochemical technique to evaluate active corrosion in rebar in concrete. The potential difference between a standard portable half-cell (usually a Cu/CuSO<sub>4</sub> standard reference electrode) and rebar is measured when the half-cell is placed on the surface of an RC element. HCP testing equipment is shown in figure 15. When there is active corrosion in the rebar, the electrical current induced by corrosion causes a lower potential compared to the reference electrode. According to ASTM C876-15, *Standard Test Method for Corrosion Potentials of Uncoated Reinforcing Steel in Concrete*, a measured potential lower than -350 mV

corresponds to a 90-percent probability of active corrosion, and a measured potential higher than  $-200$  mV corresponds to a 90-percent probability of no active corrosion.<sup>(41)</sup> The spatial distribution of corrosion potential can be mapped when the reference electrode is shifted along a line or grid on the surface of a member.<sup>(42)</sup> An example HCP measurement contour map is shown in figure 16.



Source: FHWA.

**Figure 15. Photo. HCP testing equipment.**



Source: FHWA.

**Figure 16. Graph. Contour map of active corrosion for a concrete bridge deck.<sup>(32)</sup>**

Half-cell measurements should be taken on a contaminant-free concrete surface, as the presence of isolating layers like asphalt and other coatings can make measurements erroneous or impossible.

## UT-MIRA

UT-MIRA uses shear waves polarized in the horizontal plane (shear horizontal (SH) waves) to detect objects under the concrete surface in a pulse–echo manner. A UT-MIRA tomographer in shown in figure 17 and figure 18. SH waves with a center frequency between 25 and 80 kHz can be generated by a short-burst, high-amplitude pulse through a dry-point contact. When SH waves are reflected by an object, the time from the start of the motion to the arrival of the echo is measured. If the wave speed is known, the depth of the object can be calculated as shown in figure 19.

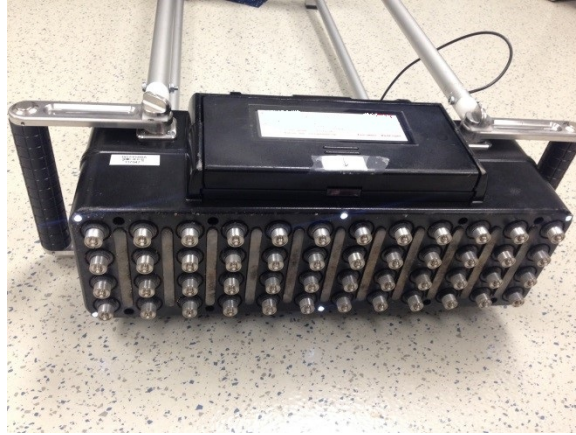
A UT-MIRA tomographer has a matrix antenna of 48 transducers with dry-dot contact and ceramic wear-resistant tips. The antenna is a 12×4 matrix of 12 blocks with 4 transducers in each block. Each transducer can be depressed up to  $\frac{1}{3}$  inch with an independent spring for complete contact of the antenna with the concrete surface. When one block of four transducers acts as the transmitter, the other blocks act as receivers. This pitch–catch configuration is repeated until each of the 11 blocks of transducers has acted as a transmitter. Data are analyzed using the synthetic aperture focusing technique (SAFT) to present a 2D cross-sectional image below the antenna (figure 20).<sup>(43)</sup> All data can be transferred to a computer and three-dimensional (3D) visualization software used to view different slices of the internal structure (figure 21).

UT-MIRA tomographers have been used to detect objects, such as rebar, delamination, and interface, in concrete bridge decks.<sup>(32,44)</sup> Scanning a concrete bridge deck with an overlay is challenging because the majority of the input energy is reflected by the overlay–deck interface.



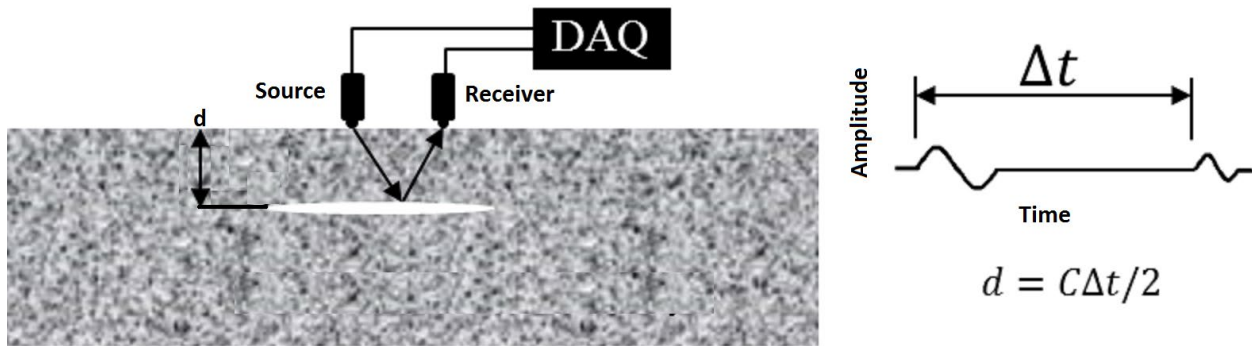
Source: FHWA.

**Figure 17. Photo. Top view of a UT-MIRA tomographer.**



Source: FHWA.

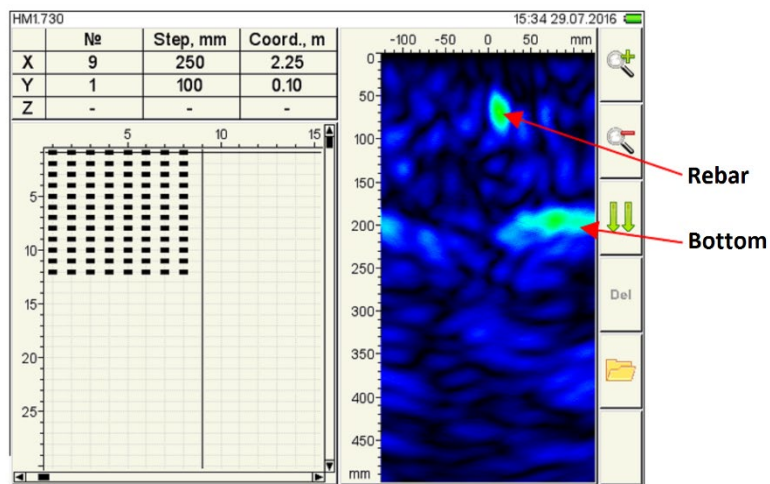
Figure 18. Photo. Bottom view of a UT-MIRA tomographer.



Source: FHWA.

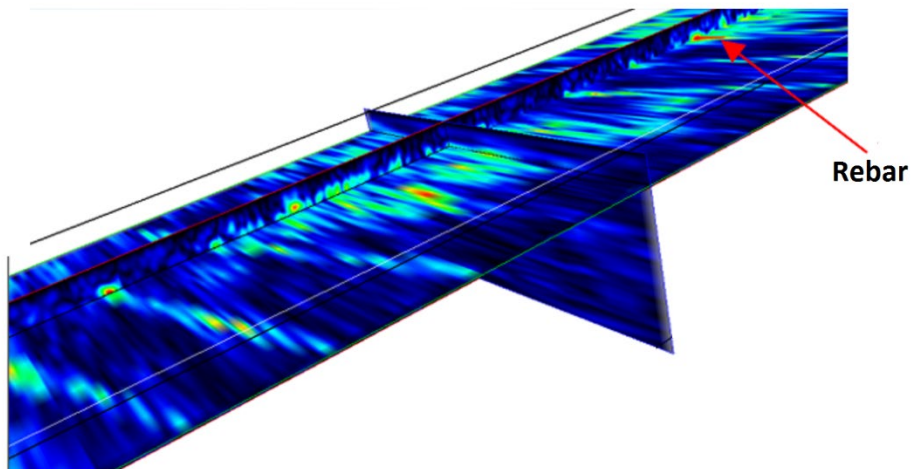
DAQ = data acquisition;  $C$  = shear wave velocity;  $\Delta t$  = difference in time.

Figure 19. Illustration. Ultrasonic pulse-echo.



Source: FHWA.

Figure 20. Graph. UT-MIRA B-scan from a test location.



Source: FHWA.

**Figure 21. Graph. 3D UT-MIRA scan of a concrete bridge deck.**

## IR

The IR method uses a sledgehammer with an embedded load cell to strike the concrete surface and a nearby geophone coupled to the concrete surface to record the surface motion and locate delaminations and voids in concrete bridge decks (figure 22). The fast Fourier transforms of the recorded impact force and velocity provide the force and velocity spectra, respectively, and then the velocity spectrum can be divided by the force spectrum to get the surface mobility spectrum (i.e., flexibility spectrum). The inverse ratio is the dynamic stiffness spectrum (i.e., mechanical impedance).

The spectrum from damaged areas is significantly different from that of sound areas.<sup>(32)</sup> A damaged area can be identified by a relatively large mobility in the contour plot of the average mobility of a concrete bridge deck. If the concrete plate response is approximated by the response of a single-degree-of-freedom (SDOF) system, the experimental mobility spectrum can be matched against the theoretical counterpart of the assumed SDOF system by varying its stiffness and damping.

The IR method has been used to detect debonding of overlays but requires a relatively large debonded area to create the flexural plate response, making it challenging when the overlay isolates the concrete bridge deck from the direct impact.<sup>(37)</sup>



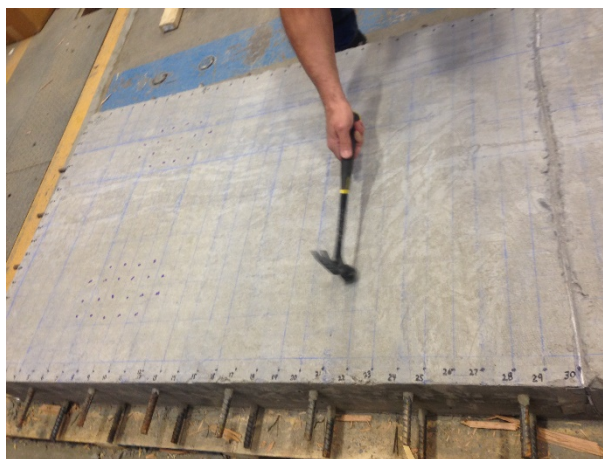
Source: FHWA.

**Figure 22. Photo. IR testing.**

## **SOUNDING**

The sounding method involves tapping the concrete structure with a hammer or dragging a chain along the surface and listening to the sound. Sounding is a fast, economical method for approximating delaminations in concrete bridge decks. Chain dragging is faster than hammer sounding, but hammer sounding can be used to more accurately define delamination boundaries. Figure 23 shows hammer sounding. An intact area makes a clear ringing sound, whereas a delaminated area produces a dull, hollow sound. An impact excites the flexural oscillation of a delaminated area and creates a drum-like effect with a hollow sound. The hollow sound typically ranges from 1 to 3 kHz, which is audible for a human ear.

Sounding has been used to detect debonding of thin overlays but is more difficult with thicker overlays.<sup>(37)</sup> Existing overlays must be removed to conduct sounding tests unless an operator has access to the underside of the concrete bridge deck.<sup>(38)</sup> The sounding method is subjective, and results depend on the operator's skill and experience.



Source: FHWA.

**Figure 23. Photo. Sounding with a hammer.**

## **RANK OF NDE TECHNOLOGIES FOR THE OVERLAY STUDY**

The literature review in the preceding sections identified nine NDE technologies with the potential to detect and characterize deterioration in concrete bridge decks with various overlays. Table 3 analyzes the applicability of each technology for specific defects. Six technologies (IE, UT, USW, IRT, Sounding, IR, and GPR) can detect overlay debonding and deck delamination. Three technologies (ER, HCP, and GPR) can detect rebar corrosion. Only one technology (USW) can detect vertical cracks. Table 4 ranks NDE technologies for each defect based on the accuracy provided by Gucunski et al.<sup>(32)</sup>

**Table 3. Analysis matrix of NDE technologies.**

Method	Overlay			Concrete Bridge Deck			
	Debonding	Vertical Crack	Concrete Degradation	Delamination	Rebar Corrosion	Vertical Crack	Concrete Degradation
IRT	✓	✗	✗	✓ Limited to depths up to 3–5 inches	✗	✗	✗
GPR	✓	✗	✗	✓	✓	✗	✗
ER	✗	✗	✗	✗	✓	✗	✗
HCP	✗	✗	✗	✗	✓	✗	✗
IE	✓ Asphalt overlays at low temperatures	✗	✗	✓ Works from both sides	✗	✗	✗
USW	✓	✓	✓	✓	✗	✓ If accessible from underside	✓
UT	Needs verification	✗	✗	✓ If accessible from underside	✗	✗	✗
IR	✓	✗	✗	✓ If accessible from underside	✗	✗	✗
Sounding	✓	✗	✗	✓ If accessible from underside	✗	✗	✗

✓ = applicable.

✗ = not applicable.

**Table 4. Ranking of NDE technologies for each defect based on accuracy.**

Ranking	Overlay			Concrete Bridge Deck			
	Debonding	Vertical Crack	Concrete Degradation	Delamination	Rebar Corrosion	Vertical Crack	Concrete Degradation
1	IE	USW	USW	IE	ER	USW	USW
2	USW	X	X	UT	HCP	X	X
3	IRT	X	X	USW	GPR	X	X
4	Sounding	X	X	IRT	X	X	X
5	IR	X	X	Sounding	X	X	X
6	GPR	X	X	IR	X	X	X
7	UT	X	X	GPR	X	X	X

X = no other effective technology.

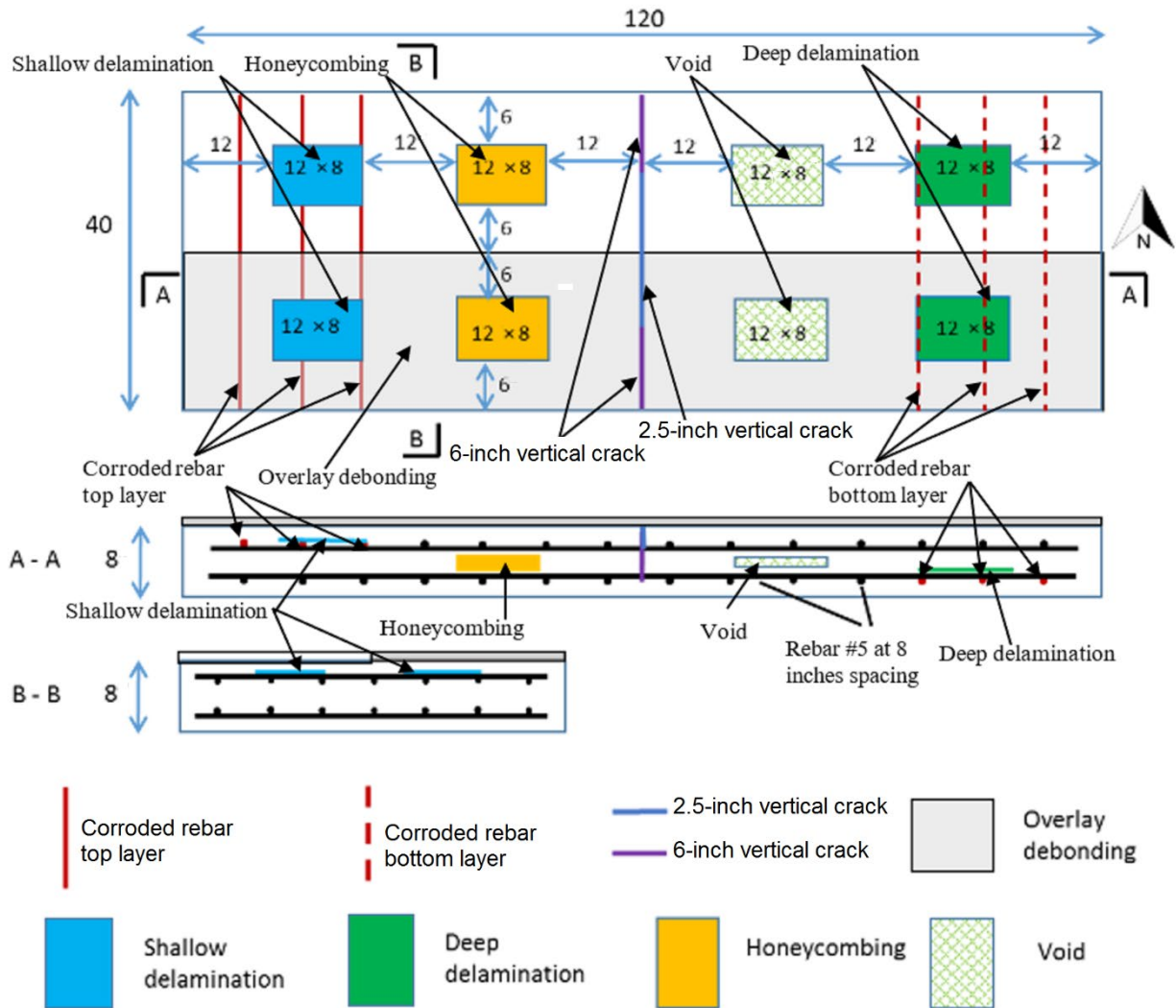


## CHAPTER 4. DESIGNING SMALL-SCALE SPECIMENS

This chapter describes the design of small-scale specimens for laboratory testing. Two finite element (FE) simulation efforts, one regarding boundary-effect analysis and the other heat-transfer analysis, are also covered in this chapter.

### SMALL-SCALE SPECIMEN DESIGN

Eight identical concrete specimens were designed and built with various artificial defects, including delamination at the upper and lower rebar levels, honeycombing, voids, vertical cracks, and precorroded rebar within an elevated chloride content environment. The procedures for designing and building the concrete specimens and creating artificial defects are covered in chapter 5. The design of the small-scale specimens with artificial defects is shown in figure 24. To simulate actual concrete bridge decks, the specimens have dimensions of 120×40×8 inches, use a normal-weight concrete mix with a water to cement ratio of 0.37 and a 28-d minimum compressive strength of 4,000 psi, and have two mats of uncoated steel reinforcement with No. 5 bars at a spacing of 8 inches in both transverse (the topmost layer) and longitudinal directions. To simulate real-world conditions, the specimens have 11 artificial defects, including 2 shallow delaminations, 2 deep delaminations, 2 areas of honeycombing, 2 voids, 1 vertical crack, and 2 pieces of corroded rebar mat within an elevated chloride content environment.

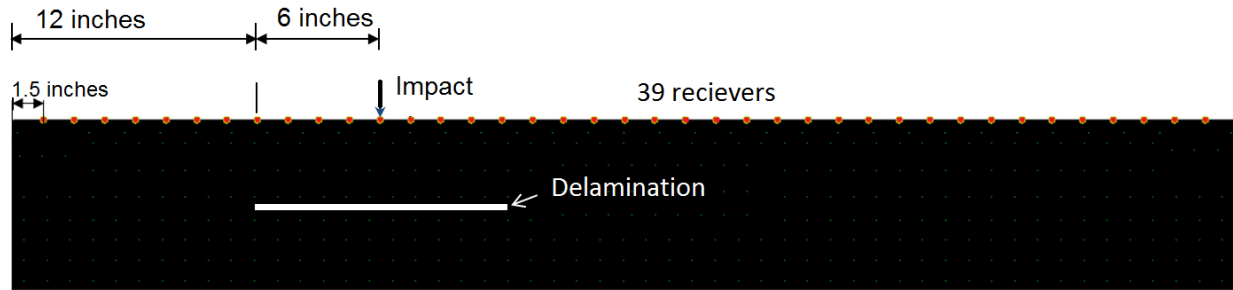


Source: FHWA.  
Note: Units are in inches.

**Figure 24. Illustration. Design of the small-scale specimens with artificial defects.**

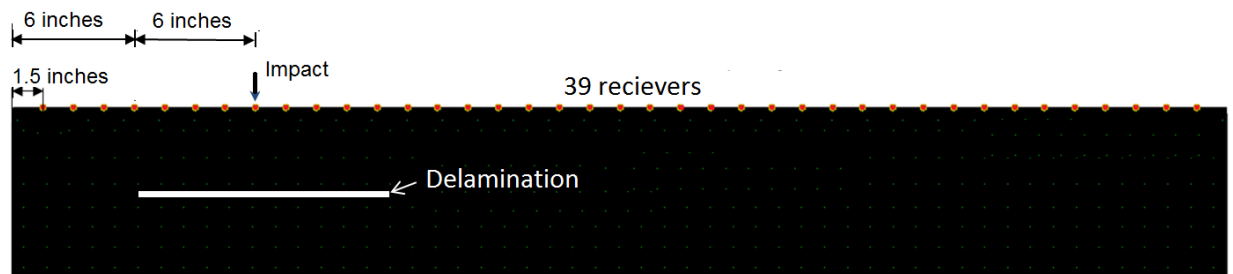
## BOUNDARY EFFECT ANALYSIS

Four 2D FE simulations were conducted to study the effect of boundary reflections on the IE and USW tests. Cases 1 and 2 had a delamination 12 inches from the left edge. Case 1 had a reflecting lateral boundary and case 2 had an absorbing lateral boundary. Cases 3 and 4 had a delamination 6 inches from the left edge. Case 3 had a reflecting lateral boundary and case 4 had an absorbing lateral boundary. The 2D FE models are shown in figure 25 and figure 26.



Source: FHWA.

**Figure 25. Illustration. FE model with delamination 12 inches from the left edge for cases 1 and 2.**



Source: FHWA.

**Figure 26. Illustration. FE model with delamination 6 inches from the left edge for cases 3 and 4.**

The details of the FE models were as follows:

- Concrete properties included a density of 150 lb/ft<sup>3</sup>, a Poisson's ratio of 0.2, Rayleigh damping of  $\alpha = 40$  and  $\beta = 6 \times 10^{-9}$ , and a Young's modulus of 5,076 ksi.
- Thickness was 8 inches, thickness resonant frequency was 9.7 kHz, and width was 5 ft.
- One delamination with a width of 12 inches at a depth of 4 inches was present.
- Meshing size was 0.5 inches (approximately 200,000 elements) with a time step of 1  $\mu$ s.
- A downward point load was applied on top of the delamination 1.5 inches from its left edge.

The point load was defined by the piecewise sine curve shown in figure 27:

$$F(t) = \begin{cases} -F_{amp}[\sin(t/t_c)]^2 & 0 < t < t_c \\ 0 & t > t_c \end{cases}$$

**Figure 27. Equation. Point load function.**

Where:

$F(t)$  = impact function.

$t$  = time in seconds.

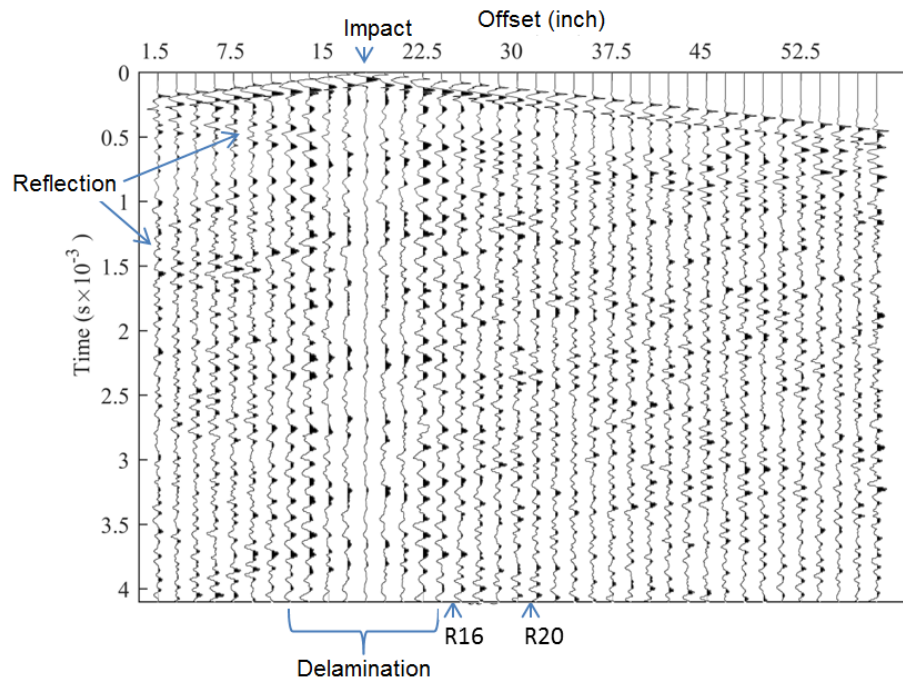
$F_{amp}$  = amplitude of the impact force (56 lbf in this study).

$t_c$  = contact duration of impact in seconds (0.1 ms in this study).

The point load was applied at the top center of the delamination. The vertical acceleration data from 39 locations with an interval of 1.5 inches on the top surface were extracted.

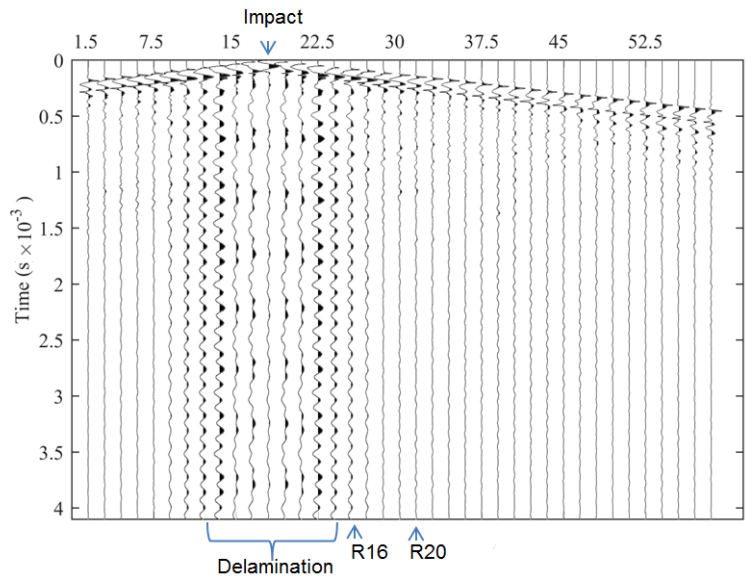
### Cases 1 and 2

Data from the 39 locations in cases 1 and 2 are shown in figure 28 and figure 29, respectively. Receivers Nos. 16 and 20 were 6 and 12 inches from the impact, respectively, which was the same as the setup for the PSPA. Data from receiver No. 16 are from an IE test and shown in figure 30. The time-domain signals from cases 1 and 2 were in agreement at the beginning and started to show differences after the reflection waves arrived (figure 30). The frequency domain spectra for cases 1 and 2 had the same dominant peak at 7.3 kHz, which researchers believed was the flexural frequency of the delamination (figure 31). Data from receivers Nos. 16 and 20 are from a USW test using PSPA and shown in figure 32. The reflection waves affected the far receiver more than the near receiver (figure 32). The phase difference between the two receivers was obtained from the cross-power spectrum analysis. Overall, the phase differences of cases 1 and 2 were in agreement. Case 2, with the absorbing lateral boundary, was smoother than case 1 (figure 33).



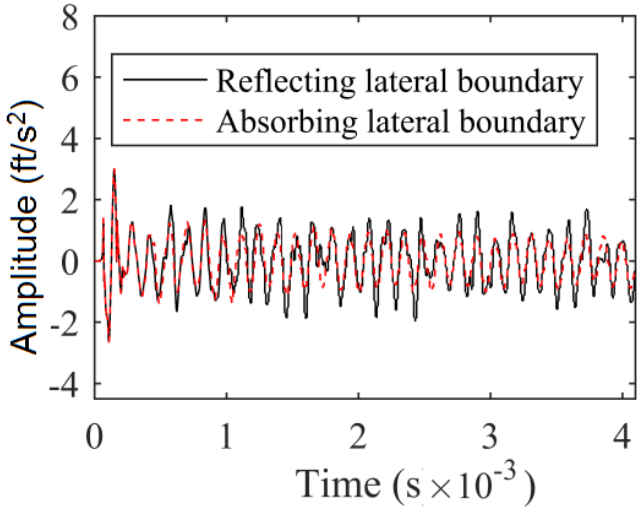
Source: FHWA.  
R16 = receiver 16; R20 = receiver 20.

**Figure 28. Graph. Time histories of accelerations received for case 1.**



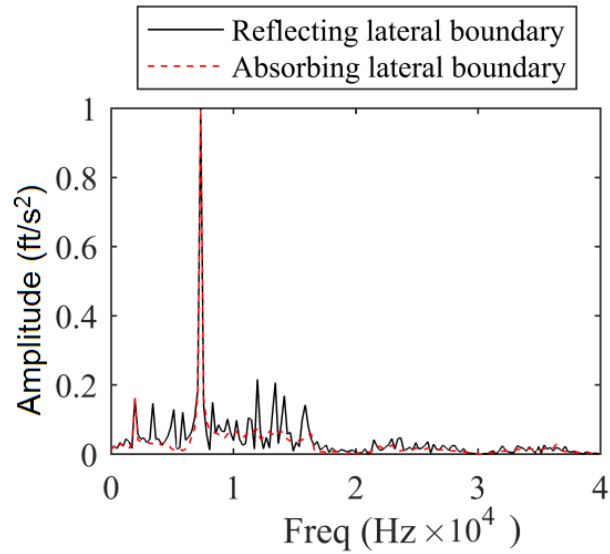
Source: FHWA.  
 R16 = receiver 16; R20 = receiver 20.

**Figure 29. Graph. Time histories of accelerations received for case 2.**



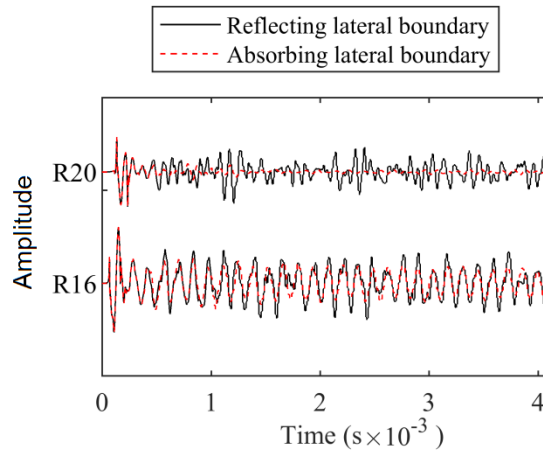
Source: FHWA.

**Figure 30. Graph. Data from receiver No. 16 from an IE test.**



Source: FHWA.

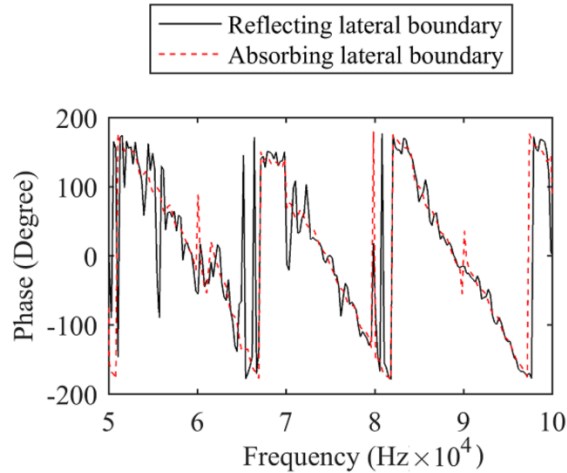
**Figure 31. Graph. Frequency spectrum of data from receiver No. 16 from an IE test.**



Source: FHWA.

R16 = receiver 16; R20 = receiver 20.

**Figure 32. Graph. Data from receivers Nos. 16 and 20 from a USW test.**

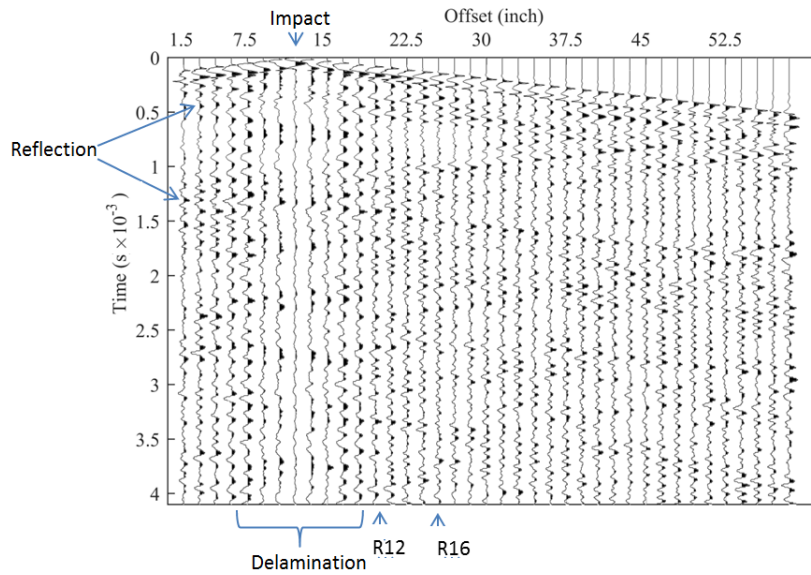


Source: FHWA.

**Figure 33. Graph. Phase differences between receivers Nos. 16 and 20 from a USW test.**

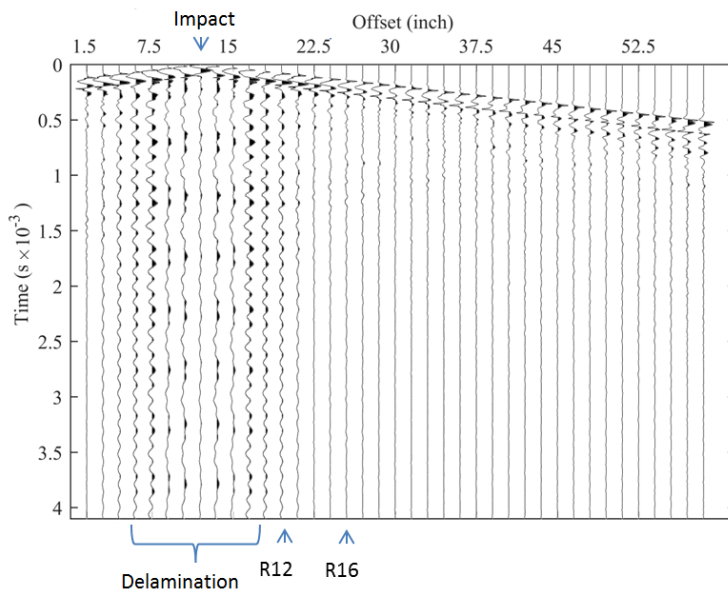
### Cases 3 and 4

Data from the 39 locations in cases 3 and 4 are shown in figure 34 and figure 35, respectively. Receivers Nos. 12 and 16 were 6 and 12 inches away from the impact, which was the same as the setup for the PSPA. Data from receiver No. 12 are from an IE test and shown in figure 36. The time-domain signals from cases 3 and 4 were in agreement at the beginning and started to show differences after the reflection waves arrived (figure 36). The frequency domain spectra for cases 3 and 4 had the same dominant peak at 7.3 kHz, which researchers believed was the flexural frequency of the delamination (figure 37). Data from receivers Nos. 12 and 16 are from a USW test using PSPA and shown in figure 38. The reflection waves affected the far receiver more than the near receiver (figure 38). The phase difference between the two receivers was obtained from the cross-power spectrum analysis. Overall, the phase differences of cases 3 and 4 were in agreement. Case 4, with absorbing lateral boundary, was smoother than case 3 (figure 39).



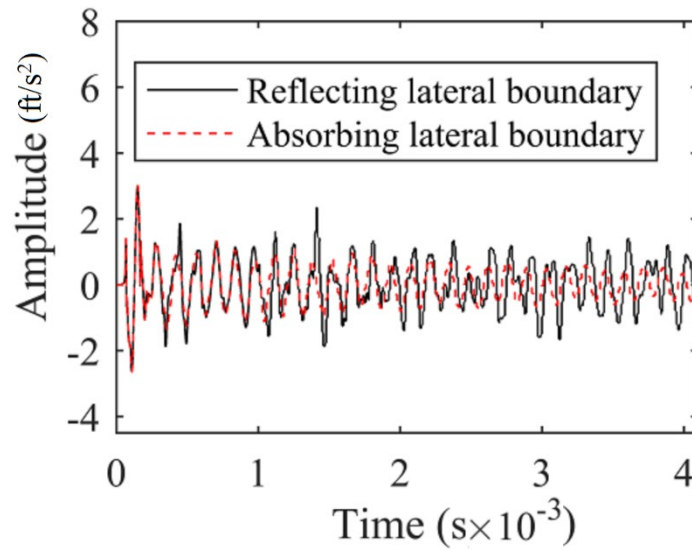
Source: FHWA.  
 R12 = receiver 12; R16 = receiver 16.

**Figure 34. Graph. Time histories of accelerations received for case 3.**



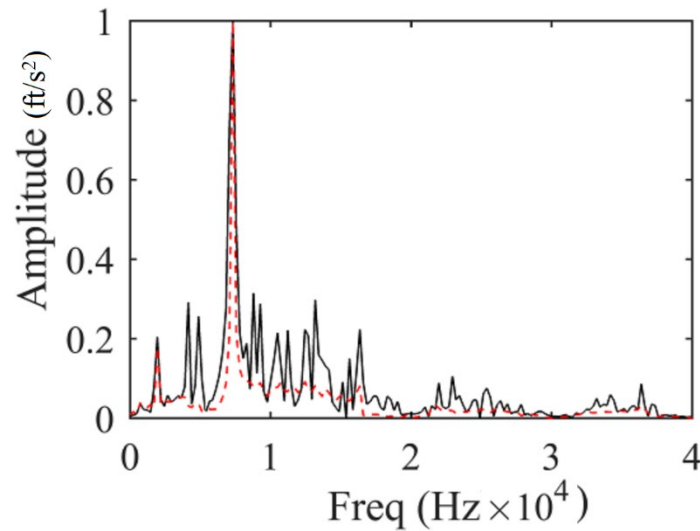
Source: FHWA.  
 R12 = receiver 12; R16 = receiver 16.

**Figure 35. Graph. Time histories of accelerations received for case 4.**



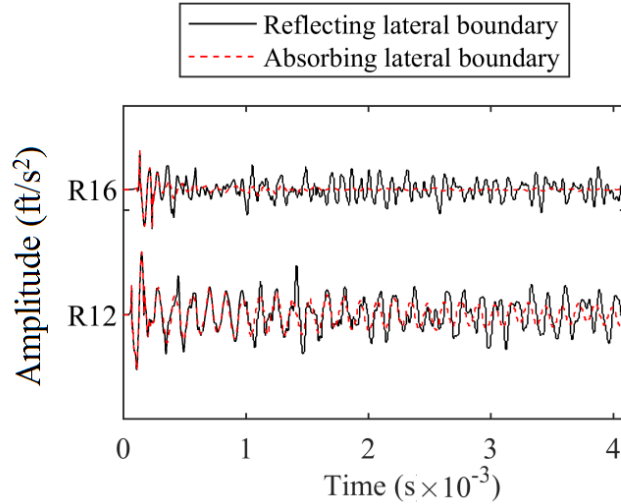
Source: FHWA.

**Figure 36. Graph. Data from receiver No. 12 from an IE test.**



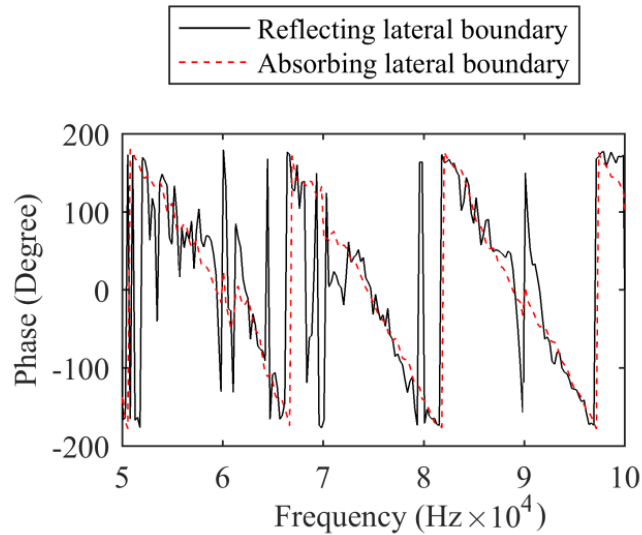
Source: FHWA.

**Figure 37. Graph. Frequency spectrum of data from receiver No. 12 from an IE test.**



Source: FHWA.  
R12 = receiver 12; R16 = receiver 16.

**Figure 38. Graph. Data from receivers Nos. 12 and 16 from a USW test.**



Source: FHWA.

**Figure 39. Graph. Phase differences between receivers Nos. 12 and 16 from a USW test.**

Results of the four FE simulations indicated the data suffer reflections from the two lateral boundaries for the models with reflecting boundaries, the IE test detected the flexural mode frequency of the delamination with boundary reflections, and the USW test captured the phase difference between two receivers with boundary reflections.

## HEAT-TRANSFER ANALYSIS

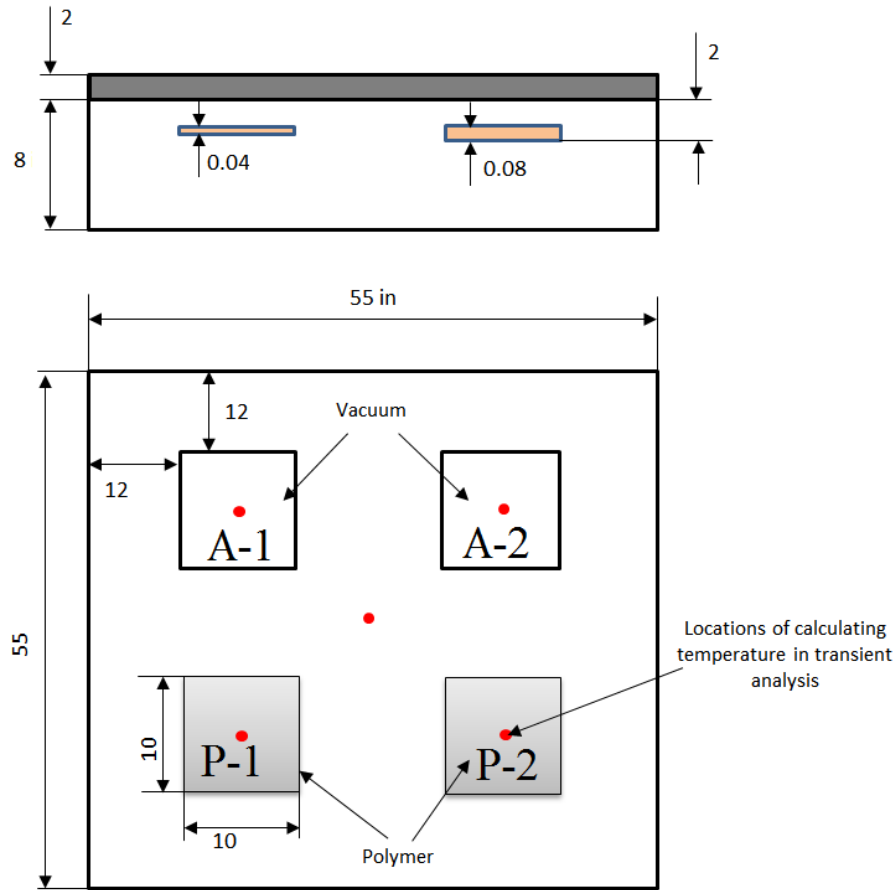
Heat-transfer analysis was performed with ABAQUS 6.16 for three different FE models to help researchers understand the capability of the IR method to detect delaminations. Delamination in concrete can be simulated by a thin layer of air, which is difficult to artificially create in a concrete specimen. Instead, researchers simulated delamination with a layer of foam insulation because it is made mostly of air.<sup>(45)</sup> The thin, flexible layer of foam insulation was sandwiched between two layers of transparent thermoplastic plates. In the FE model, the overall delamination thicknesses of 0.04 and 0.08 inch were considered for the combined air voids and foam insulation. To simplify the model, the air voids were modeled as a vacuum due to the small density and thermal conductivity factor, and the transparent thermoplastic plates were replaced by concrete material. The simplification yielded more conservative results since thermal conduction of the air void delamination was decreased and thermal conduction of the artificial delamination was increased. In addition to concrete slabs, 2 inches of asphalt overlay without a waterproof membrane was also simulated in the FE analysis. Thermal properties of the concrete, asphalt overlay, and foam insulation used to simulate a delamination in the FE analysis are shown in table 5.

**Table 5. Properties of the materials used in the heat-transfer analysis.**

<b>Material Type</b>	<b>Density lb/ft<sup>3</sup> (kg/m<sup>3</sup>)</b>	<b>Conductivity BTU/hr-ft<sup>2</sup>-F-in (W/m-K)</b>	<b>Specific Heat BTU/lb-F (J/kg-K)</b>
Normal-weight concrete	129.0 (2,400.0)	11.80 (1.70)	0.210 (880.000)
Hot-mix asphalt	86.0 (1,600.0)	8.30 (1.20)	0.220 (920.000)
Foam insulation	2.3 (40.0)	0.28 (0.04)	0.215 (900.000)

The schematic geometry of the model containing four delaminations is shown in figure 40. A concrete specimen of 55×55×8 inches was built, and the delaminations were 10×10 inches. The two delaminations on the left were modeled with a thickness of 0.04 inch (A-1 and P-1 in figure 40, where A indicates that the defect was modeled as a vacuum material and P indicates the polymer material) and the two delaminations on the right were modeled with a thickness of 0.08 inch (A-2 and P-2 in figure 40). The ambient temperature was set at 68°F

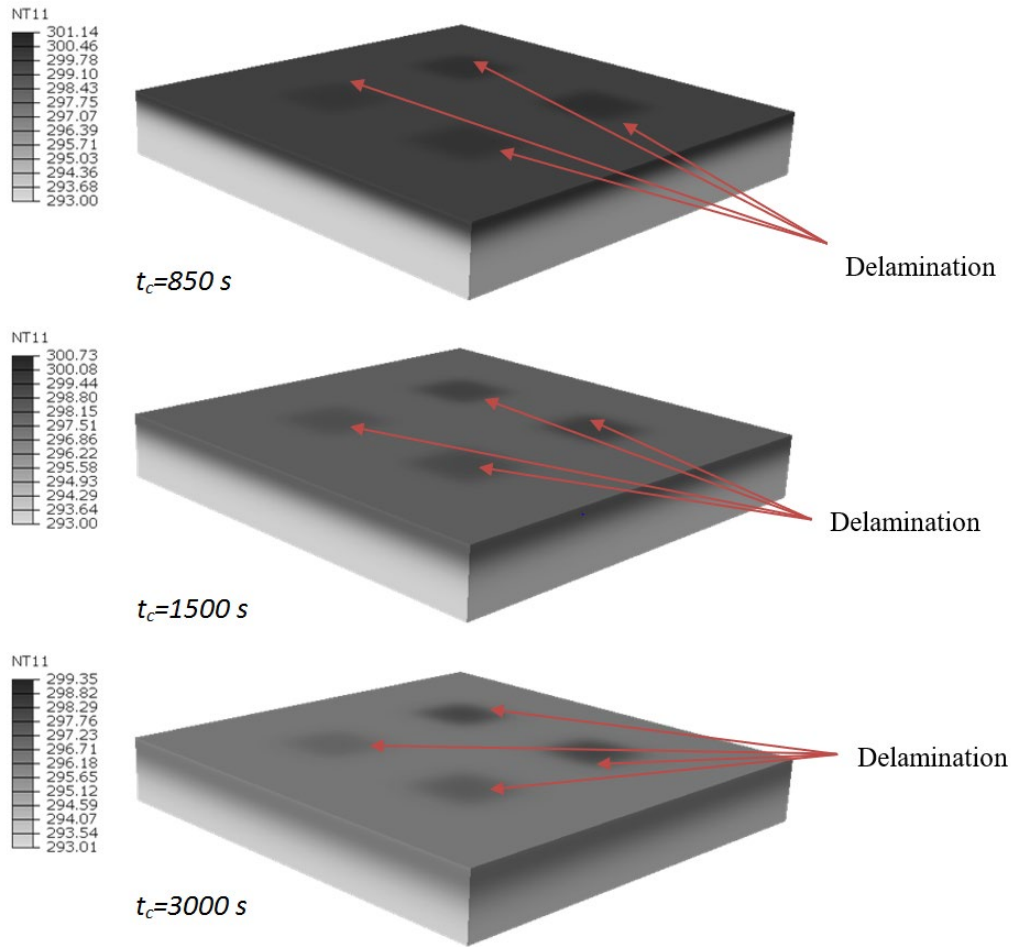
Three FE models with slight differences were investigated. In the first FE model, the delaminations were set 2 inches from the top surface of the concrete without overlay to simulate shallow delaminations. In the second FE model, the delaminations were set 2 inches from the top surface of the concrete with 2 inches of asphalt overlay with no waterproof membrane. In the third FE model, the delaminations were set 6 inches from the top surface of concrete without an overlay to simulate deep delaminations.



Source: FHWA.  
 Note: Measurements are in inches.

**Figure 40. Illustration. Geometry of a concrete slab with defects for heat-transfer analysis.**

In the first FE model, a heat influx of  $1,200 \text{ W/m}^2$  was applied to the top surface of the concrete for the first 1,000 s, and then the concrete was cooled for 3,000 s. The contour map of temperatures at different times in the cooling period for shallow delaminations is shown in figure 41. Time histories of the temperatures acquired from shallow delamination defect points on the top surface of the concrete are shown in figure 42. The greatest temperature difference was approximately  $3.6^\circ\text{F}$  from the 0.08-inch air voids, and the lowest temperature difference was approximately  $1.4^\circ\text{F}$  from the sandwiched structure with 0.04-inch foam insulation.

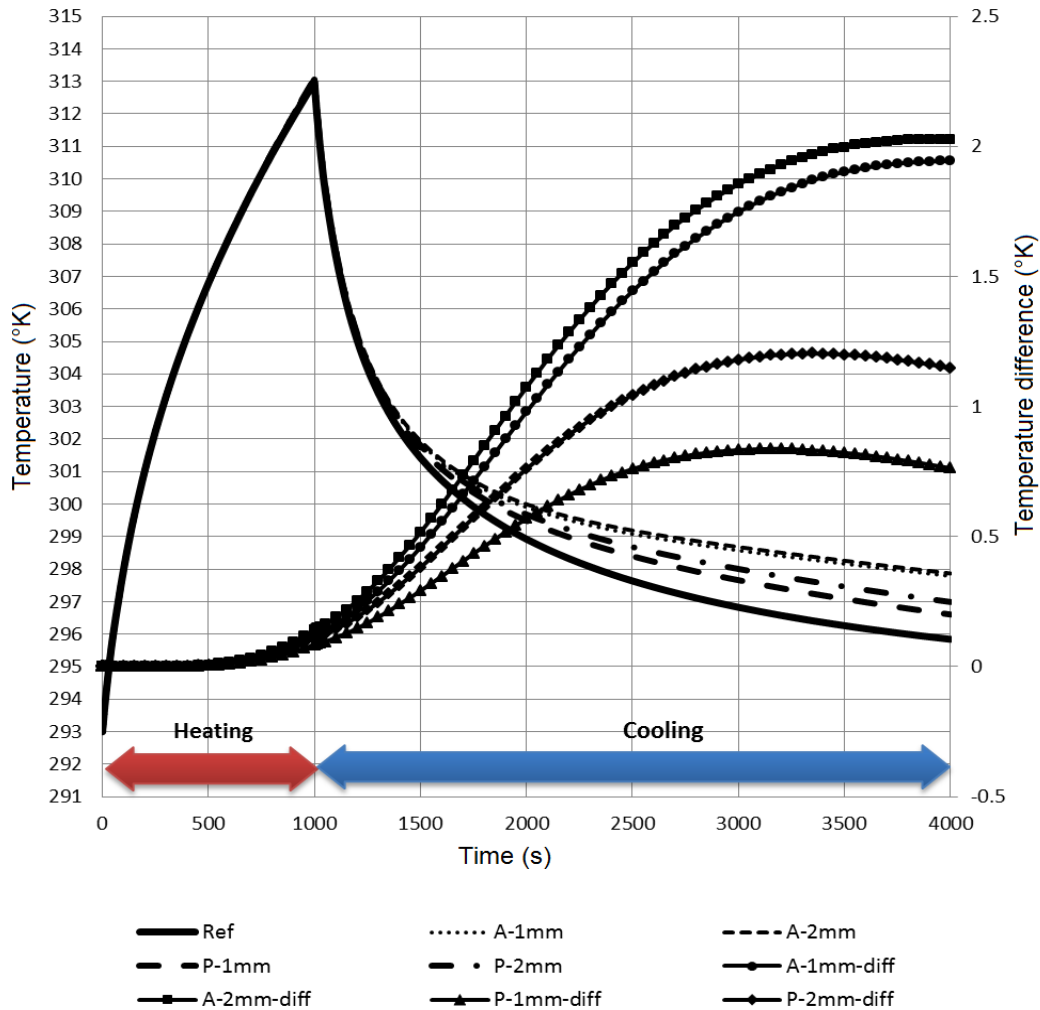


Source: FHWA.

$1^{\circ}\text{K} = -458^{\circ}\text{F}$ .

NT11 = surface temperature in  $^{\circ}\text{K}$ .

**Figure 41. Plots. Temperatures at different times in the cooling period for shallow delaminations.**



Source: FHWA.

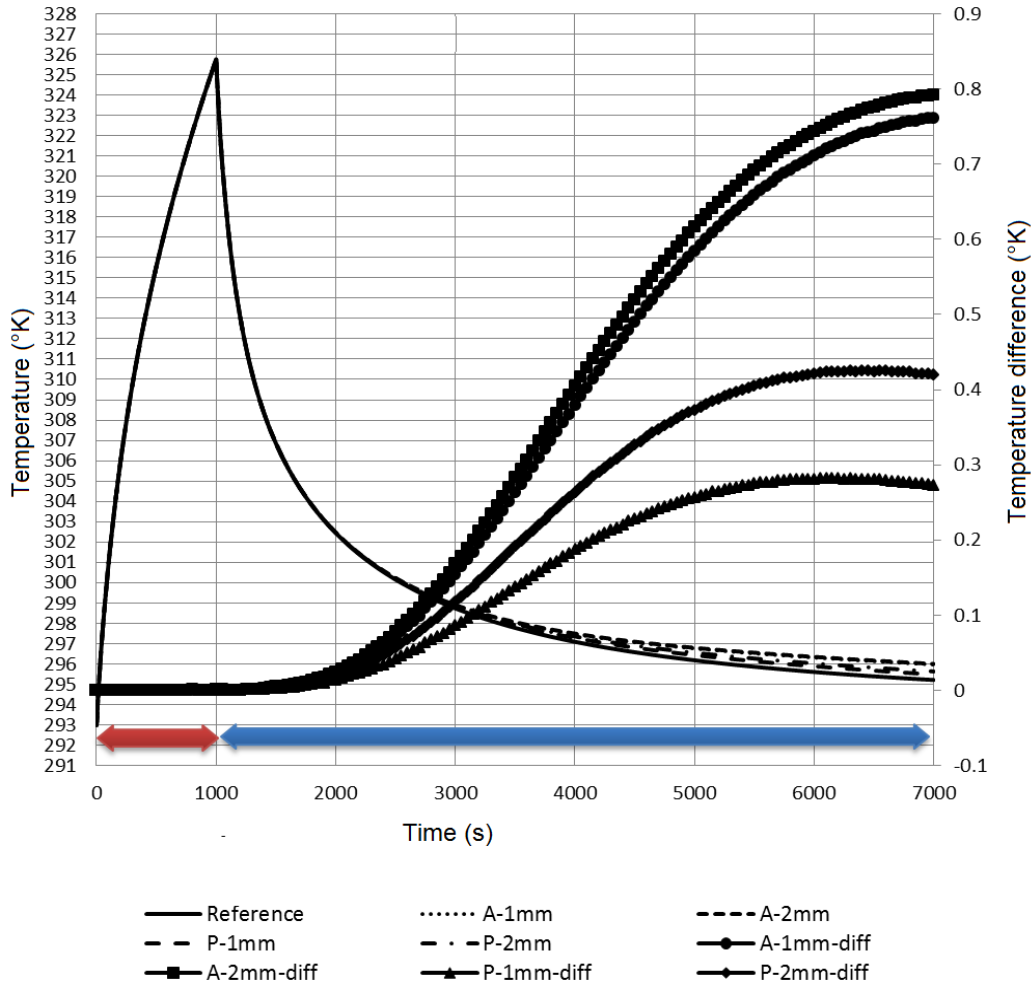
1°K = -458°F.

1 mm = 0.04 inch.

Ref = time history of the temperature for a reference point on the intact surface; A-1mm = time history of the temperature for a point on the air void defect with 1-mm thickness; A-2mm = time history of the temperature for a point on the air void defect with 2-mm thickness; P-1mm = time history of the temperature for a point on the polymer defect with 1-mm thickness; P-2mm = time history of the temperature for a point on the polymer defect with 2-mm thickness; A-1mm-diff = time history of the temperature difference relative to the reference point for a point on the air void defect with 1-mm thickness; A-2mm-diff = time history of the temperature difference relative to the reference point for a point on the air void defect with 2-mm thickness; P-1mm-diff = time history of the temperature difference relative to the reference point for a point on the polymer defect with 1-mm thickness; P-2mm-diff = time history of the temperature difference relative to the reference point for a point on the polymer defect with 2-mm thickness.

**Figure 42. Graph. Temperature change at shallow delamination defect points for 2-inch-deep delamination without an overlay.**

In the second FE model, a heat influx of  $1,200 \text{ W/m}^2$  was applied to the top surface of the 2-inch asphalt overlay for the first 1,000 s, and then the concrete was cooled for 6,000 s. The time histories of the temperature data acquired from shallow delamination defect points on the top surface are shown in figure 43. The greatest temperature difference was approximately  $1.4^\circ\text{F}$  from the 0.08-inch air voids, and the lowest temperature difference was approximately  $0.6^\circ\text{F}$  from the sandwiched structure with 0.04-inch foam insulation.



Source: FHWA.

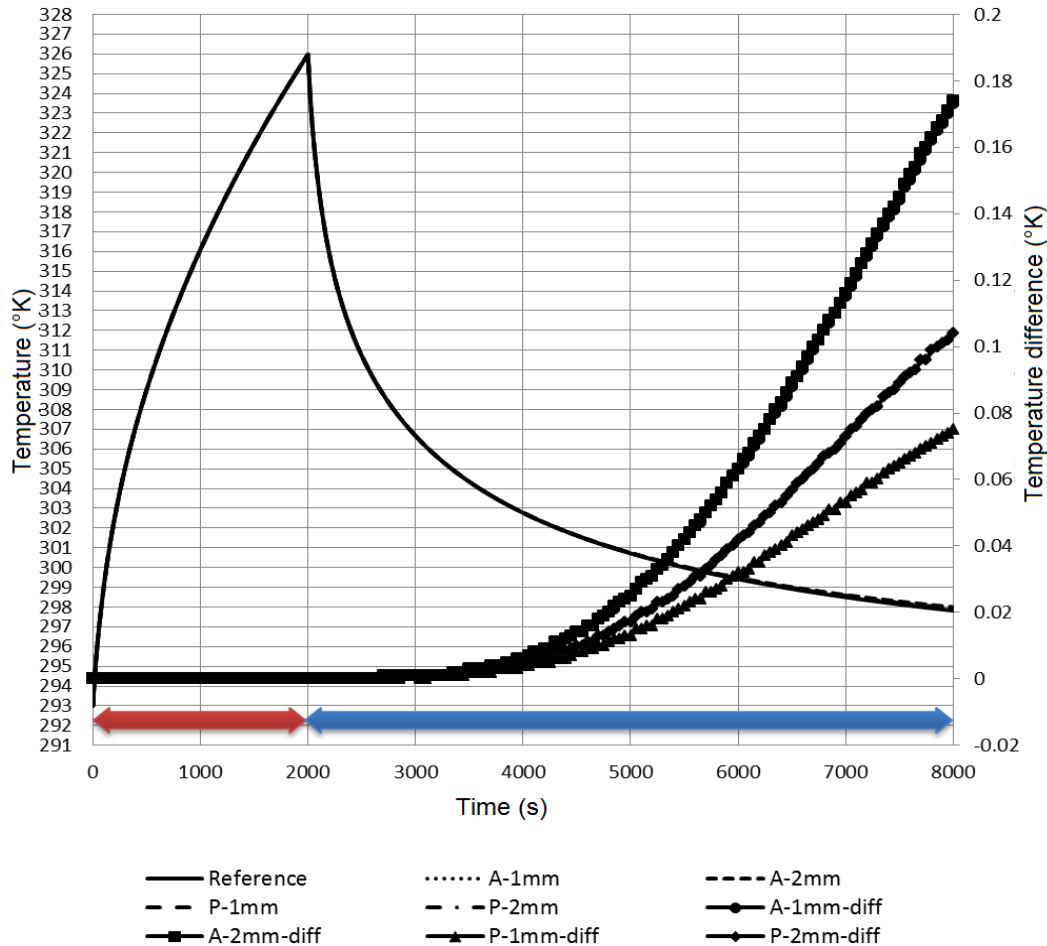
1°K = -458°F.

1 mm = 0.04 inch.

Ref = time history of the temperature for a reference point on the intact surface; A-1mm = time history of the temperature for a point on the air void defect with 1-mm thickness; A-2mm = time history of the temperature for a point on the air void defect with 2-mm thickness; P-1mm = time history of the temperature for a point on the polymer defect with 1-mm thickness; P-2mm = time history of the temperature for a point on the polymer defect with 2-mm thickness; A-1mm-diff = time history of the temperature difference relative to the reference point for a point on the air void defect with 1-mm thickness; A-2mm-diff = time history of the temperature difference relative to the reference point for a point on the air void defect with 2-mm thickness; P-1mm-diff = time history of the temperature difference relative to the reference point for a point on the polymer defect with 1-mm thickness; P-2mm-diff = time history of the temperature difference relative to the reference point for a point on the polymer defect with 2-mm thickness.

**Figure 43. Graph. Temperature change at shallow delamination defect points for 2-inch-deep delamination with an asphalt overlay and no waterproof membrane.**

In the third FE model, a heat influx of  $1,200 \text{ W/m}^2$  was applied to the top surface of the concrete for the first 2,000 s, and then the concrete was cooled for 6,000 s. The time histories of the temperature data acquired from shallow delamination defect points on the top surface are shown in figure 44. The greatest temperature difference was approximately  $0.32^\circ\text{F}$  from the 0.08-inch air voids, and the lowest temperature difference was approximately  $0.14^\circ\text{F}$  from the sandwiched structure with 0.04-inch foam insulation. The temperature differences were still increasing at the end of the analysis.



Source: FHWA.

1°K = -458°F.

Ref = time history of the temperature for a reference point on the intact surface; A-1mm = time history of the temperature for a point on the air void defect with 1-mm thickness; A-2mm = time history of the temperature for a point on the air void defect with 2-mm thickness; P-1mm = time history of the temperature for a point on the polymer defect with 1-mm thickness; P-2mm = time history of the temperature for a point on the polymer defect with 2-mm thickness; A-1mm-diff = time history of the temperature difference relative to the reference point for a point on the air void defect with 1-mm thickness; A-2mm-diff = time history of the temperature difference relative to the reference point for a point on the air void defect with 2-mm thickness; P-1mm-diff = time history of the temperature difference relative to the reference point for a point on the polymer defect with 1-mm thickness; P-2mm-diff = time history of the temperature difference relative to the reference point for a point on the polymer defect with 2-mm thickness.

**Figure 44. Graph. Temperature change at deep delamination defect points for 6-inch-deep delamination without an overlay.**

From the heat-conduction analysis, the sandwiched structures simulated real-world delamination (i.e., air voids) well. Using a thicker layer of foam insulation would increase the temperature difference. It was difficult to detect the 6-inch-deep delaminations from the top surface of the concrete using IRT because of the very small temperature difference.

## CHAPTER 5. CONSTRUCTING THE SMALL-SCALE SPECIMENS

This chapter describes the construction of the eight identical concrete specimens and the creation of artificial defects therein. A method for accelerating corrosion for precorroded rebar is also described in this chapter. The artificial defects covered are delamination, honeycombing, voids, vertical cracks, and corroded rebar.

### CREATING ARTIFICIAL DEFECTS

#### Delaminations

Delaminations were simulated by a thin, 12×8-inch rectangle built with transparent thermoplastic and plastic gutter guard, as shown in figure 45-A and figure 45-B. Two transparent thermoplastic sheets with a thickness of 0.093 inch were cut to size, two layers of plastic gutter guard were placed between the sheets to create an air gap, and then the edges were sealed with duct tape. The transparent thermoplastic sheets were secured to the rebar cage using baling wire and rebar ties to ensure they stayed in place during the concrete pouring and vibrating operations, as shown in figure 45-C and figure 45-D. These artificial delaminations simulated shallow and deep delaminations by placing them at the top and bottom rebar levels, respectively.



Source: FHWA.

A. Transparent thermoplastic and plastic gutter guard.



Source: FHWA.

B. Assembled artificial delamination.



Source: FHWA.

C. Artificial shallow delamination.



Source: FHWA.

D. Artificial deep delamination.

**Figure 45. Photos. Artificial delamination.**

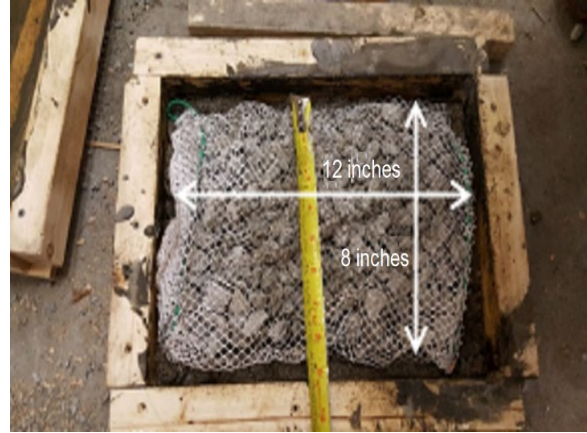
### **Honeycombing**

Honeycombing was simulated by a bag of loose aggregate, as shown in figure 46-A. Mesh laundry bags were cut into smaller bags, 12 lb of aggregate was placed in each bag, and then the edges were stitched with baling wire. Wood molds were built with an inner dimension of 14×10×2 inches. A thin layer of concrete containing anticrack fiber was placed on the bottom of each mold, a bag of aggregate was positioned in the mold with all four sides 1 inch from the edge of the mold, and then the sides and the top were covered with concrete, as shown in figure 46-B through figure 46-E. The cured blocks were secured to the rebar cage using baling wire and foam pieces to ensure they stayed in place during concrete pouring and vibrating operations, as shown in figure 46-F.



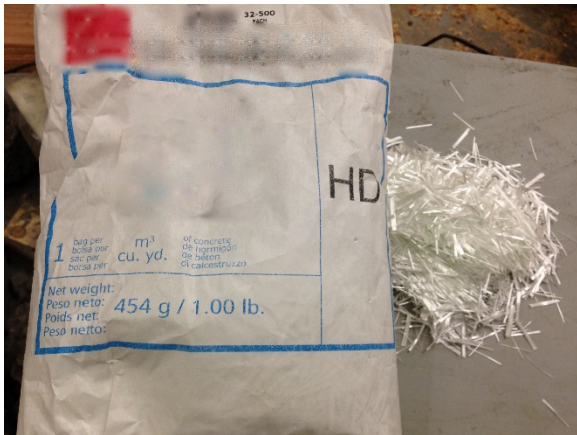
Source: FHWA.

A. Coarse aggregate in a mesh laundry bag.



Source: FHWA.

D. Aggregate bag in the mold.



Source: FHWA.

B. Anticrack fiber.



Source: FHWA.

E. Aggregate bag covered with concrete.



Source: FHWA.

C. Mold with a thin layer of concrete.



Source: FHWA.

F. Installed artificial honeycombing.

**Figure 46. Photos. Artificial honeycombing.**

## Voids

Foam insulation boards with a dimension of 12×8×2 inches were used to simulate voids within concrete, as shown in figure 47-A. The foam insulation boards were secured to the rebar cage using foam pieces on the top and bottom to ensure they stayed in place during concrete pouring and vibrating operations, as shown in figure 47-B.



Source: FHWA.

A. Foam insulation board.



Source: FHWA.

B. Installed artificial void.

**Figure 47. Photos. Artificial void.**

## Vertical Cracks

Corrugated plastic sheets with a height of either 6 or 2.5 inches, a thickness of 0.16 inch, and a length of 10 inches were used to simulate vertical cracks, as shown in figure 48-A and figure 48-B. The sheets were secured to the mold using wire and duct tape to ensure they stayed in place during concrete pouring and vibrating operations, as shown in figure 48-C.



Source: FHWA.

A. 6-inch corrugated plastic sheet.



Source: FHWA.

B. 2.5-inch corrugated plastic sheet.



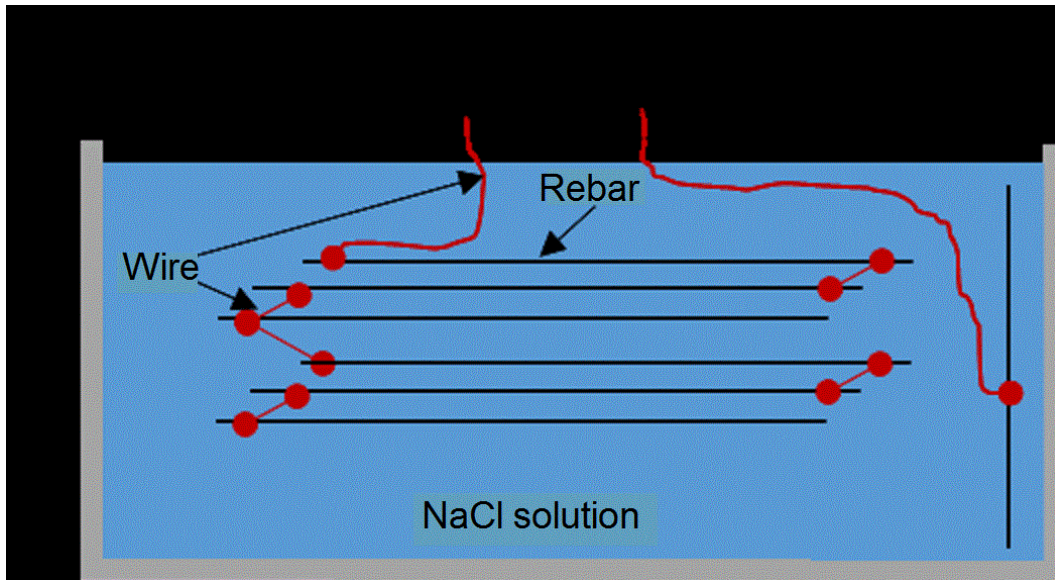
Source: FHWA.

C. Installed corrugated plastic sheet.

**Figure 48. Photos. Artificial vertical crack.**

## Precorroded Rebar

An accelerated corrosion setup was used to introduce corrosion to the new, intact rebar, as shown in figure 49. The rebar was precorroded by placing it in a tub of saturated NaCl solution and applying 1-A direct current (DC) with the positive pole connected to a rebar set and the negative pole connected to a single rebar. Both the set and the single rebar were submerged in the NaCl solution, as shown in figure 50-A through figure 50-F. After 2 weeks, the rebar was severely corroded.



Source: FHWA.

**Figure 49. Illustration. Accelerated corrosion setup.**



Source: FHWA.

A. Rebar in a frame.



Source: FHWA.

D. Rust in the tub after accelerated corrosion.



Source: FHWA.

B. Rebar connected with wires.



Source: FHWA.

E. Corroded rebar.



Source: FHWA.

C. Accelerated corrosion.



Source: FHWA.

F. Intact versus corroded rebar.

**Figure 50. Photos. Precorroded rebar with accelerated corrosion.**

## ASSEMBLING AND CONSTRUCTING THE SPECIMENS

A rebar cage and formwork with artificial defects before and after casting is shown in figure 51-A through figure 51-D. Measured depths of the defects after assembly are listed in table 6. The specimens were cast with a dimension of 120×40×8 inches using a wooden formwork and normal-strength concrete, which has a 28-d average compressive strength of 4,665 psi from laboratory tests of concrete cylinders. Eight specimens were named and marked S1 to S8.



Source: FHWA.

A. Assembled rebar with defects.



Source: FHWA.

C. Curing concrete.



Source: FHWA.

B. Pouring concrete.



Source: FHWA.

D. After curing and removing form.

**Figure 51. Photos. Installed artificial defects and construction of specimens.**

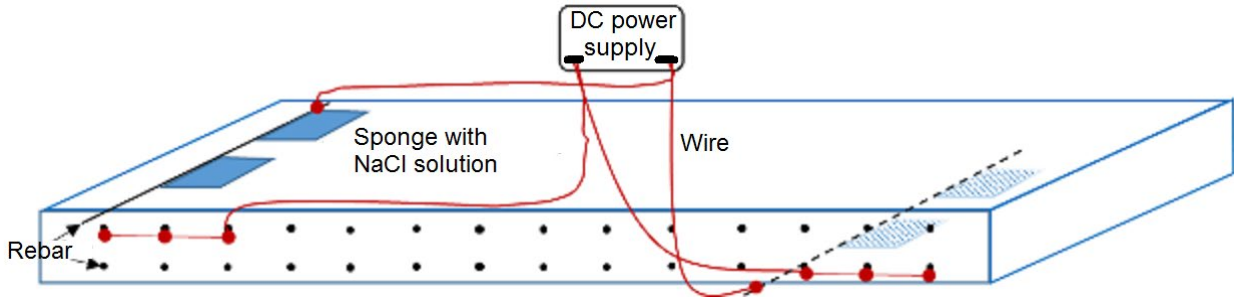
**Table 6. Depth of defects after assembly.**

Specimen		Shallow Delaminations (Inch)	Honeycombing (Inch)	Voids (Inch)	Deep Delaminations (Inch)
S1	North	1.85	3.76	3.53	5.23
	South	1.94	3.64	3.42	5.15
S2	North	1.64	3.68	3.75	5.38
	South	1.55	3.74	3.78	5.56
S3	North	1.65	4.04	3.89	5.39
	South	1.70	3.89	3.59	5.24
S4	North	1.90	3.89	3.82	5.26
	South	1.78	3.83	3.76	5.31
S5	North	1.10	3.59	3.33	5.40
	South	1.24	3.63	3.64	5.50
S6	North	1.28	4.06	3.68	5.45
	South	1.28	3.92	3.83	5.52
S7	North	1.23	3.49	3.59	5.41
	South	1.30	3.54	3.30	5.36
S8	North	1.31	3.54	3.68	5.29
	South	1.38	3.48	3.53	5.23

Note: The orientation is defined in figure 24.

### **ACCELERATED CORROSION FOR PRECORRODED REBAR**

The artificial defects created with the preceding procedures can be detected only by stress-wave-based methods (e.g., IE and UT) and not by corrosion-related methods (e.g., GPR, HCP, and ER). Unlike the corrosion mechanism in concrete bridge decks, there is not an elevated chloride content environment in the concrete surrounding the six pieces of precorroded rebar in each specimen, and no active corrosion takes place in the rebar after the specimens are cured. To simulate active corrosion, an accelerated corrosion setup was used to introduce active corrosion to the precorroded rebar for HCP tests and an elevated chloride content environment to the concrete surrounding the precorroded rebar for GPR and ER tests (figure 52). The positive end of the DC power supply—which was set to 2 amps—was connected to the precorroded rebar, and the negative end was connected to the rebar that was placed on the concrete surface near the target rebar and attached to sponges saturated with an NaCl solution. After 1 week of accelerated corrosion, active rebar corrosion was visible, and some specimens had small cracks due to the expansion of the actively corroded rebar (figure 53, figure 54-A, and figure 54-B).



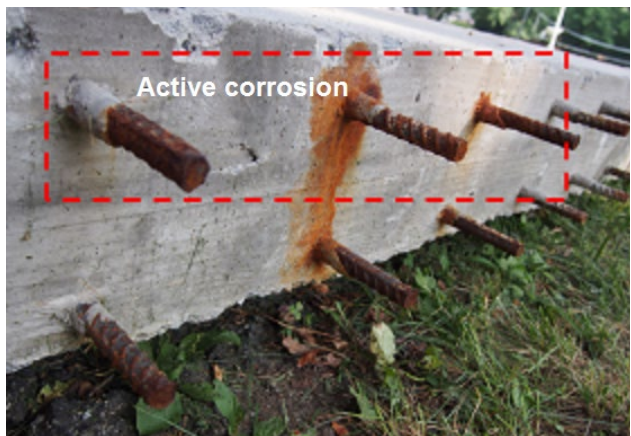
Source: FHWA.

**Figure 52. Illustration. Accelerated corrosion setup.**



Source: FHWA.

**Figure 53. Photo. Accelerated corrosion of precorroded rebar.**



Source: FHWA.

A. Active corrosion.



Source: FHWA.

B. Crack introduced by rebar corrosion.

**Figure 54. Photos. Active corrosion and cracking after 1 week of accelerated corrosion.**

## CHAPTER 6. NDE TESTS OF LABORATORY SPECIMENS

The equipment, test spacing, and parameters of each of the nine NDE technologies covered in this report are detailed in table 7.

**Table 7. Equipment, test spacing, and parameters for nine NDE technologies.**

<b>Method</b>	<b>Equipment</b>	<b>Test Spacing</b>	<b>Parameter</b>
Sounding	Masonry hammer	4 inches	N/A
USW	Portable seismic pavement analyzer	4 inches	4 inches from the source to the near sensor, 6 inches between two sensors
IE	Custom-built system with an accelerometer and different sizes of steel spheres on spring rods	4 inches	Sampling frequency of 200 kHz
UT-MIRA	UT-MIRA (mounted on the 2D scanner)	10 inches longitudinally and 2 inches transversely	Operation frequency of 50 kHz
UT-EyeCon	UT-EyeCon (mounted on the robotic arm)	2 inches	Operation frequency of 50 kHz
IR	sMash	4 inches	Acquisition speed: 10,000 samples/s Hammer triggering sensitivity: 0.6 volts Hammer sensitivity: 0.25 mV/N Transducer sensitivity: 20 mV/(m/s) Transducer gain: 0 dB
GPR	GSSI 1.6 GHz	9 longitudinal and 29 transverse scan lines with a spacing of 4 inches	Samples: 512 Formats: 16 bits Range: 8 ns Dielectric constant: 8 Scan rate: 120 scans/s Scan/unit: 60 scans/ft Gain: 0 dB
ER	Resipod	4 inches	Dip the probe into water before each measurement

<b>Method</b>	<b>Equipment</b>	<b>Test Spacing</b>	<b>Parameter</b>
HCP	Profometer corrosion	4 inches	Measurement range: -999 mV to 340 mV Resolution: 1 mV Electrode: copper/copper sulphate
IRT	Forward-looking infrared	Full specimen	Resolution: 320 by 240 pixels Temperature range: -4 to 2,192°F Thermal sensitivity: <0.1°F at 86°F

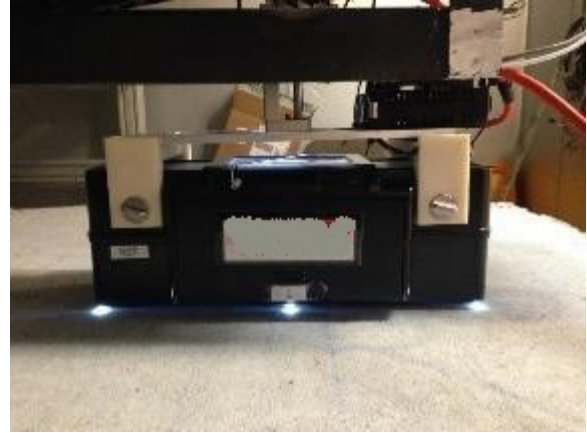
N/A = not applicable.

The surface of each specimen was cleaned before the NDE tests. No other activities on the specimens were occurring at the same time for each test. The concrete surface was saturated 30 min before the HCP test. The specimens were placed outdoors without any shade on the specimen surface for IRT tests, and the tests were performed on a sunny day with one thermal picture every 30 min between 10:00 a.m. and 4:00 p.m. The NDE tests were carried out for the eight specimens without and with overlays. Photos of NDE tests on specimens without overlays are shown in figure 55-A through figure 55-J.



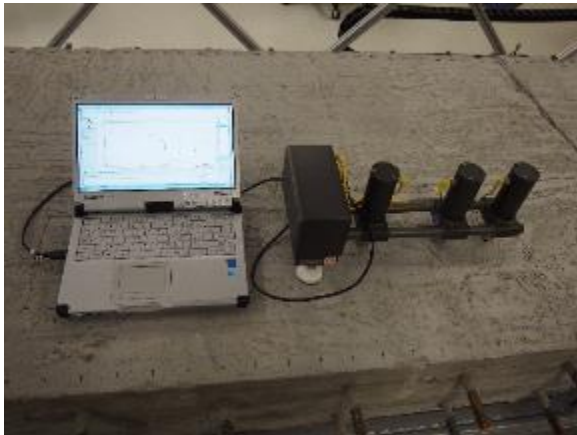
Source: FHWA.

A. Sounding.



Source: FHWA.

D. UT-MIRA attached to a 2D scanner.



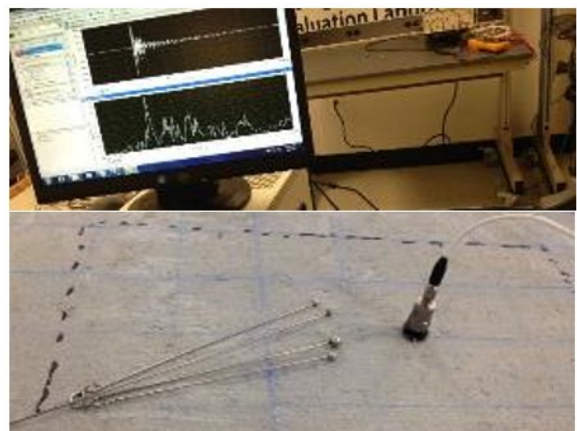
Source: FHWA.

B. USW.



Source: FHWA.

E. UT-EyeCon attached to robotic arm.



Source: FHWA.

C. IE.



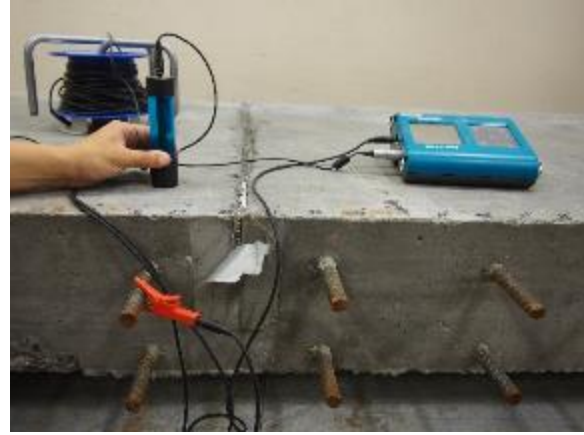
Source: FHWA.

F. IR.



Source: FHWA.

G. GPR.



Source: FHWA.

I. HCP.



Source: FHWA.

H. ER.



Source: FHWA.

J. IRT.

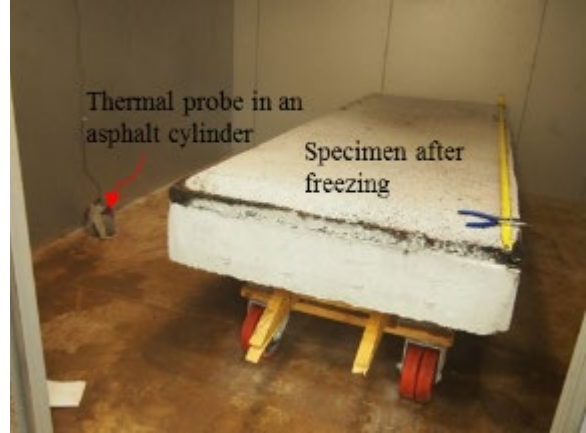
**Figure 55. Photos. NDE tests of specimens without overlays.**

Stress-wave-based NDE technologies (e.g., IE and UT) were effective at detecting subsurface defects in concrete bridge decks with asphalt overlays in cold weather, so a temperature chamber was used to achieve low temperatures for specimens with asphalt overlays, as shown in figure 56-A and figure 56-B.<sup>(54)</sup> To ensure the entire specimen reached the target temperature, each specimen was placed in the chamber overnight, and a thermal probe in a 6×6-inch asphalt cylinder was used to monitor the chamber temperature, as shown in figure 56-B. USW, IE, and UT tests of the three specimens with asphalt overlays were conducted in the chamber. To minimize the variation of the specimen temperatures after the door was open for testing, the testing time was reduced by increasing the USW test spacing to 8 inches, the IE test spacing in the longitudinal direction to 40 inches in the debonded area, and the UT-MIRA test spacing in the transverse direction to 8 inches.



Source: FHWA.

A. Chamber with door closed.



Source: FHWA.

B. Specimen in the chamber.

**Figure 56. Photos. Temperature chamber.**

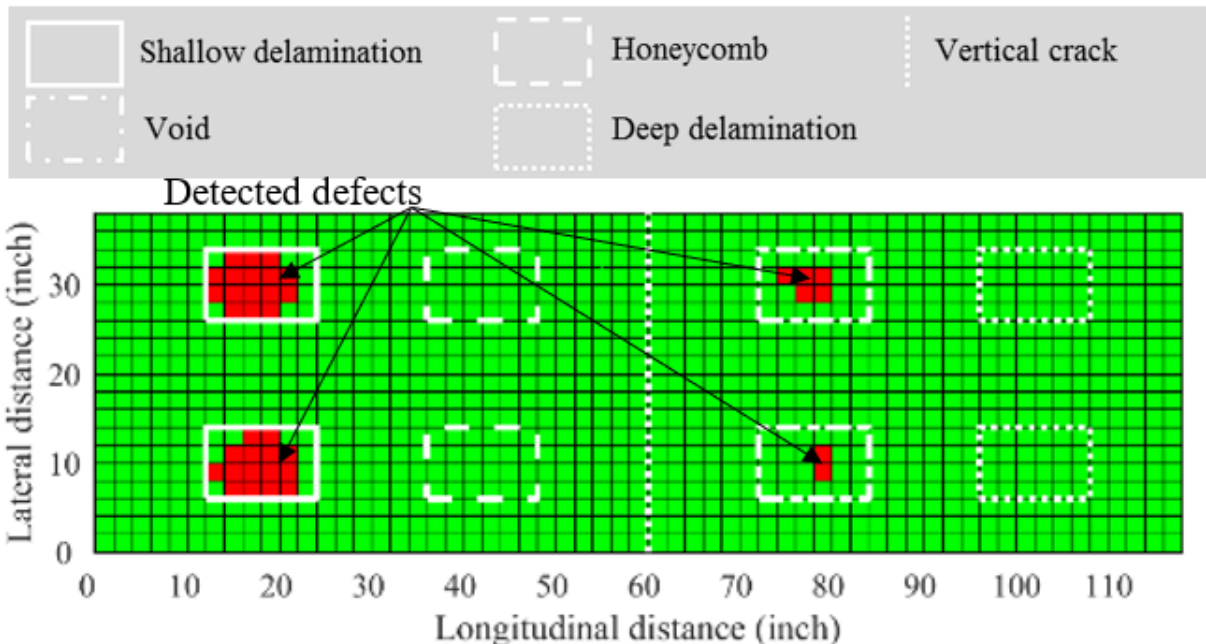


## CHAPTER 7. NDE RESULTS OF SPECIMENS WITHOUT OVERLAYS

The NDE results of eight specimens without overlays using nine NDE technologies are presented in this chapter. The results of each method are detailed in the following sections.

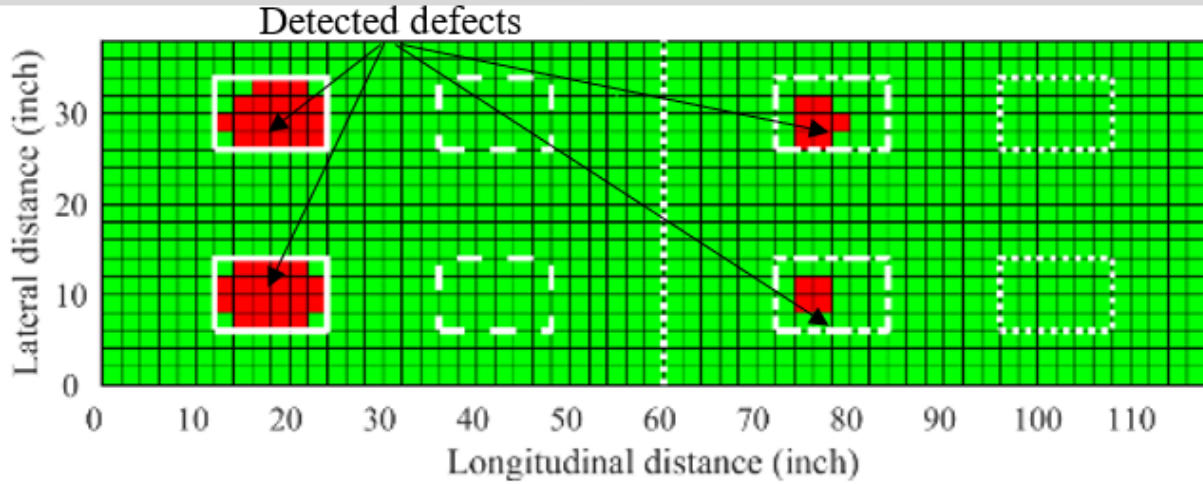
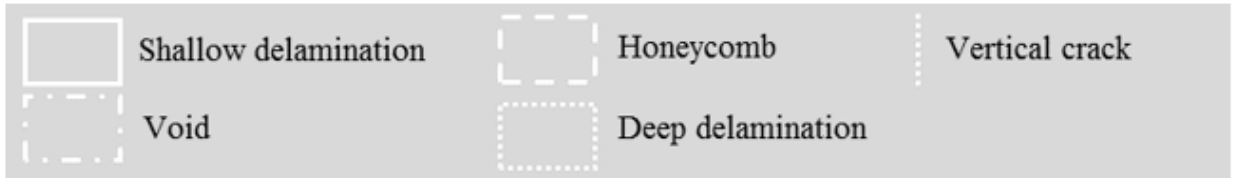
### SOUNDING

The sounding method involved tapping the concrete surface with a hammer and listening to the sound. Intact areas make clear ringing sounds, whereas defected areas produce dull, hollow sounds. The condition maps based on the sounding method are shown in figure 57-A through figure 57-H with intact areas in green and defected areas in red. The sounding method detected all shallow delaminations in eight specimens, but did not detect any deep delaminations due to their increased depths. As shown in table 6, the depths of the voids and honeycombing were close, but the sounding method only detected voids in specimens S1–S3 and did not detect any honeycombing. The voids made from foam insulation allowed for more give in the concrete than the honeycombing made from aggregate; thus, it was easier for the areas with voids to produce a dull, hollow sound than areas with honeycombing. The sounding method only identified voids in specimens S1–S3 but not in the other five specimens. The sounds from the areas with voids were similar to the sounds from the intact areas, making it challenging for the operator to identify the voids in specimens S1–S3. The sounds from the areas with voids in the other five specimens were indistinguishable for the operator. The sounding method is subjective and the results depend on the operator’s experience and skill.



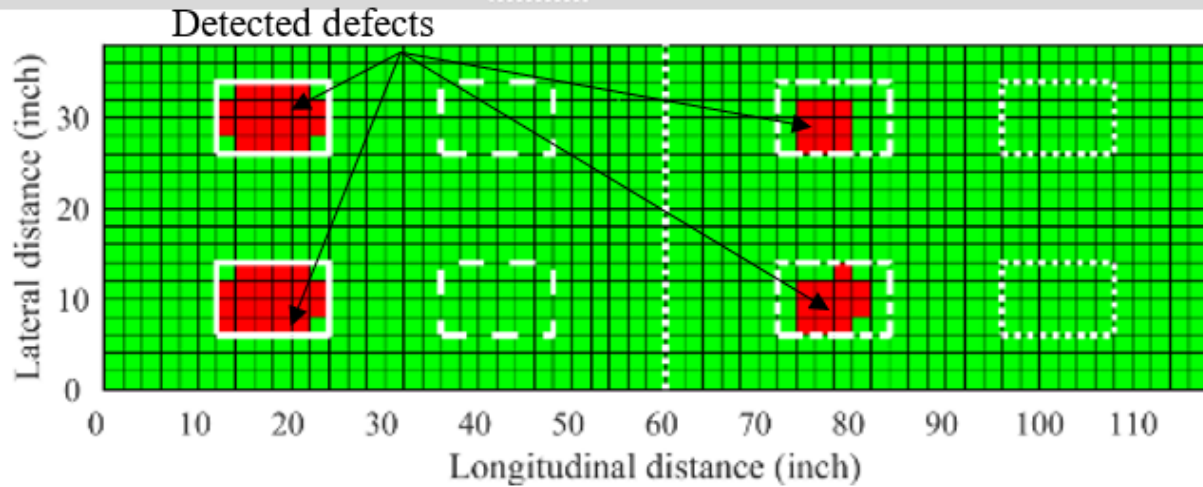
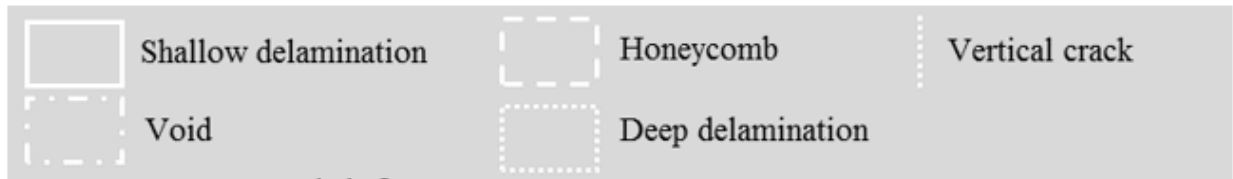
Source: FHWA.

A. S1.



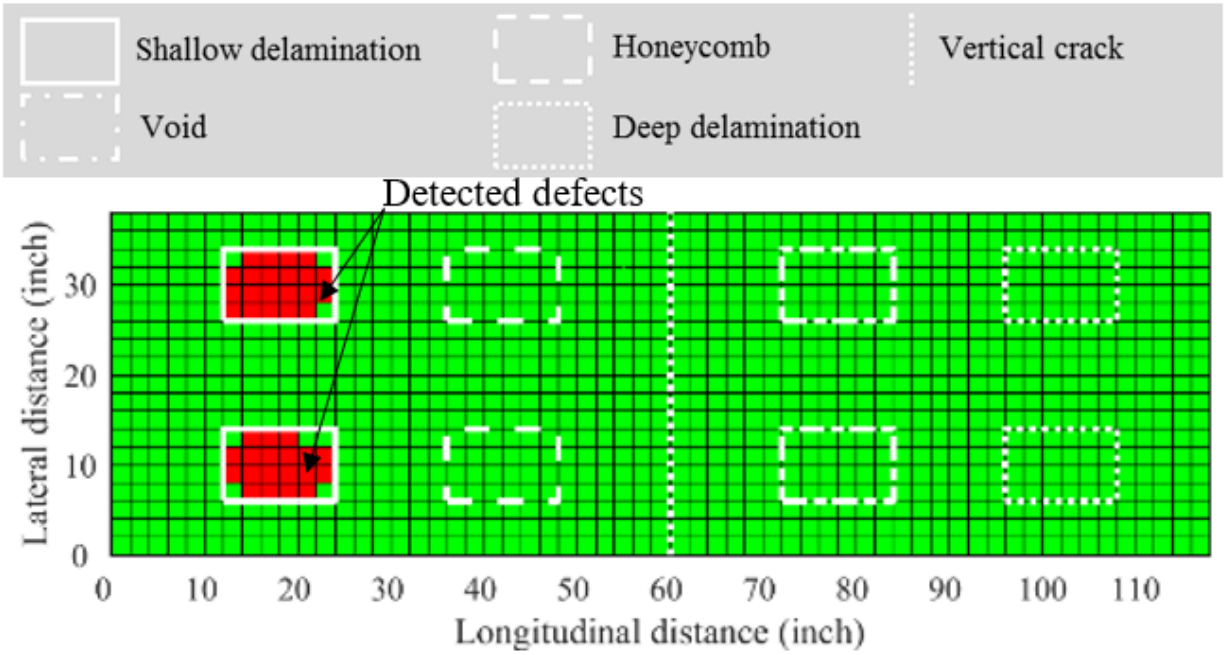
Source: FHWA.

B. S2.



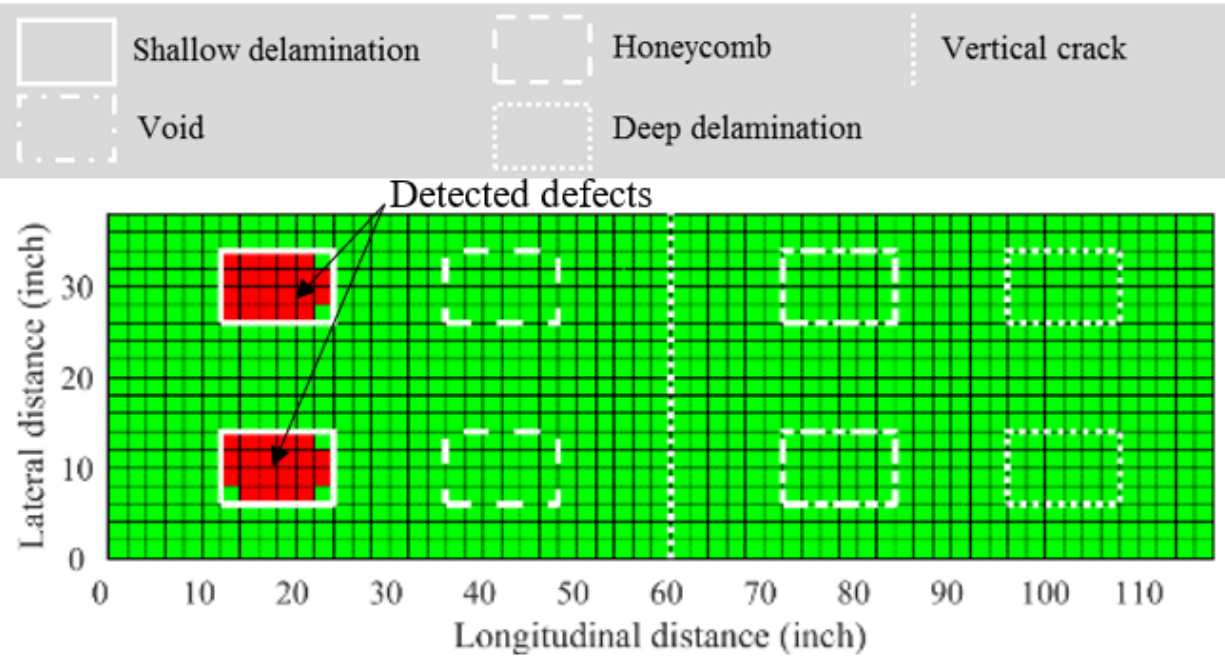
Source: FHWA.

C. S3.



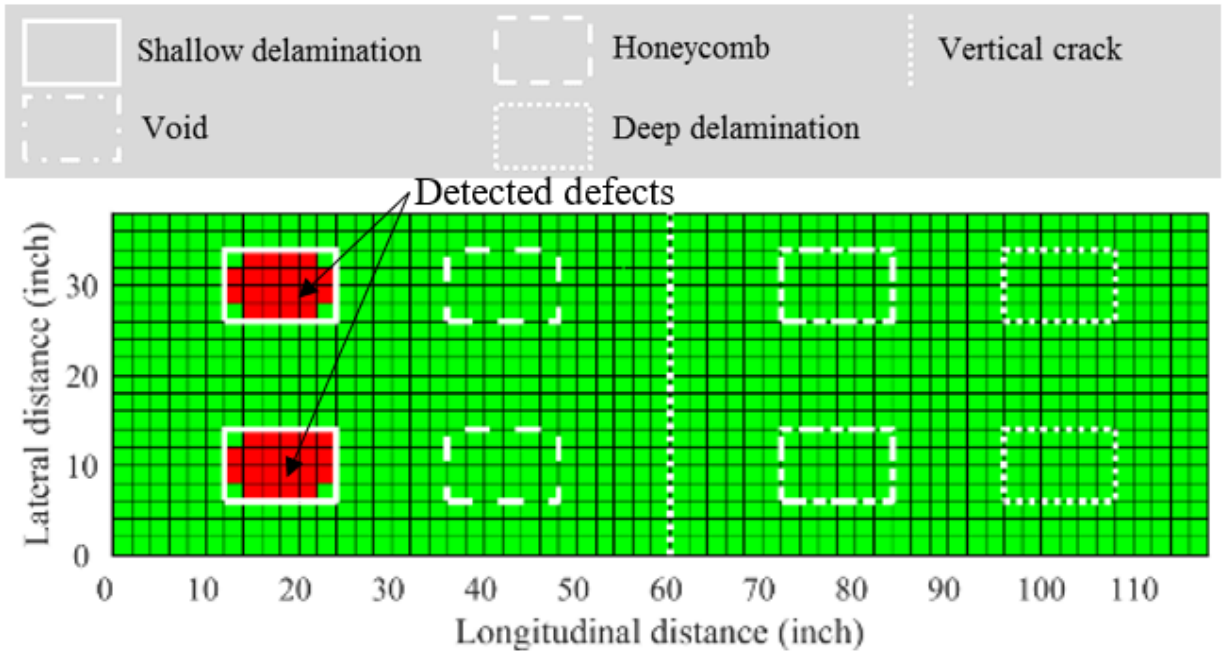
Source: FHWA.

D. S4.



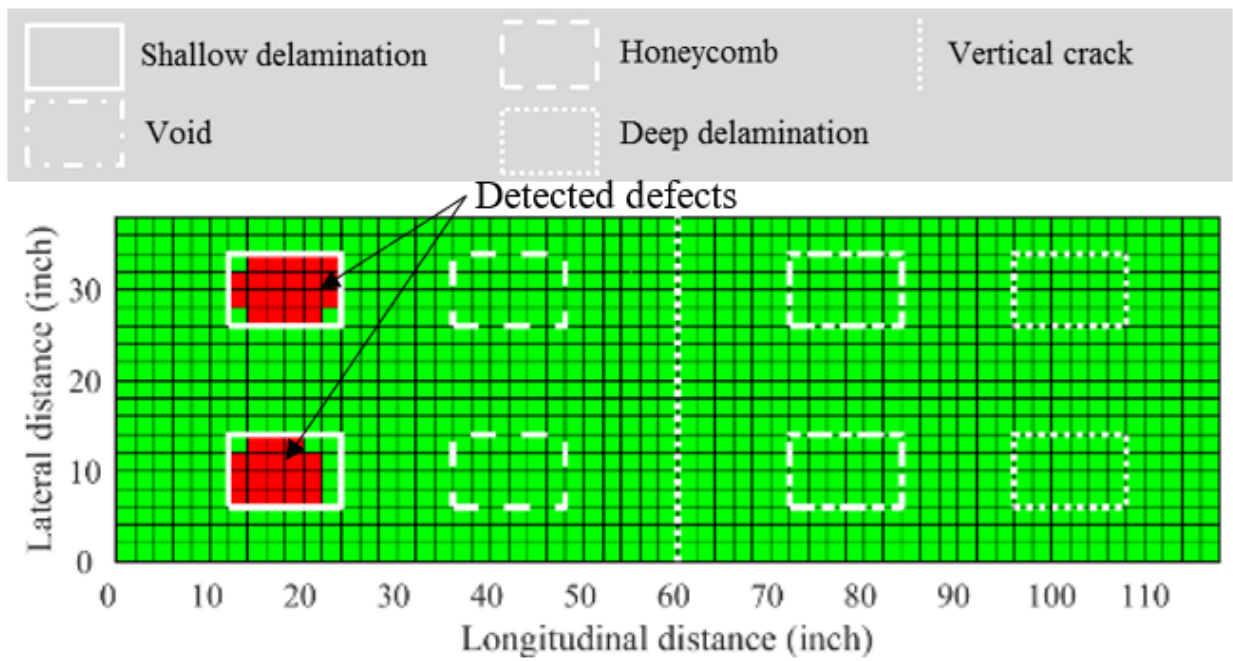
Source: FHWA.

E. S5.



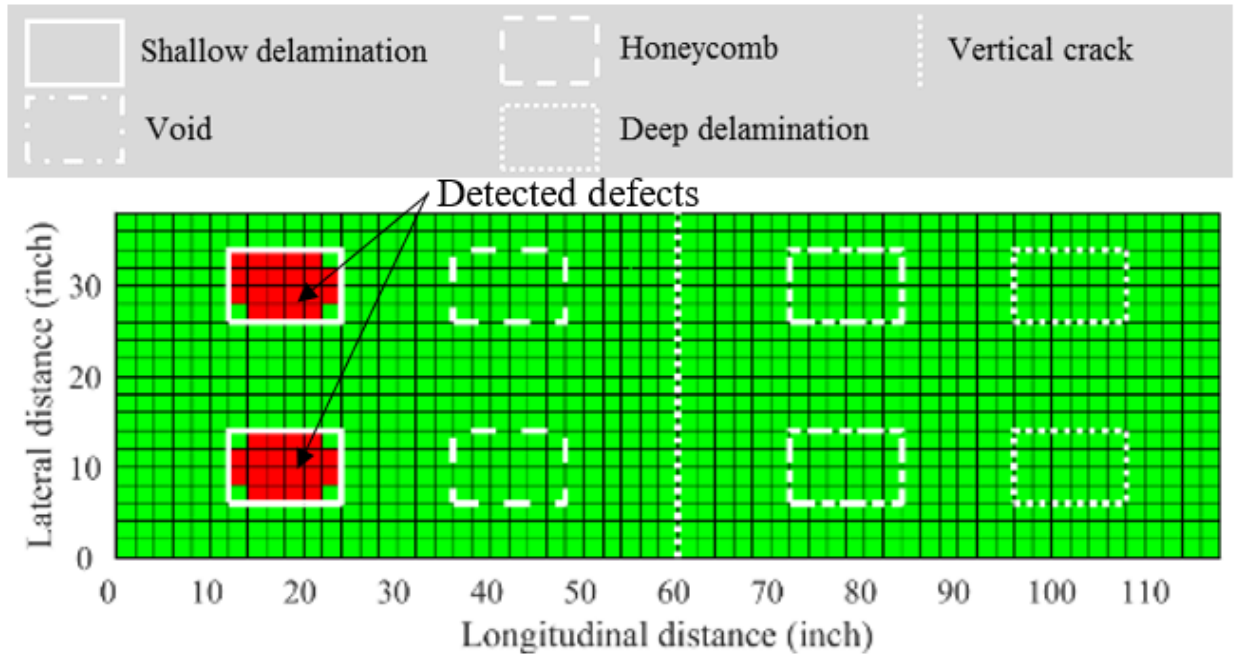
Source: FHWA.

F. S6.



Source: FHWA.

G. S7.



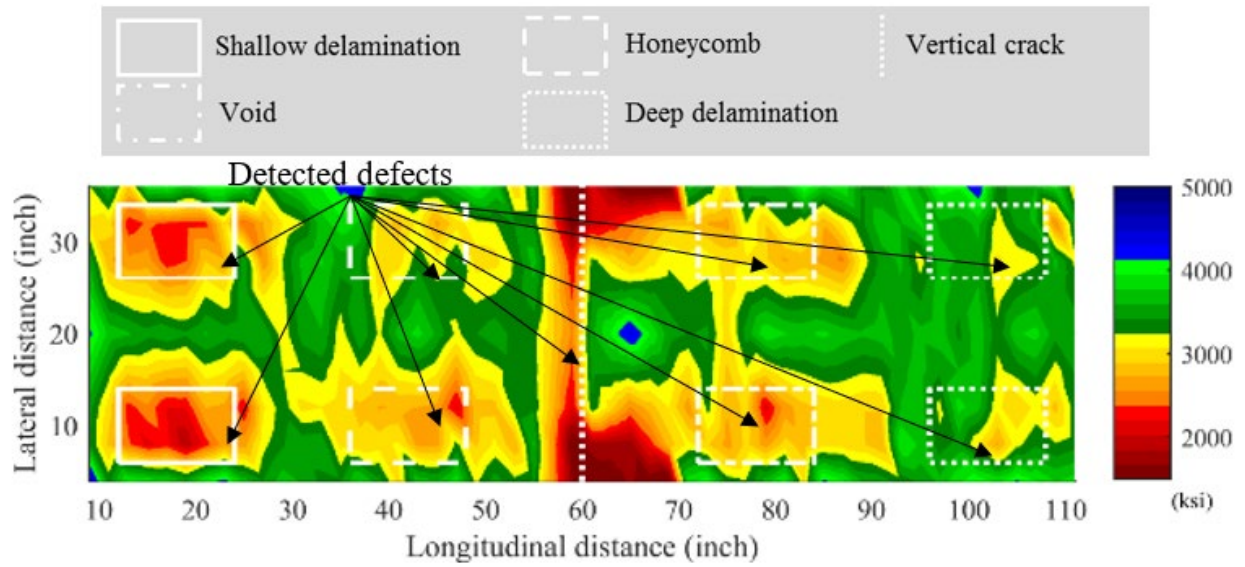
Source: FHWA.

H. S8.

**Figure 57. Graphs. NDE condition maps with sounding.**

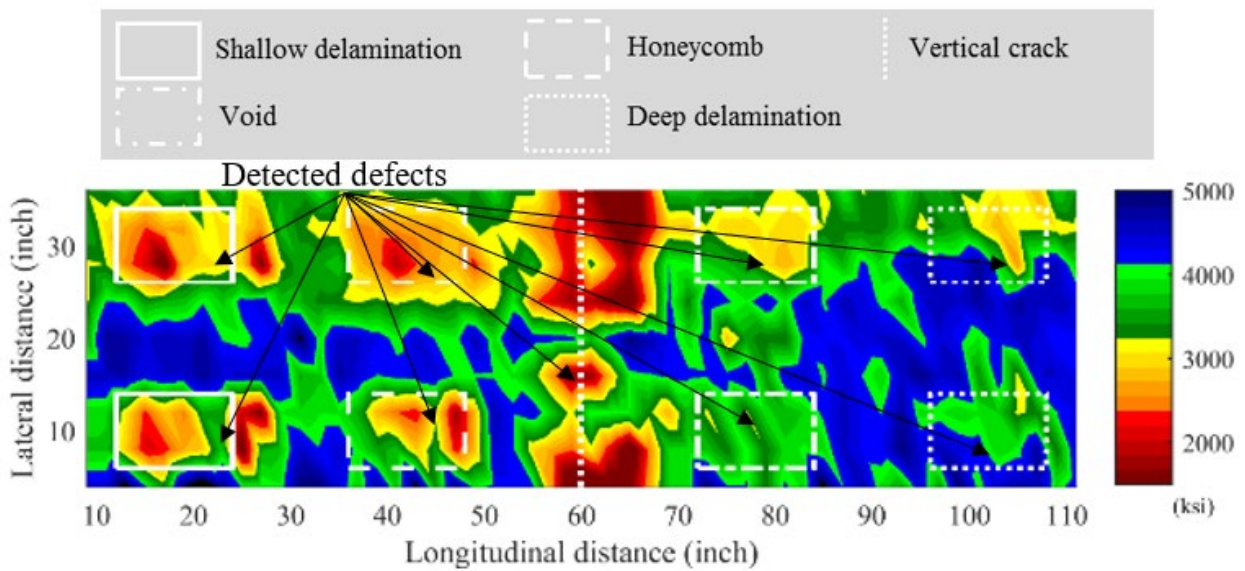
### USW METHOD

The USW method used the dispersion phenomenon of surface waves (i.e., phase velocity as a function of frequency or wavelength) to obtain an apparent modulus from each measurement location. An area with lower moduli compared to other areas indicated the presence of a defect (e.g., delamination or void). The condition maps based on the moduli measured with the USW method are shown in figure 58-A through figure 58-H. The USW method detected shallow and deep delaminations, honeycombing, voids, and vertical cracks in all eight specimens. In general, the shallow defects showed lower moduli than deep defects, and the modulus increased and the detectable area decreased as the depth of defect increased. Three of the total 16 deep delaminations (south one in S2 and S3 and north one in S4) were not clearly identified in the condition maps, indicating that detecting deep delaminations becomes more challenging as the defect depth and moduli increase and the detectable area decreases.



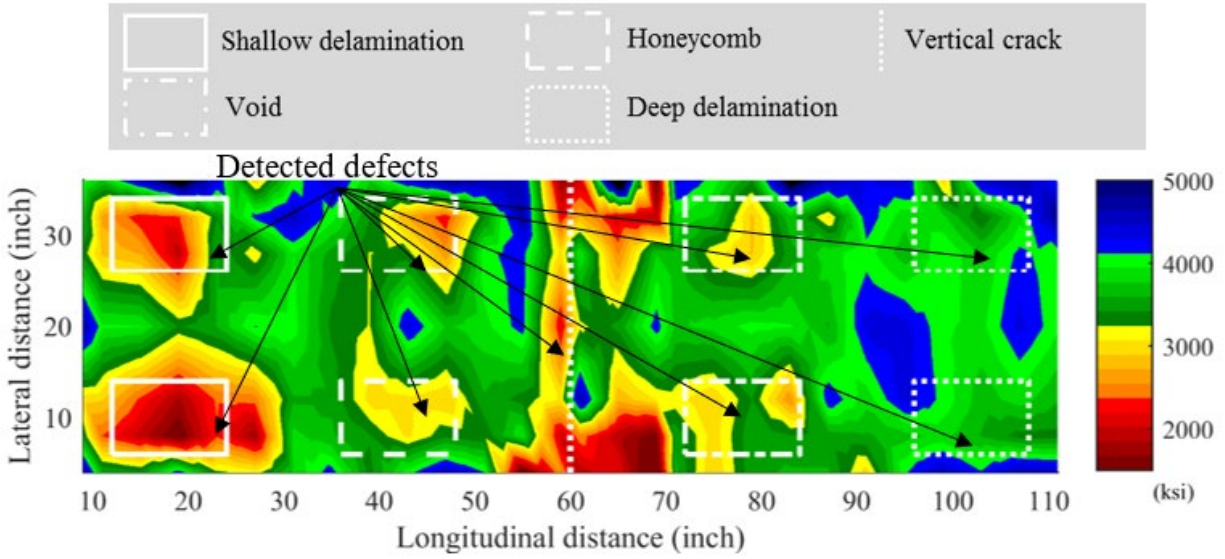
Source: FHWA.

A. S1.



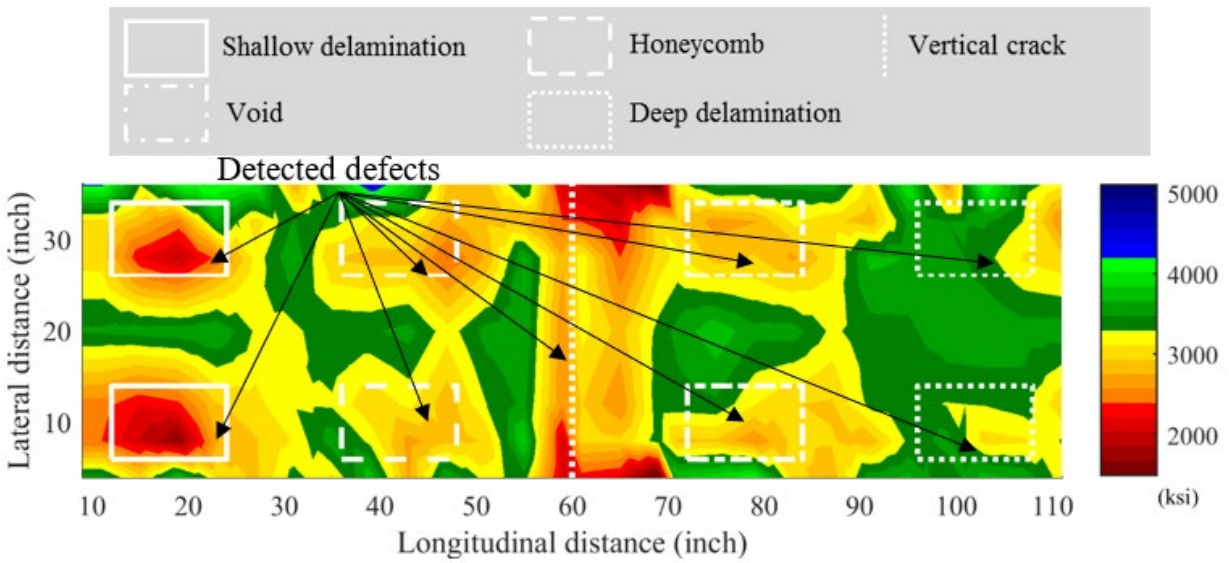
Source: FHWA.

B. S2.



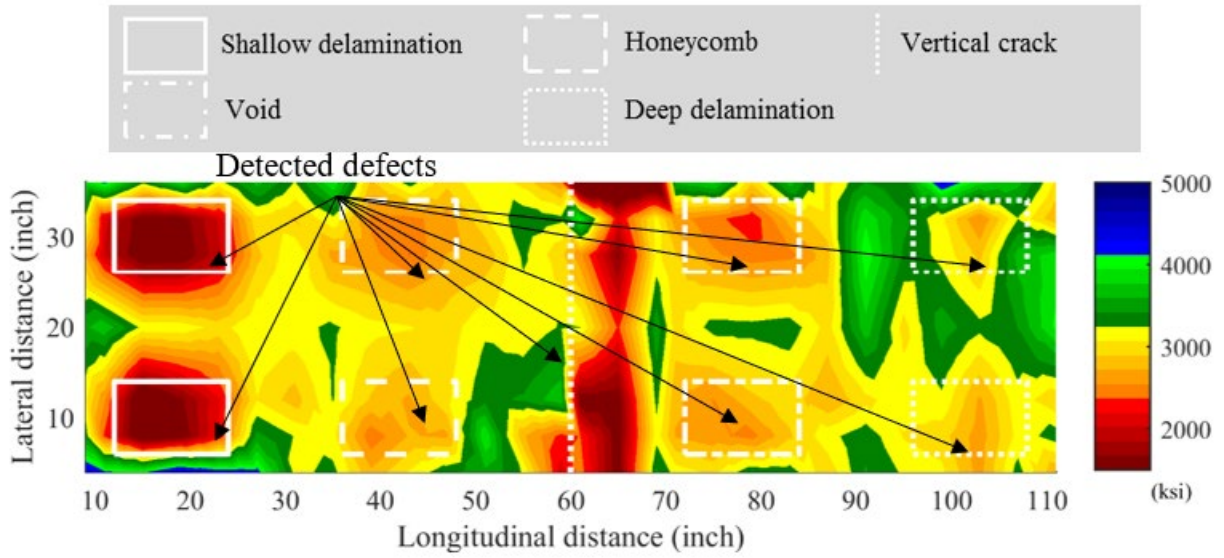
Source: FHWA.

C. S3.



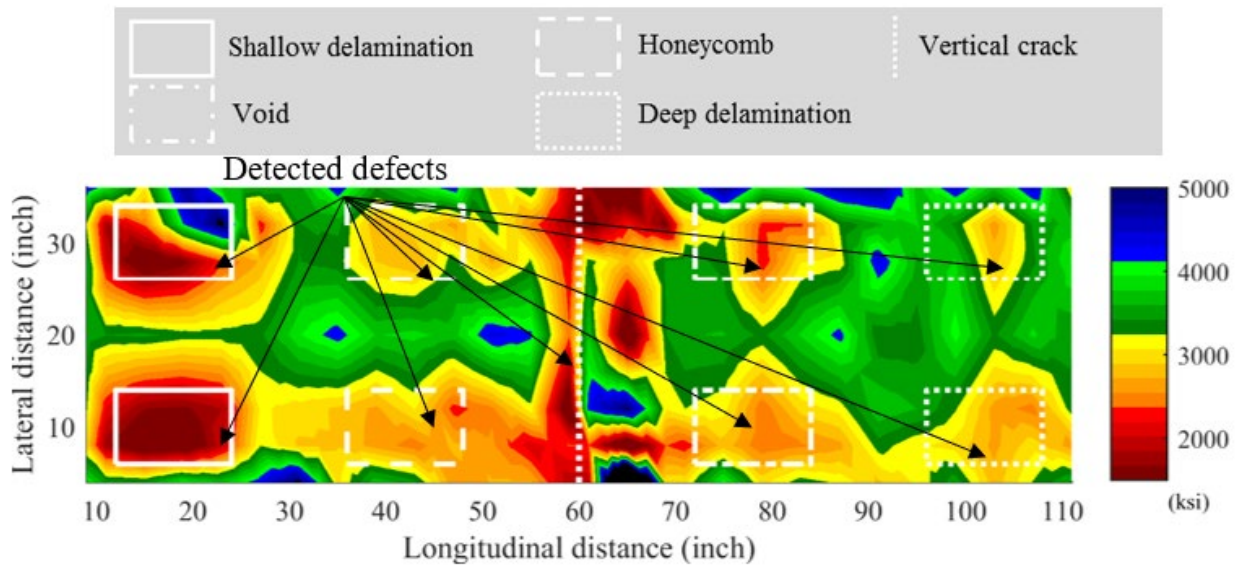
Source: FHWA.

D. S4.



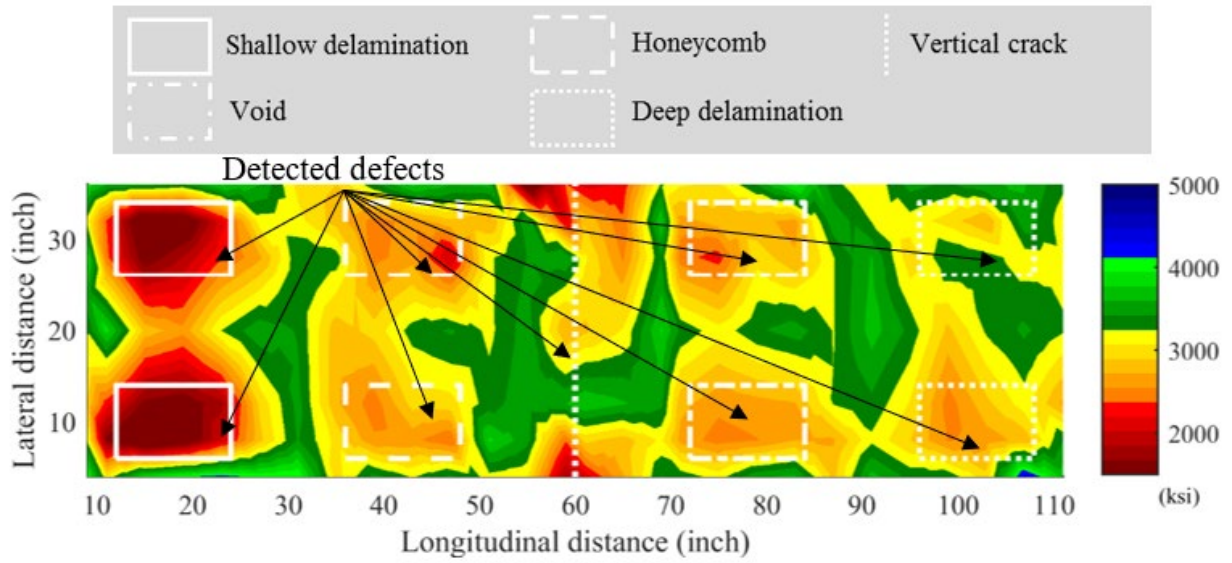
Source: FHWA.

E. S5.



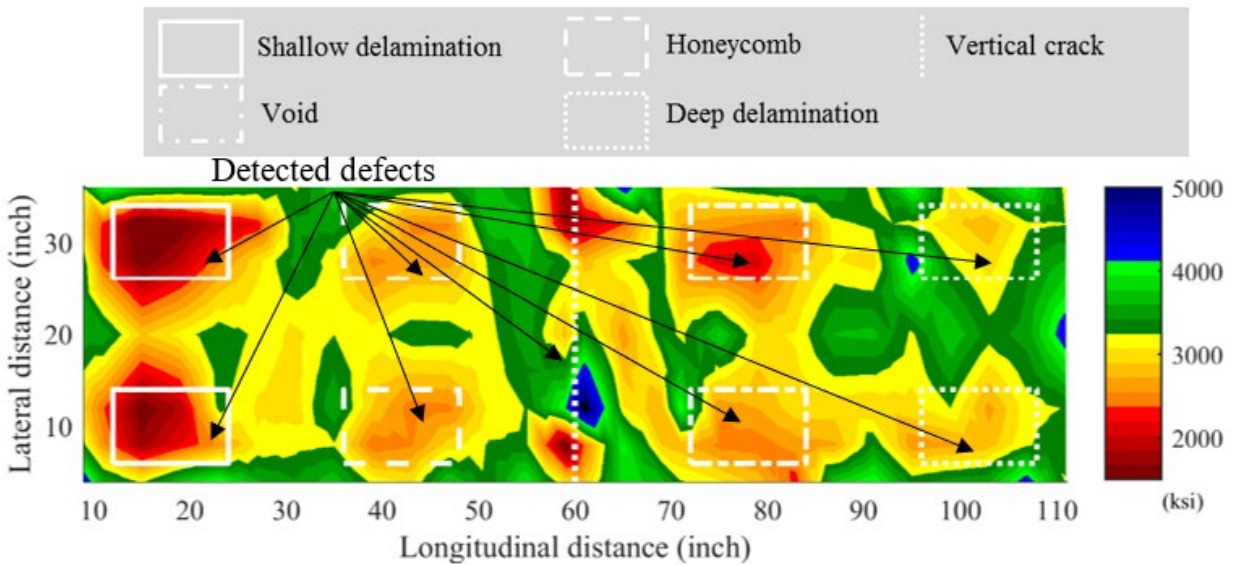
Source: FHWA.

F. S6.



Source: FHWA.

G. S7.



Source: FHWA.

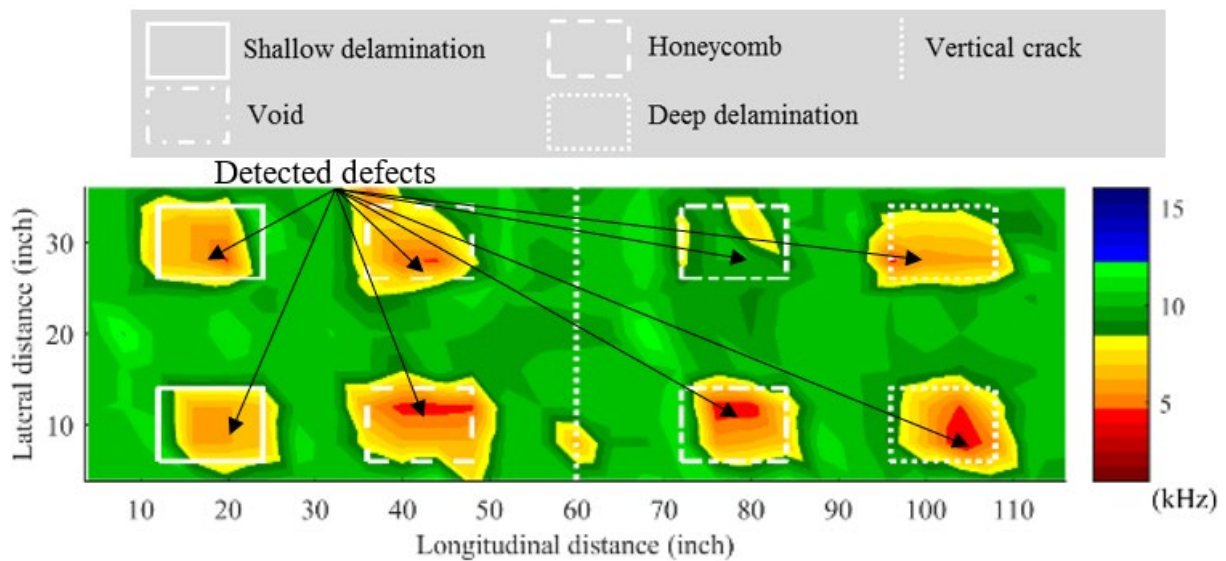
H. S8.

**Figure 58. Graphs. NDE condition maps with USW.**

## IE METHOD

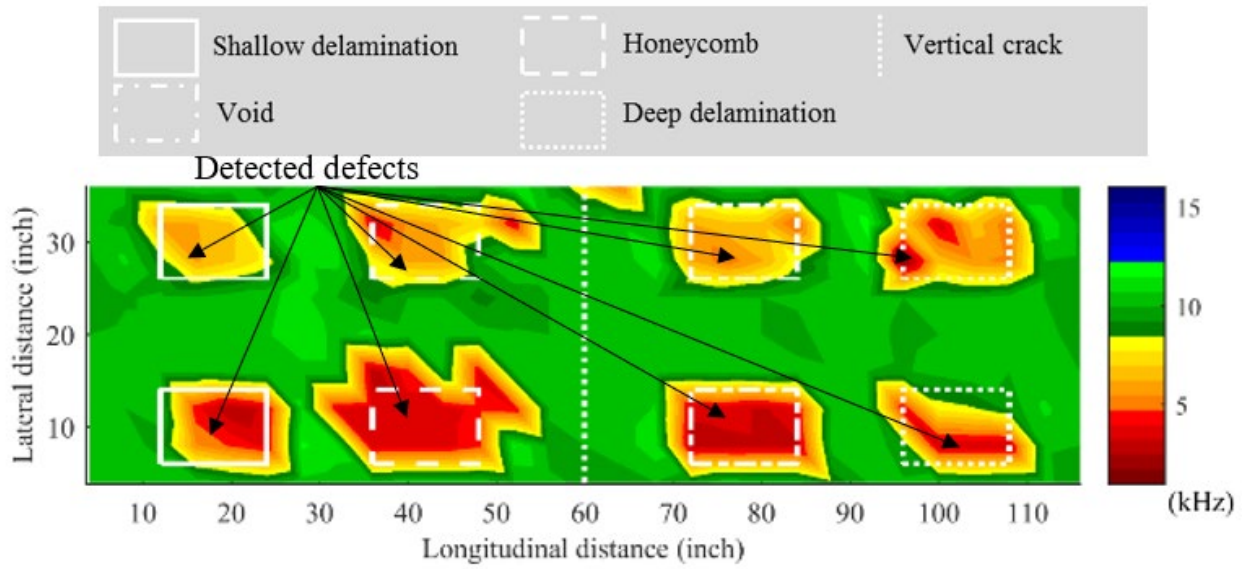
The IE method is based on the transient resonances caused by multiple reflections of stress waves between the concrete surface and the reflector (i.e., defect). The transient resonance of an area with a defect has a different dominant frequency than that of an intact area. The condition maps based on the dominant frequencies measured by the IE method are shown in figure 59-A through figure 59-H. The IE method detected shallow and deep delaminations, honeycombing, and voids in all eight specimens. Areas with detected defects showed lower frequencies than intact areas. Intact areas had the frequency of the thickness mode at about 10 kHz.

Delaminations, honeycombing, and voids had the dominant flexural mode because the width-to-depth ratios of these defects were larger than 1. The width-to-depth ratios were 5.8 for shallow delaminations, 2.3 for honeycombing, 2.3 for voids, and 1.5 for deep delaminations.<sup>(46)</sup>



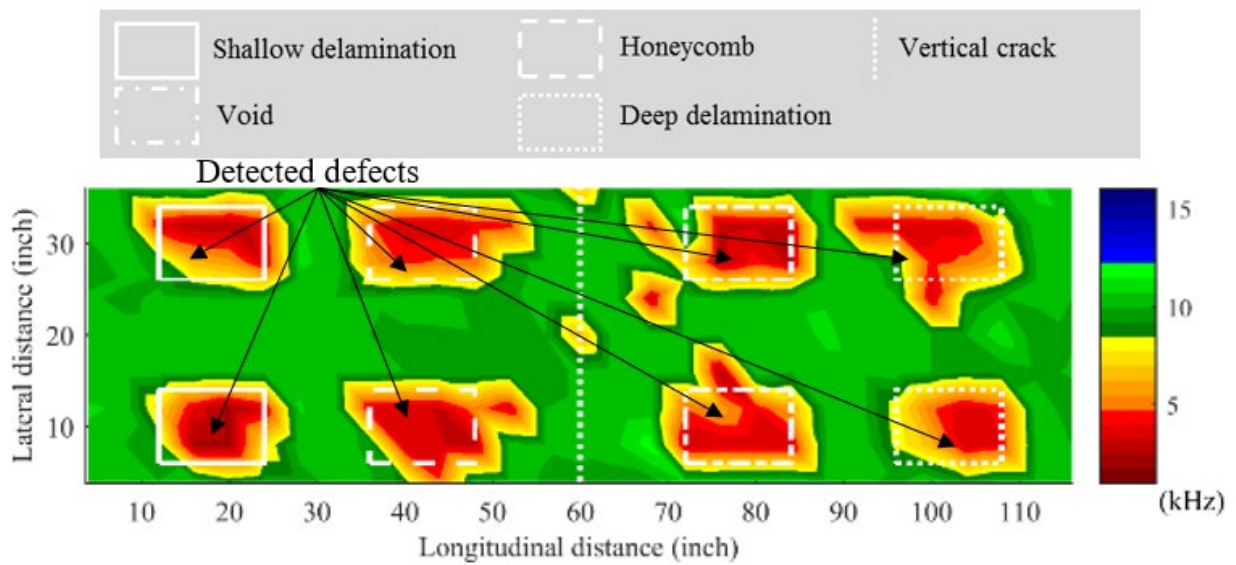
Source: FHWA.

A. S1.



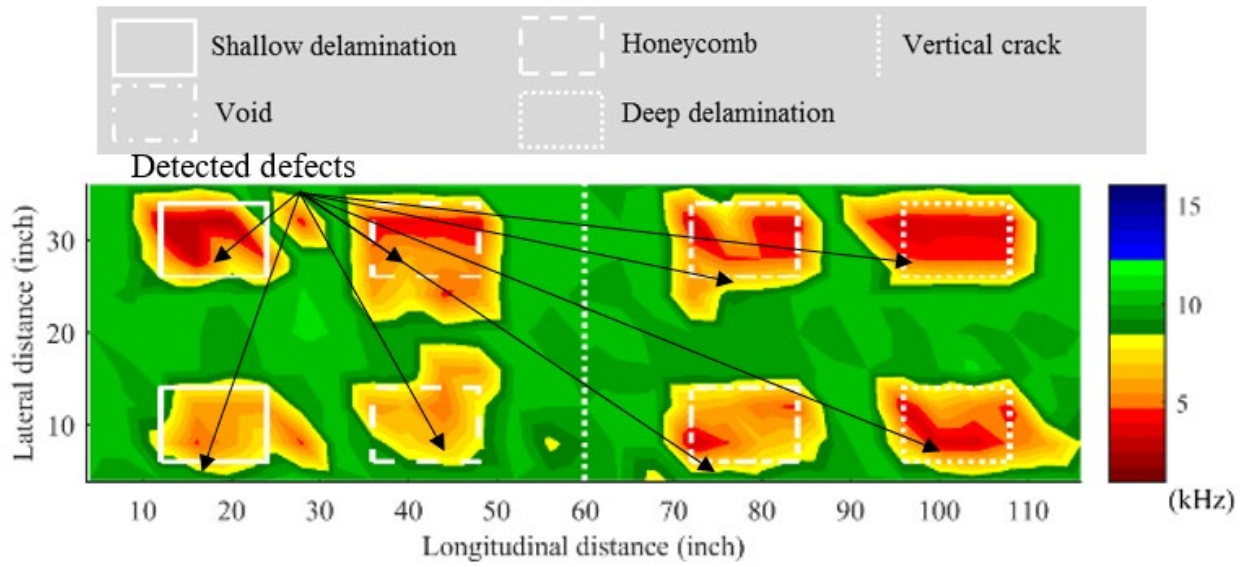
Source: FHWA.

B. S2.



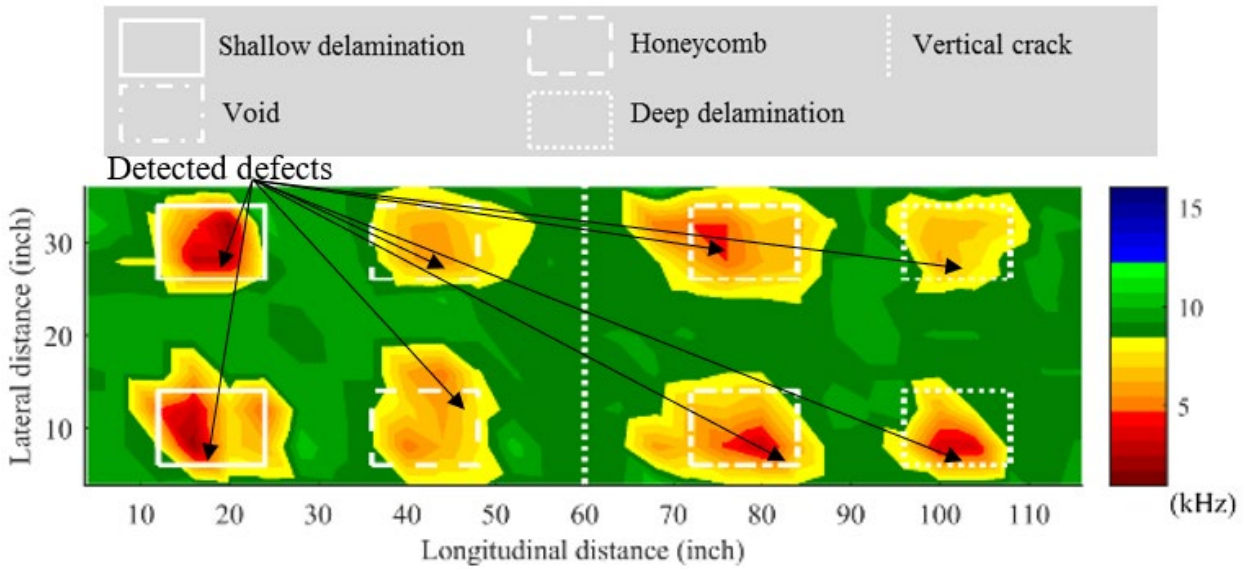
Source: FHWA.

C. S3.



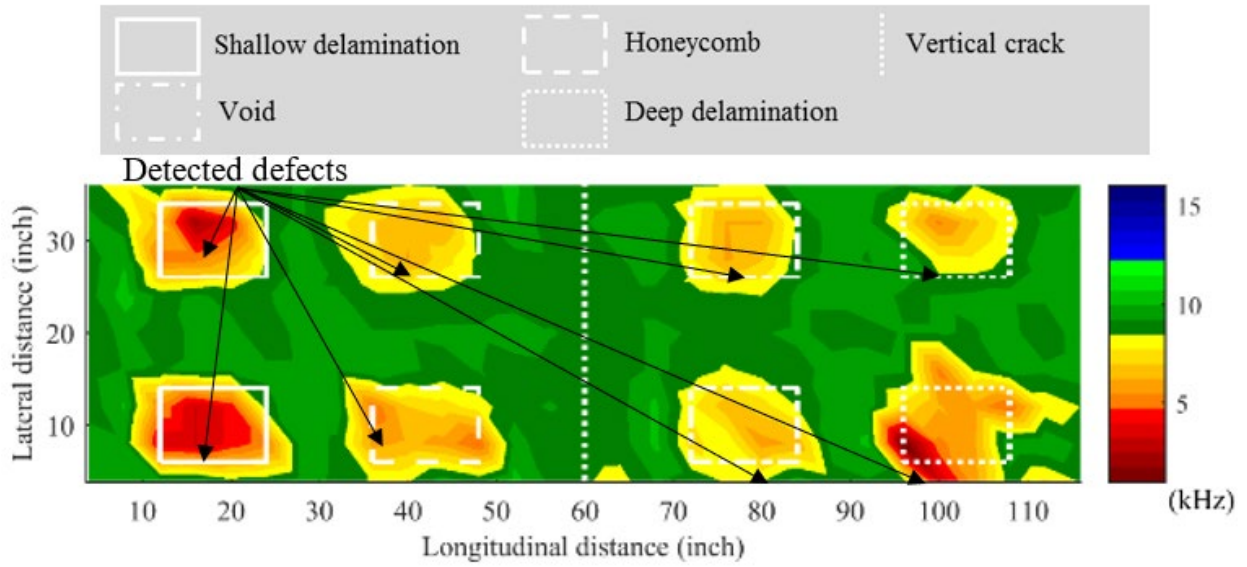
Source: FHWA.

D. S4.



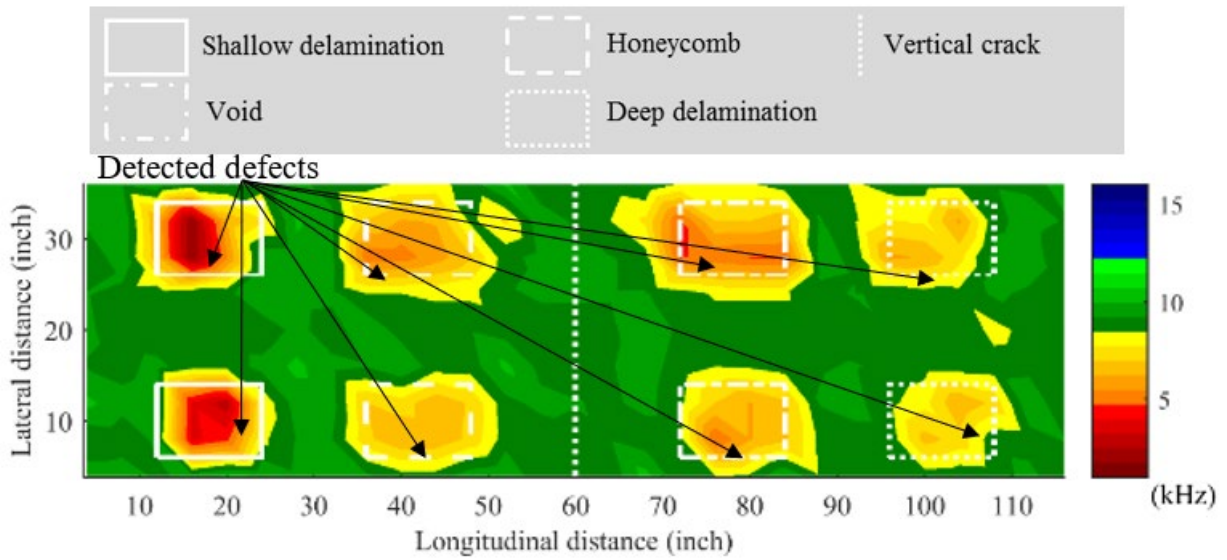
Source: FHWA.

E. S5.



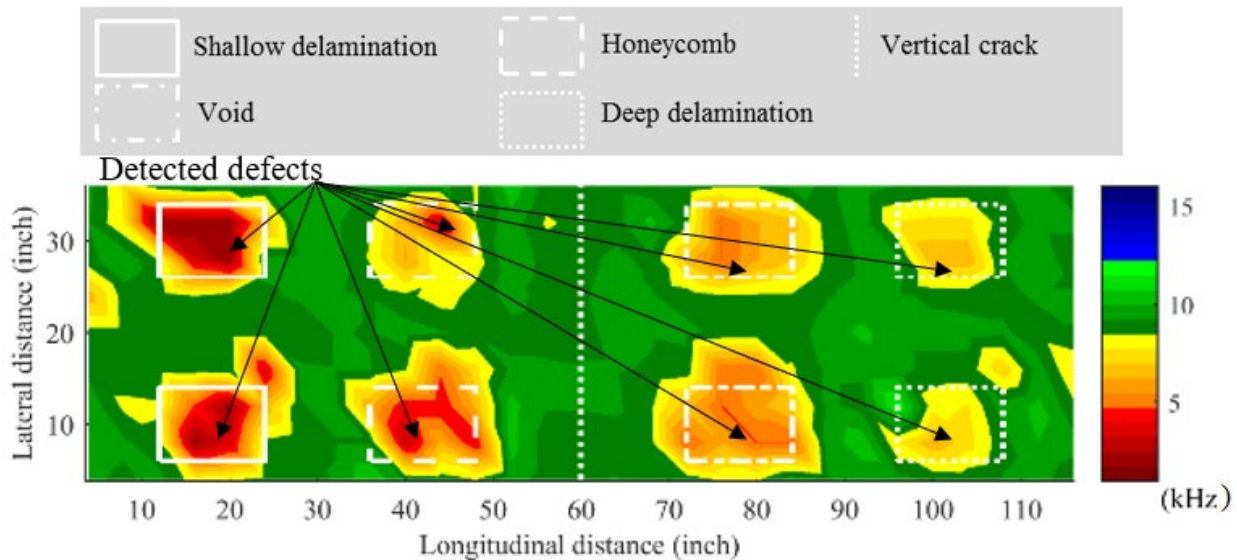
Source: FHWA.

F. S6.



Source: FHWA.

G. S7.



Source: FHWA.

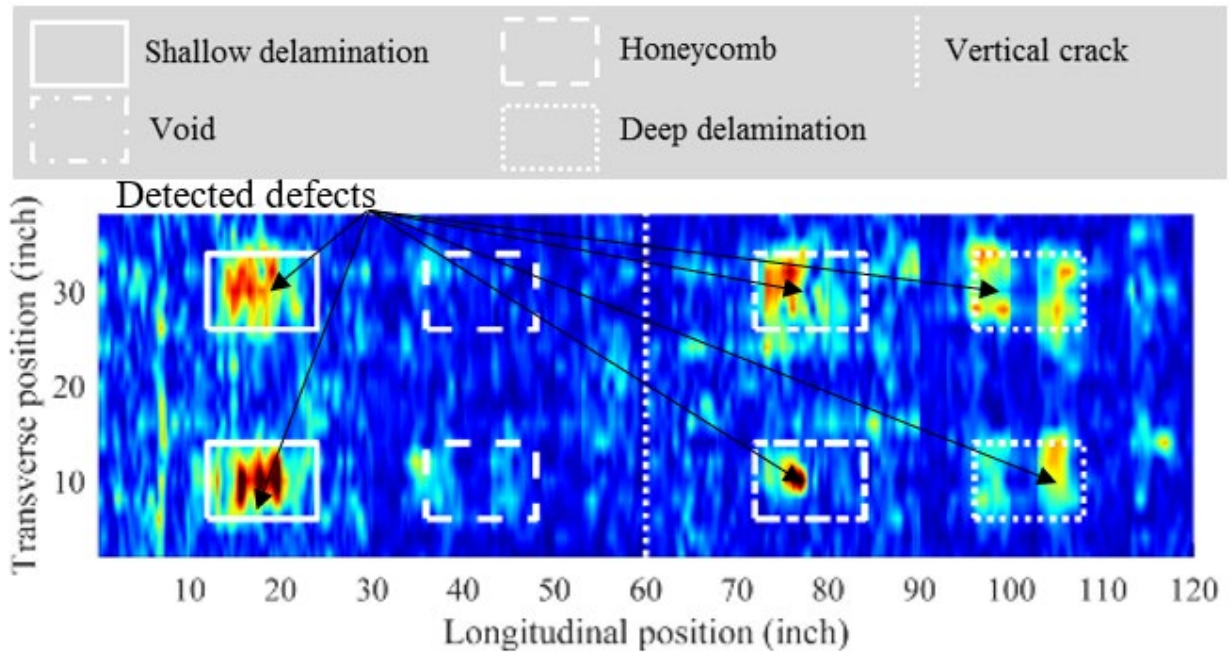
H. S8.

**Figure 59. Graphs. NDE condition maps with IE.**

## UT METHOD

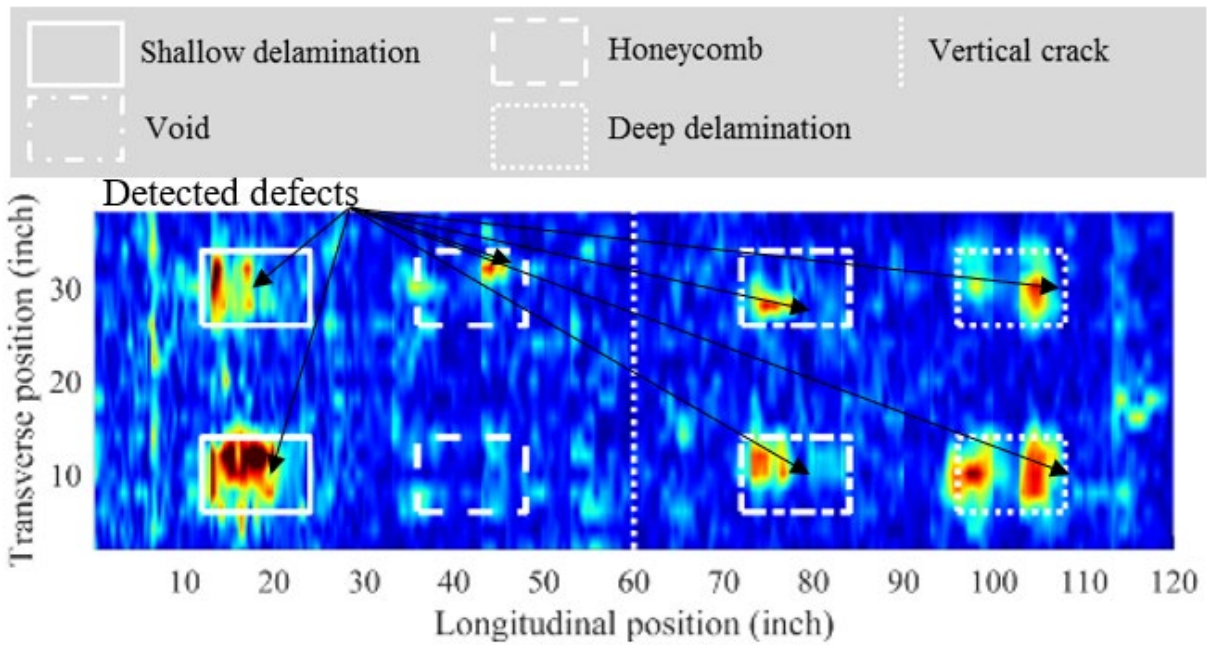
The UT method used SH waves to detect objects under the concrete surface in a pulse–echo manner. When SH waves are reflected by a reflector, the time from the start of the pulse motion to the arrival of the echo is measured. If the wave speed is known, the depth of the object can be estimated using SAFT, which can process multiple pulse–echo signals and give a B-scan—a 2D image of the cross section below the UT antenna. Combining all the B-scans gives panoramic B-, C-, and D-scans. The UT-based C-scans with UT-MIRA, B-scans with UT-MIRA, C-scans with UT-EyeCon, and B-scans with UT-EyeCon are shown in figure 60 through figure 63, respectively. Four C-scans were taken at the depth of shallow and deep delaminations, voids, and honeycombing, and then one-quarter of each C-scan in the longitudinal direction was stitched together showing the most visible defects at different depths (in the longitudinal direction from 0 to 30 inches for shallow delaminations, from 30 to 60 inches for honeycombing, from 60 to 90 inches for voids, and from 90 to 120 inches for deep delaminations). The UT method detected shallow and deep delaminations and voids in all eight specimens, but only some honeycombing in some specimens. Variation in the honeycombing resulted in wave impedances close to the intact concrete, and the reflections from the honeycombing were too weak to detect. Shallow delaminations in specimens S5–S8 were not as clear as those in specimens S1–S4 because the reflected waves from shallow delaminations interfered with the direct waves, making it challenging to separate reflection waves from direct waves and eventually undermining the resolution of each B-scan when defects were very shallow. The average depth of shallow delaminations in specimens S5–S8 was 28 percent less than that in specimens S1–S4; thus, direct waves interfered with the reflected waves from shallow delaminations in specimens S5–S8 and undermined the resolution of these shallow delaminations in the condition maps. In addition, the interference made it challenging to determine the depth of shallow delaminations (figure 63-E

through figure 63-H) because the interference strengthened the resolution of shallow delaminations but did not show the correct position of the actual delamination (figure 63-H). Voids and deep delaminations look clearer than shallow delaminations because the depth of the voids and deep delaminations was deeper than that of shallow delaminations and the reflection waves from voids and deep delaminations had the least interference with direct waves. The UT method imaged the top layer rebar and the thickness (i.e., bottom) of the specimen.



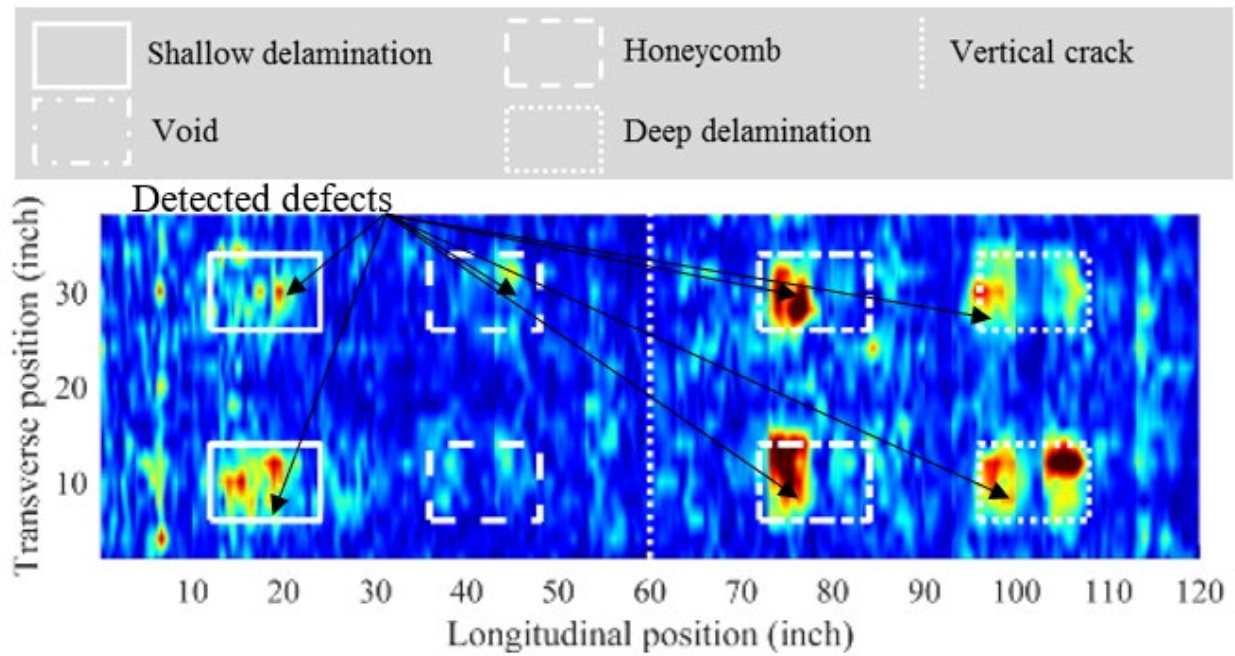
Source: FHWA.

A. S1.



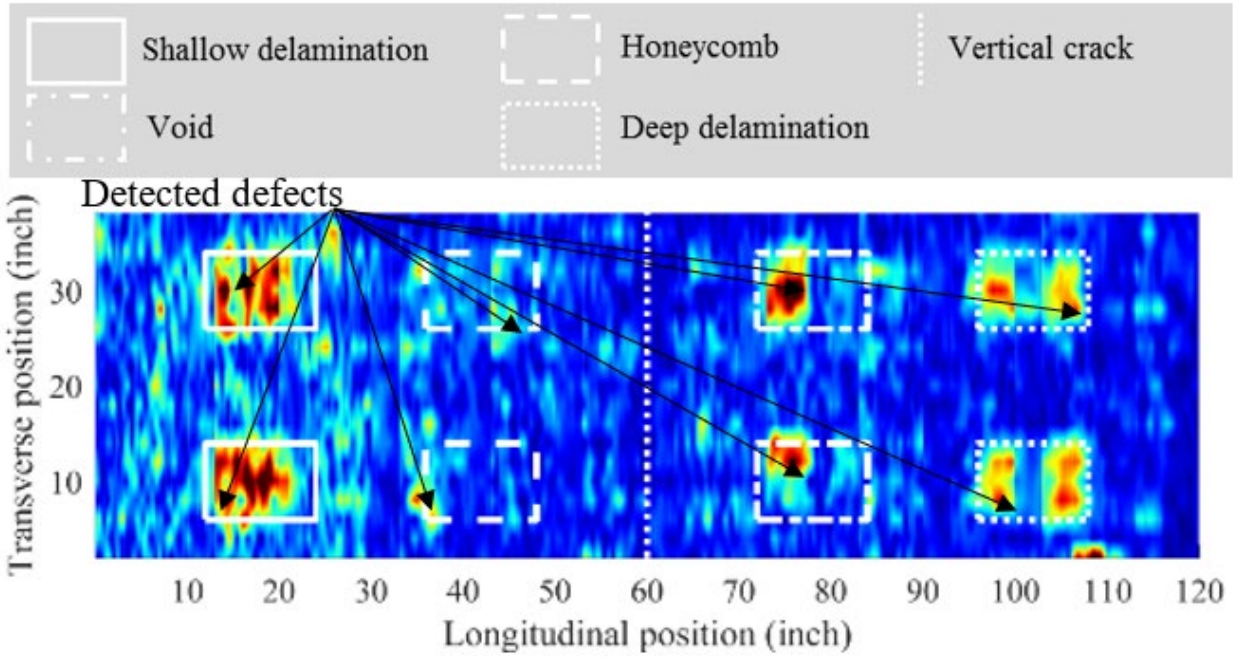
Source: FHWA.

B. S2.



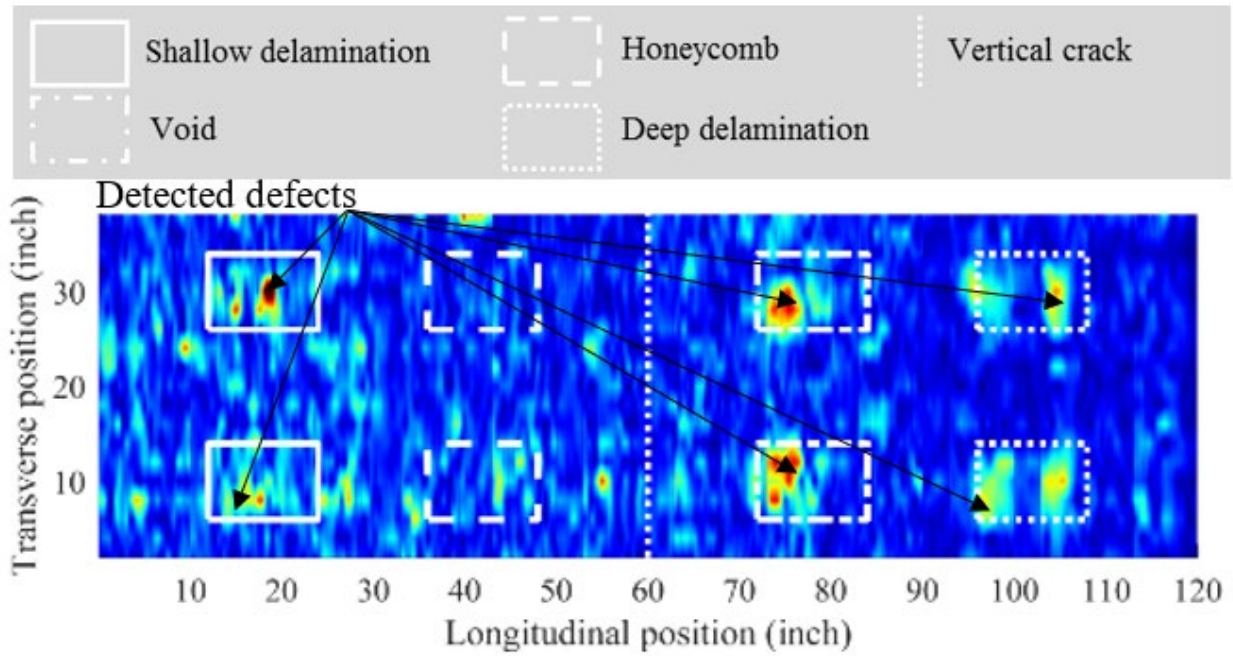
Source: FHWA.

C. S3.



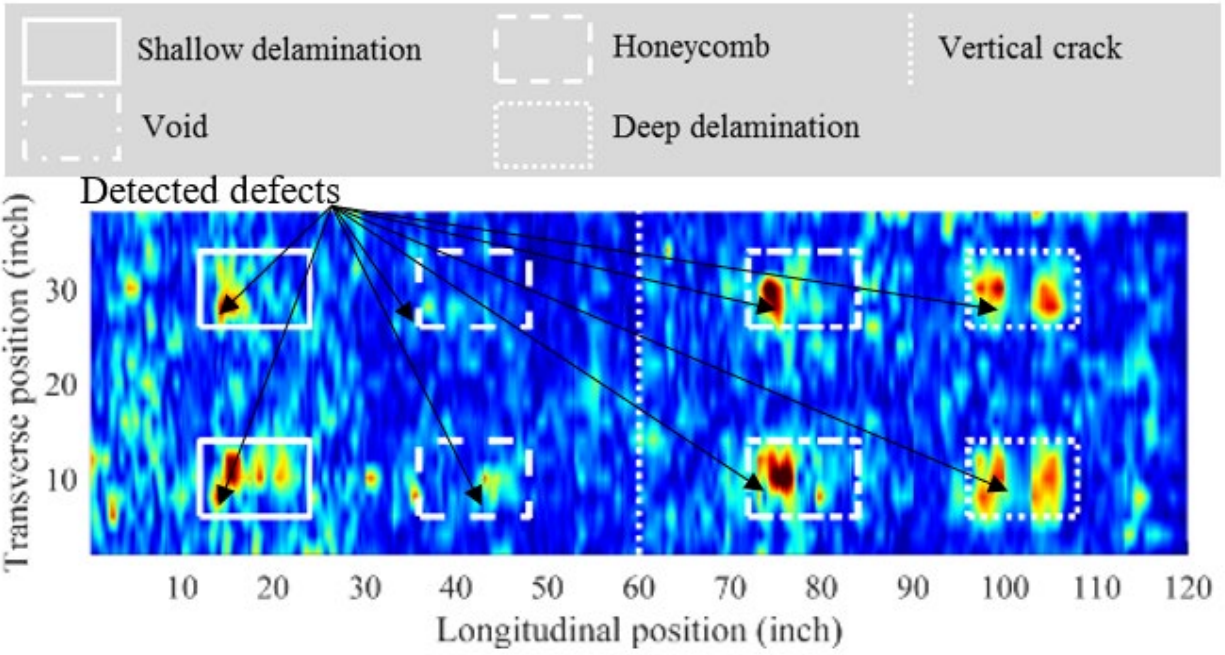
Source: FHWA.

D. S4.



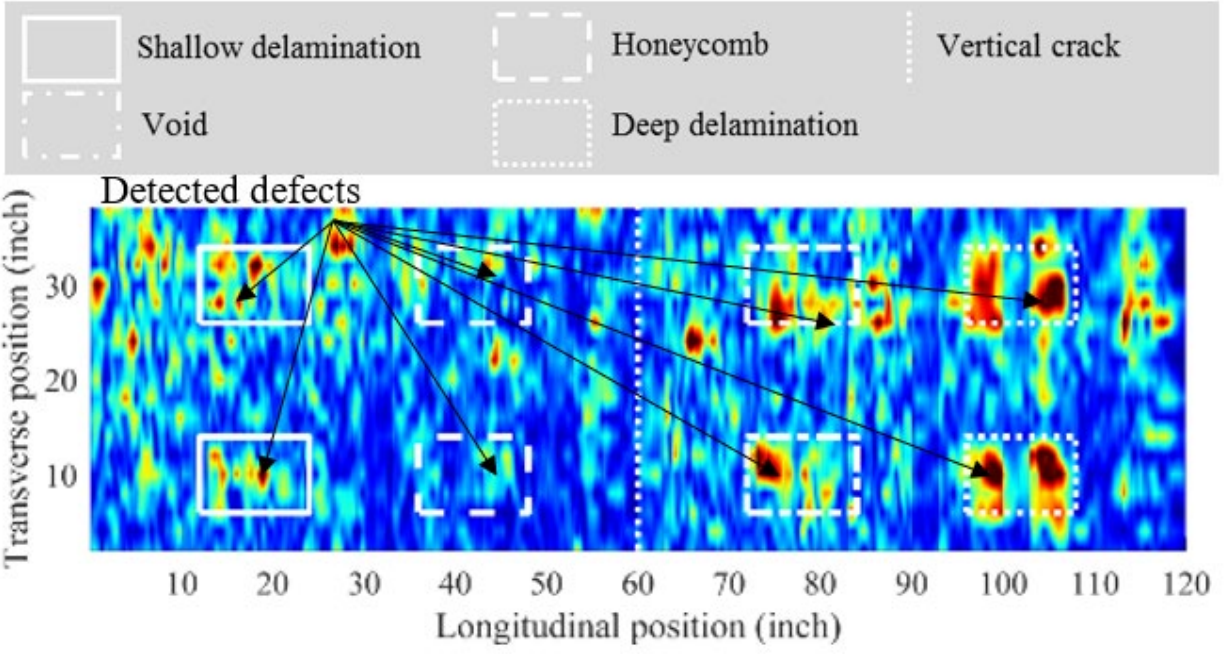
Source: FHWA.

E. S5.



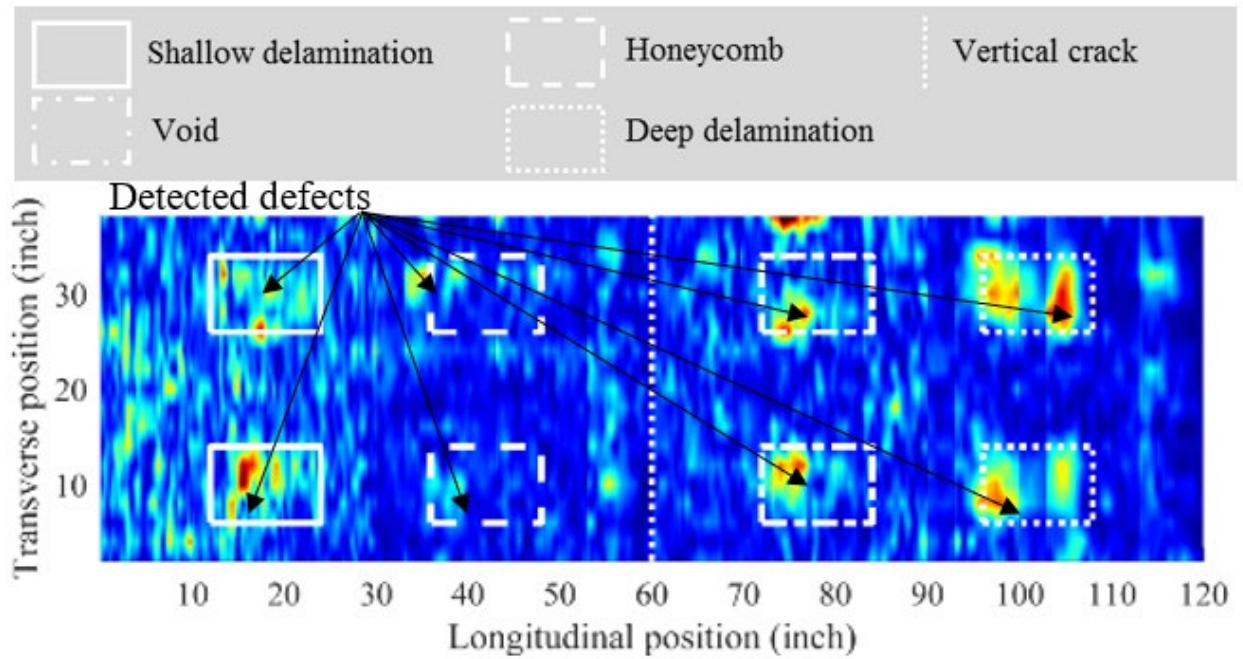
Source: FHWA.

F. S6.



Source: FHWA.

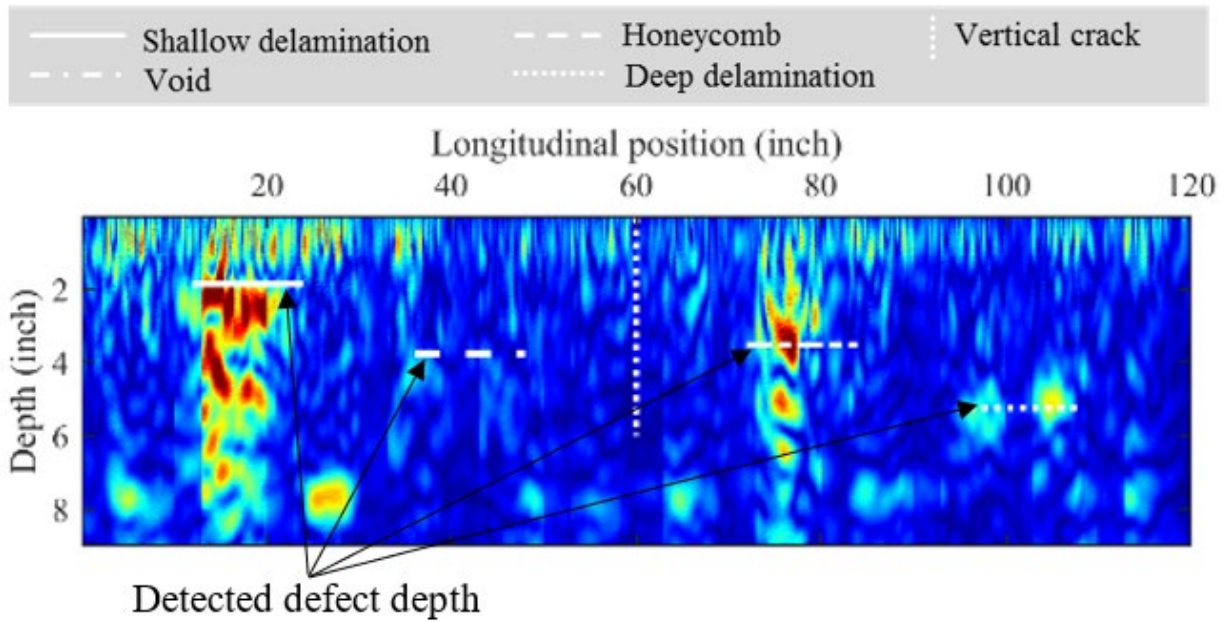
G. S7.



Source: FHWA.

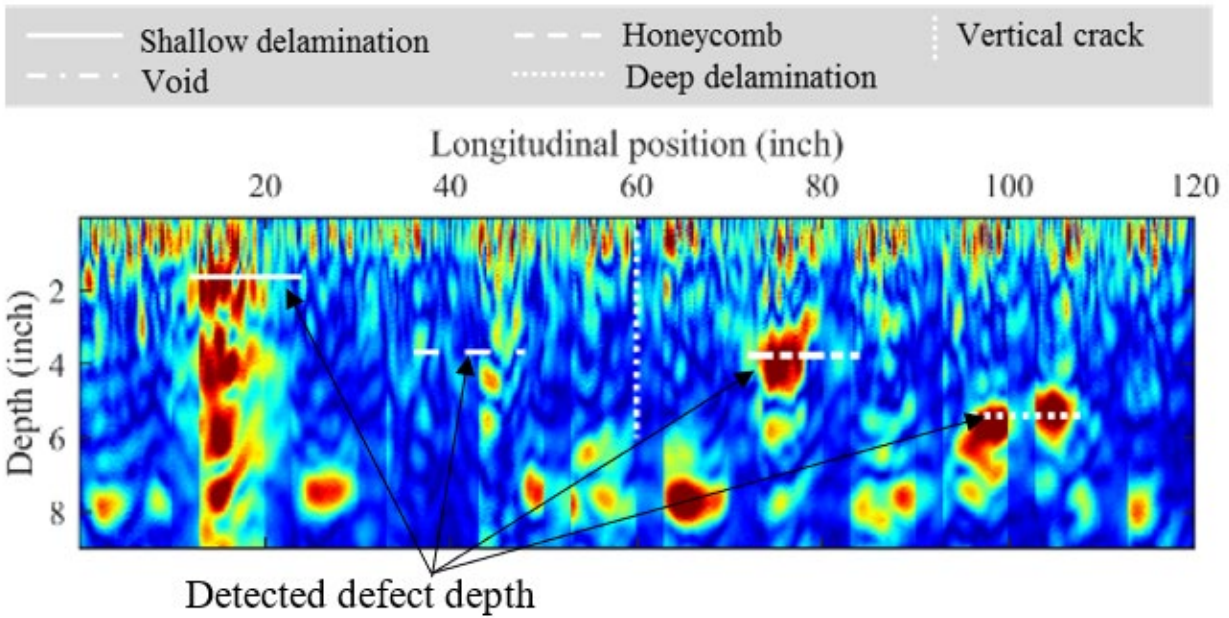
H. S8.

**Figure 60. Graphs. NDE C-scans with UT-MIRA.**



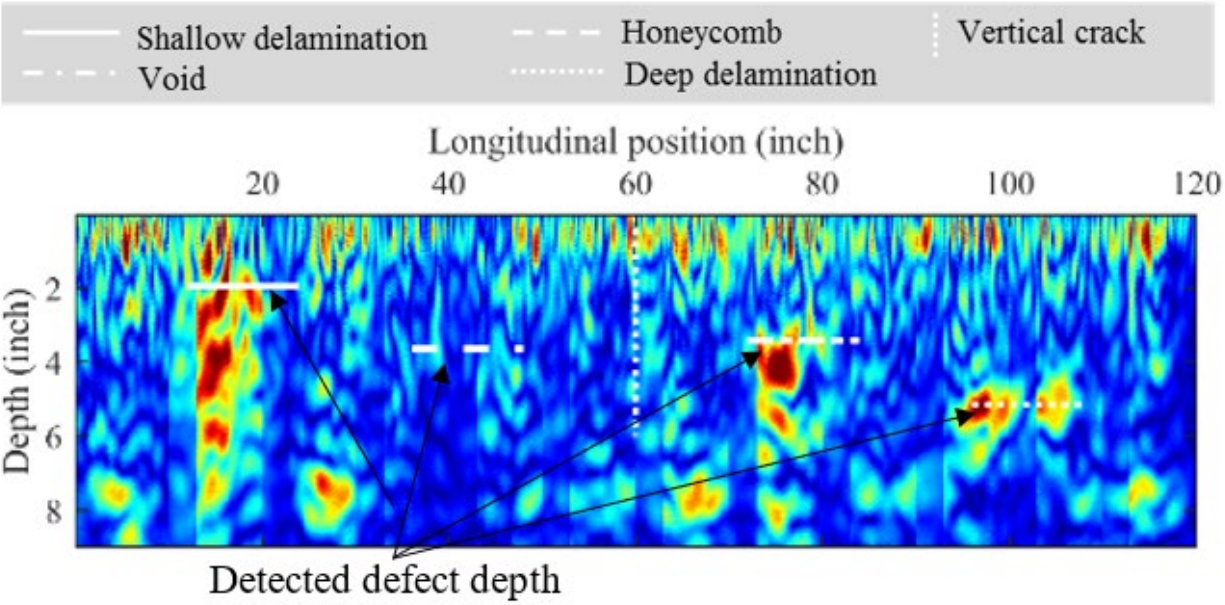
Source: FHWA.

A. S1.



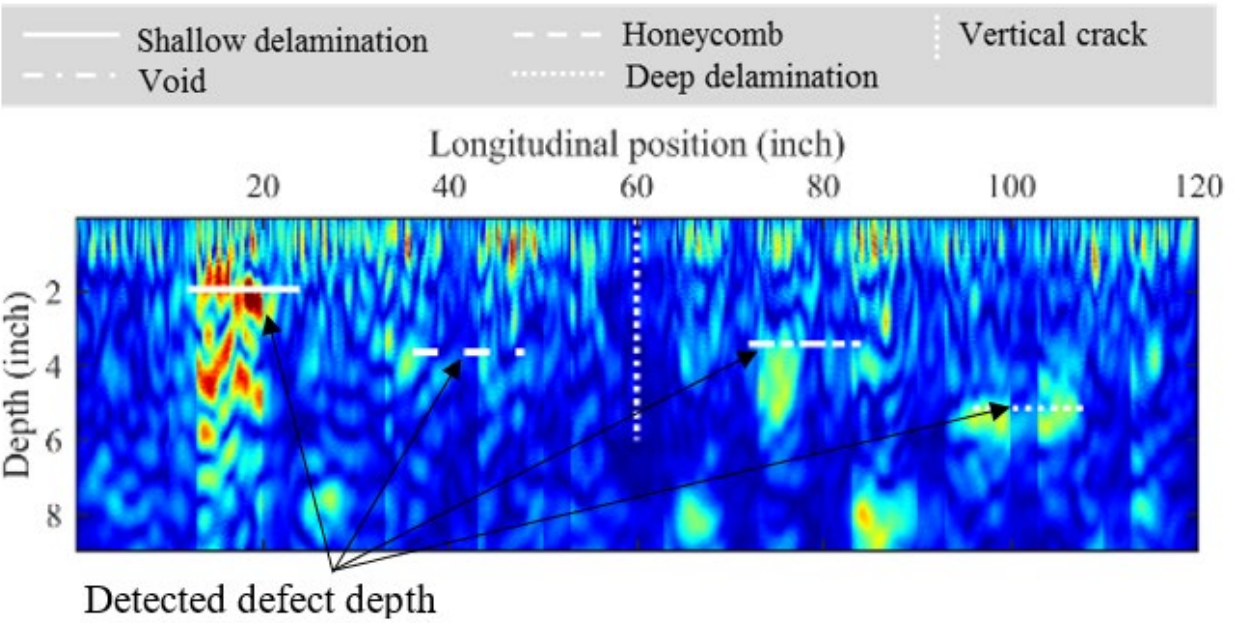
Source: FHWA.

B. S2.



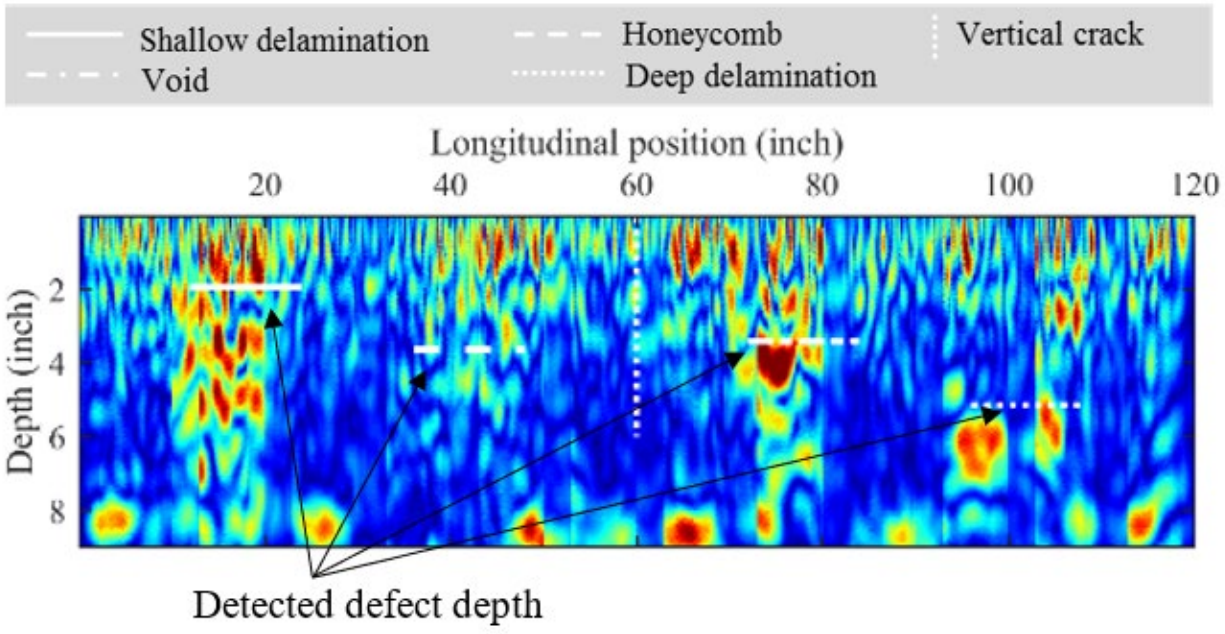
Source: FHWA.

C. S3.



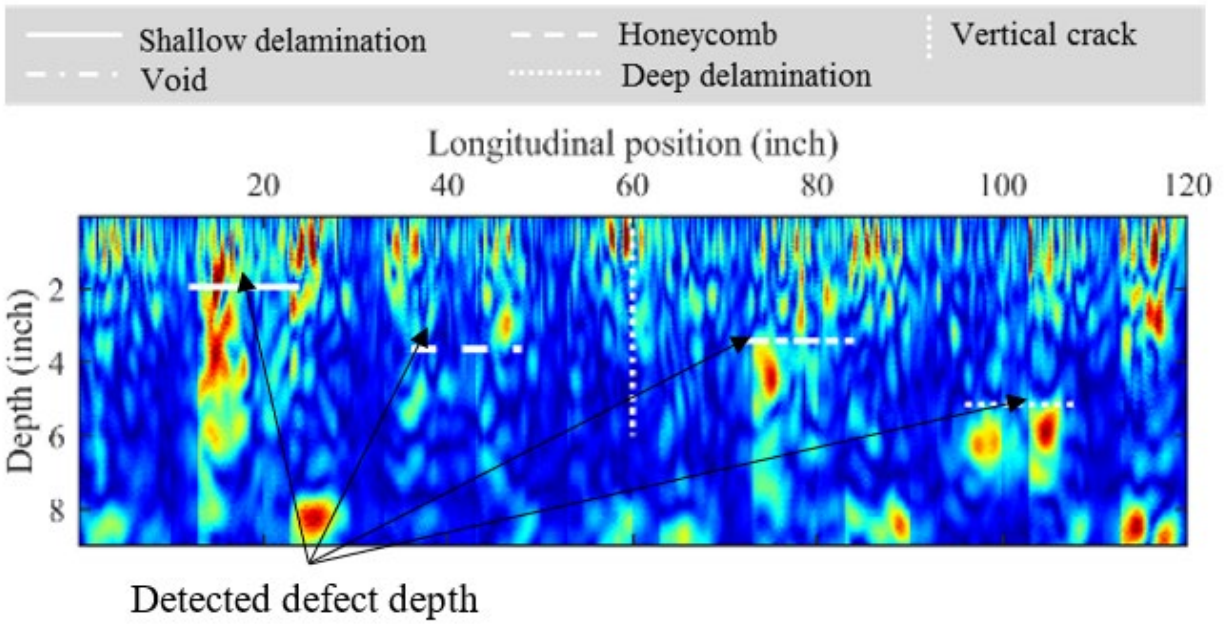
Source: FHWA.

D. S4.



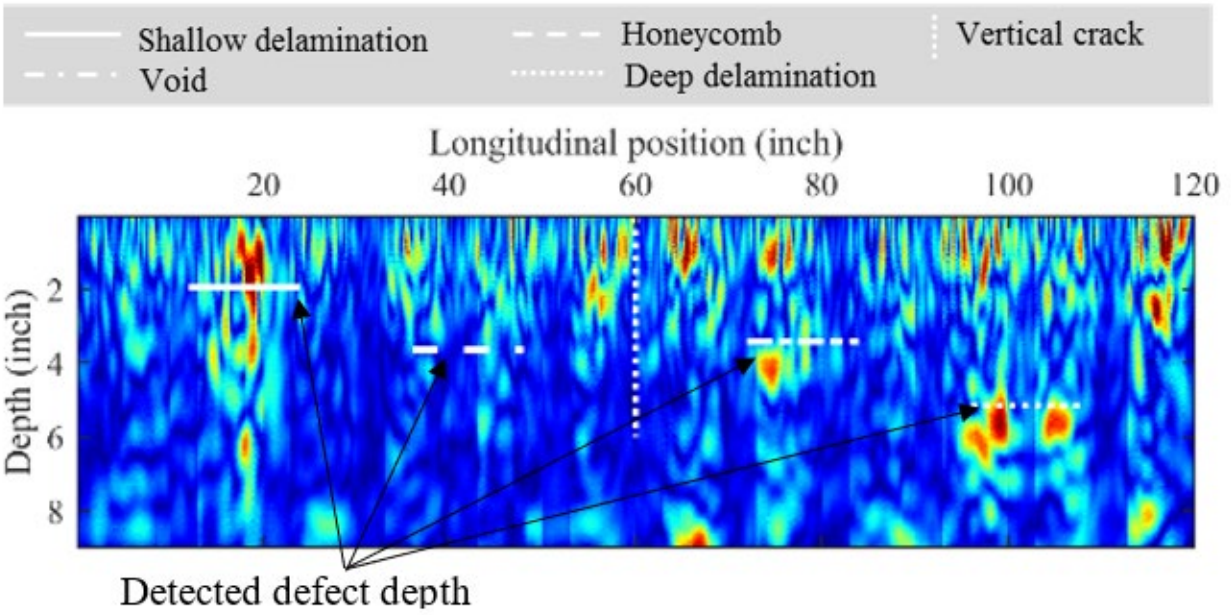
Source: FHWA.

E. S5.



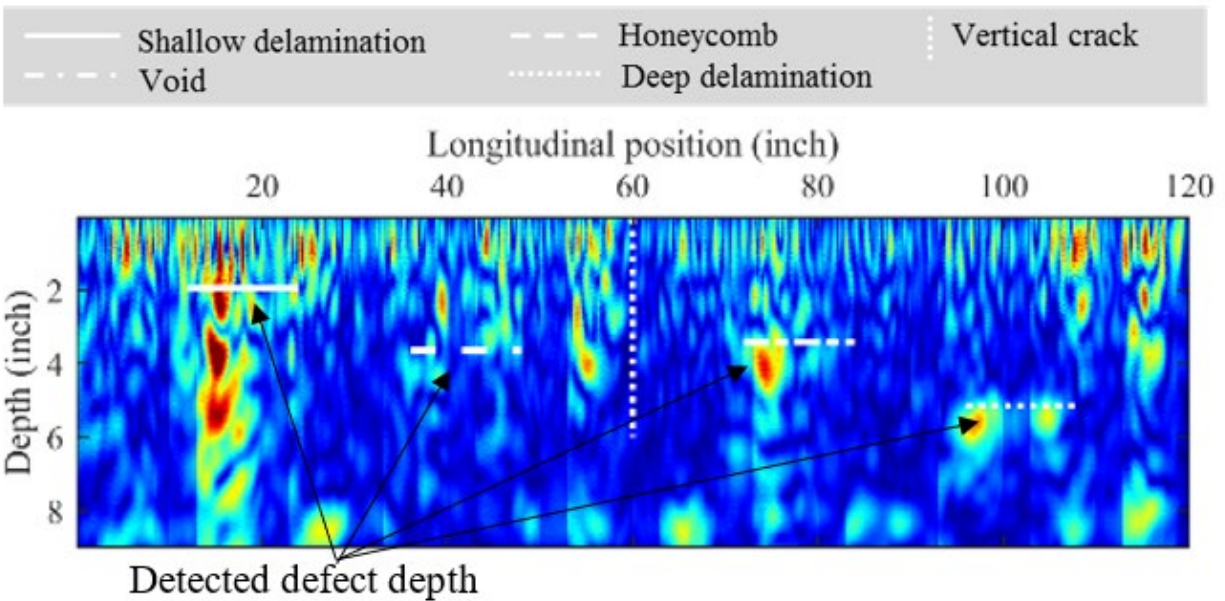
Source: FHWA.

F. S6.



Source: FHWA.

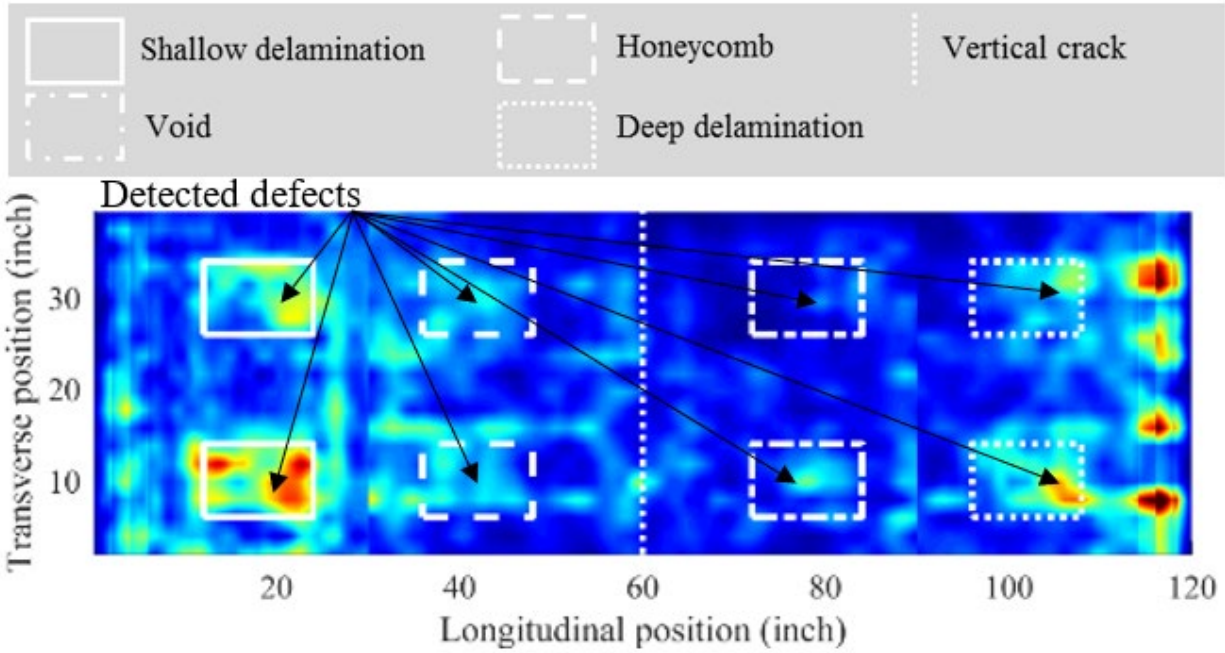
G. S7.



Source: FHWA.

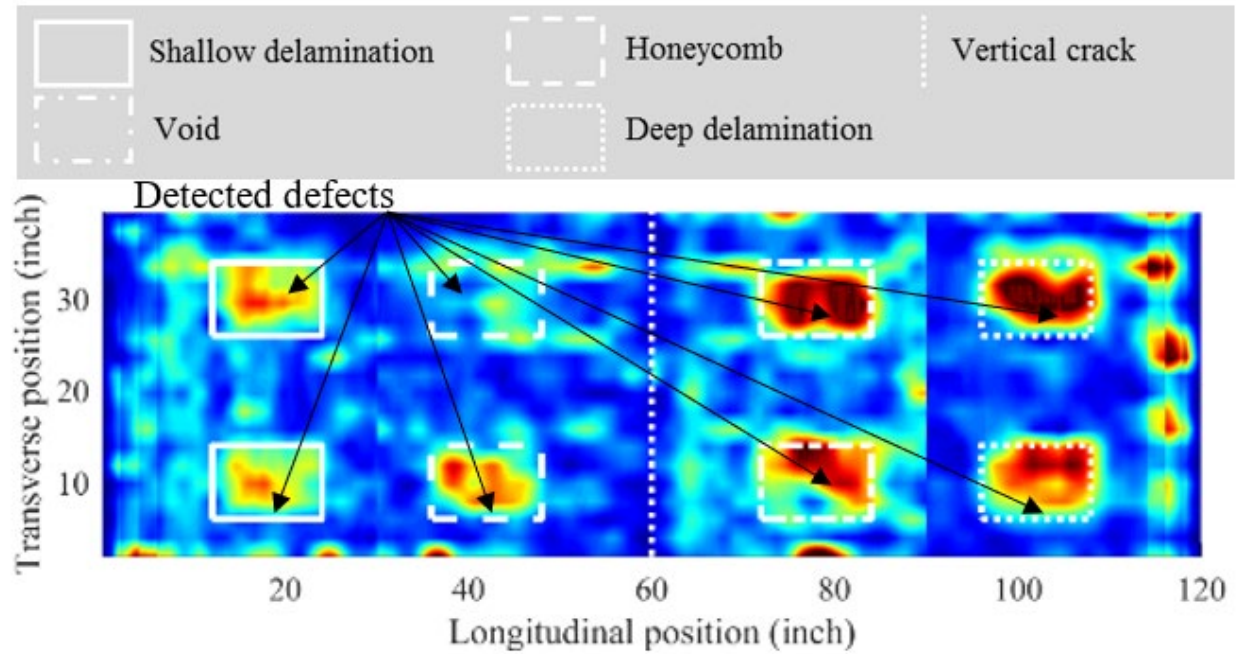
H. S8.

**Figure 61. Graphs. NDE B-scans with UT-MIRA.**



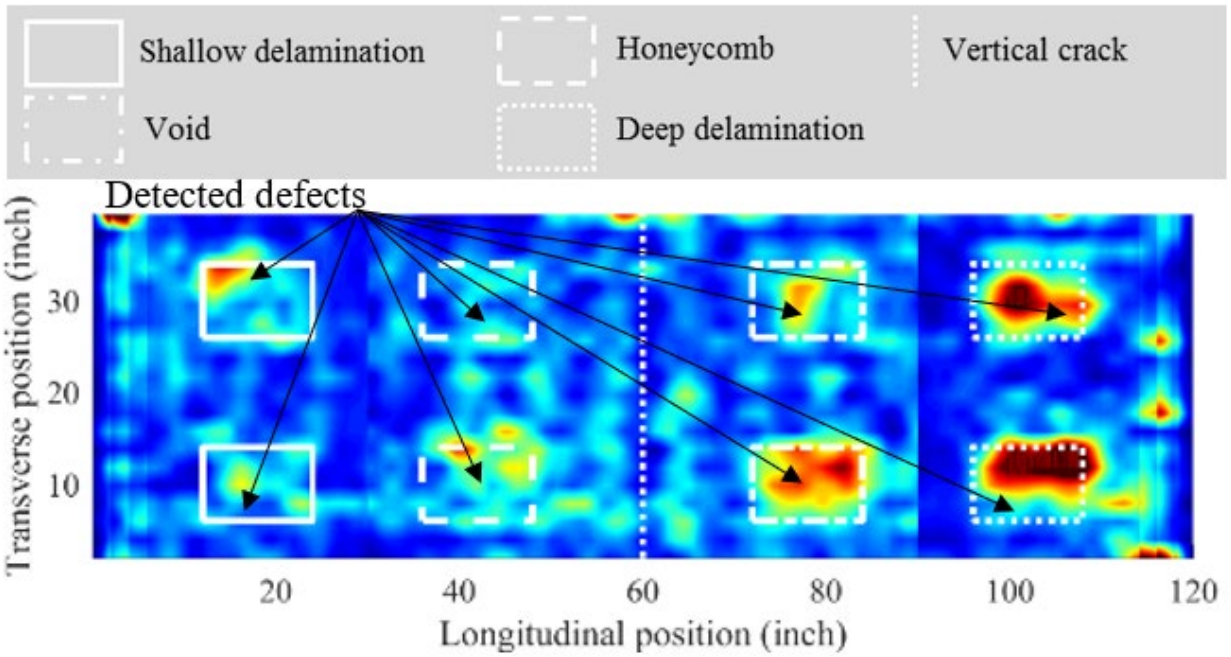
Source: FHWA.

A. S1.



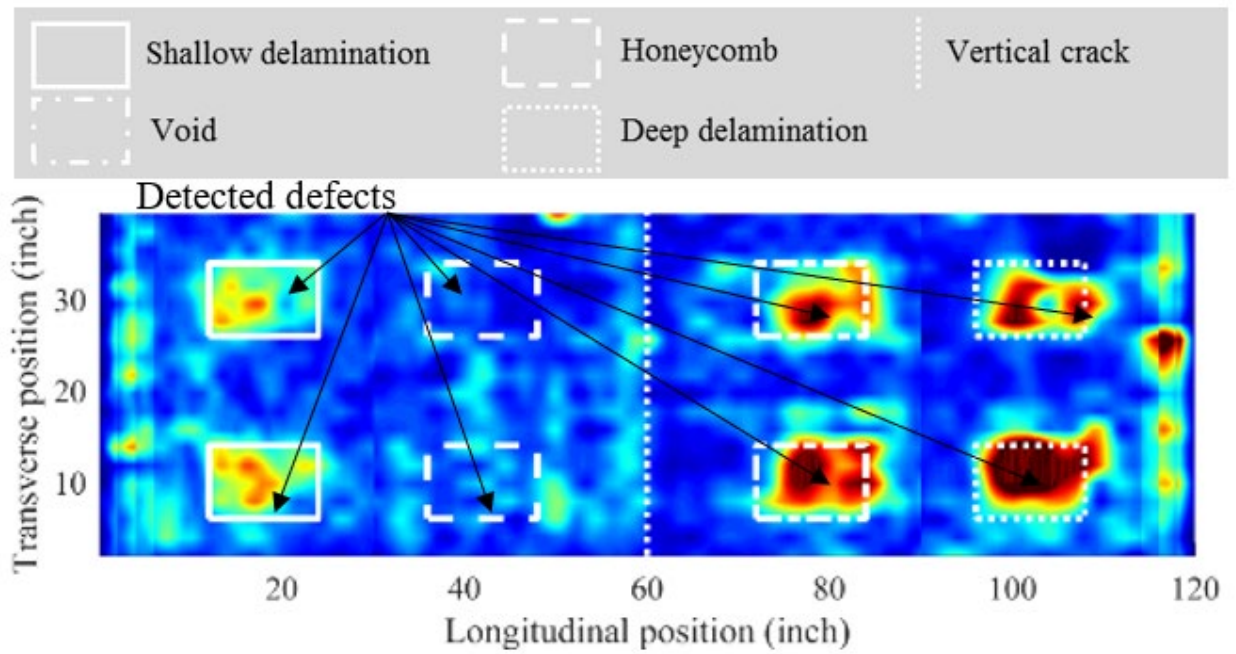
Source: FHWA.

B. S2.



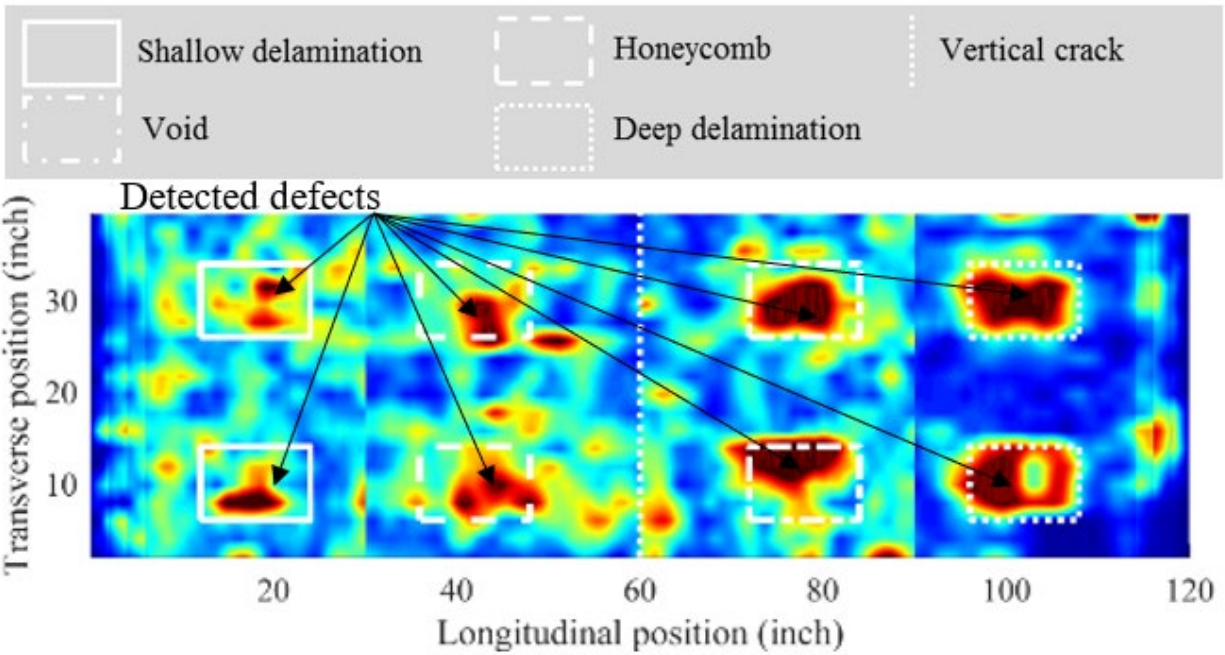
Source: FHWA.

C. S3.



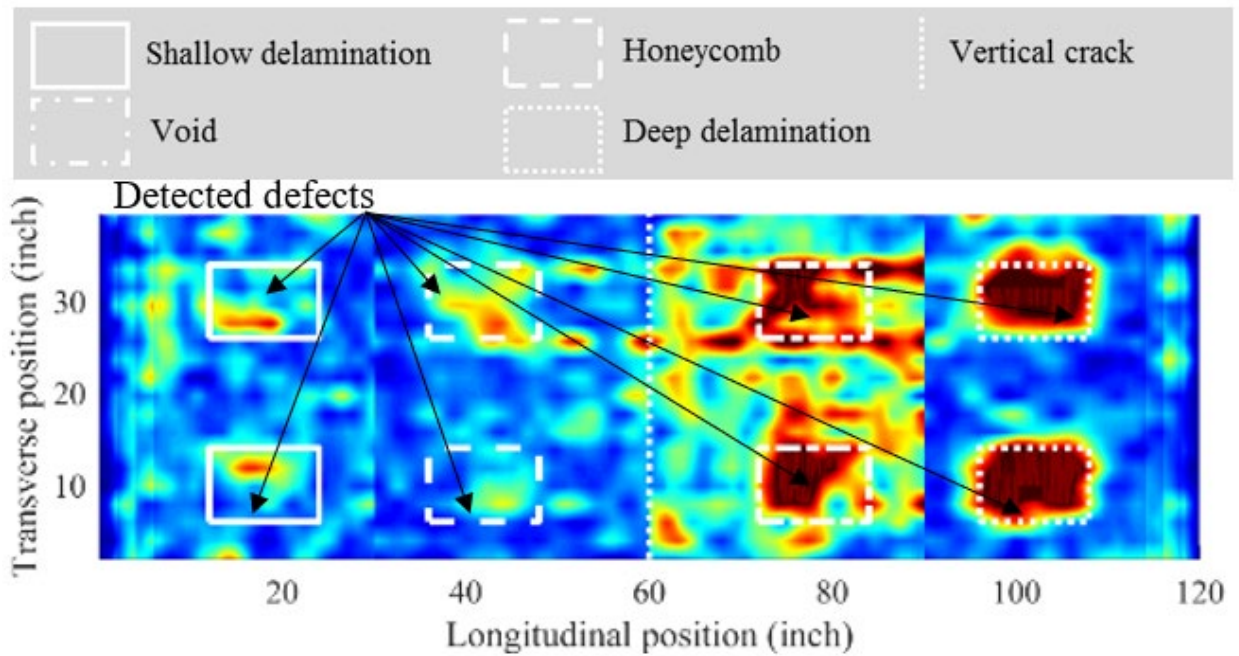
Source: FHWA.

D. S4.



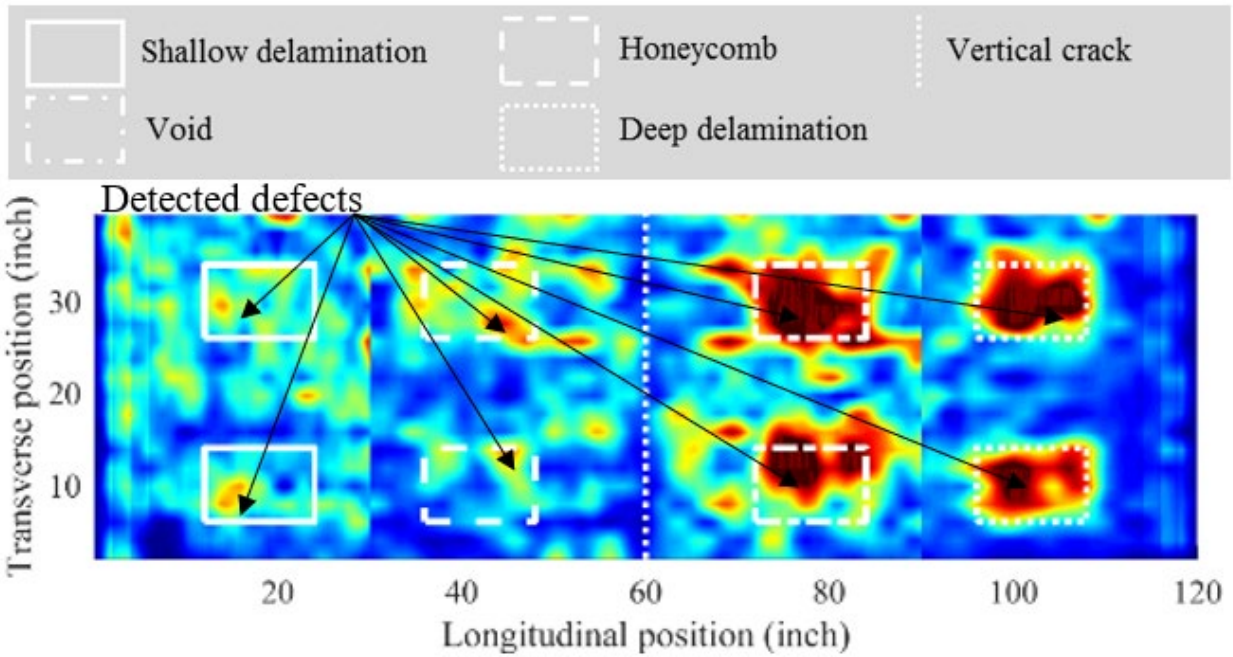
Source: FHWA.

E. S5.



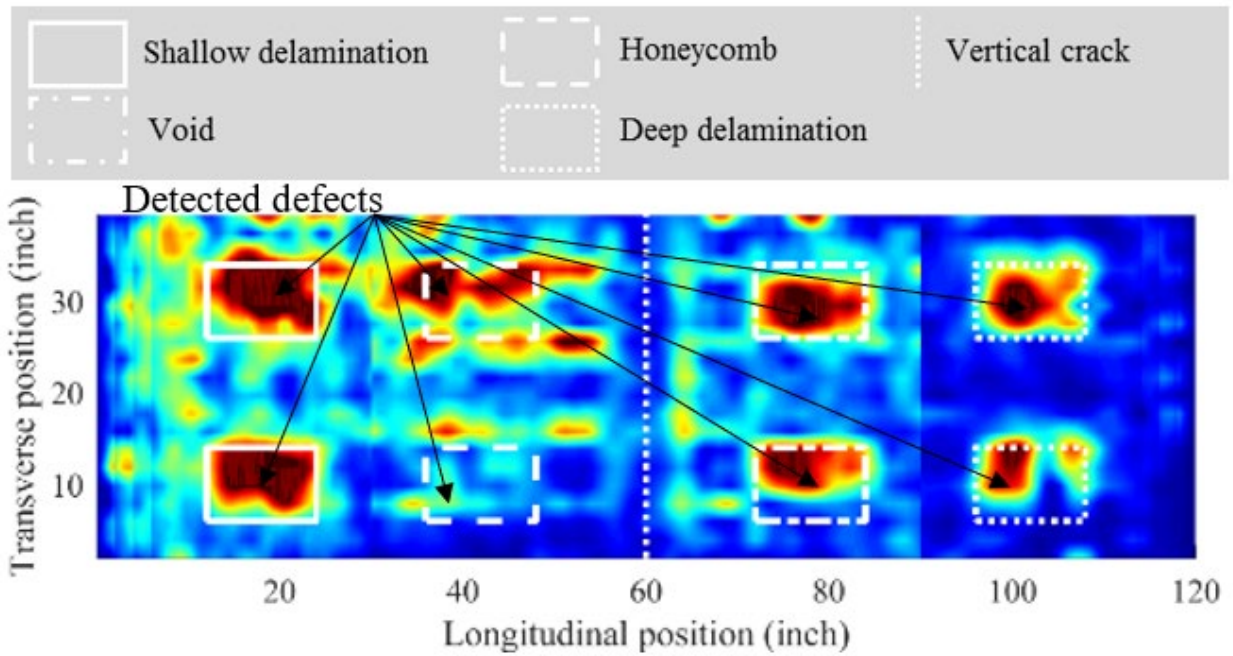
Source: FHWA.

F. S6.



Source: FHWA.

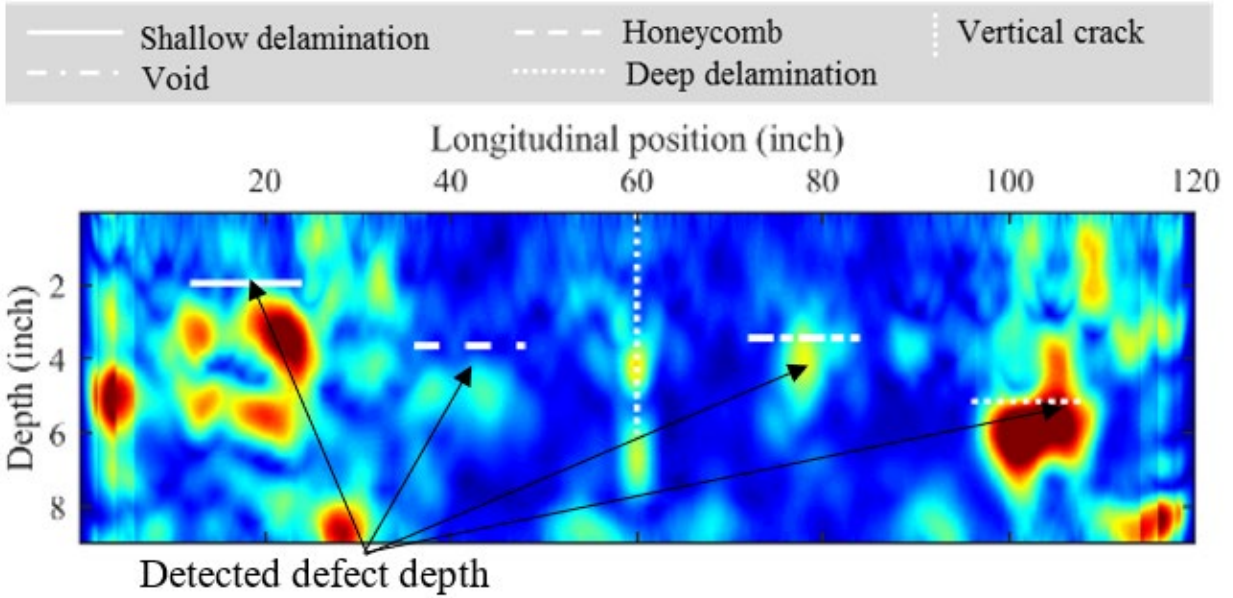
G. S7.



Source: FHWA.

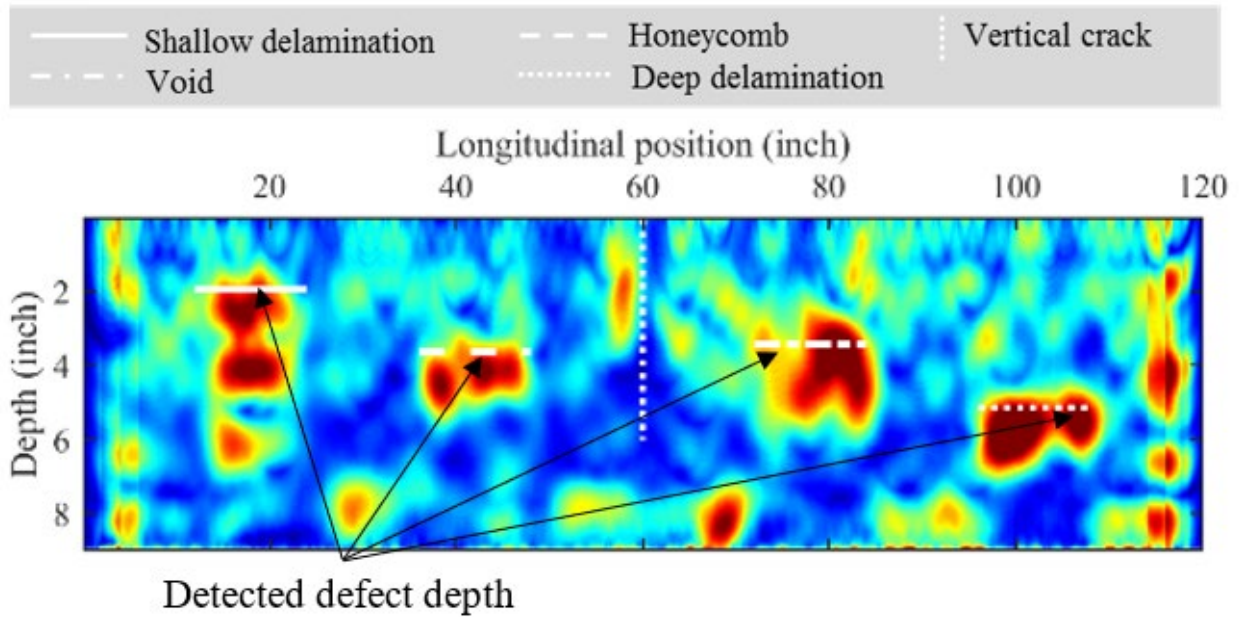
H. S8.

Figure 62. Graphs. NDE C-scans with UT-EyeCon.



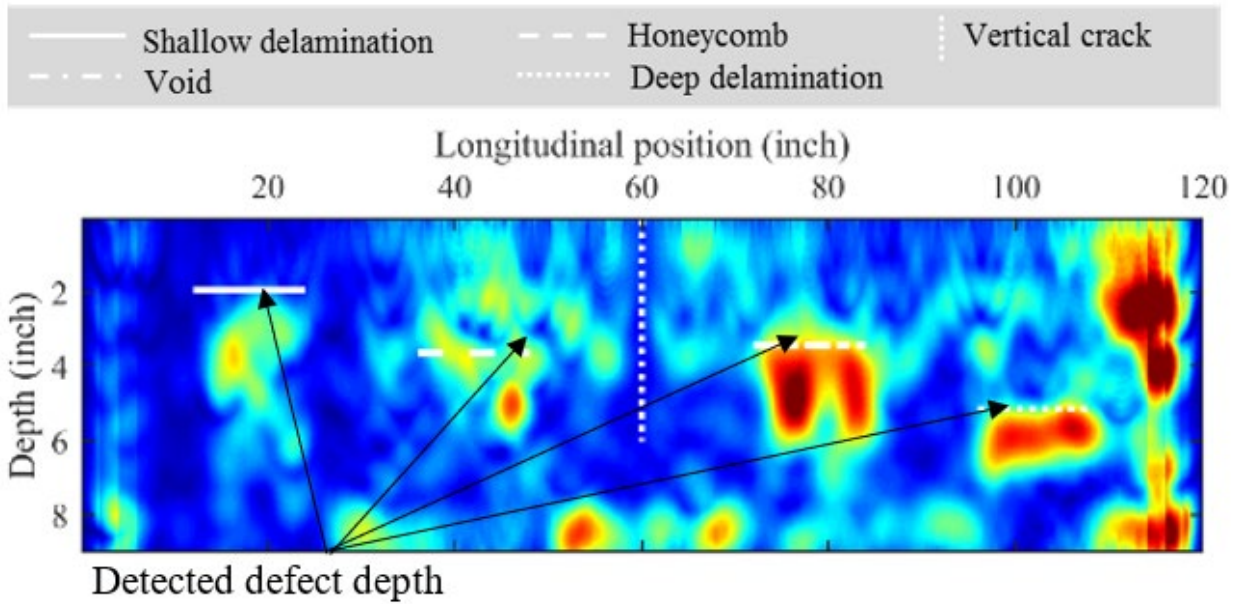
Source: FHWA.

A. S1.



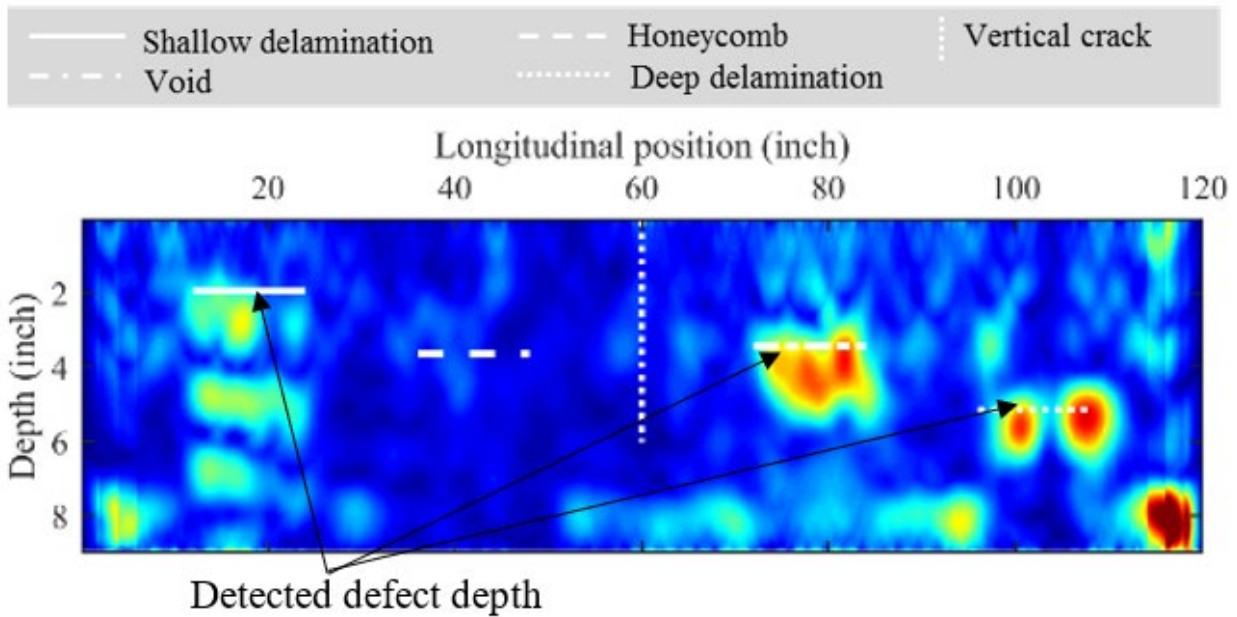
Source: FHWA.

B. S2.



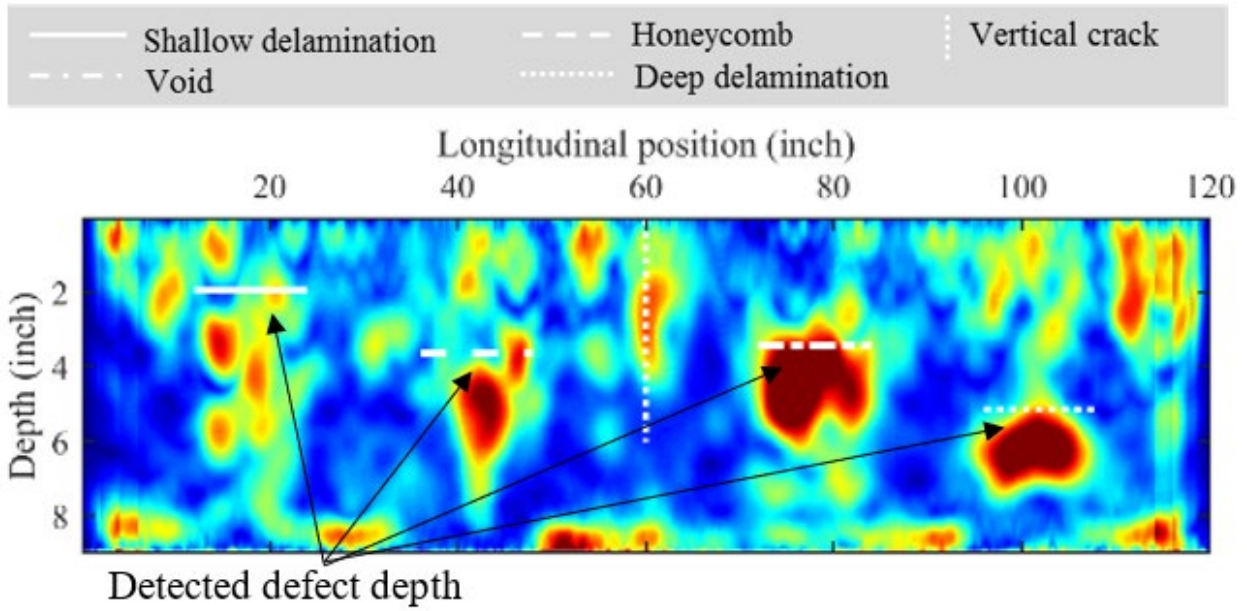
Source: FHWA.

C. S3.



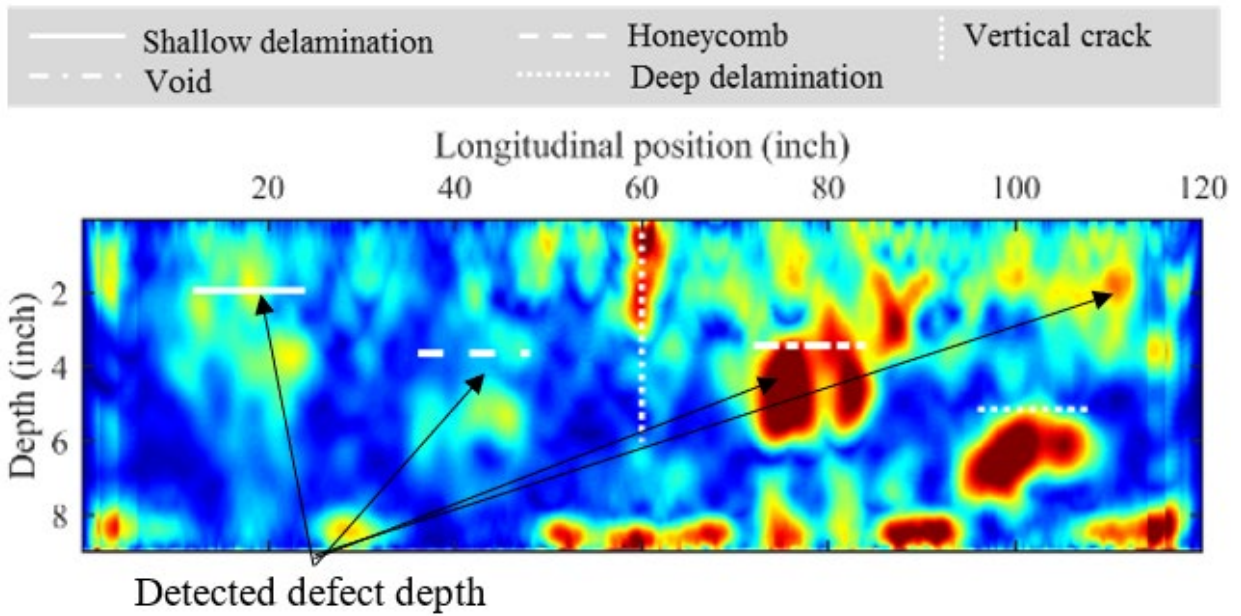
Source: FHWA.

D. S4.



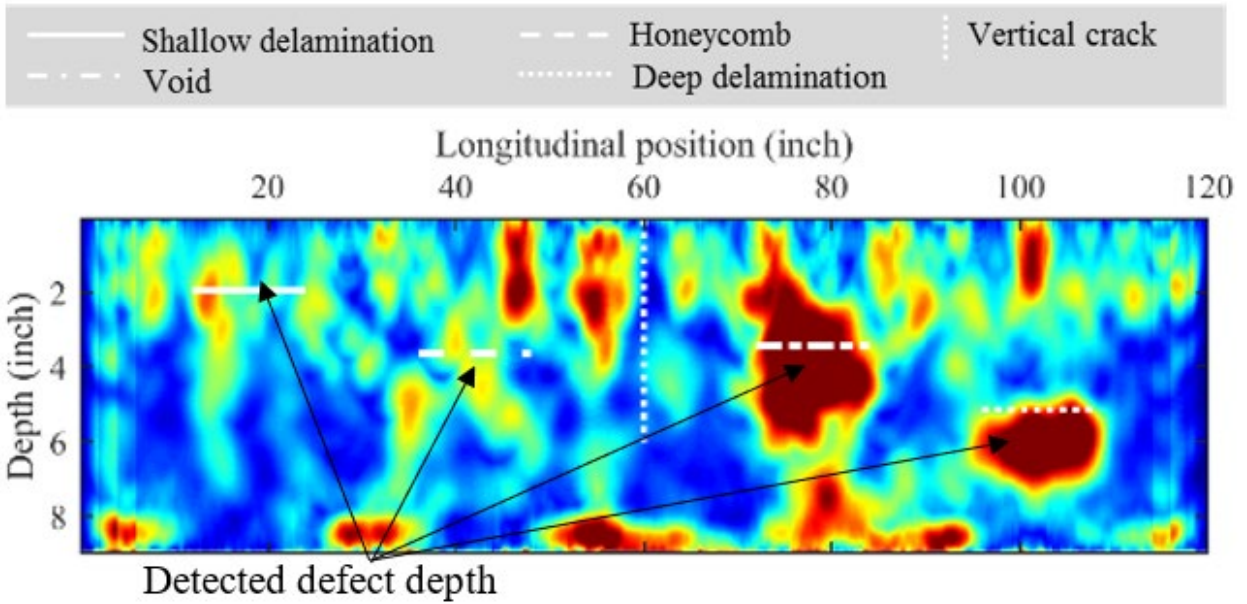
Source: FHWA.

E. S5.



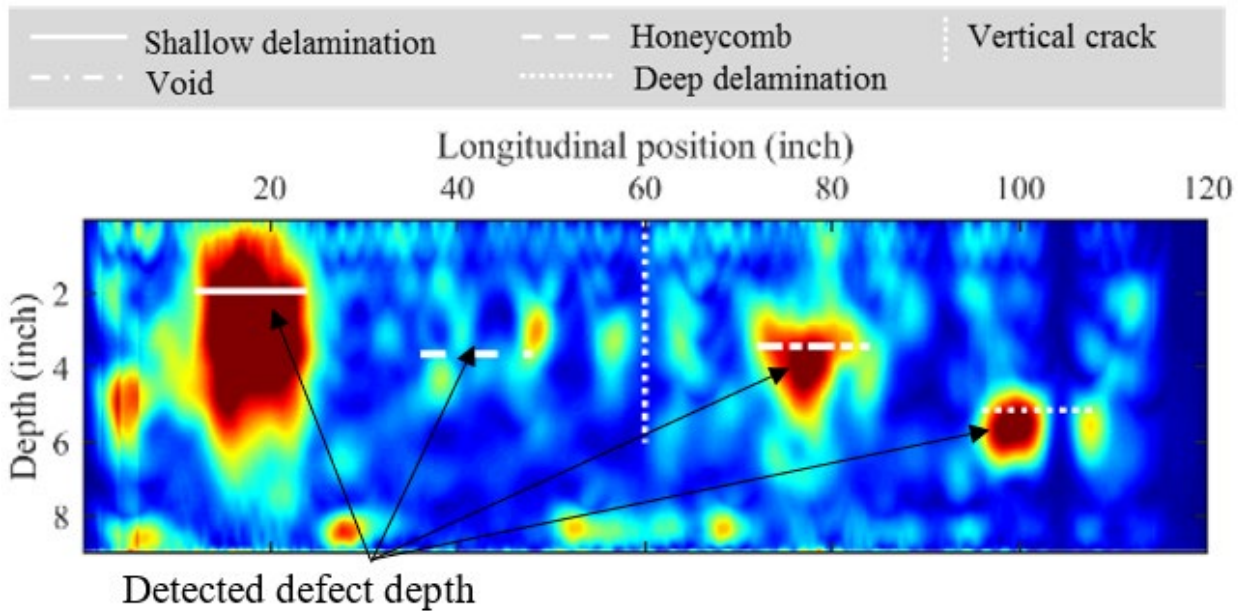
Source: FHWA.

F. S6.



Source: FHWA.

G. S7.



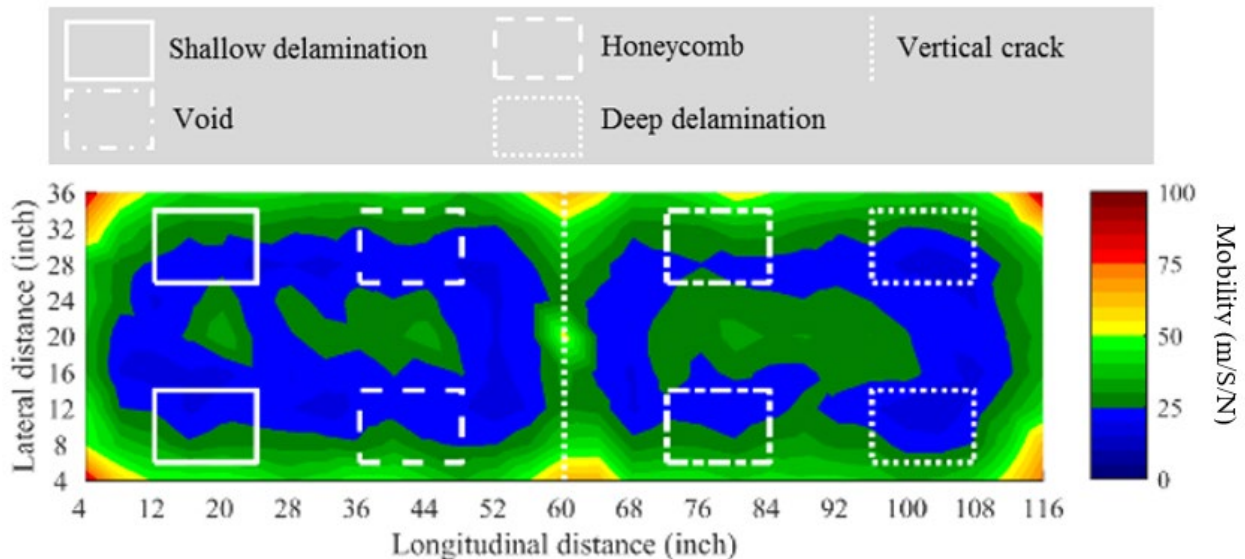
Source: FHWA.

H. S8.

Figure 63. Graphs. NDE B-scans with UT-EyeCon.

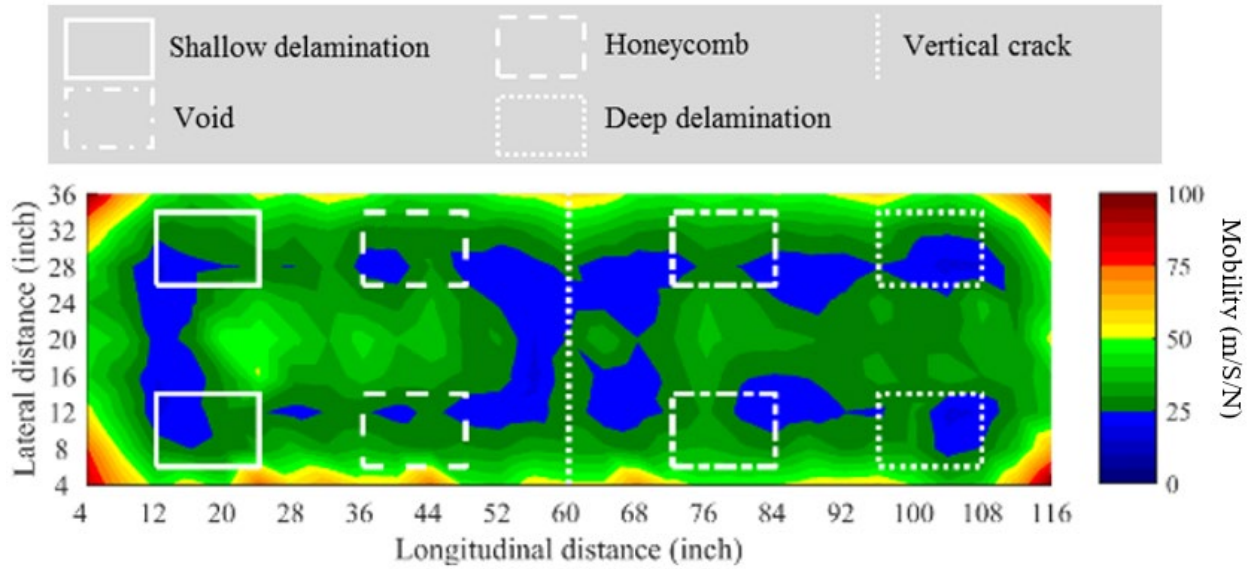
## IR METHOD

The IR method used the mobility spectrum—the velocity spectrum divided by the force spectrum—to detect delaminations and voids in concrete bridge decks. The IR method detected delaminations and voids in terms of lower mobility in concrete bridge decks. However, the results were affected by the depth-to-size ratios of the defects, and defects with large depth-to-size ratios could not be detected. At each test location, the impact force was applied by a hammer and measured by an attached load cell, and then the velocity response of the concrete bridge deck was recorded by a geophone. The condition maps based on the mobility measured by the IR method are shown in figure 64-A through figure 64-H. The IR method detected shallow delaminations in specimens S5–S8 but not in specimens S1–S4 because the shallow delaminations in specimens S1–S4 were at a 28-percent greater depth. The IR method could not detect the other defects in the specimens because the defects had larger depth-to-size ratios than the detectable shallow delaminations.



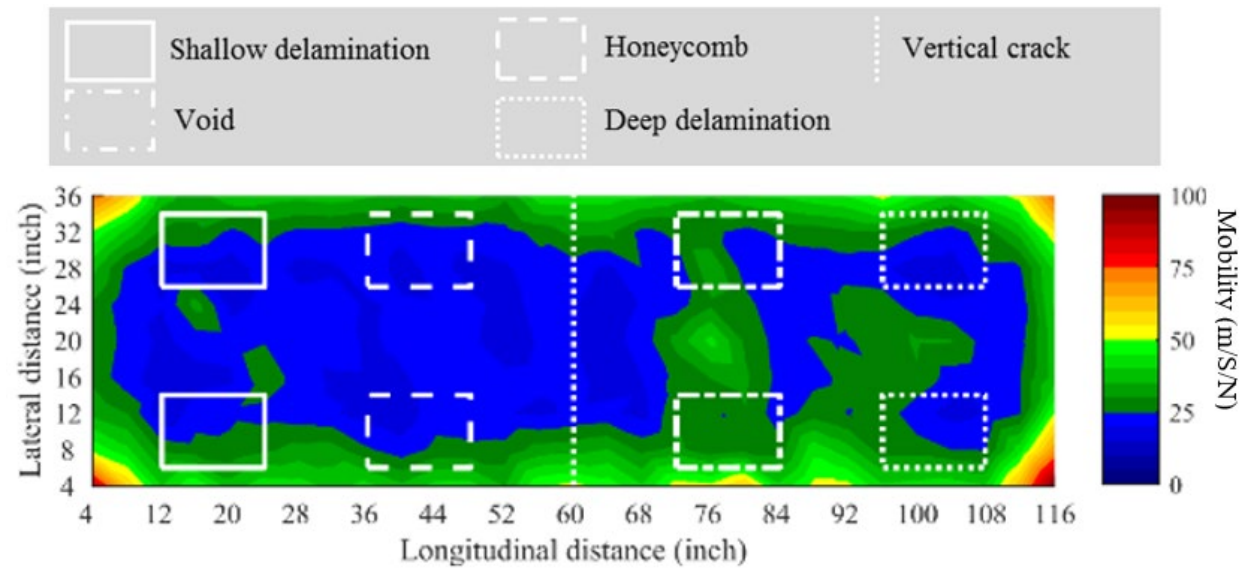
Source: FHWA.  
1 m/S/N = 0.74 ft/s/lb ft.  
Note: No defects detected.

A. S1.



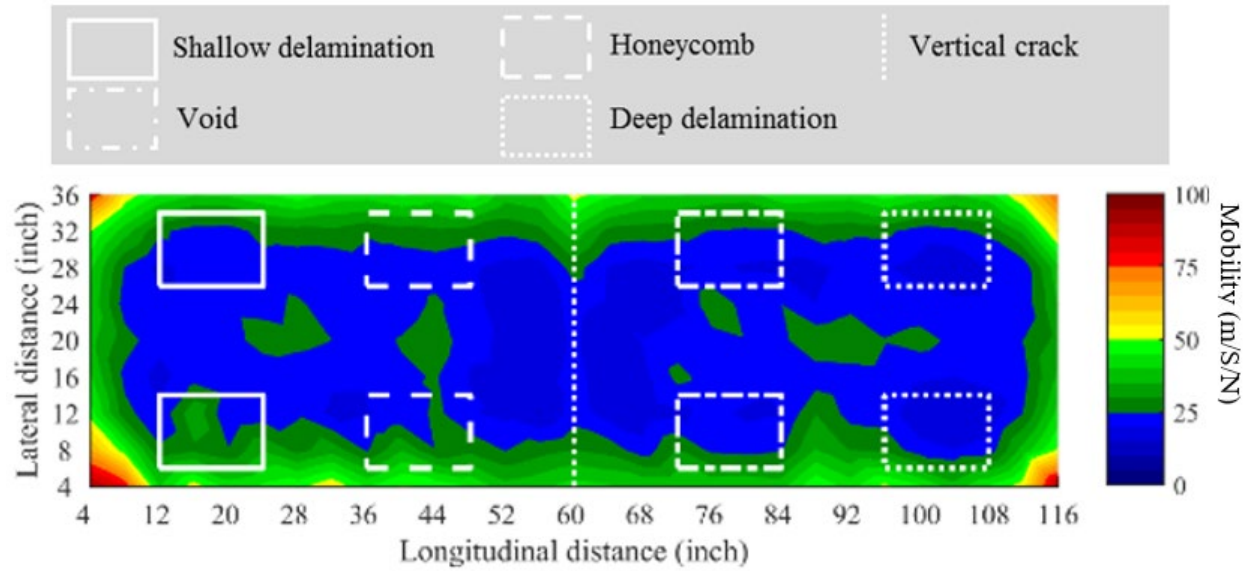
Source: FHWA.  
 1 m/S/N = 0.74 ft/s/lb ft.  
 Note: No defects detected.

B. S2.



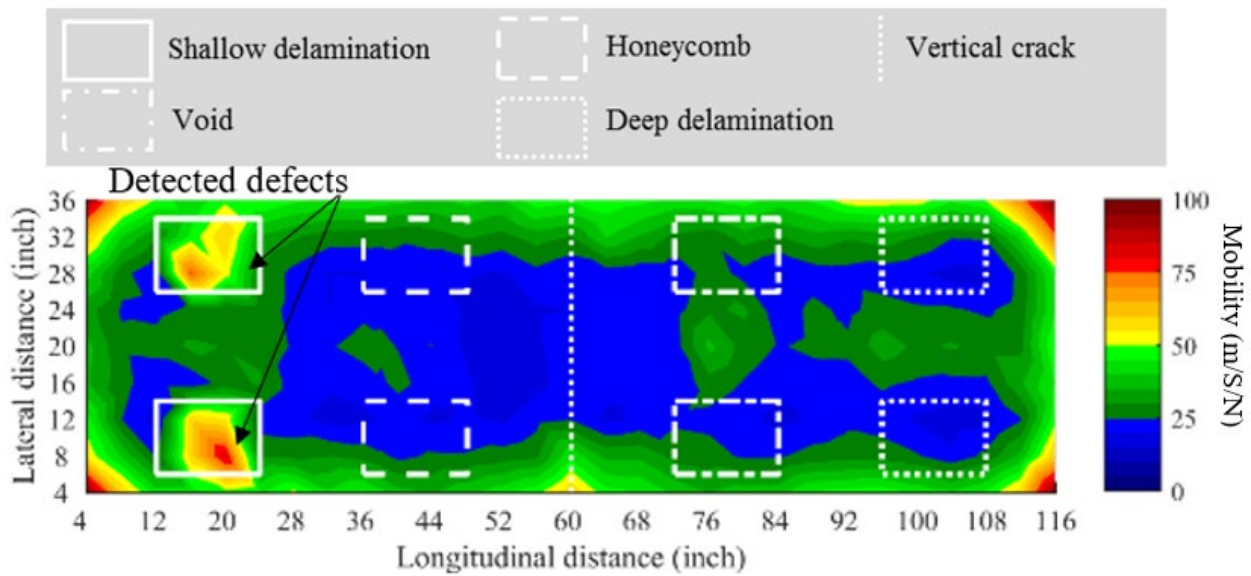
Source: FHWA.  
 1 m/S/N = 0.74 ft/s/lb ft.  
 Note: No defects detected.

C. S3.



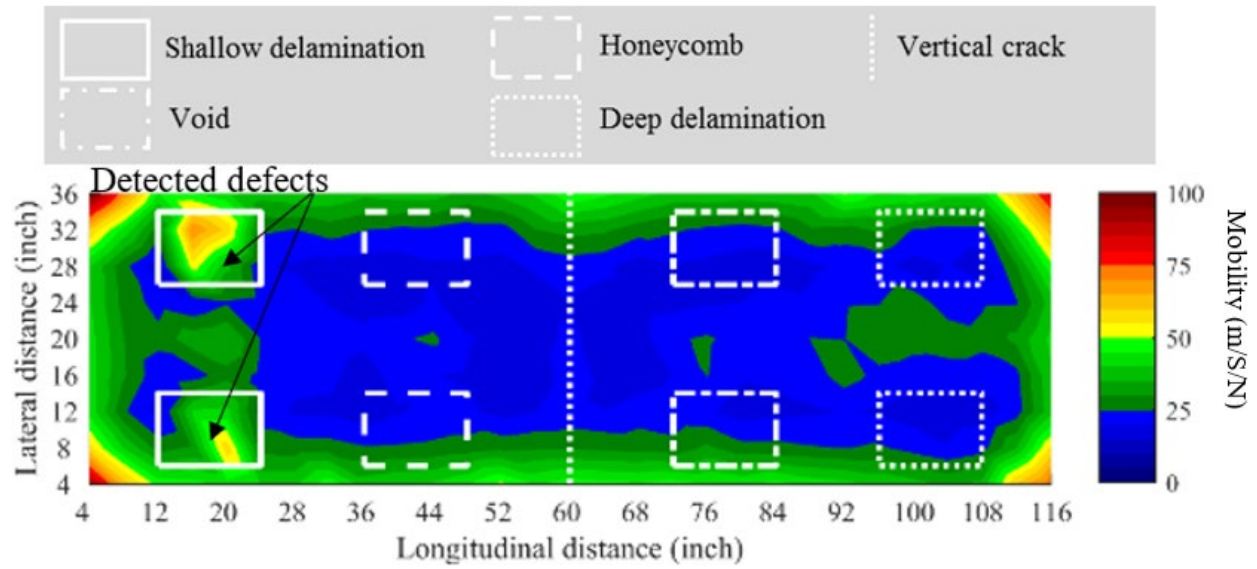
Source: FHWA.  
 1 m/S/N = 0.74 ft/s/lb ft.  
 Note: No defects detected.

D. S4.



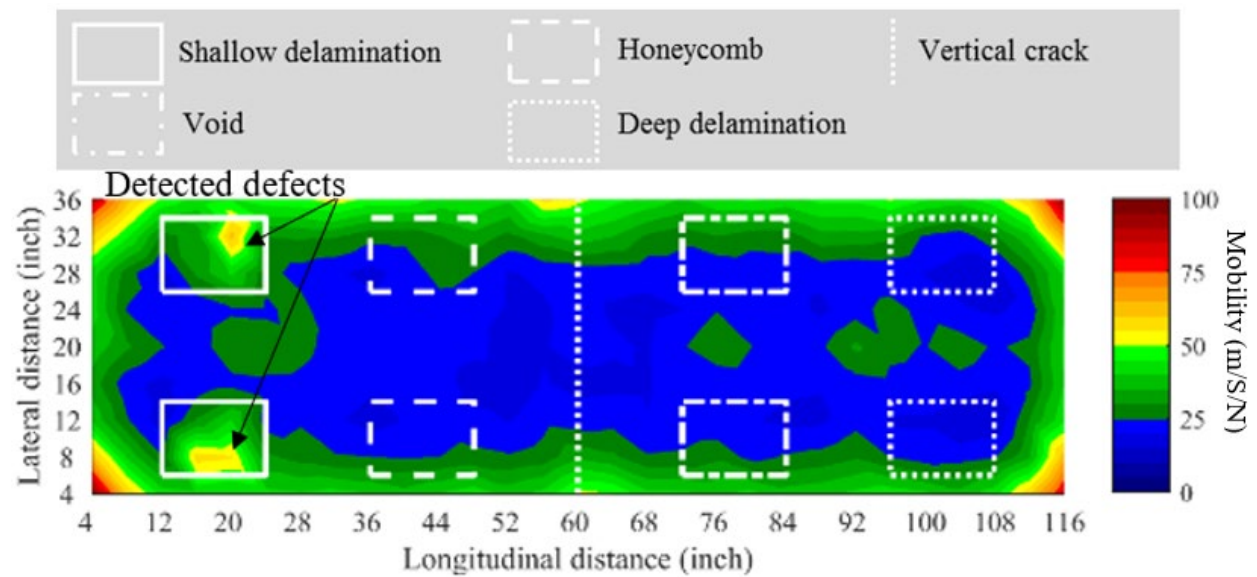
Source: FHWA.  
 1 m/S/N = 0.74 ft/s/lb ft.

E. S5.



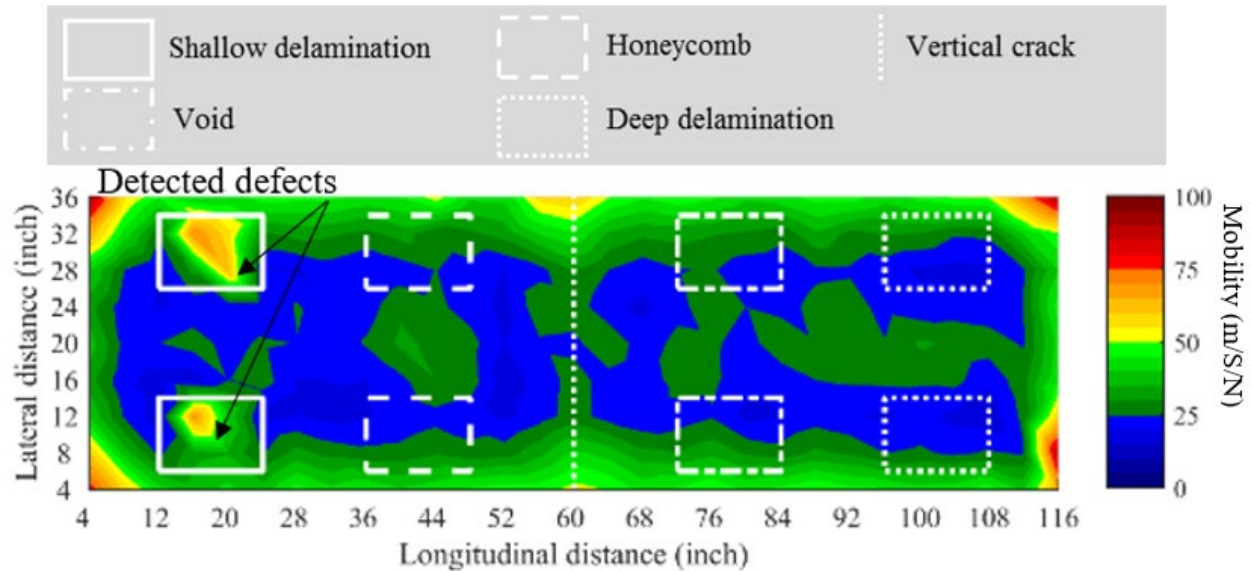
Source: FHWA.  
 1 m/S/N = 0.74 ft/s/lb ft.

F. S6.



Source: FHWA.  
 1 m/S/N = 0.74 ft/s/lb ft.

G. S7.



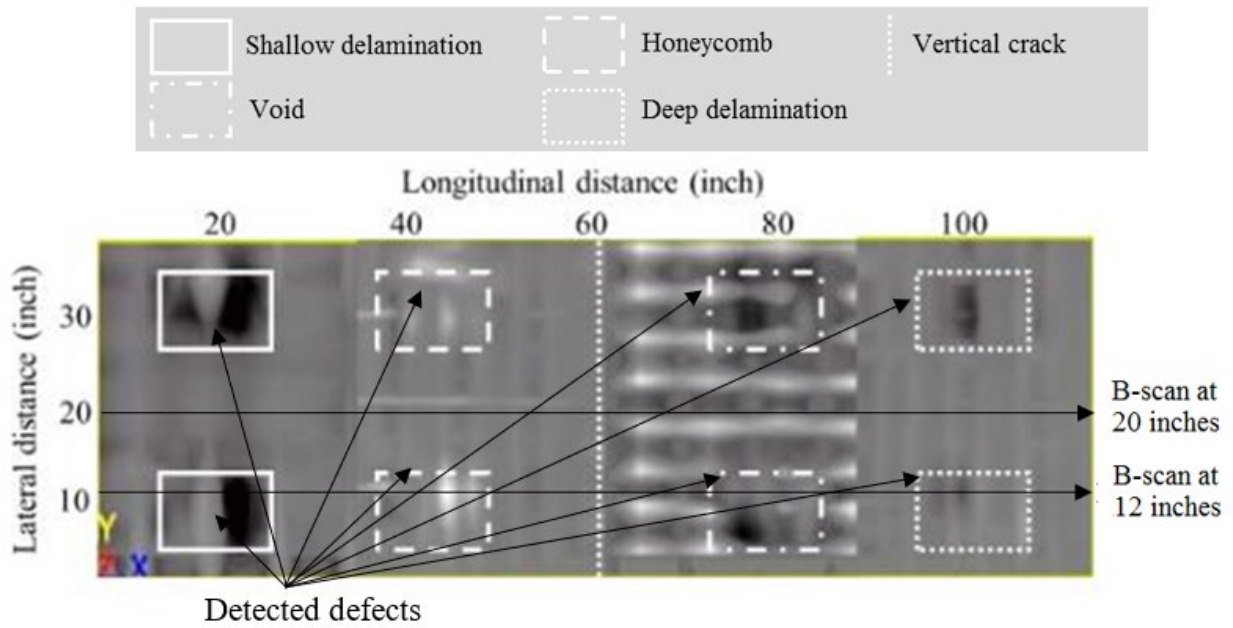
Source: FHWA.  
 1 m/S/N = 0.74 ft/s/lb ft.

H. S8.

**Figure 64. Graphs. NDE condition maps with IR.**

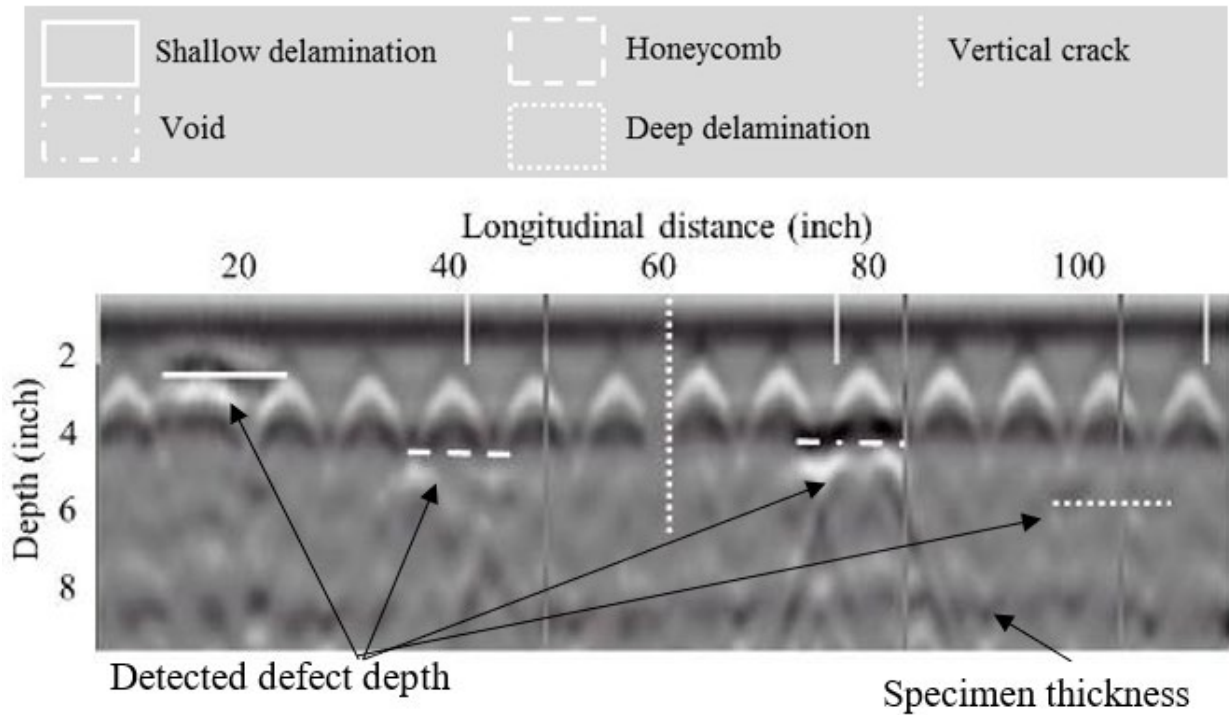
## GPR METHOD

The GPR method transmitted EM waves into the concrete and recorded reflected EM waves when the dielectric constants of reflectors (e.g., rebar or delamination) differed from that of the concrete. Defects, rebar, and secondary objects show a different brightness than solid concrete on a visualized map. There are two ways to process the reflected EM waves: combining all data together to construct different scans (e.g., B-, C-, or 3D scans) to detect defects, such as voids, delaminations, and honeycombing; and measuring the attenuation of EM waves reflected from the top layer rebar and presenting results in a condition map to quantify the severity of the corrosive environment where the EM waves traveled through the concrete. Figure 65-A through -D show the C-scan, two GPR B-scans at 12 and 20 inches along the longitudinal direction of the slabs, and a condition map of specimen S1 before accelerated corrosion was applied to the specimen. As shown in figure 65, the GPR C- and B-scan at  $y$  equals 12 inches detected shallow delaminations, honeycombing, voids, deep delaminations, the top layer rebar, and the thickness of the specimen, but not the vertical crack. The precorroded rebar could not be distinguished from in the GPR B-scan at  $y$  equals 20 inches or in the deterioration map, indicating the rust and rough surface of the precorroded rebar did not cause the reflected EM waves to appreciably differ from the waves reflected from the intact rebar. For the areas with shallow delaminations over the precorroded rebar, the EM waves reflected from both shallow delaminations and the precorroded rebar were superimposed, which made the area in the B-scan (the B-scan at  $y$  equals 12 inches of figure 65-A) appear brighter than the areas with only the precorroded rebar (the B-scan at  $y$  equals 20 inches of figure 65-A). The GPR condition map based on the attenuation of the reflected EM waves from the top layer rebar, shown in figure 65-A through figure 65-D, did not show any corrosion-related deterioration.



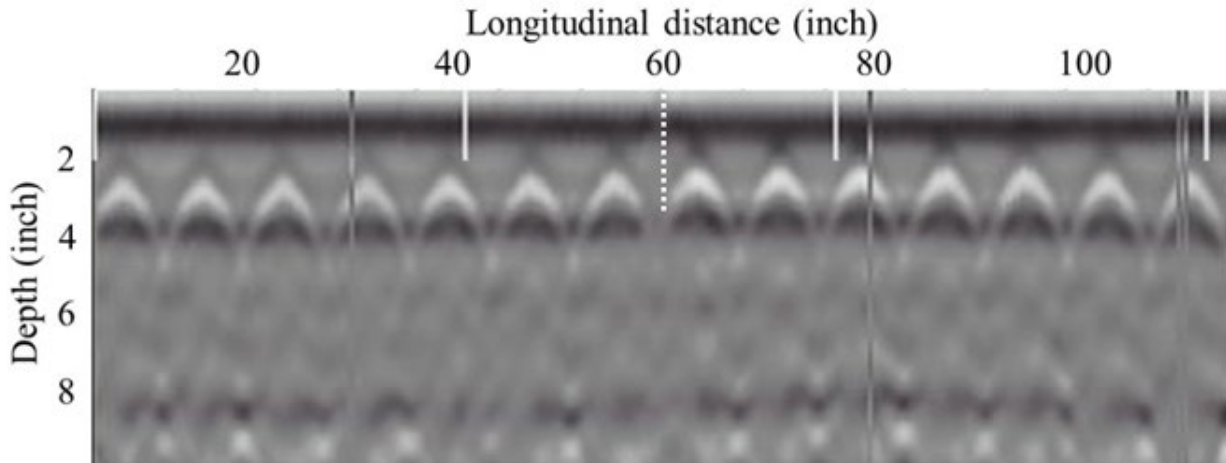
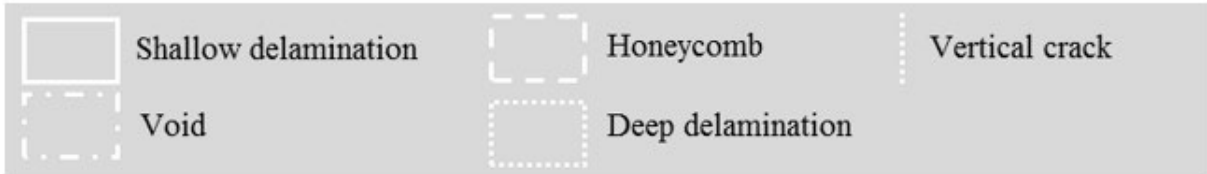
Source: FHWA.

A. C-scan.



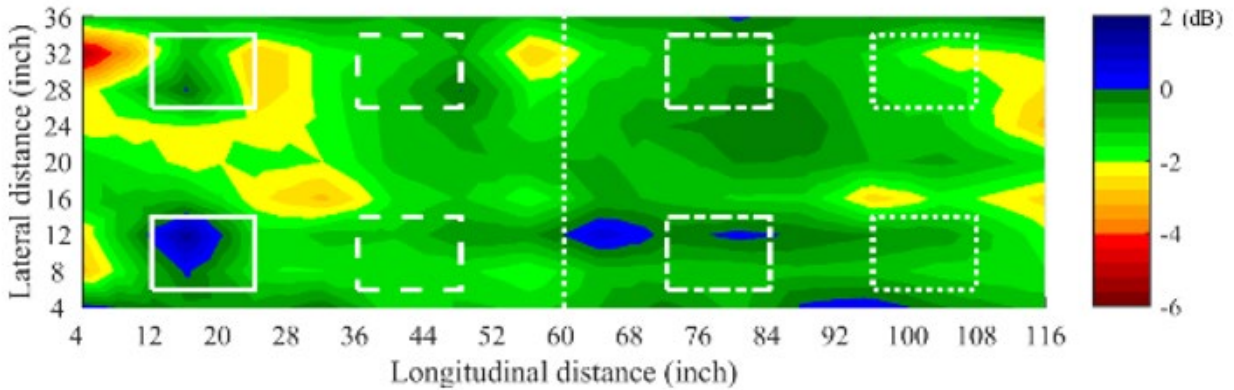
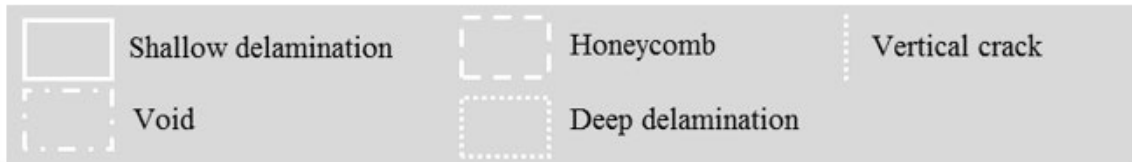
Source: FHWA.

B. B-scan at 12 inches.



Source: FHWA.  
 Note: No defects detected.

C. B-scan at 20 inches.

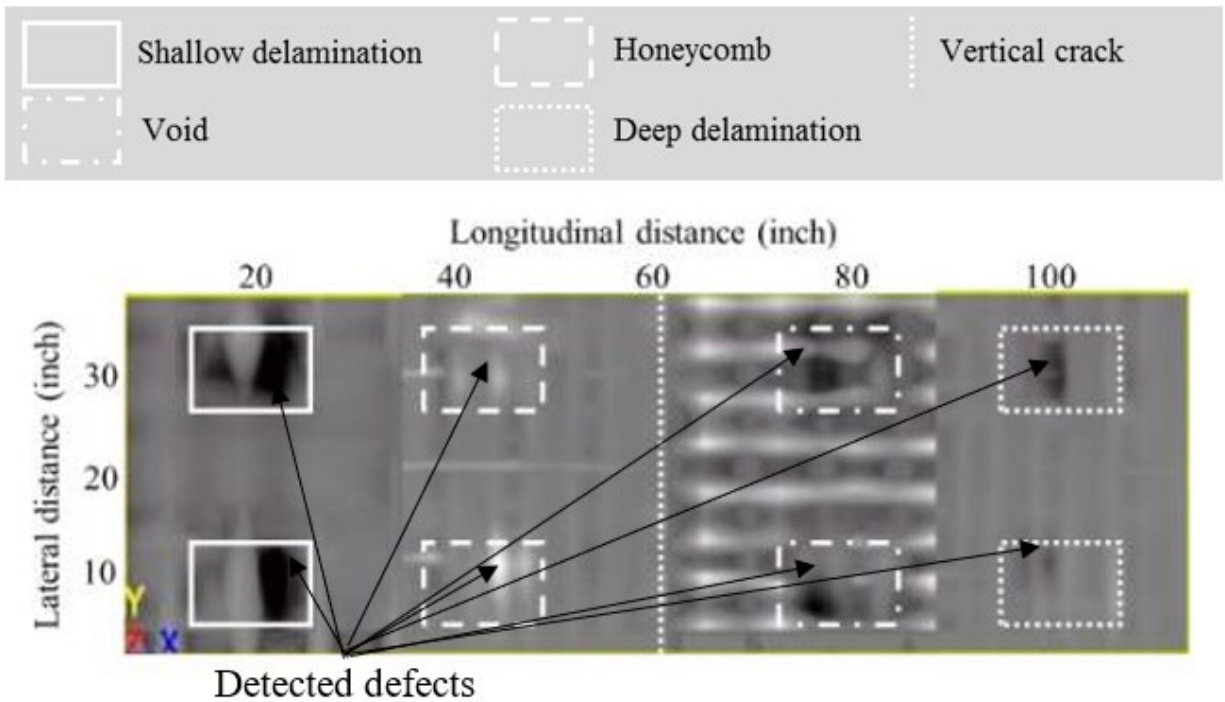


Source: FHWA.  
 Note: No defects detected.

D. Condition map.

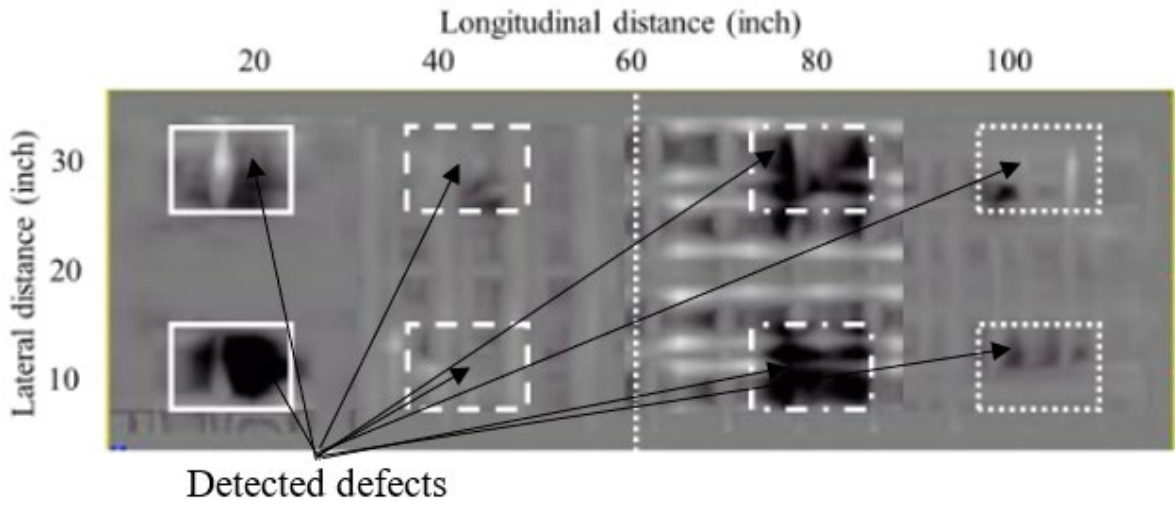
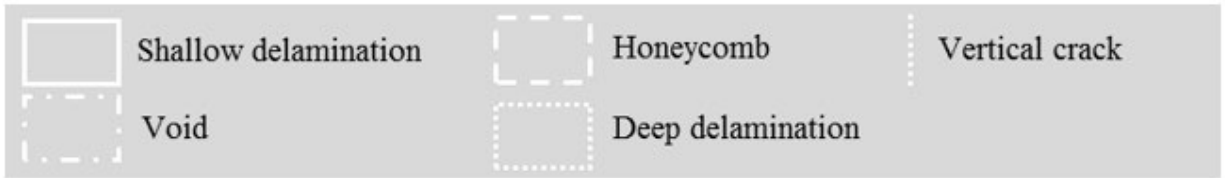
**Figure 65. Graphs. NDE B-scan and condition map of specimen S1 with GPR before accelerated corrosion.**

An elevated chloride content environment was introduced to the specimens through the accelerated corrosion procedure shown in figure 52 and figure 53. The resulting GPR C-scans, B-scans, and condition maps after depth correction are shown in figure 66 through figure 68, respectively. GPR detected shallow and deep delaminations, voids, and honeycombing in all eight specimens in C- and B-scans. The attenuation of the signals reflected by the top layer rebar was used to image the condition maps of the concrete specimens with an elevated chloride content environment after accelerated corrosion, as shown in figure 68-A through figure 68-H. The condition maps imaged the elevated chloride content environment for the three pieces of corroded rebar in the top layer in all specimens. Some results of the condition maps in the areas of shallow delamination were inaccurate because the EM wave attenuation was less than the actual value due to the superimposed reflections from shallow delaminations and the rebar.



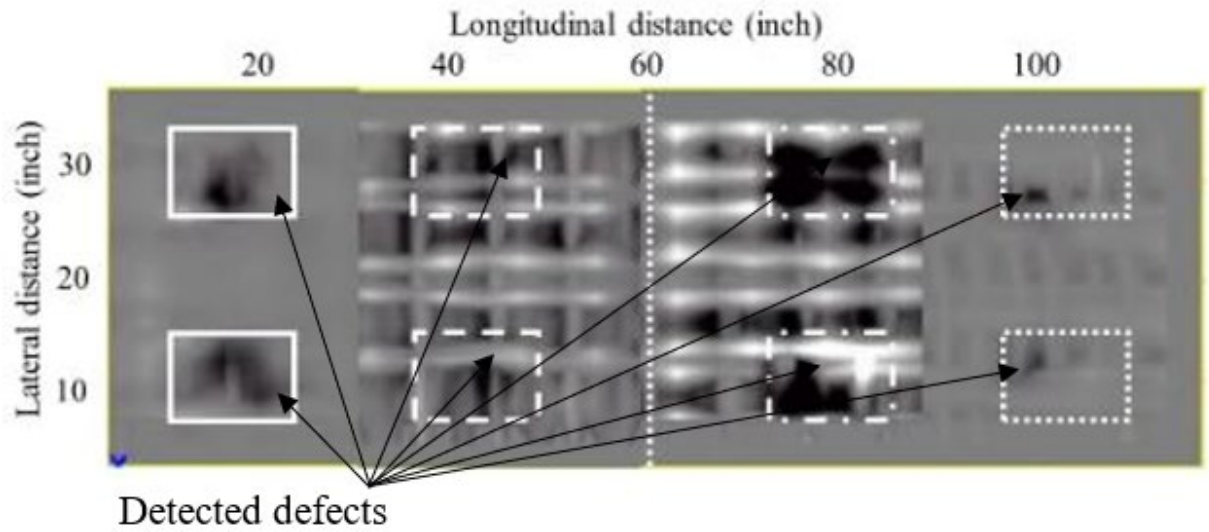
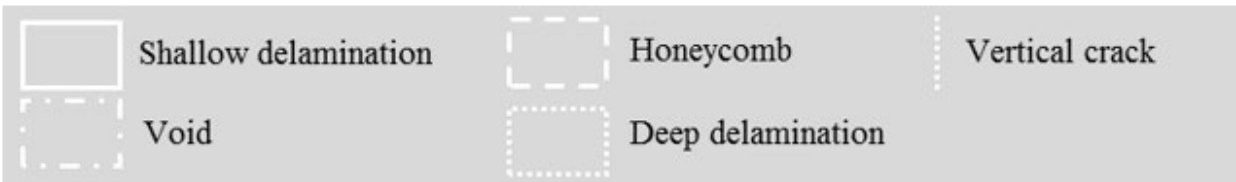
Source: FHWA.

A. S1.



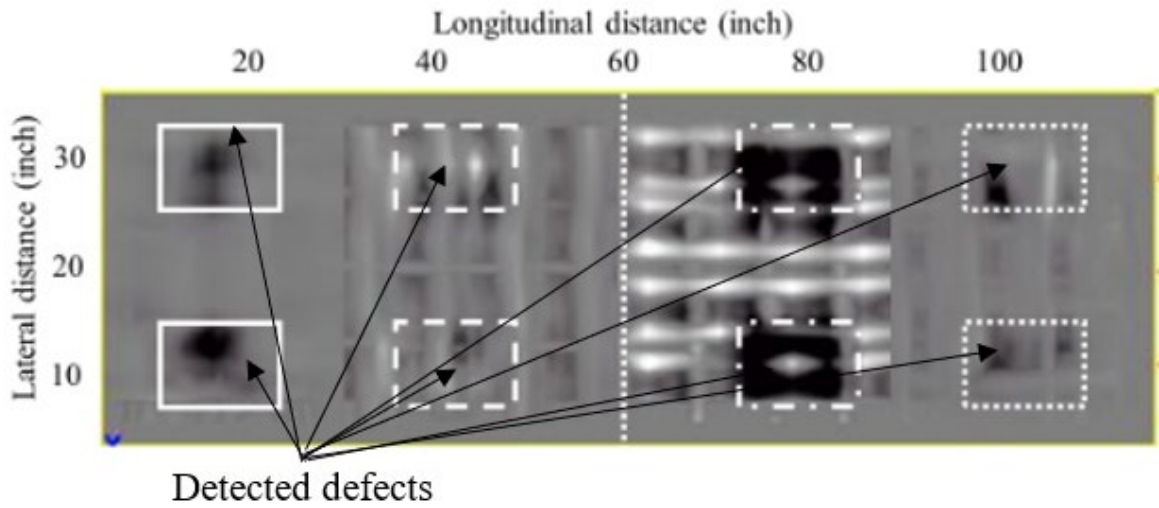
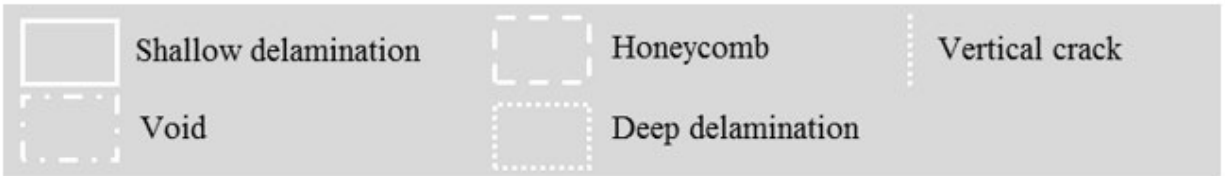
Source: FHWA.

B. S2.



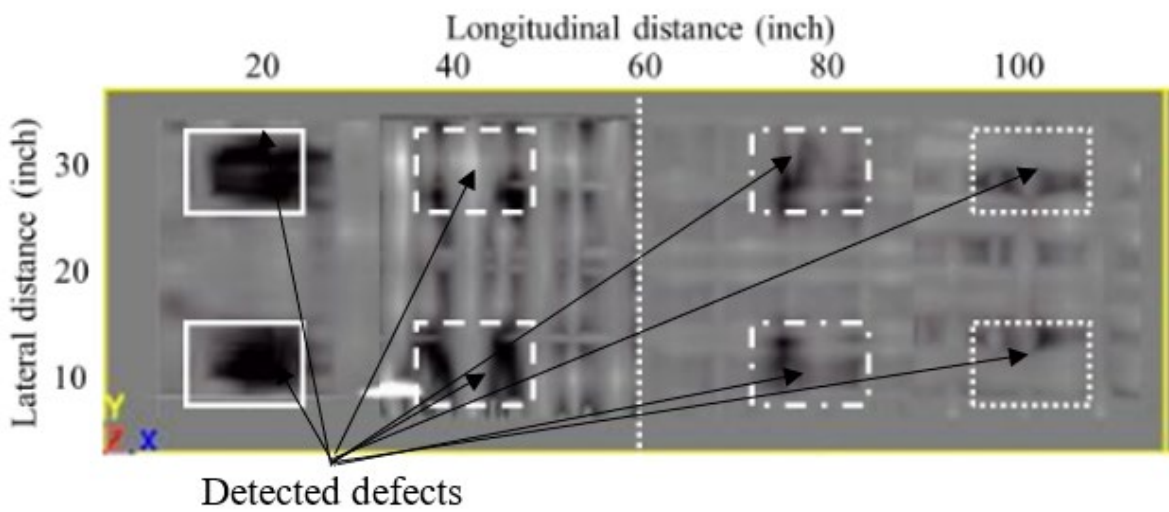
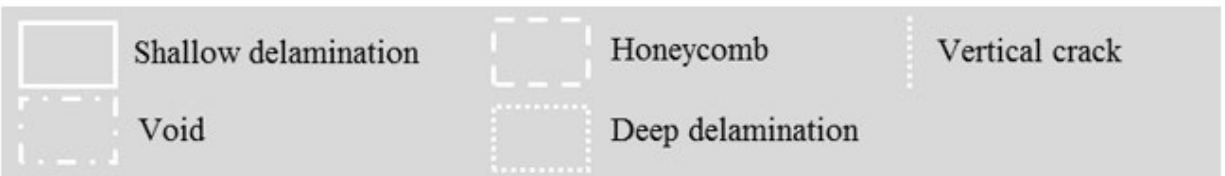
Source: FHWA.

C. S3.



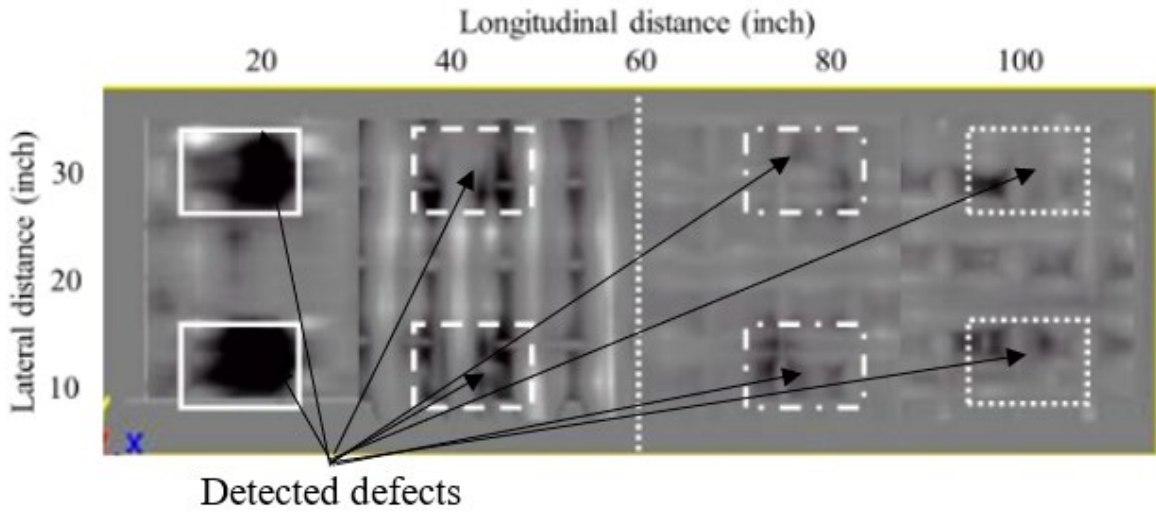
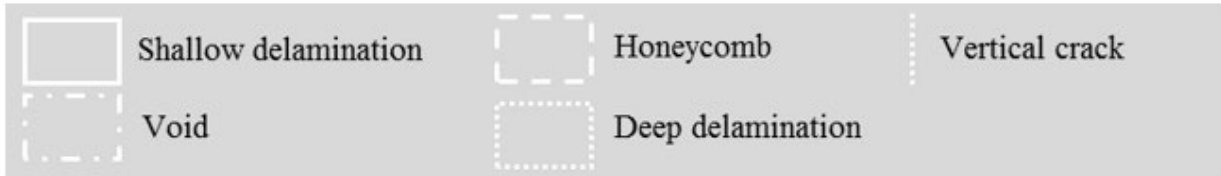
Source: FHWA.

D. S4.



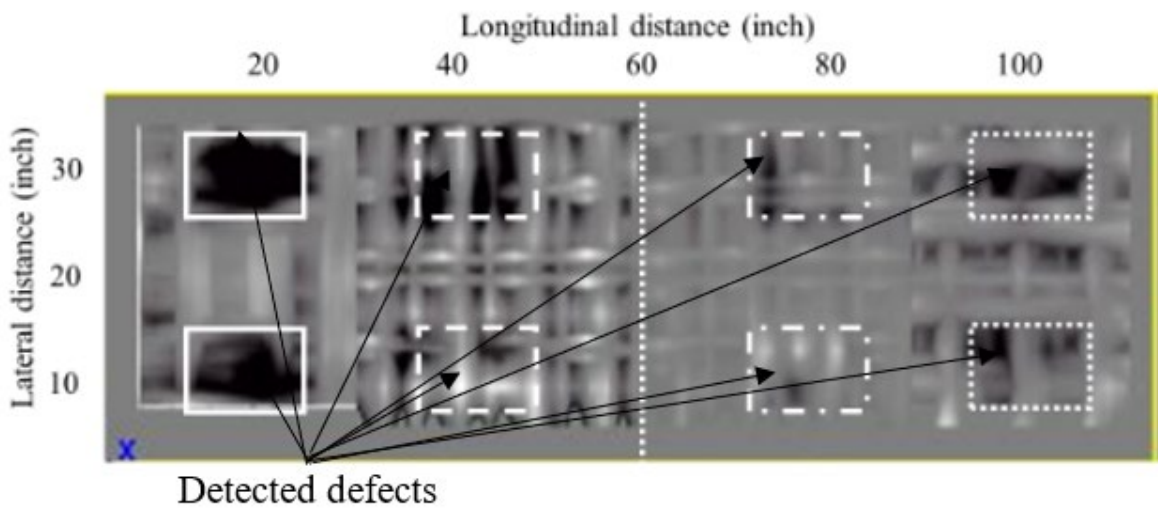
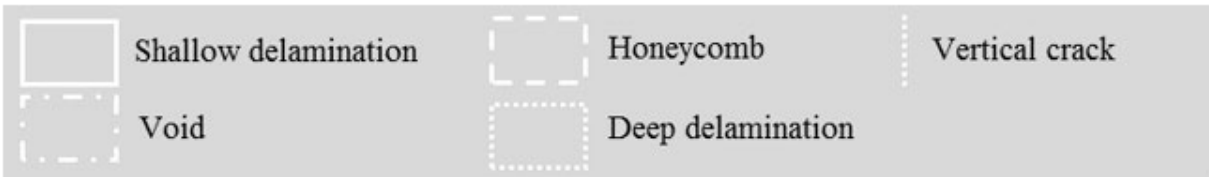
Source: FHWA.

E. S5.



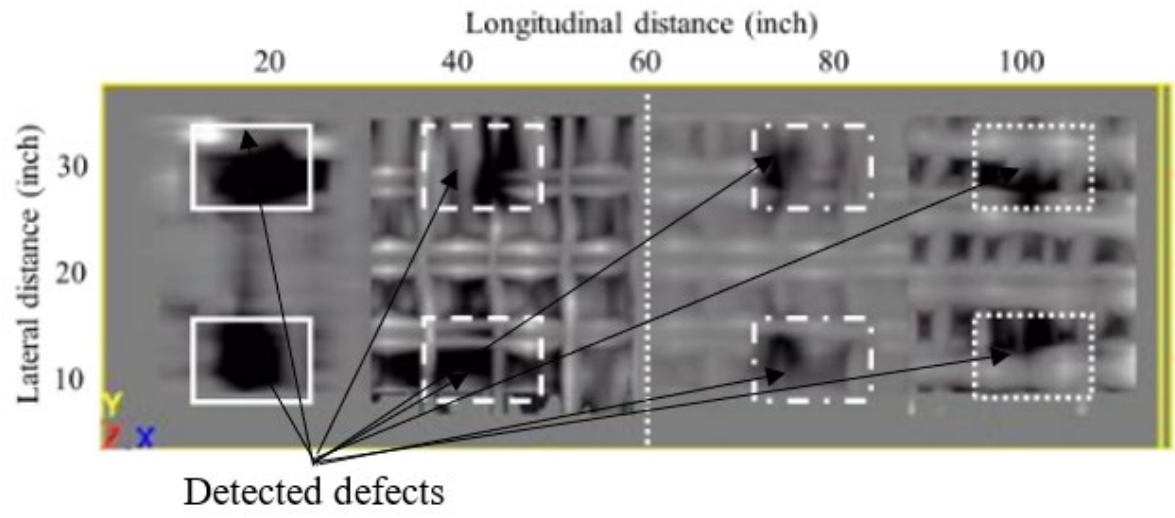
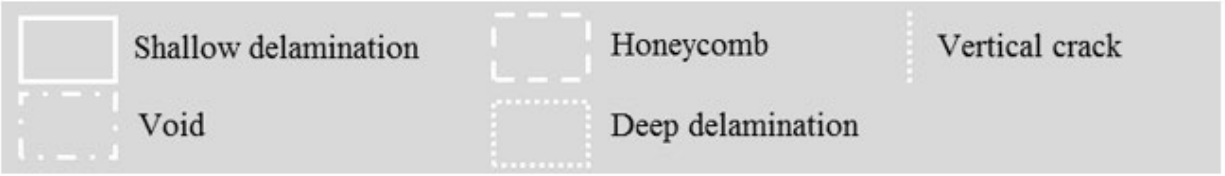
Source: FHWA.

F. S6.



Source: FHWA.

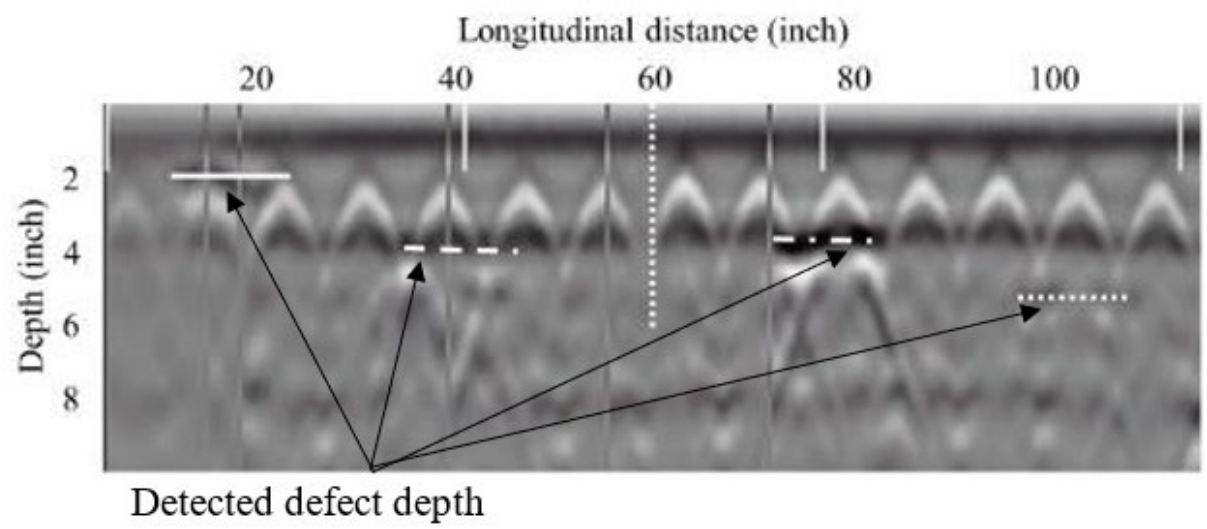
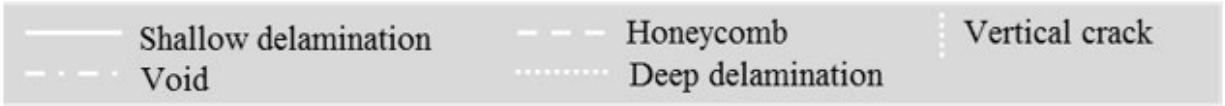
G. S7.



Source: FHWA.

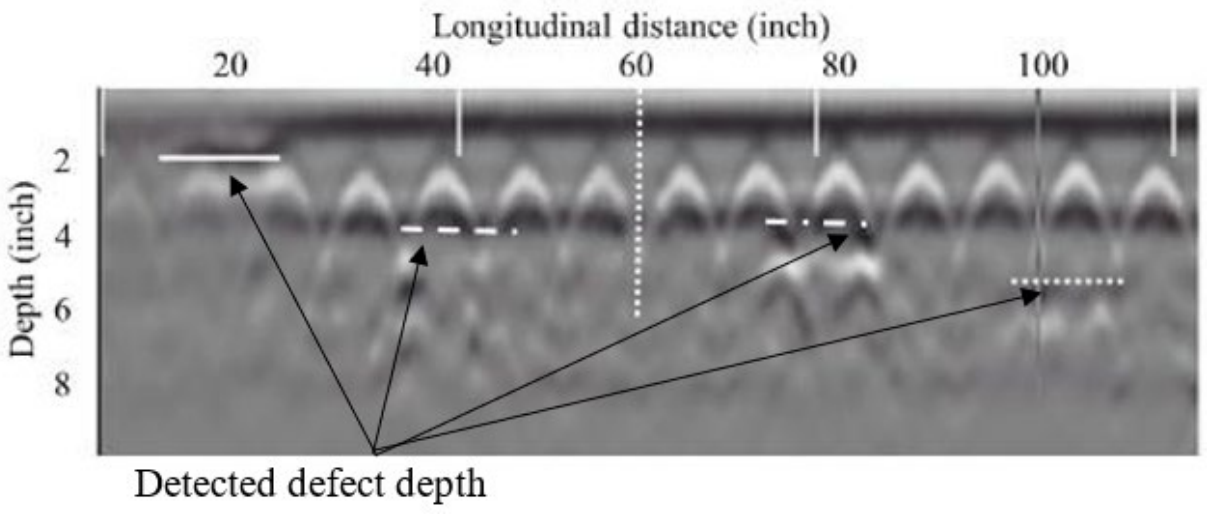
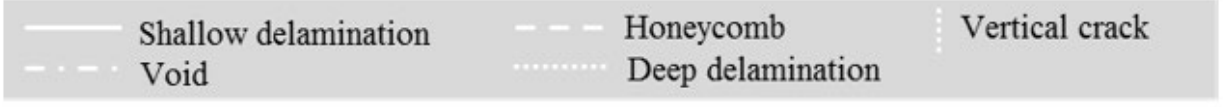
H. S8.

**Figure 66. Graphs. NDE C-scans with GPR after accelerated corrosion.**



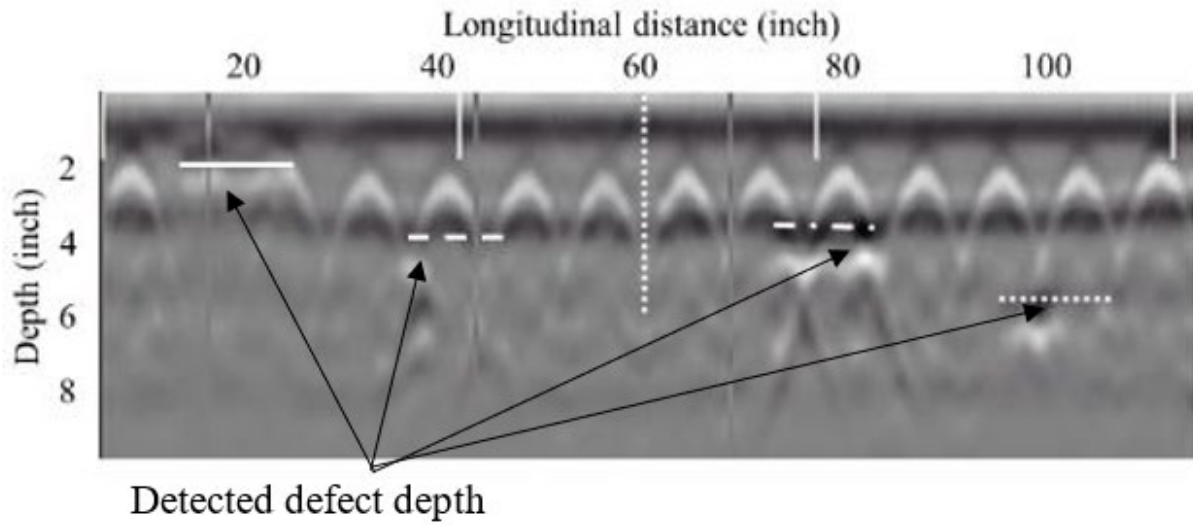
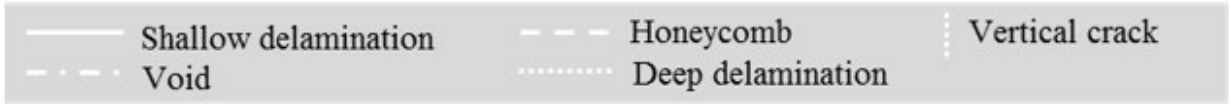
Source: FHWA.

A. S1.



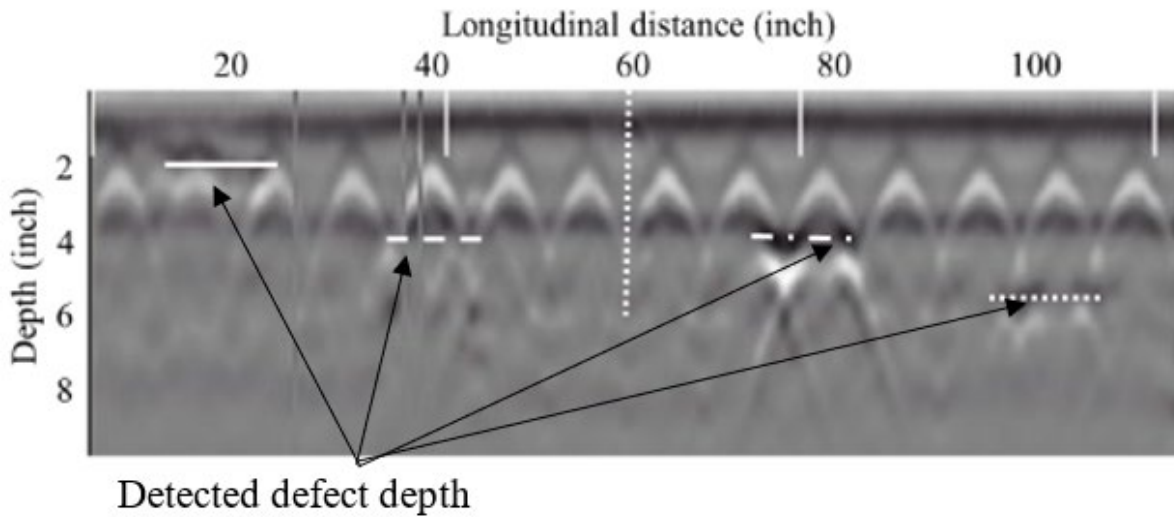
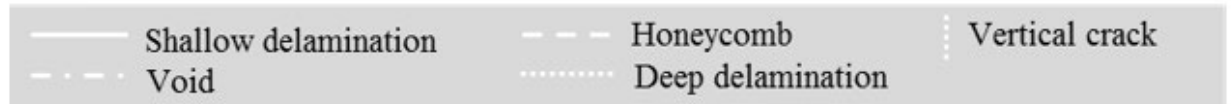
Source: FHWA.

B. S2.



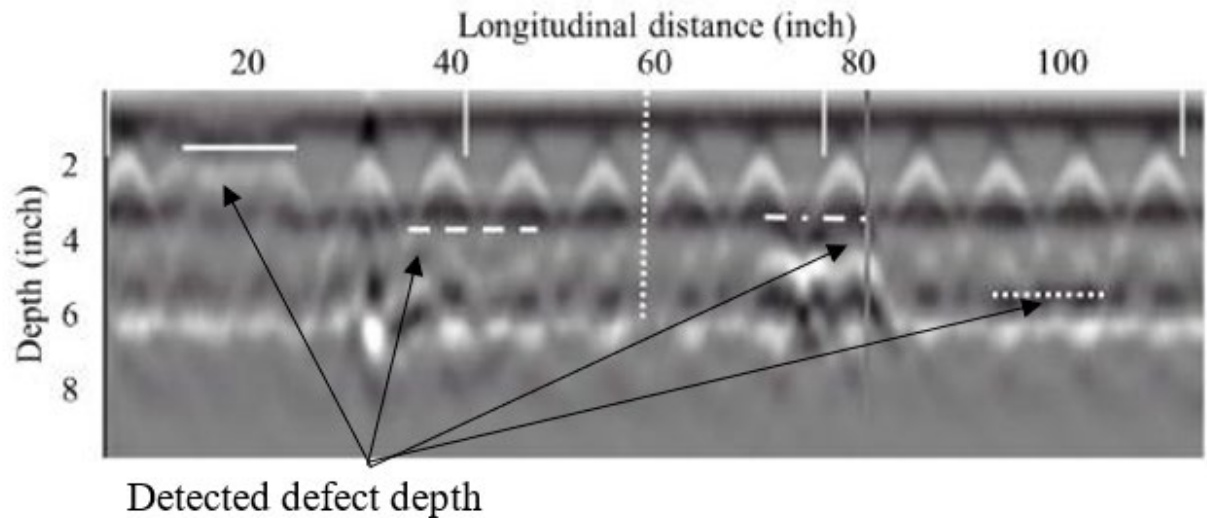
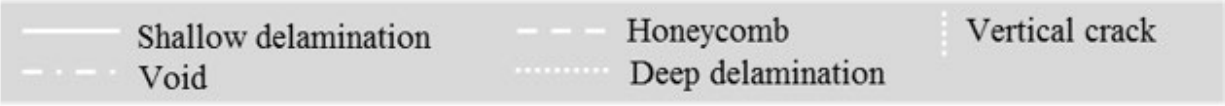
Source: FHWA.

C. S3.



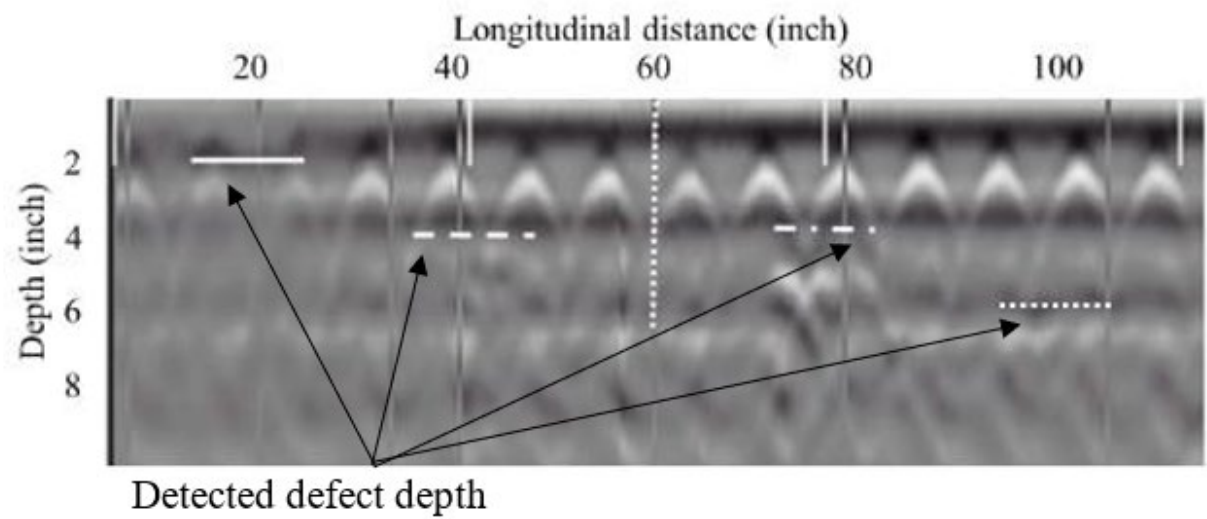
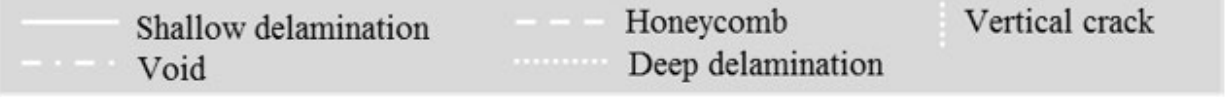
Source: FHWA.

D. S4.



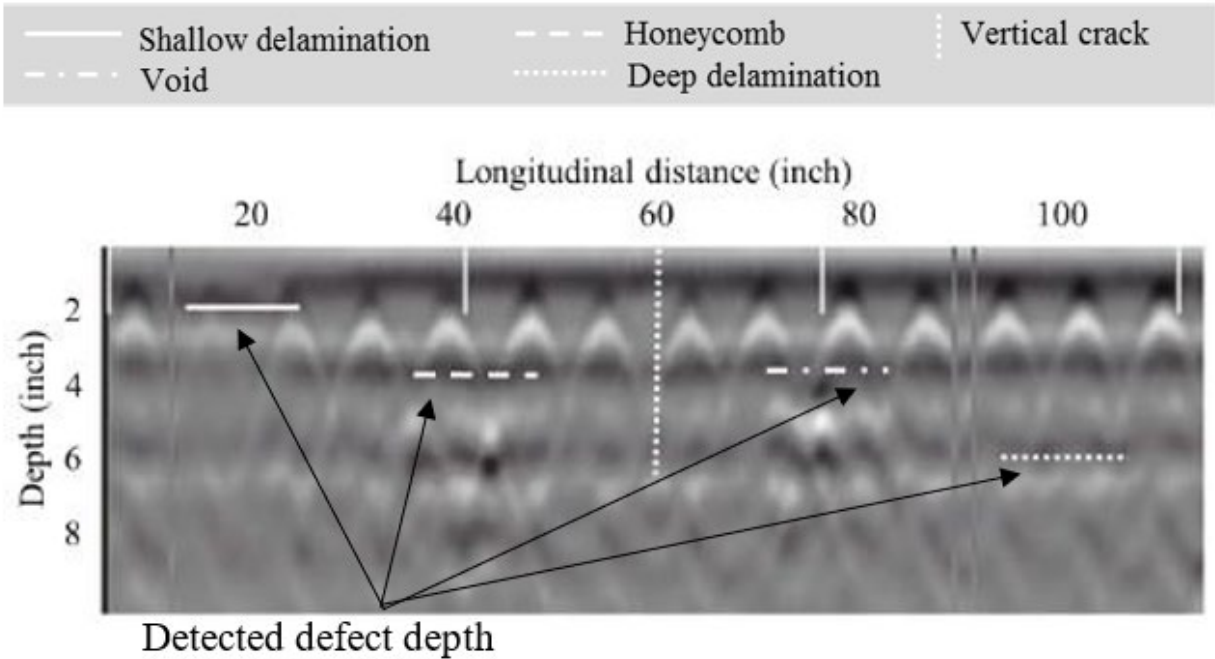
Source: FHWA.

E. S5.



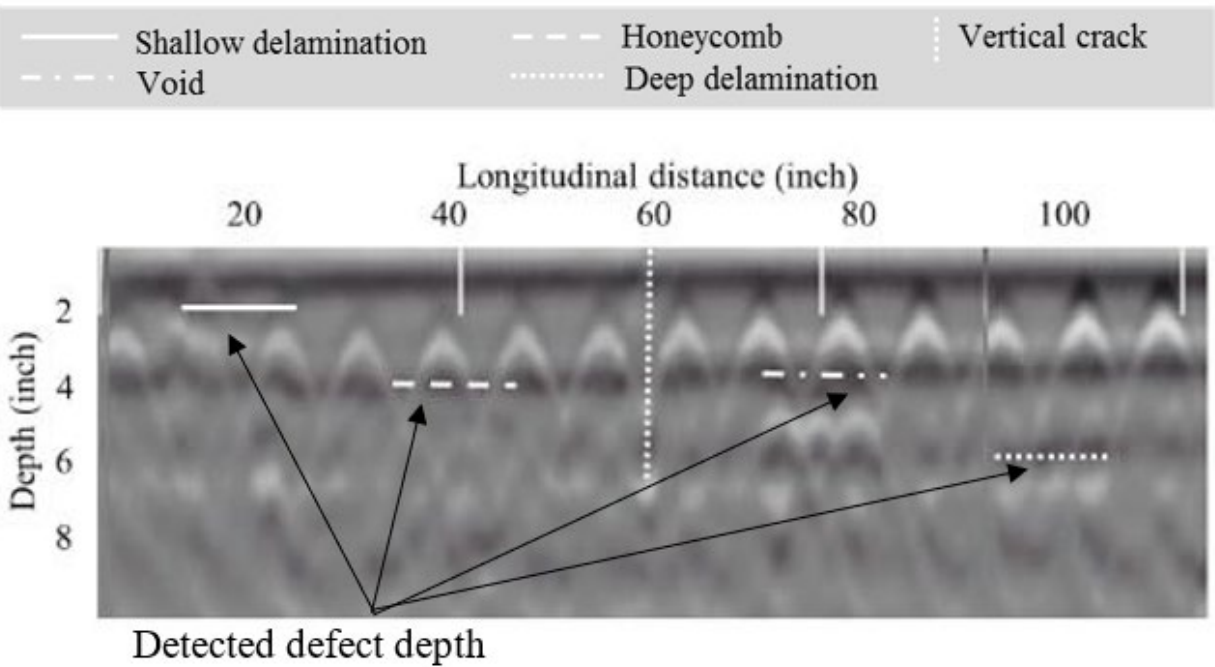
Source: FHWA.

F. S6.



Source: FHWA.

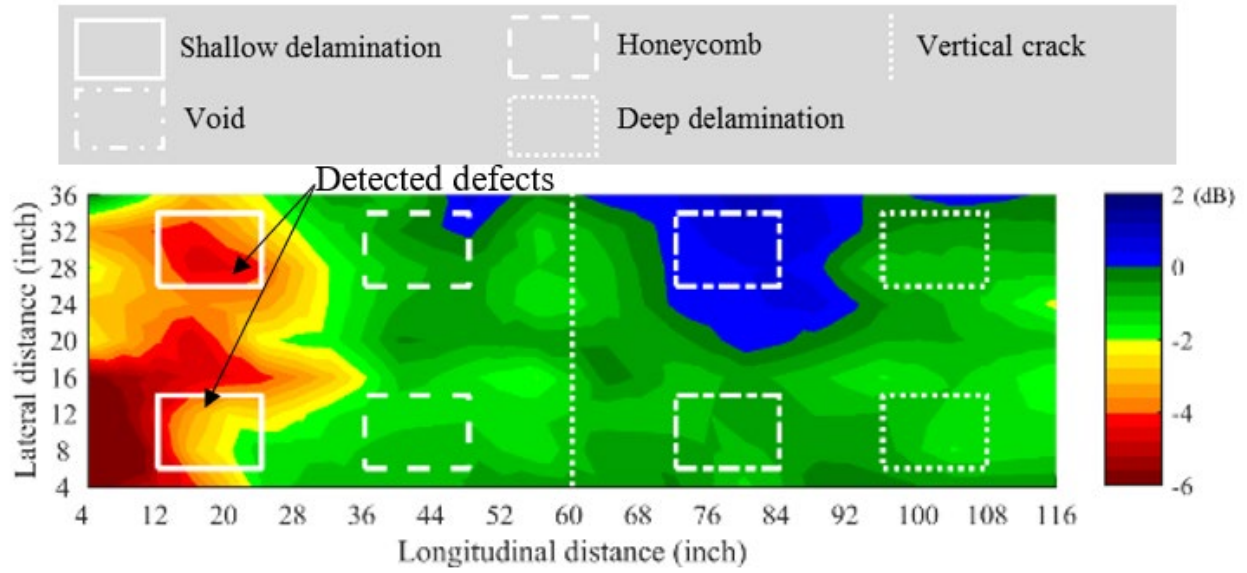
G. S7.



Source: FHWA.

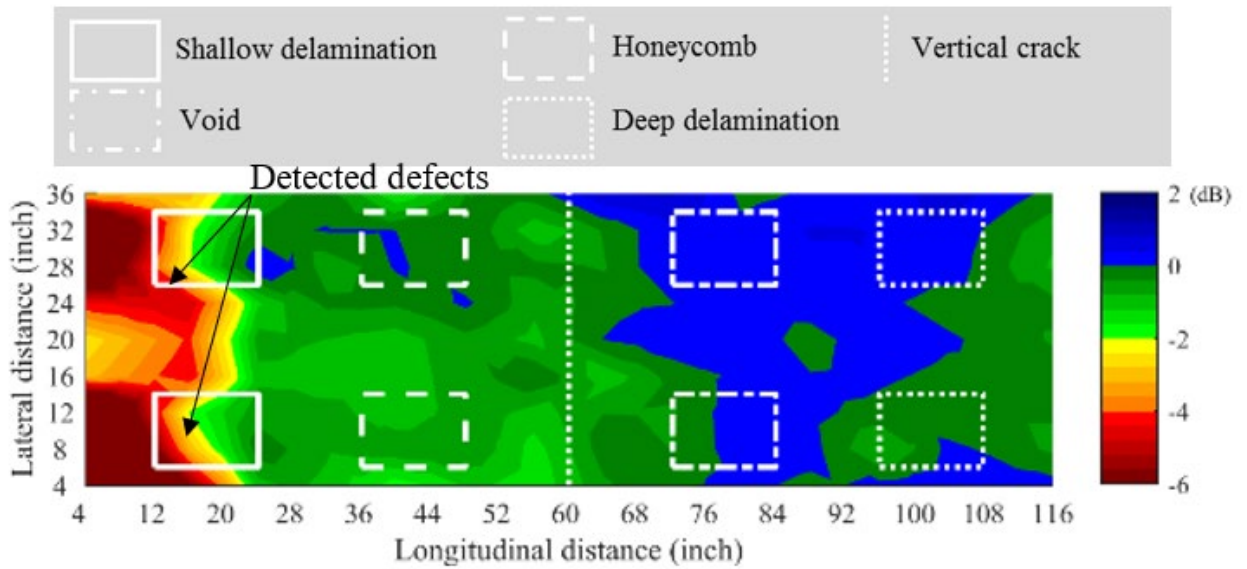
H. S8.

Figure 67. Graphs. NDE B-scans with GPR after accelerated corrosion.



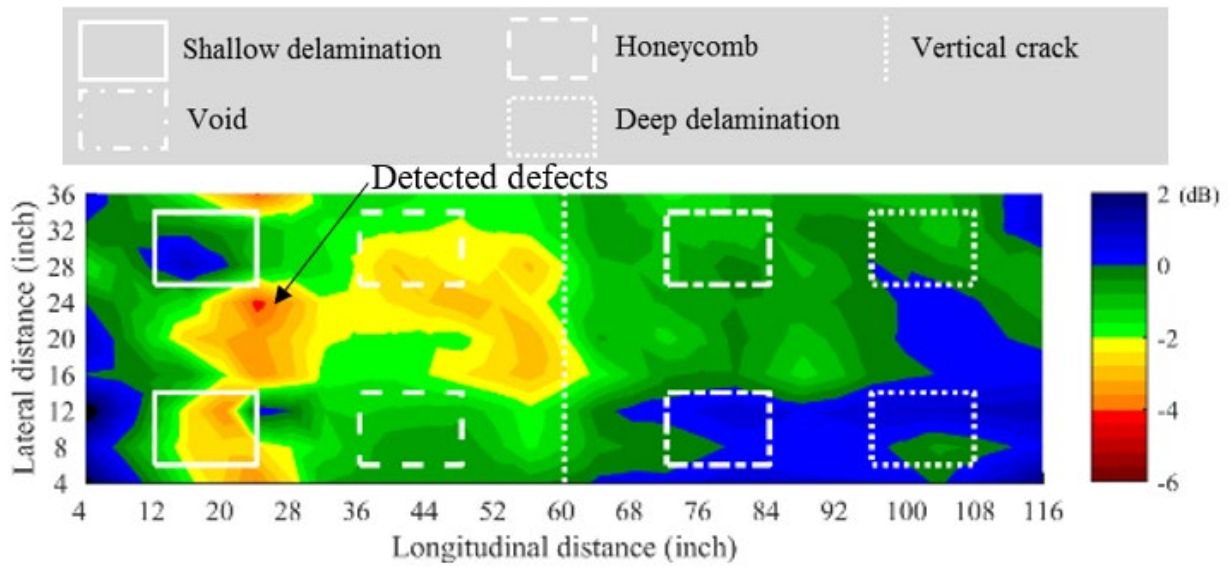
Source: FHWA.

A. S1.



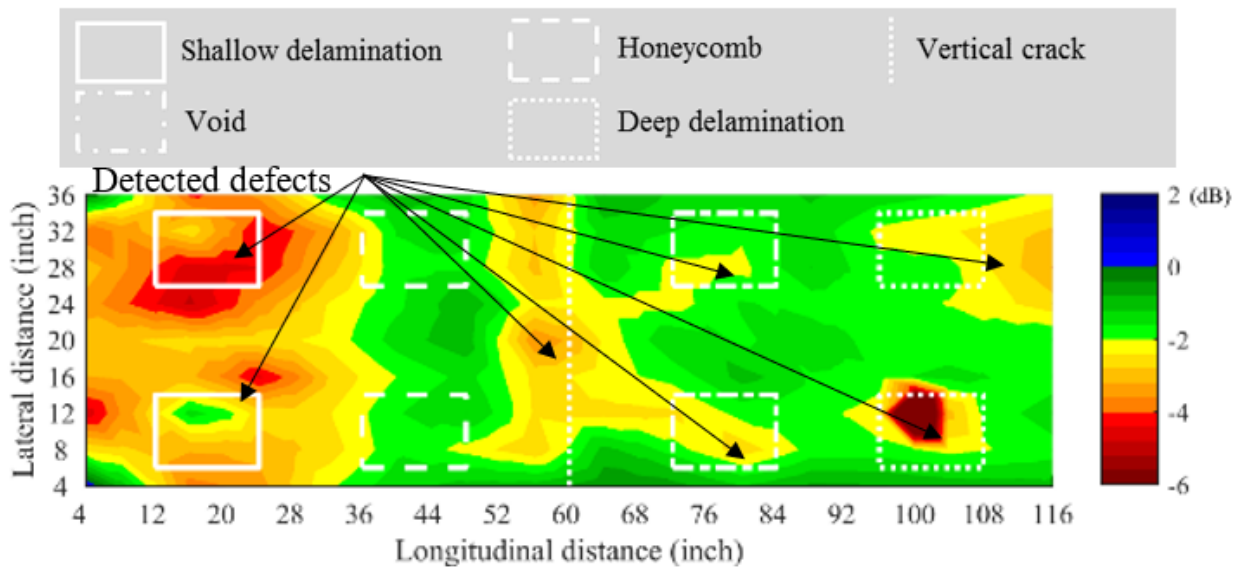
Source: FHWA.

B. S2.



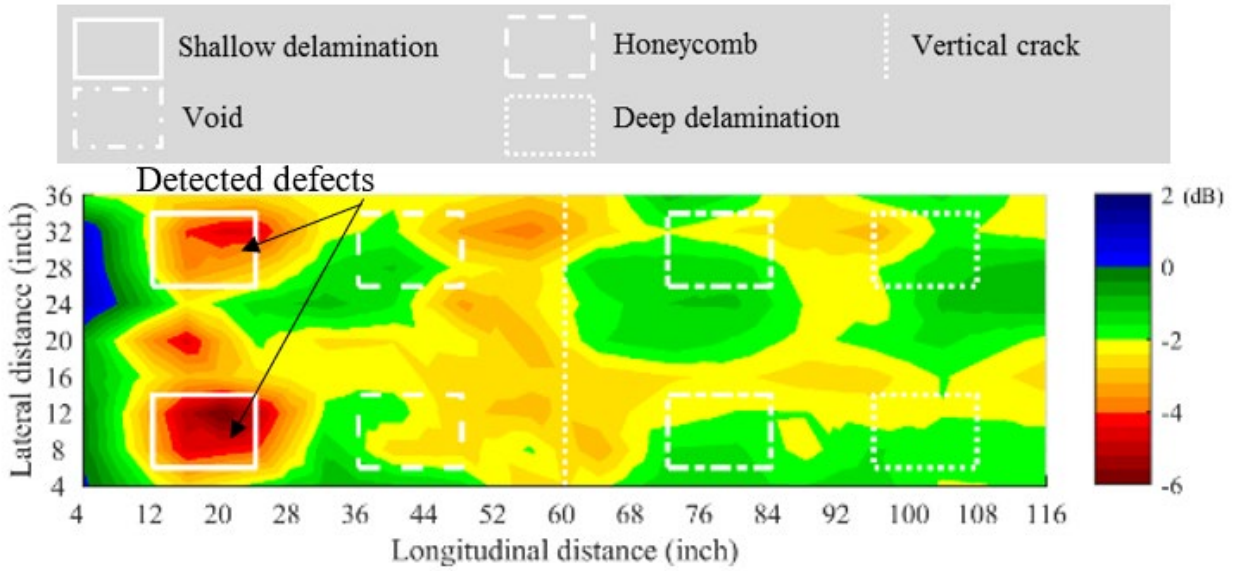
Source: FHWA.

C. S3.



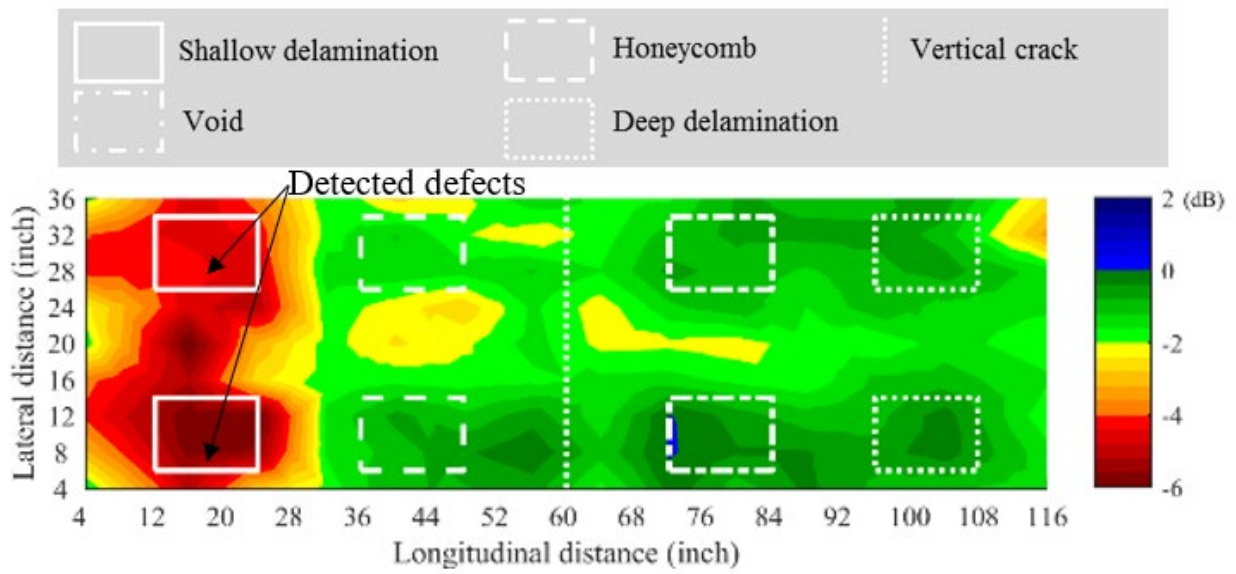
Source: FHWA.

D. S4.



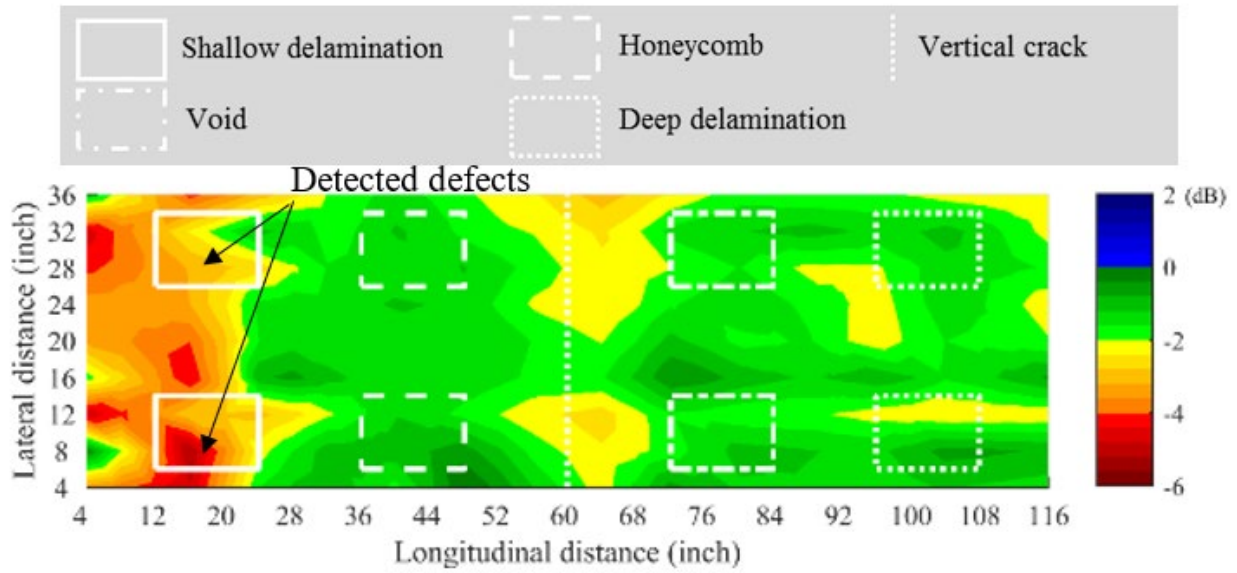
Source: FHWA.

E. S5.



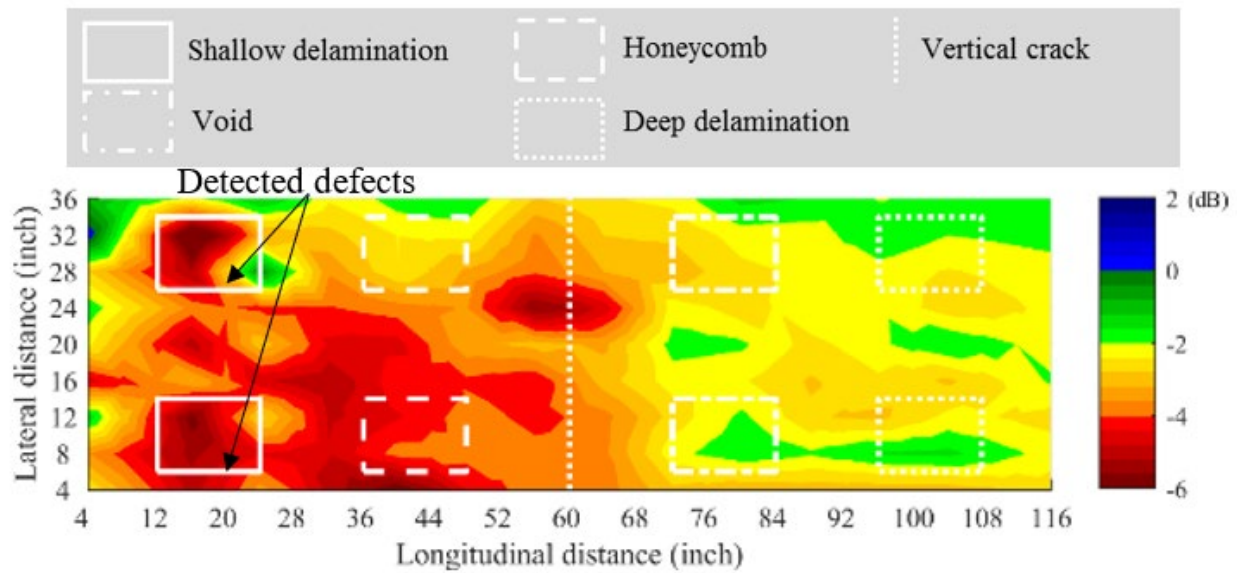
Source: FHWA.

F. S6.



Source: FHWA.

G. S7.



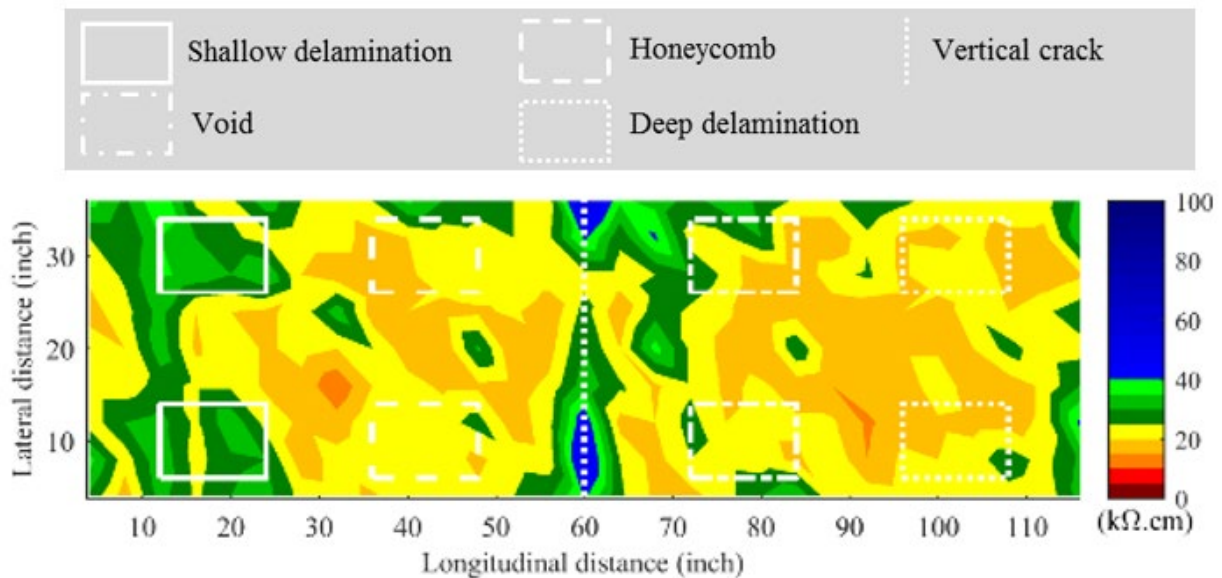
Source: FHWA.

H. S8.

**Figure 68. Graphs. NDE condition maps with GPR after accelerated corrosion.**

## ER METHOD

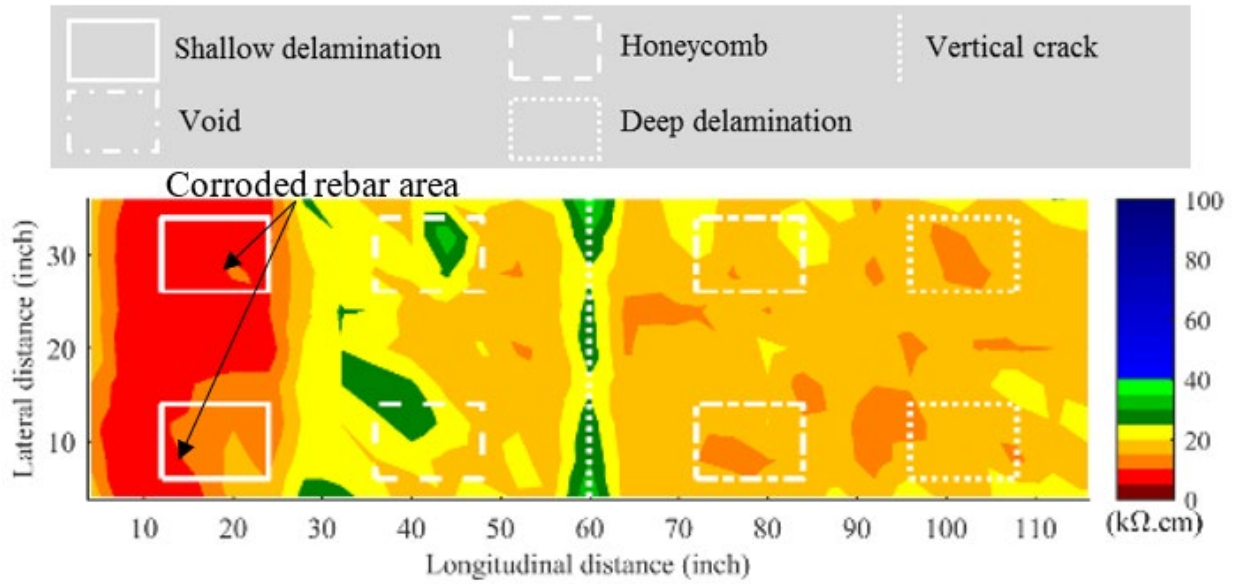
The ER method measured concrete resistivity using a Wenner probe with current applied between the outer electrodes and electric potential measured between the two inner probes. Resistivity was used to characterize concrete's susceptibility to corrosion by characterizing its corrosive environment since the elevated chloride content of the corrosive environment in the concrete decreased the ER of concrete. Figure 69 shows the condition map of specimen S1 based on the ER method before applying accelerated corrosion to the specimens (figure 52 and figure 53). As shown in figure 69, areas with precorroded rebar could not be detected by the ER method. Figure 70-A through figure 70-H show the condition maps based on the ER method after the elevated chloride content environment was introduced by applying accelerated corrosion to the specimens. ER detected the elevated chloride content environment for the top layer rebar and the vertical cracks when the resistivity probe was at an angle relative to the directions of the cracks with two probes on one side of the crack and the other two probes on the other side.<sup>(47-49)</sup> The difference between the condition maps is due to the different levels and uneven distribution of chloride content introduced by the sponge saturated with NaCl solution in different specimens.



Source: FHWA.

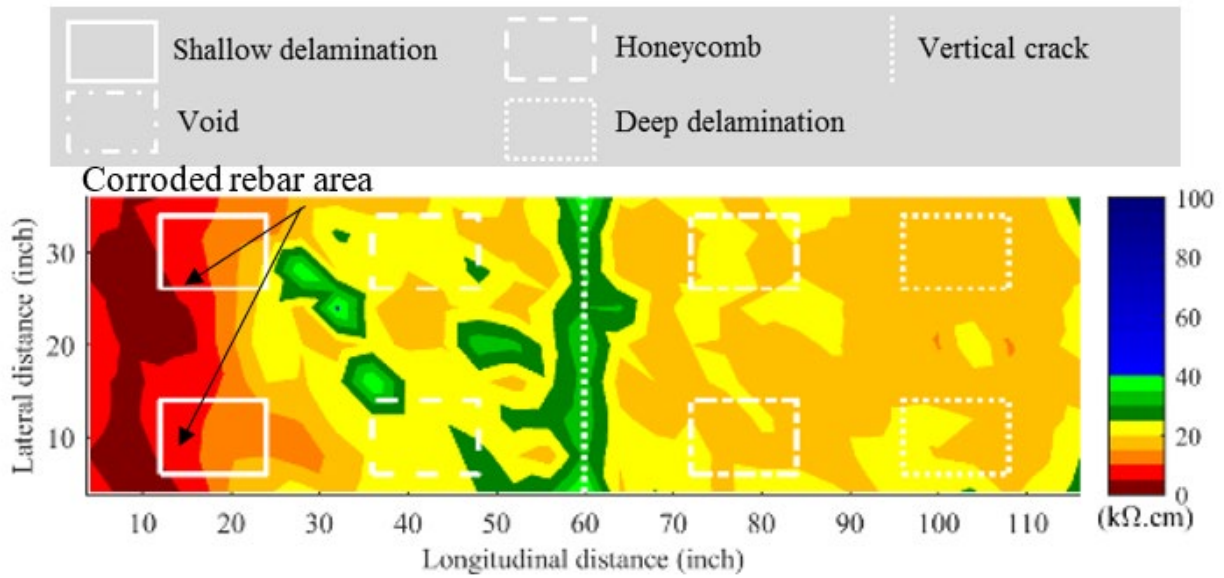
Note: Precorroded rebar not detected.

**Figure 69. Graph. NDE condition map of specimen S1 with ER before accelerated corrosion.**



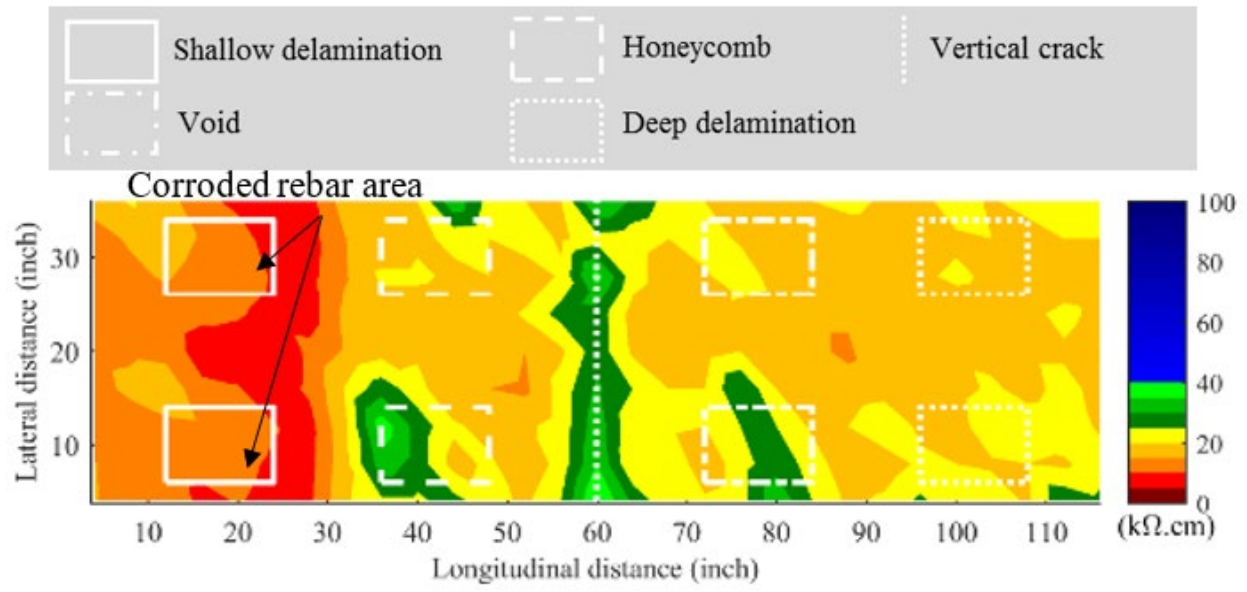
Source: FHWA.

A. S1.



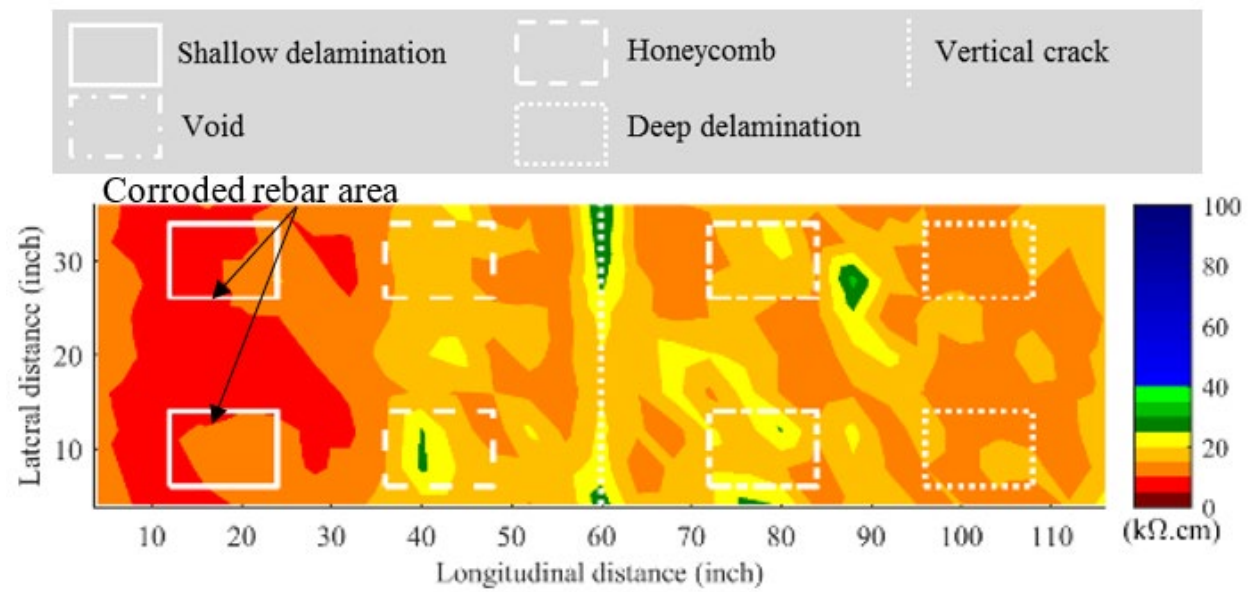
Source: FHWA.

B. S2.



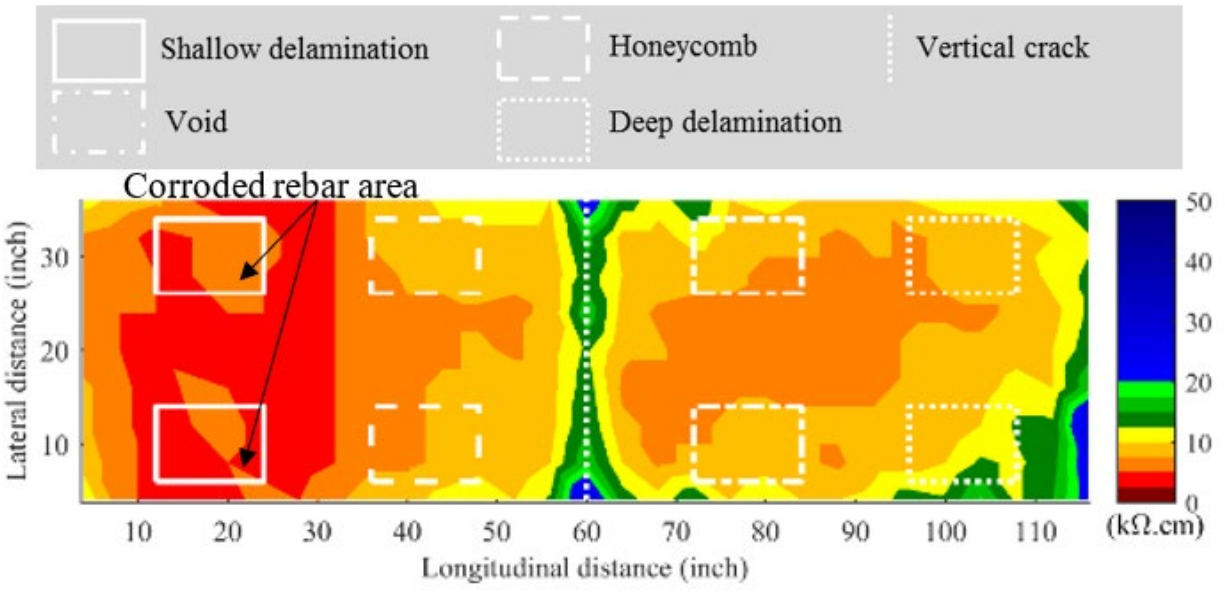
Source: FHWA.

C. S3.



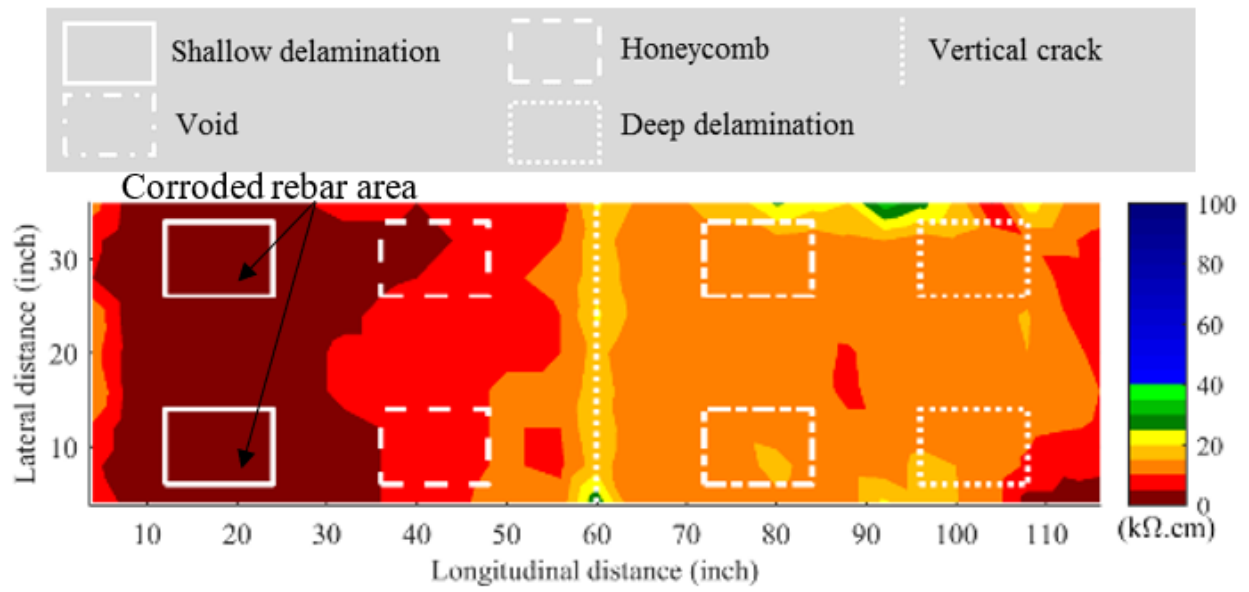
Source: FHWA.

D. S4.



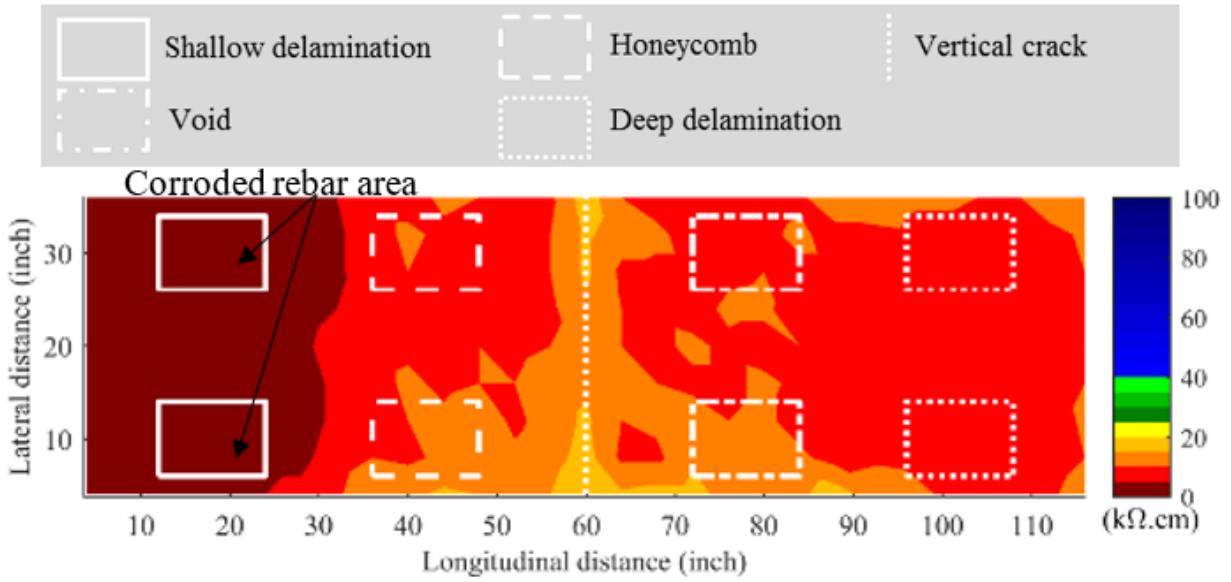
Source: FHWA.

E. S5.



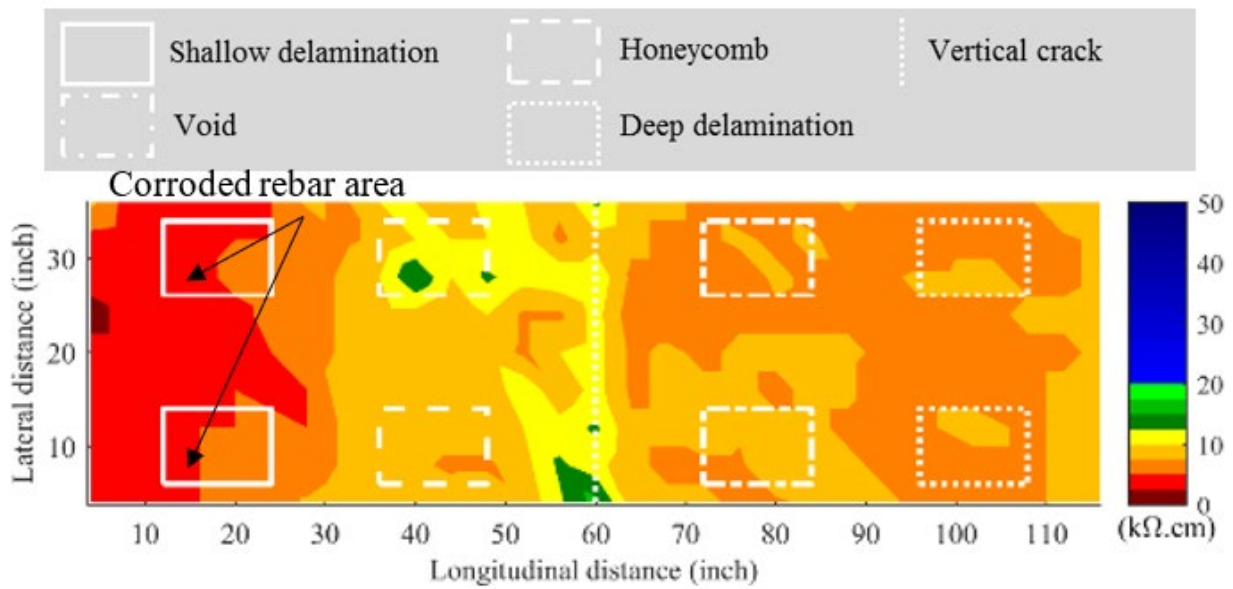
Source: FHWA.

F. S6.



Source: FHWA.

G. S7.



Source: FHWA.

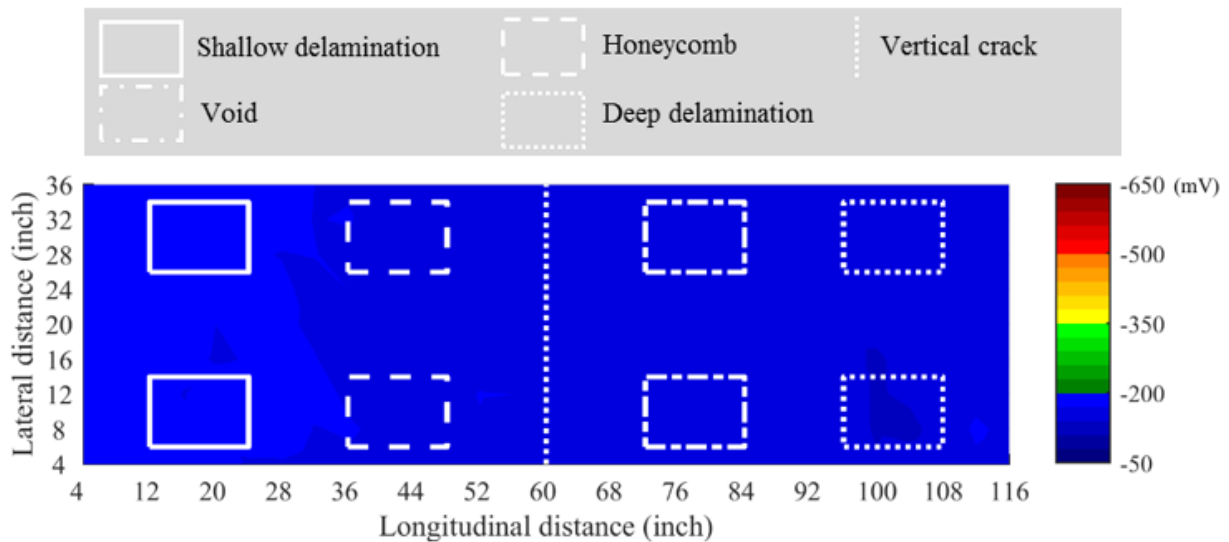
H. S8.

**Figure 70. Graphs. NDE condition maps with ER after accelerated corrosion.**

## HCP METHOD

When active corrosion reactions in the rebar increase, electrical potential decreases. The HCP method measured the electrical potential difference between the rebar in the concrete and a standard half-cell electrode to quantify the level of active corrosion. According to ASTM C876-15, *Standard Test Method for Corrosion Potentials of Uncoated Reinforcing Steel in Concrete*, an HCP value less than  $-350$  mV means a 90-percent probability of corrosion.<sup>(50)</sup>

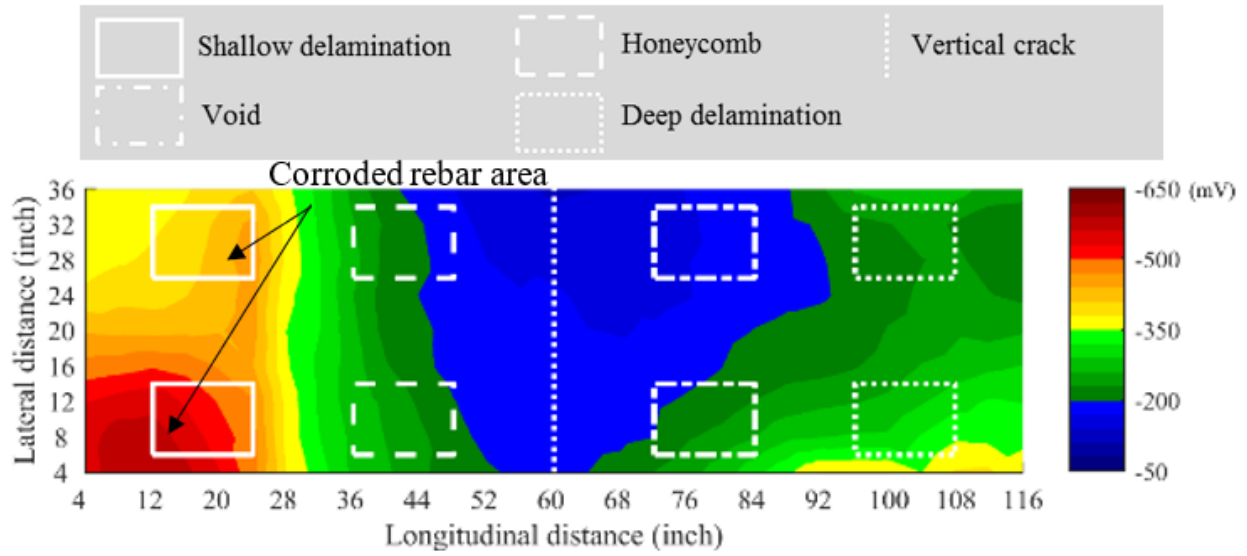
Figure 71 shows the condition map of specimen S1 based on HCP before accelerated corrosion was applied to the specimen. There was no active corrosion in the precorroded rebar. Figure 72-A through figure 72-H show the condition maps from HCP tests after active corrosion was introduced by applying accelerated corrosion to the specimens (figure 52 and figure 53). HCP detected active corrosion in the top layer rebar in all eight specimens. However, because it was more difficult for the NaCl solution to penetrate the concrete from the bottom, HCP could not detect active corrosion in the bottom layer rebar.



Source: FHWA.

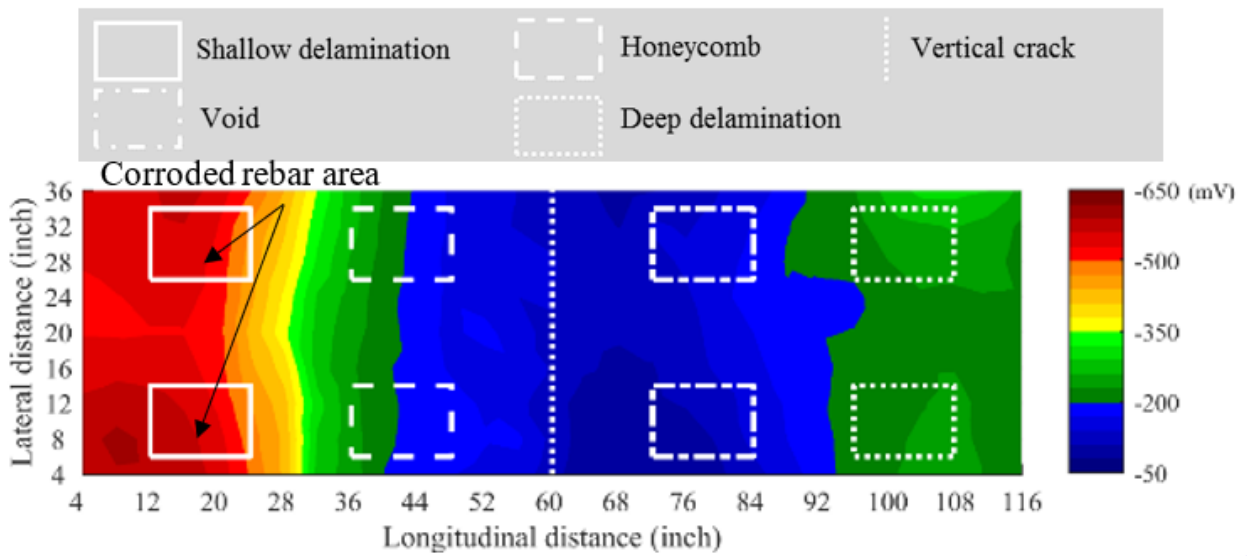
Note: Precorroded rebar not detected.

**Figure 71. Graph. NDE condition map of specimen S1 with HCP before accelerated corrosion.**



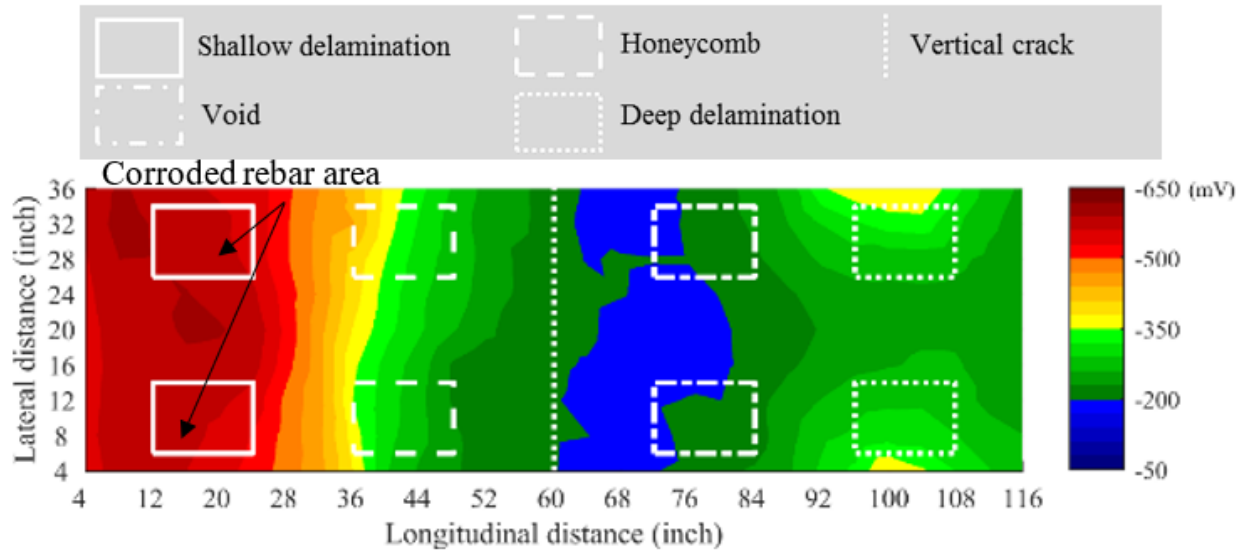
Source: FHWA.

A. S1.



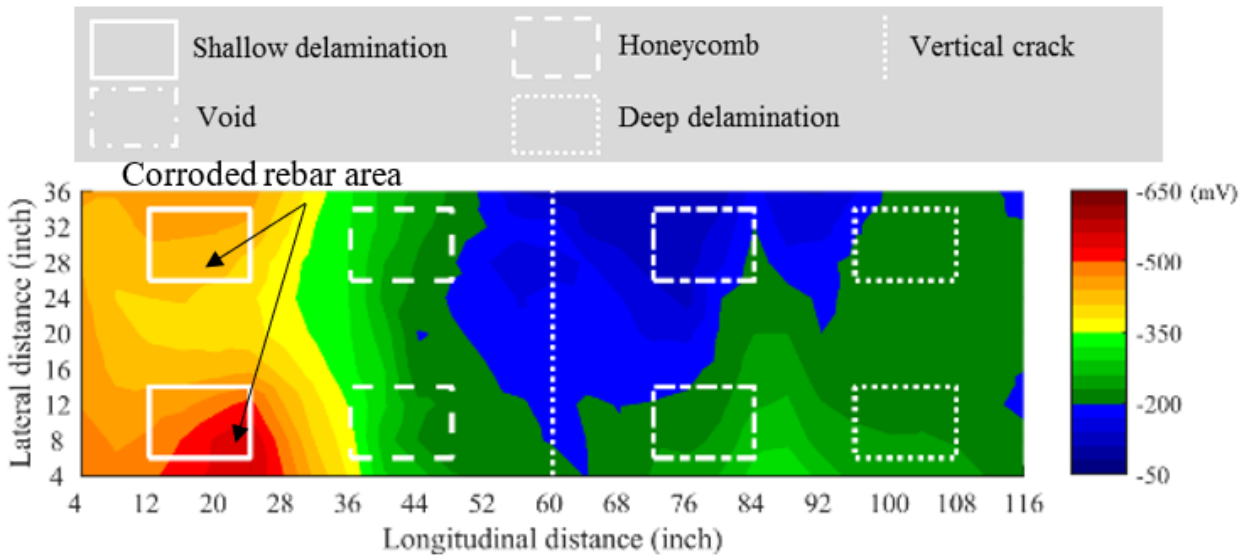
Source: FHWA.

B. S2.



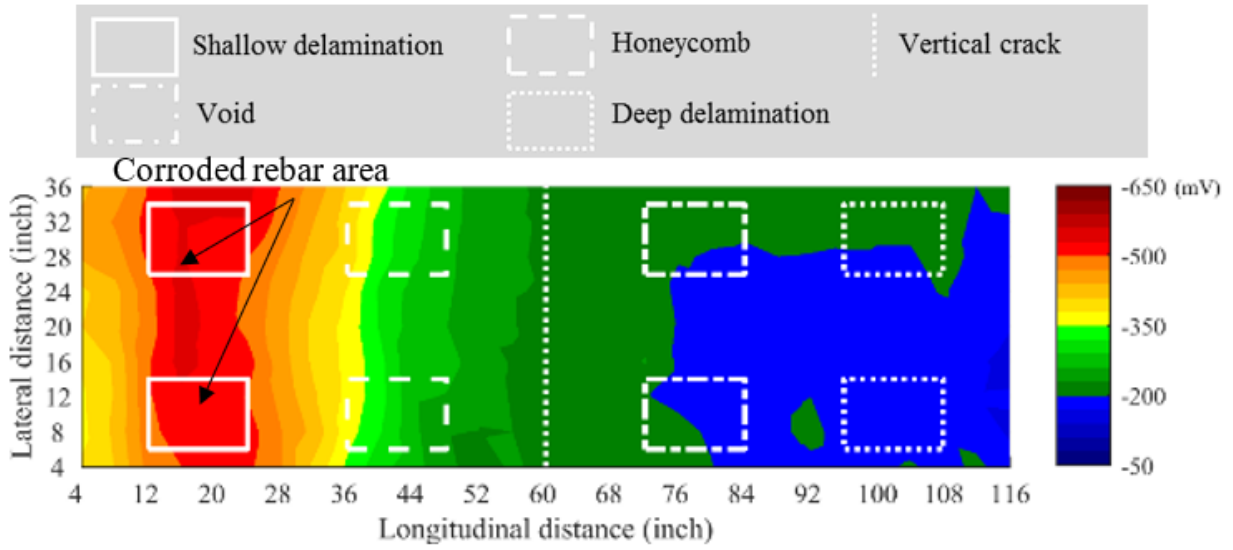
Source: FHWA.

C. S3.



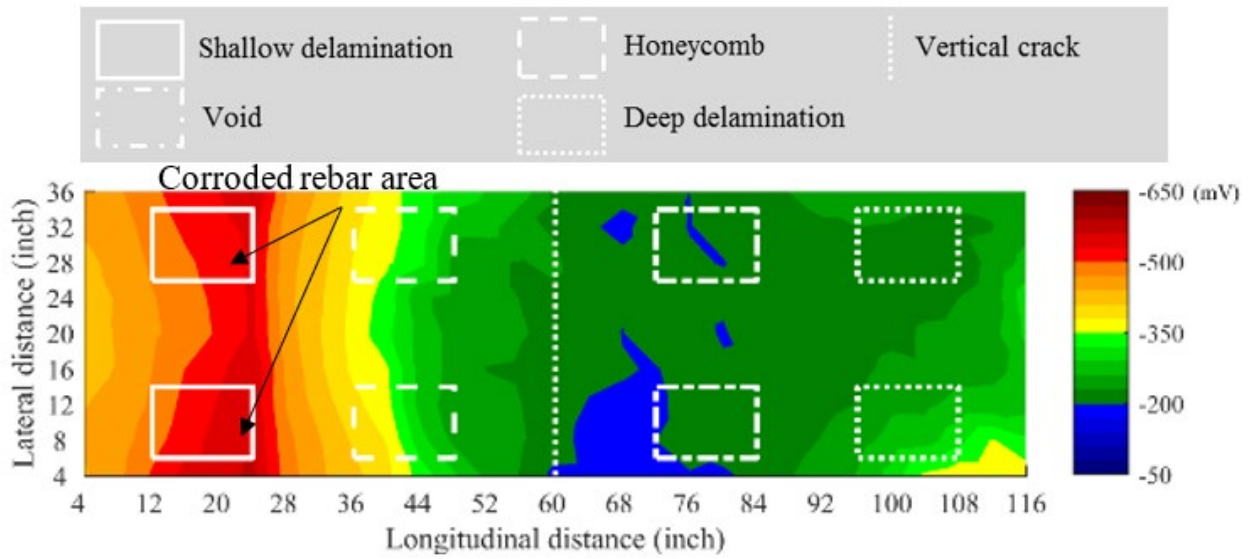
Source: FHWA.

D. S4.



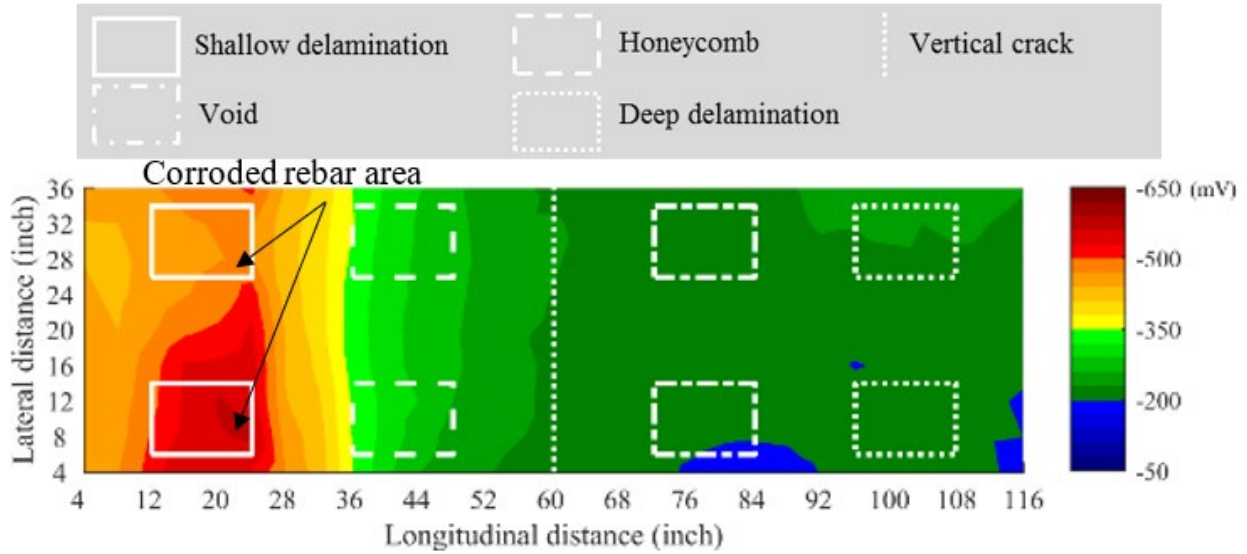
Source: FHWA.

E. S5.



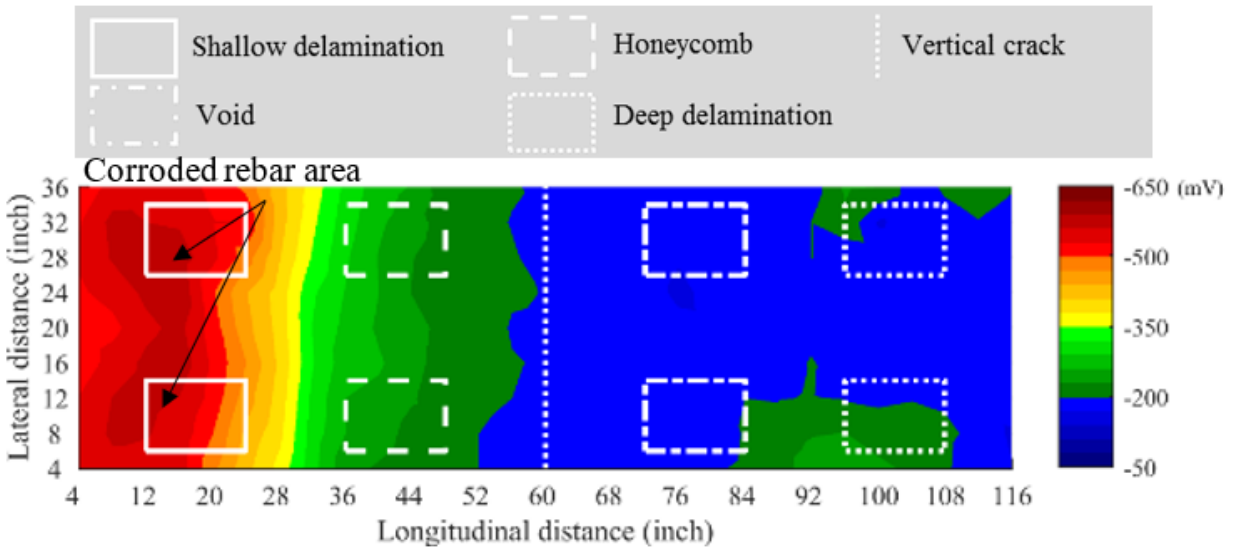
Source: FHWA.

F. S6.



Source: FHWA.

G. S7.



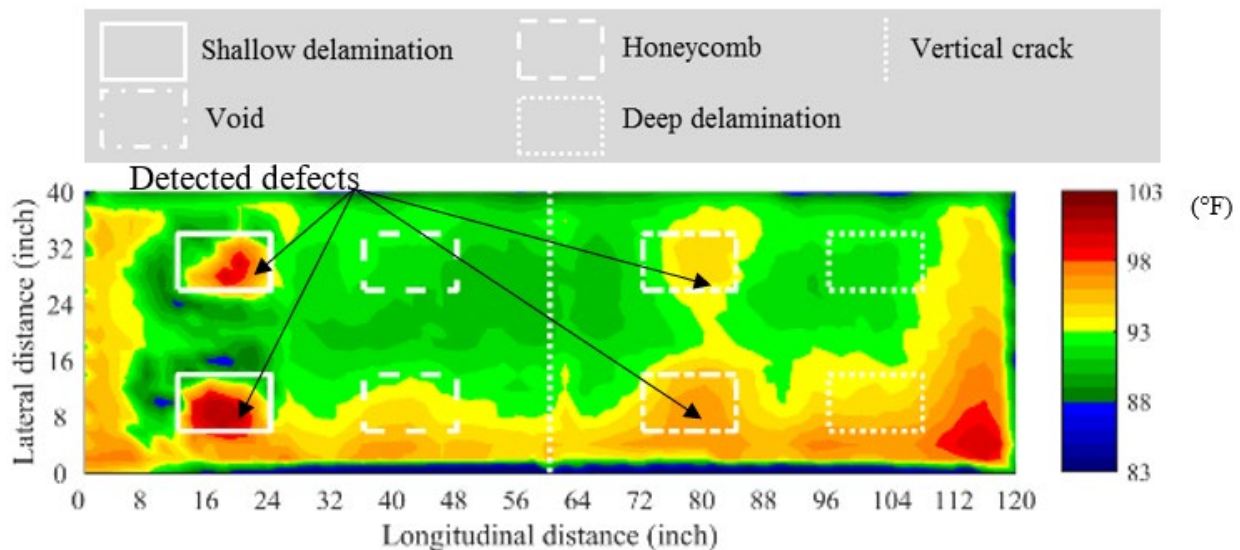
Source: FHWA.

H. S8.

**Figure 72. Graphs. NDE condition maps with HCP after accelerated corrosion.**

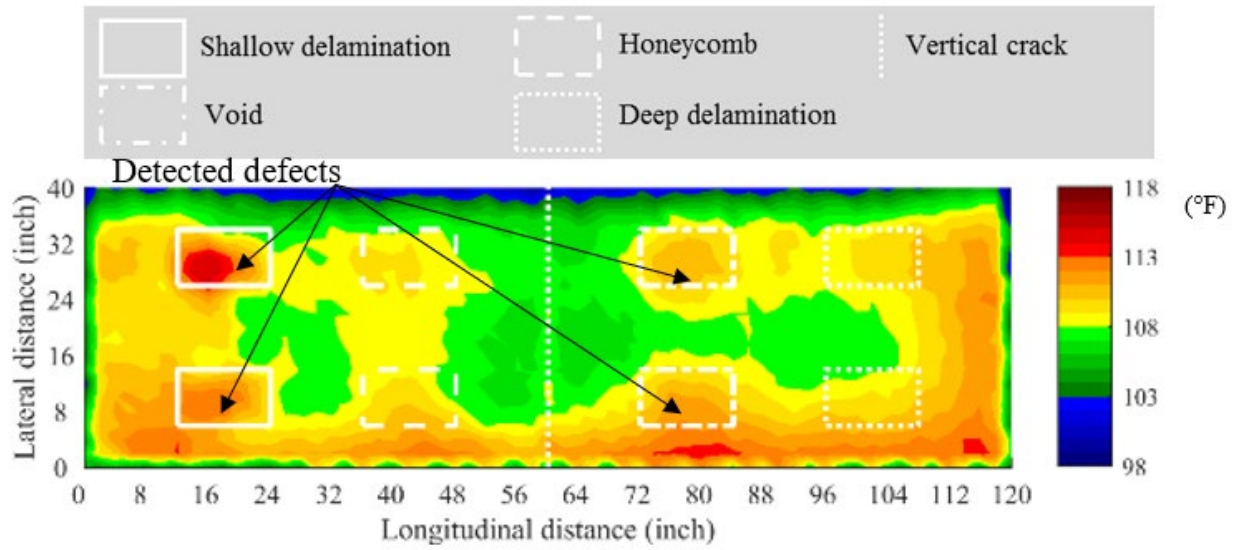
## IRT METHOD

Areas with defects have different thermodynamics than intact areas, and thus surface areas with underlying defects exhibit different temperatures from surface areas with intact subsurfaces. The IRT method collected surface temperature data and presented the data in a contour map. ASTM D4788 suggests IRT tests be carried out after a specimen is exposed to direct sunlight for a minimum of 3 h and a minimum temperature difference of 33°F be used to differentiate defected and intact areas.<sup>(51)</sup> Since the size of the specimens was relatively small compared to full-scale concrete bridge decks, the surface temperature of the specimens was significantly affected by the boundary condition. Under this circumstance, the temperature difference needed to be 2°F to detect defects. The condition maps based on IRT are shown in figure 73-A through figure 73-H and figure 74-A through figure 74-H. IRT data acquired at 3:00 p.m. (figure 73) show shallow delaminations in all eight specimens, and voids were detected in most specimens. The IRT method detected honeycombing and surface cracking in some specimens but could not detect deep delaminations in any specimens. In addition to temperature data per ASTM D4788, the condition maps for the temperature differences between 3:00 p.m. and 11:00 a.m. were provided as a supplement and shown in figure 74-A through figure 74-H. Compared with the surface temperature at 3:00 p.m. in figure 73-A through figure 73-H, the temperature difference in figure 74-A through figure 74-H improved the detection of voids and honeycombing for some specimens.



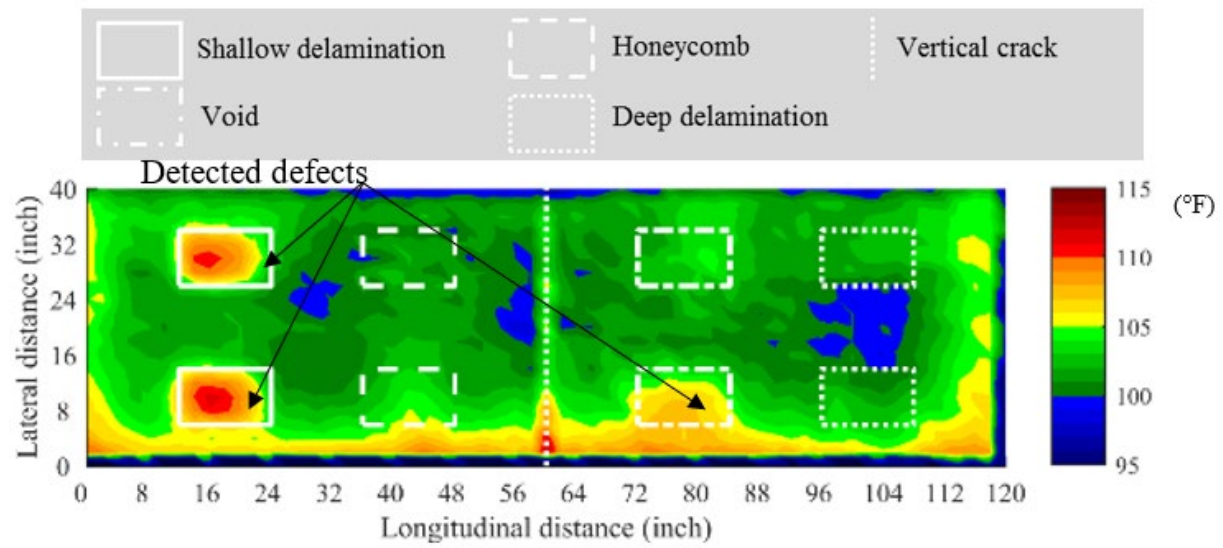
Source: FHWA.

A. S1.



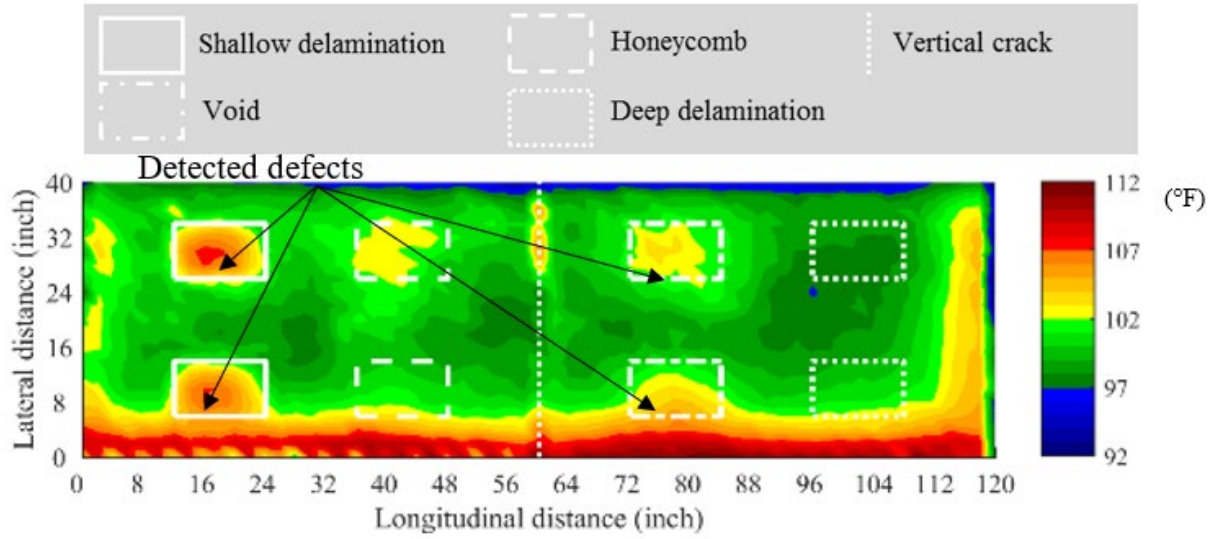
Source: FHWA.

B. S2.



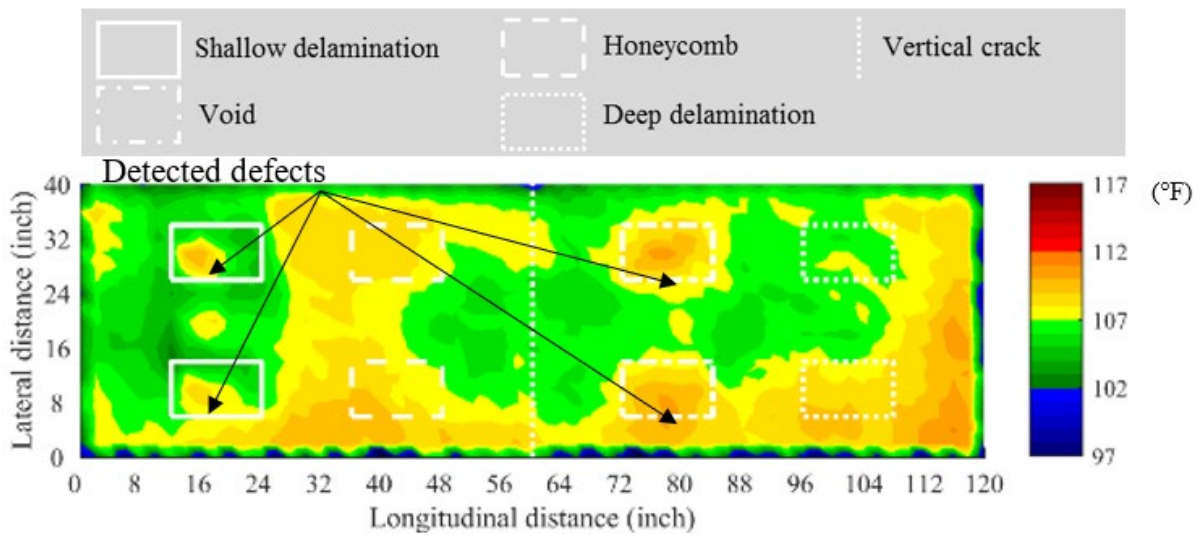
Source: FHWA.

C. S3.



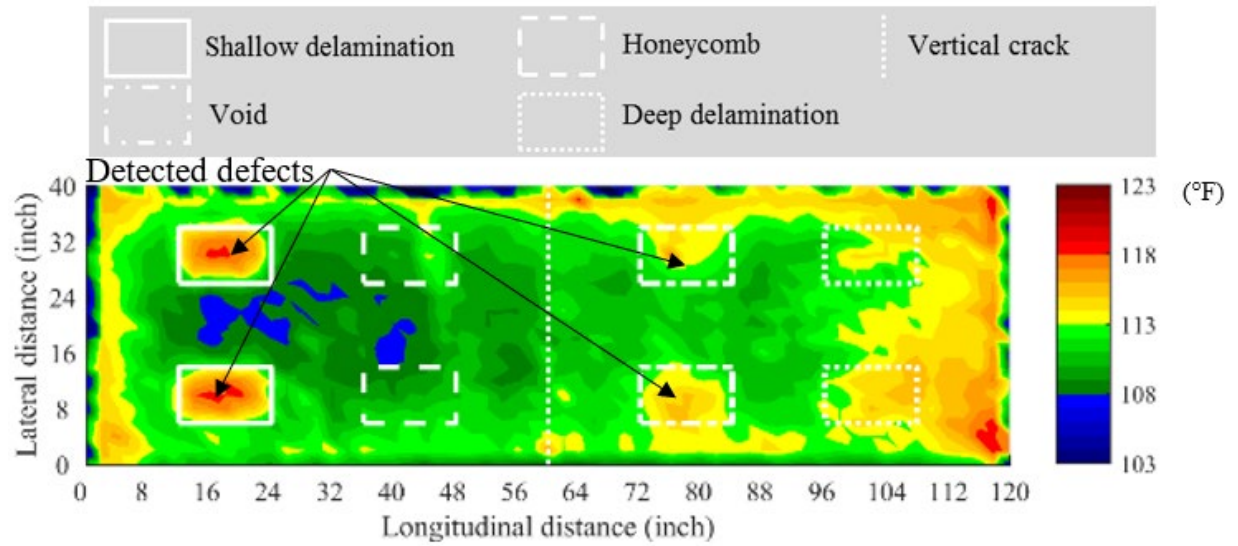
Source: FHWA.

D. S4.



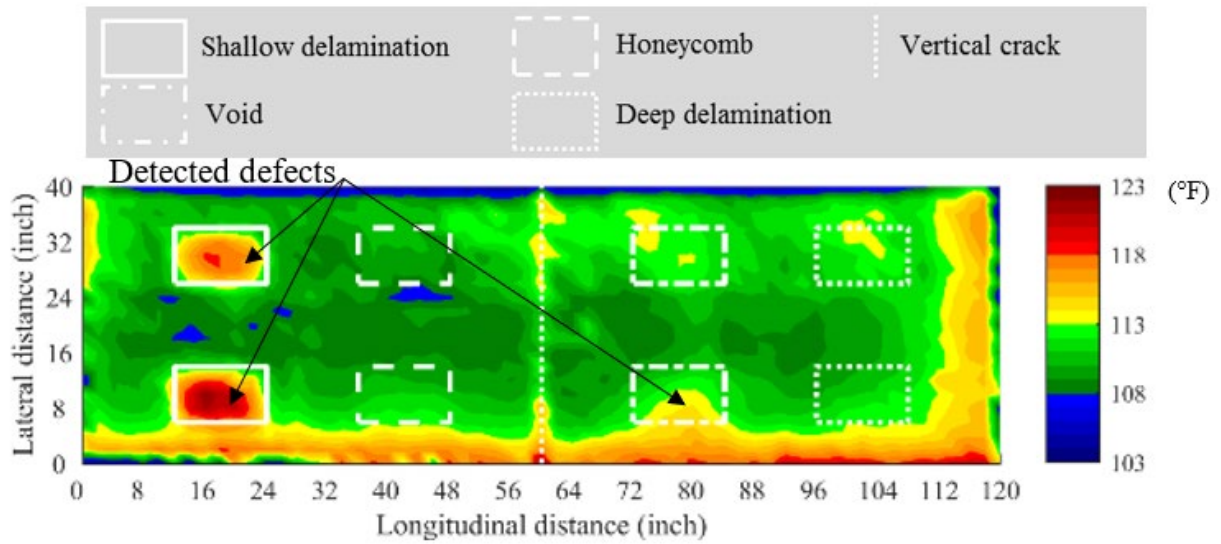
Source: FHWA.

E. S5.



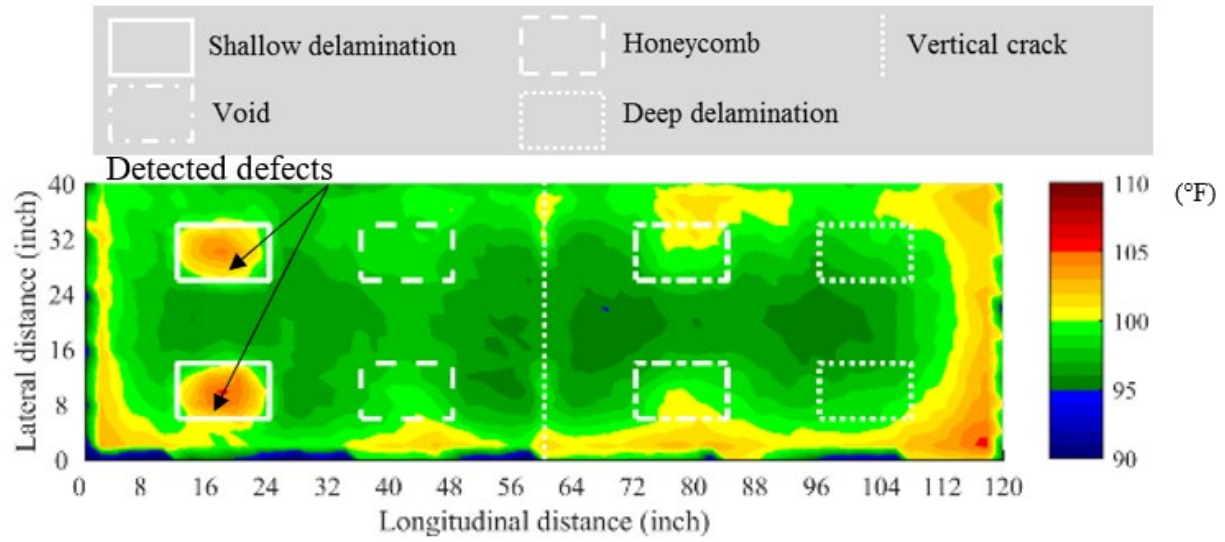
Source: FHWA.

F. S6.



Source: FHWA.

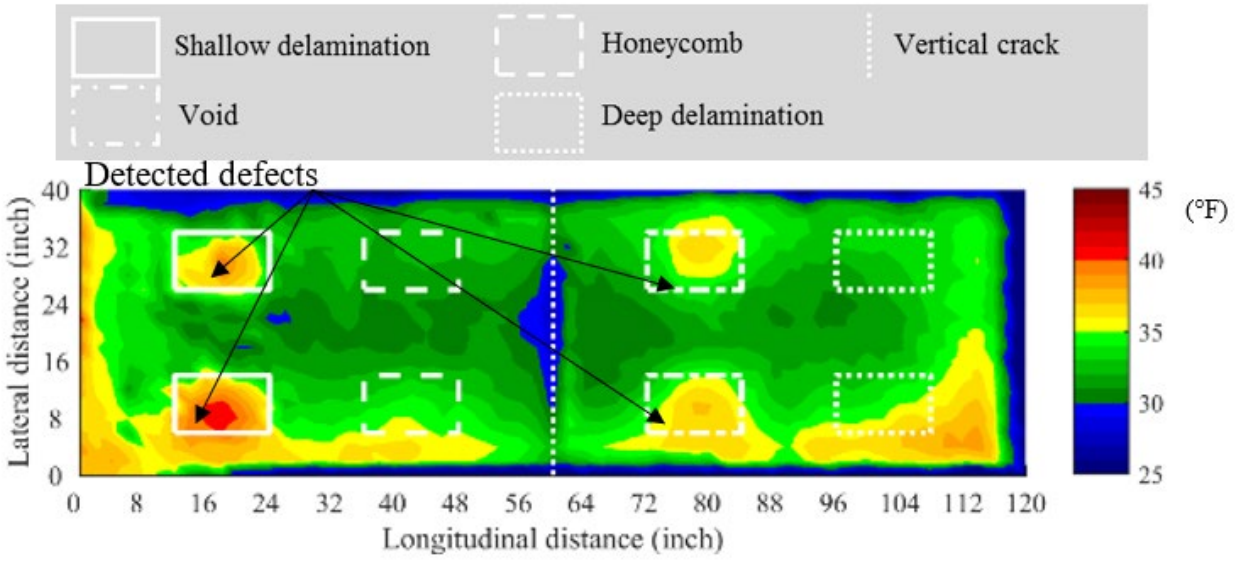
G. S7.



Source: FHWA.

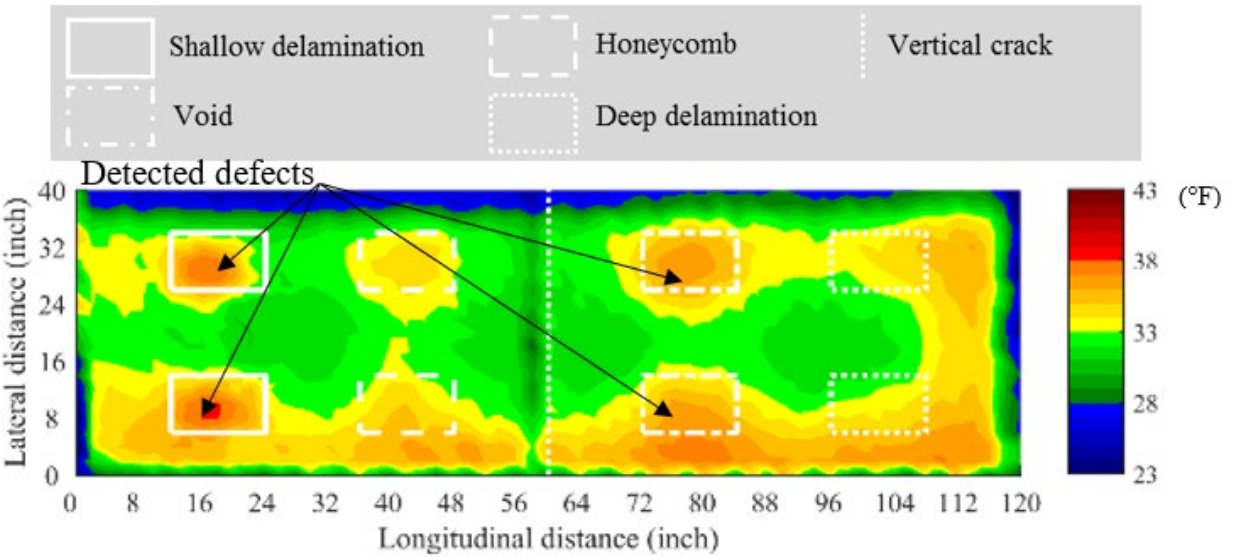
H. S8.

**Figure 73. Graphs. NDE IRT (temperature at 3:00 p.m.).**



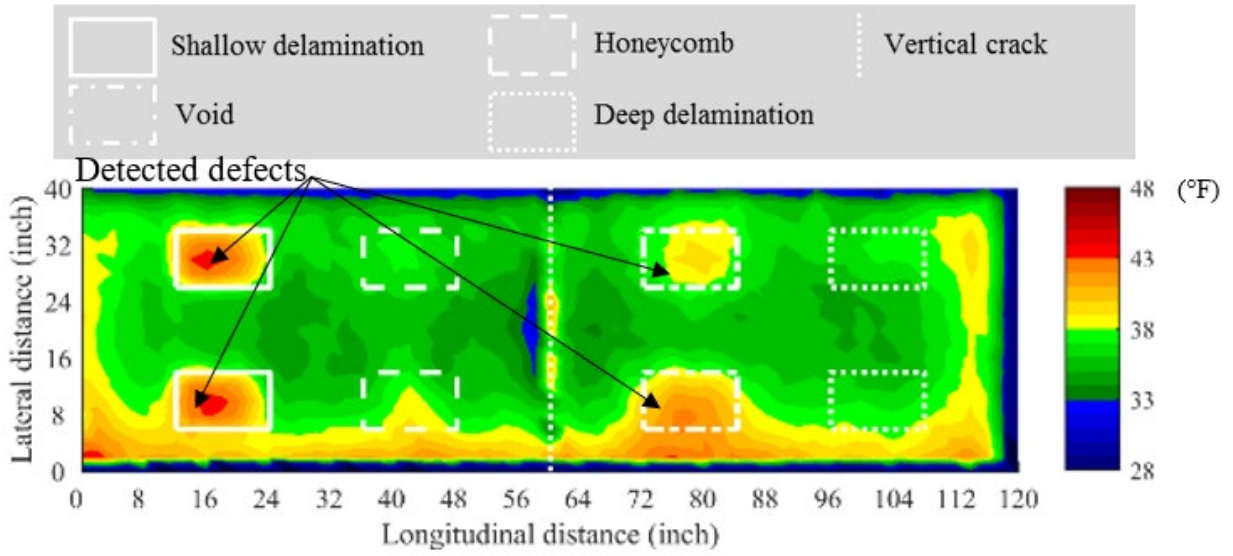
Source: FHWA.

A. S1.



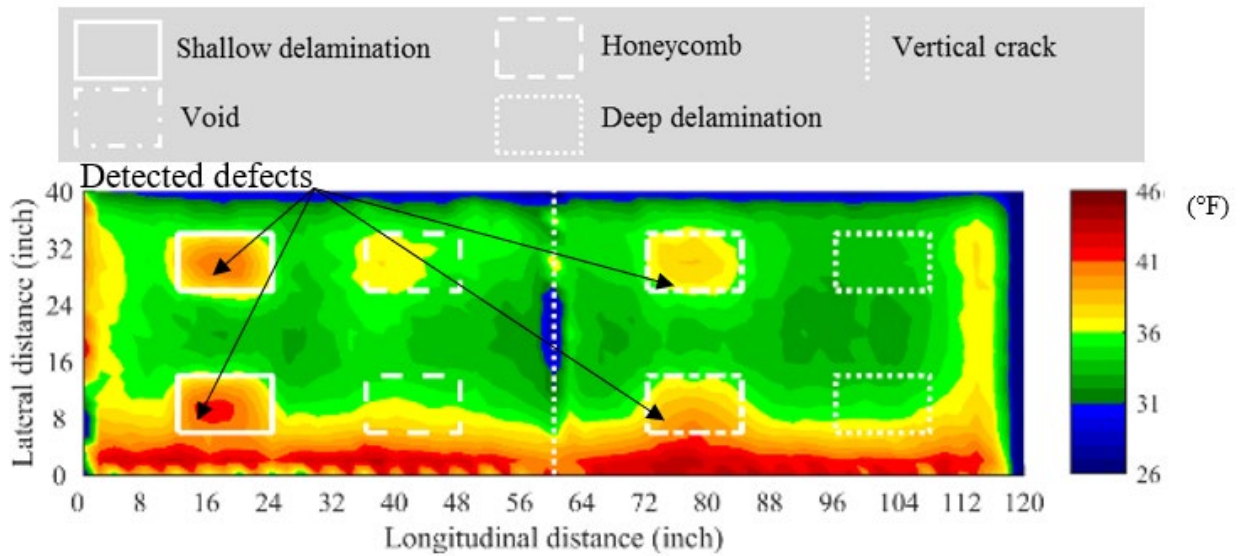
Source: FHWA.

B. S2.



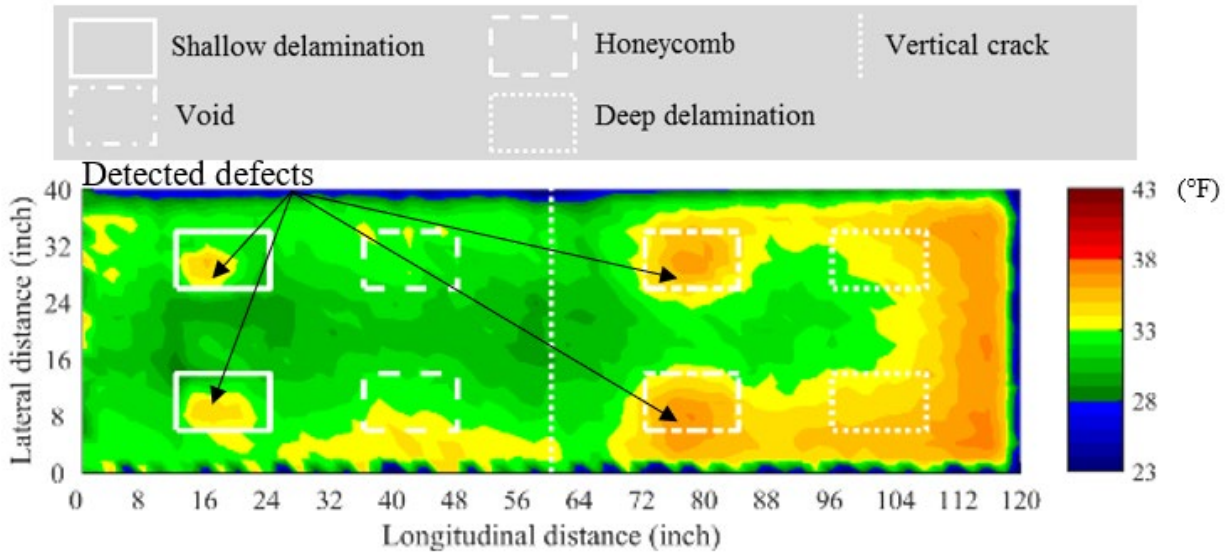
Source: FHWA.

C. S3.



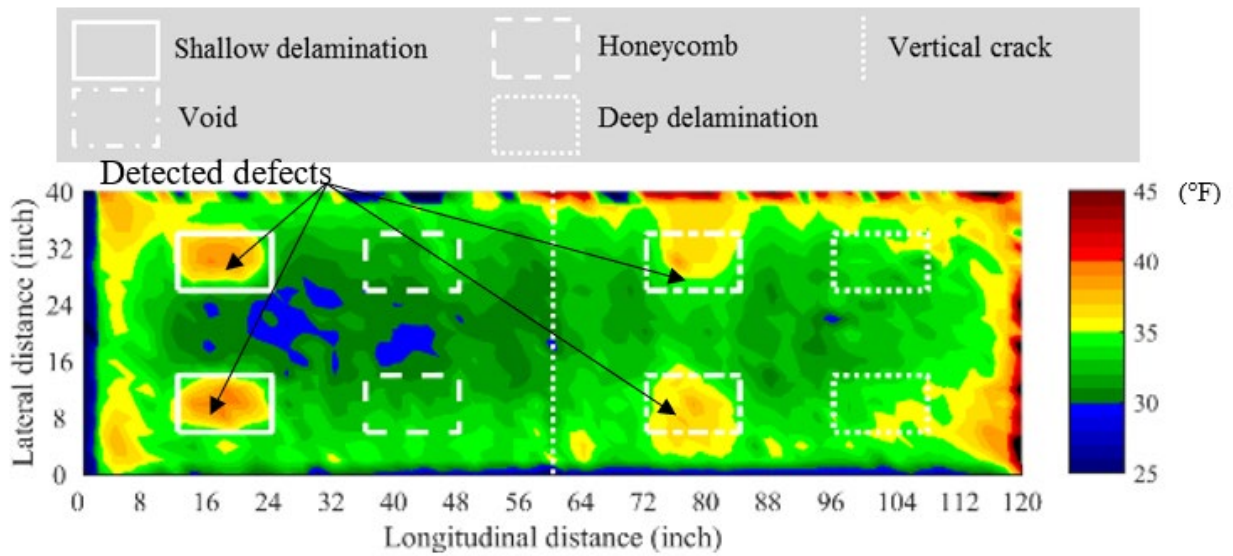
Source: FHWA.

D. S4.



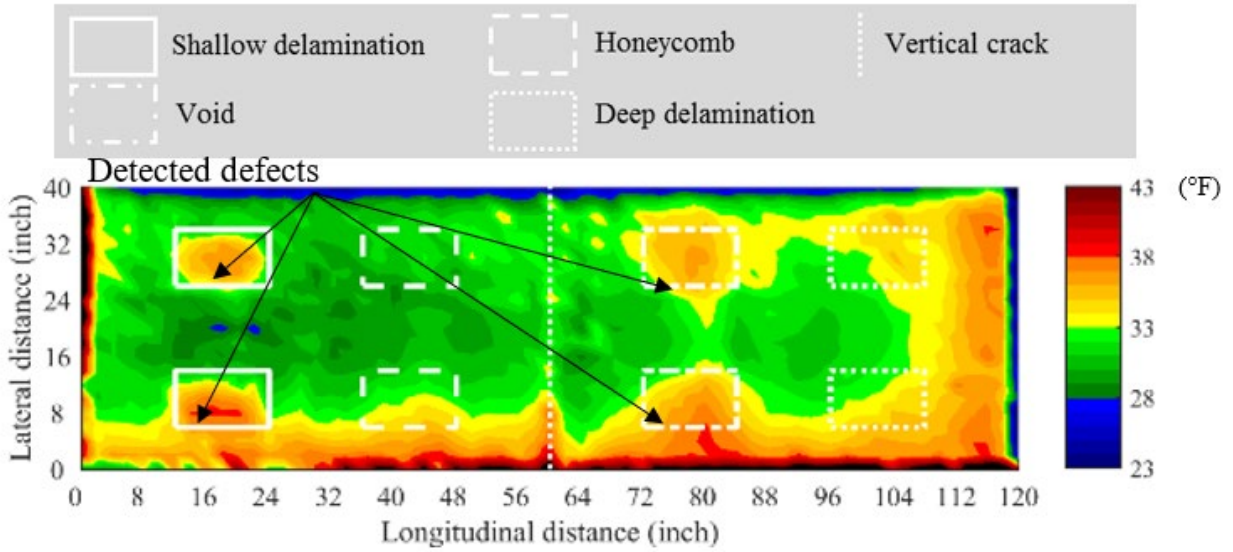
Source: FHWA.

E. S5.



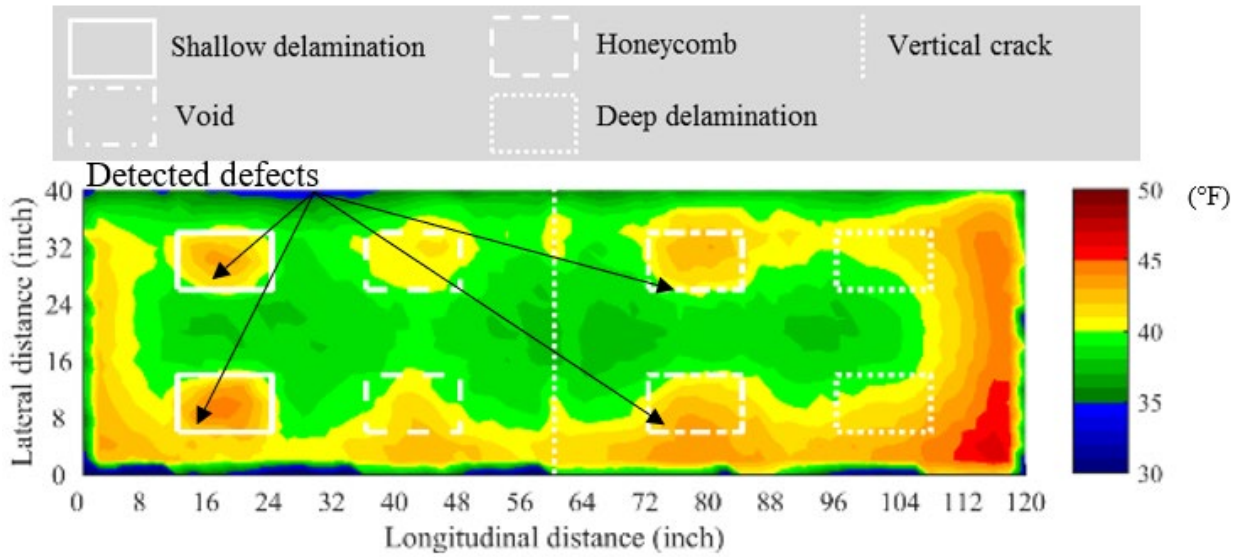
Source: FHWA.

F. S6.



Source: FHWA.

G. S7.



Source: FHWA.

H. S8.

Figure 74. Graphs. NDE IRT (temperature difference 11:00 a.m. to 3:00 p.m.).

## SUMMARY

Based on the test results of eight concrete specimens with no overlays, the applicability of the nine NDE technologies on concrete bridge decks with no overlays is summarized in table 8. Highlights of the findings include the following:

- The sounding method detected shallow delaminations in all specimens and voids in some specimens. The sounds from areas with voids were close to those from intact areas, making it challenging for the operator to identify voids; the sounds from areas with voids were indistinguishable to the operator from those from intact areas in some specimens. The sounding method is subjective, and the results depend on the operator's experience and skill.
- The USW method detected delaminations, voids, honeycombing, and vertical cracks through strong fluctuations in the dispersion curve, which led to a lower modulus than that from intact areas. Density measurements throughout each specimen provided an NDE condition map showing deteriorated areas with lower moduli and intact areas with higher moduli. In general, the modulus increased and the detectable area decreased as the depth of defects increased. Missing 3 of the total 16 deep delaminations in the USW condition maps indicated it became more challenging to detect defects as their depth increased and the detectable area decreased.
- The IE method detected delaminations, voids, and honeycombing. Density measurements throughout each specimen provided an NDE condition map showing deteriorated areas with dominant frequencies different from those of intact areas.
- The UT method detected rebar, delaminations, honeycombing, and voids through C- and B-scans. Some honeycombing had wave impedance close to that of intact concrete, and the reflections from this honeycombing were too weak to detect. Shallow delaminations in specimens S5–S8 were not as clear as those in specimens S1–S4. Because shallow delaminations in specimens S5–S8 were an average depth of 28 percent less than those in specimens S1–S4, direct waves interfered with reflection waves, making it challenging to detect the depth of shallow delaminations. This interference sometimes strengthened the resolution of shallow delaminations but could not show their correct position.
- The IR method only detected shallow delaminations and could not detect any other defects in the specimens.
- The GPR method detected rebar, delaminations, voids, and honeycombing from C- and B-scans and provided deterioration condition maps related to the elevated chloride content environment. The deterioration maps reflected the severity of the elevated chloride content environment introduced by the NaCl solution but not the condition of precorroded rebar. The GPR condition maps could not detect shallow delaminations because shallow delaminations were simulated by an air gap between two pieces of transparent thermoplastic and were not induced by corrosion.

- The ER method measured the resistivity of concrete and correlate it to a corrosion rate.
- The HCP method detected active rebar corrosion in the specimens.
- The IRT method detected shallow delaminations, voids, honeycombing, and vertical cracks in some specimens but could not detect deep delaminations in any specimens. Temperature differences between 3:00 p.m. and 11:00 a.m. resulted in more voids and honeycombing being detected at 11:00 a.m. than 3:00 p.m.

**Table 8. Applicability of NDE technologies for detecting defects in concrete bridge deck specimens without overlays.**

<b>Method</b>	<b>Defect</b>						
	<b>Shallow Delamination</b>	<b>Honeycombing</b>	<b>Void</b>	<b>Deep Delamination</b>	<b>Vertical Crack</b>	<b>Active Rebar Corrosion</b>	<b>Concrete Corrosive Environment</b>
Sounding	Yes	No	Yes*	No	No	No	No
USW	Yes	Yes	Yes	Yes	Yes	No	No
IE	Yes	Yes	Yes	Yes	No	No	No
UT-MIRA	Yes	Yes	Yes	Yes	No	No	No
UT-EyeCon	Yes	Yes	Yes	Yes	No	No	No
IR	Yes	No	No	No	No	No	No
GPR	Yes	Yes	Yes	Yes	No	No	Yes
ER	No	No	No	No	Yes	No	Yes
HCP	No	No	No	No	No	Yes	No
IRT	Yes	Yes*	Yes*	No	Yes*	No	No

\*NDE method detected defects in some specimens but not all.



## CHAPTER 8. CONSTRUCTION OF OVERLAYS

Seven of the eight specimens were randomly selected for overlays. Each specimen and its respective overlay are listed in table 9. The abbreviation for each specimen with an overlay listed in table 9 is used hereinafter.

**Table 9. Specimens and their respective overlays.**

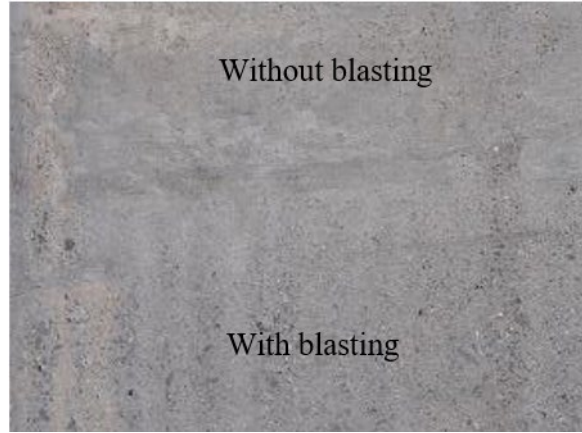
Details	Specimen						
	S1	S3	S4	S5	S6	S7	S8
Overlay	Epoxy polymer	LMC	Asphalt with a sheet membrane	Asphalt with a liquid membrane	Silica fume-modified concrete	Asphalt without a membrane	PPC
Abbreviation	S1E	S3L	S4AS	S5AL	S6S	S7A	S8P

Epoxy, latex, silica fume, and polyester polymer overlays were constructed by experts in the Virginia Transportation Research Council. One half of each specimen was covered with a plastic sheet to create debonding of the overlay. The other half of each specimen was shot blasted so the overlay bonded better to the concrete, as shown in figure 75-A through figure 75-D. Each overlay was placed within 24 h after shot blasting to minimize carbonation and ensure good bonding.



Source: FHWA.

A. Shot blasting.



Source: FHWA.

C. Close-up after shot blasting.



Source: FHWA.

B. After shot blasting.



Source: FHWA.

D. Plastic sheet for debonding.

**Figure 75. Photos. Concrete surface preparation for overlays.**

### **EPOXY POLYMER OVERLAY**

Epoxy polymer overlay was placed in two layers on S1E, as shown in figure 76-A through figure 76-F. Epoxy application rates were 2.5 gal per 100 ft<sup>2</sup> for layer one (8 lb mixed) and 5 gal per 100 ft<sup>2</sup> for layer two (15.3 lb mixed). Shortly after spreading epoxy layer one, calcined bauxite aggregate was spread over the surface. After the epoxy cured for 30 min, excess aggregate was swept away and the procedure was repeated for the second layer of epoxy. During the application, the ambient temperature was around 89°F.



Source: FHWA.

A. Epoxy mixing.



Source: FHWA.

D. Sweeping away excess aggregate.



Source: FHWA.

B. Epoxy layer one.



Source: FHWA.

E. Epoxy layer two.



Source: FHWA.

C. Aggregate layer one.



Source: FHWA.

F. Aggregate layer two.

**Figure 76. Photos. Constructing an epoxy polymer overlay.**

## LATEX AND SILICA FUME-MODIFIED CONCRETE OVERLAYS

Latex and silica fume-modified concrete overlays with a thickness of 1.5 inches were placed on specimens S3L and S6S, respectively, as shown in figure 77-A through figure 77-C. The concrete surface was fully saturated with water before applying each overlay. The 28-d compressive strengths of the latex and silica fume overlays were 5,490 and 9,430 psi, respectively.



Source: FHWA.

A. Saturated concrete surface.



Source: FHWA.

B. Latex overlay.



Source: FHWA.

C. Silica fume overlay.

**Figure 77. Photos. Constructing latex and silica fume-modified concrete overlays.**

## POLYESTER POLYMER OVERLAY

A polyester polymer overlay was applied in two layers on S8P with a total overlay thickness of 0.75 inches, as shown in figure 78-A through figure 78-D. One-third gal of high molecular weight methacrylate primer was applied to the concrete surface with a brush, and then 3 oz of polymer and 1 gal of high molecular weight methacrylate primer were mixed for 30 s. Resin and high molecular weight methacrylate primer were mixed for 2 min, and sand and rock were added and mixed for another 3 min. The mixed polyester concrete was leveled with a wooden screed. Fine sand was applied to excess after smoothing with the screed. The 28-d compressive strength of polyester polymer overlay was 6,240 psi.



Source: FHWA.

A. Priming the concrete surface.



Source: FHWA.

C. Spreading a thin layer of dry aggregate.



Source: FHWA.

B. Applying the polyester polymer mixture.



Source: FHWA.

D. Finished polyester polymer overlay.

**Figure 78. Photos. Constructing a polyester polymer overlay.**

After the overlay construction, latex and silica fume-modified overlays were covered by wet burlap and plastic sheeting to allow the concrete to cure for 7 d, as shown in figure 79.



Source: FHWA.

**Figure 79. Photo. Latex and silica fume overlays after construction.**

## ASPHALT OVERLAY

Samples of liquid and sheet membranes are shown in figure 80-A and figure 80-B, respectively. Before applying the membranes, the concrete surface was sand blasted so the overlay bonded better to the concrete. Liquid membrane, the construction of which is shown in figure 81-A through figure 81-F, was applied on specimen S5AL. The liquid membrane consisted of three layers: the bottom primer, middle membrane, and top coat. Dry aggregate was placed right after spraying the top coat, and all three layers set rapidly. Because the hot-mix asphalt was applied at a temperature as high as 300°F, parchment paper, which can withstand temperatures up to 420°F, was used to create debonding on one half of specimen S5AL.



Source: FHWA.

A. Liquid membrane.



Source: FHWA.

B. Sheet membrane.

**Figure 80. Photos. Samples of liquid and sheet membranes.**



Source: FHWA.

A. Surface preparation.



Source: FHWA.

D. Top coat.



Source: FHWA.

B. Bottom primer.



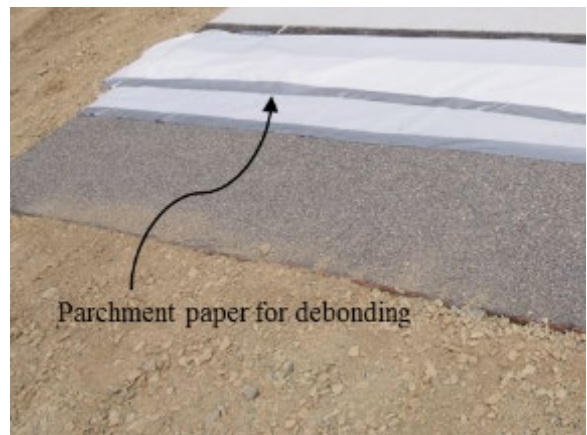
Source: FHWA.

E. Applying a thin layer of dry aggregate.



Source: FHWA.

C. Middle membrane.



Source: FHWA.

F. Parchment paper for debonding.

**Figure 81. Photos. Installing a liquid membrane and parchment paper for debonding.**

Sheet membrane was applied on specimen S4AS, as shown in figure 82-A and figure 82-B. A thin layer of asphalt primer was sprayed onto the concrete surface. One half of the membrane bottom was torched to ensure good bonding with the concrete surface, and the other half was not torched to create debonding. A layer of parchment paper was added between the specimen and the membrane without torching to guarantee debonding when the hot-mix asphalt was placed.



Source: FHWA.

A. Installing sheet membrane.



Source: FHWA.

B. Parchment paper for debonding.

**Figure 82. Photos. Installation of sheet membrane and parchment paper for debonding.**

Parchment paper was also used to create debonding on one half of specimen S7A, as shown in figure 83.



Source: FHWA.

**Figure 83. Photo. Parchment paper installation for debonding on an asphalt overlay with no waterproof membrane.**

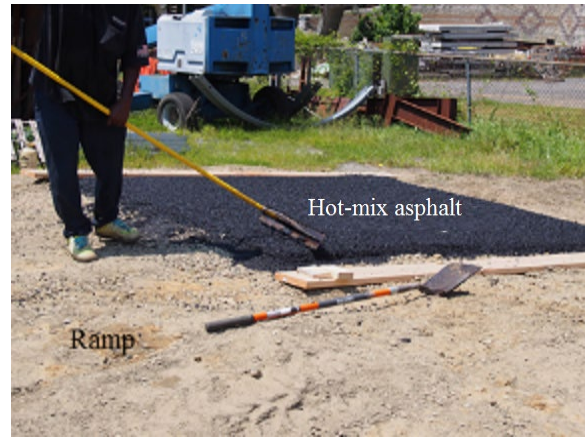
The construction of asphalt overlays on three specimens is shown in figure 84-A through figure 84-D. The three specimens were lined up side by side, and an aggregate ramp surrounding the specimens was built to provide access for an asphalt-compaction roller. Asphalt-coating primer was applied to the half of each specimen that needed bonding. The hot-mix asphalt with Virginia Department of Transportation mix SM-9.5A was applied by a Virginia class A paving

contractor. An asphalt-compaction roller and plate compactor compacted the asphalt, during which a nuclear density gauge was used to ensure uniform and adequate compaction. The asphalt overlay was cut along the side of each specimen using a metal-cutting saw 4 d after paving.



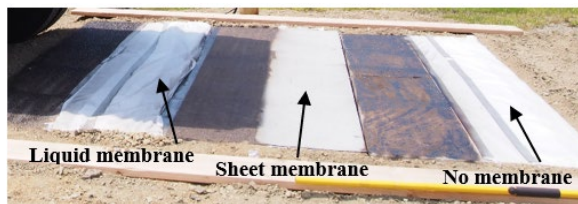
Source: FHWA.

A. Specimens surrounded by a ramp.



Source: FHWA.

C. Applying hot-mix asphalt.



Source: FHWA.

B. Asphalt-primer coating.



Source: FHWA.

D. Asphalt compaction and density measurement.

**Figure 84. Photos. Constructing asphalt overlays on three specimens.**



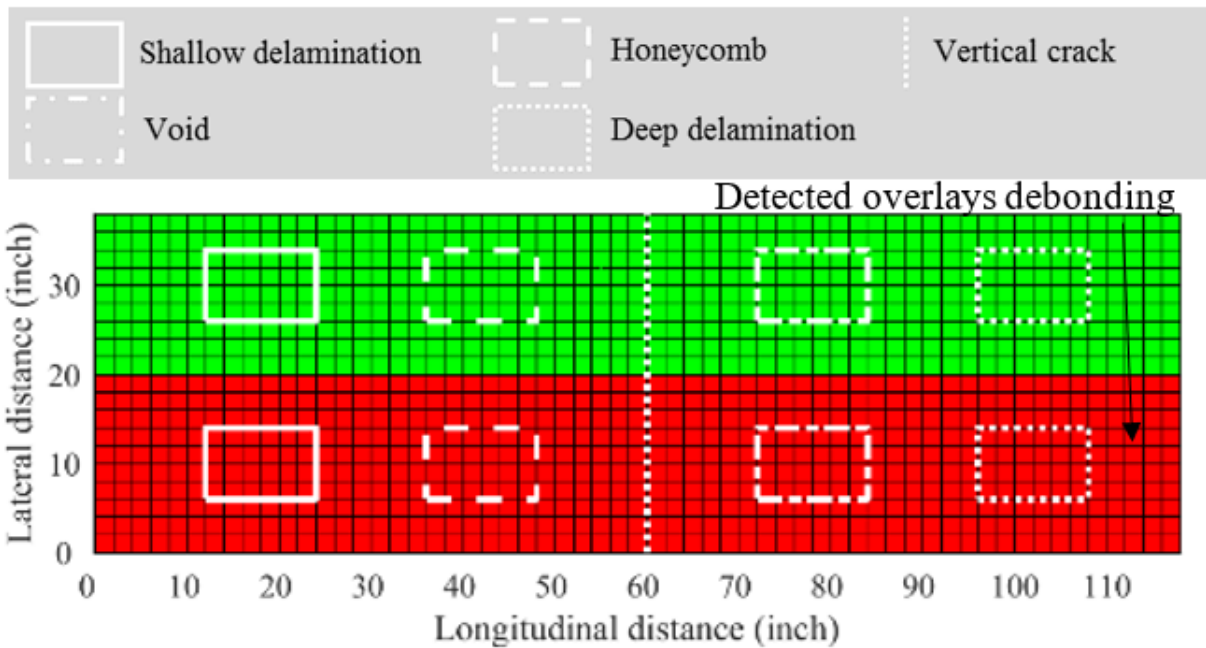
## CHAPTER 9. NDE RESULTS OF SPECIMENS WITH OVERLAYS

The results of nine NDE technologies on seven specimens with seven types of overlays are discussed in this chapter.

### SOUNDING CONDITION MAPS

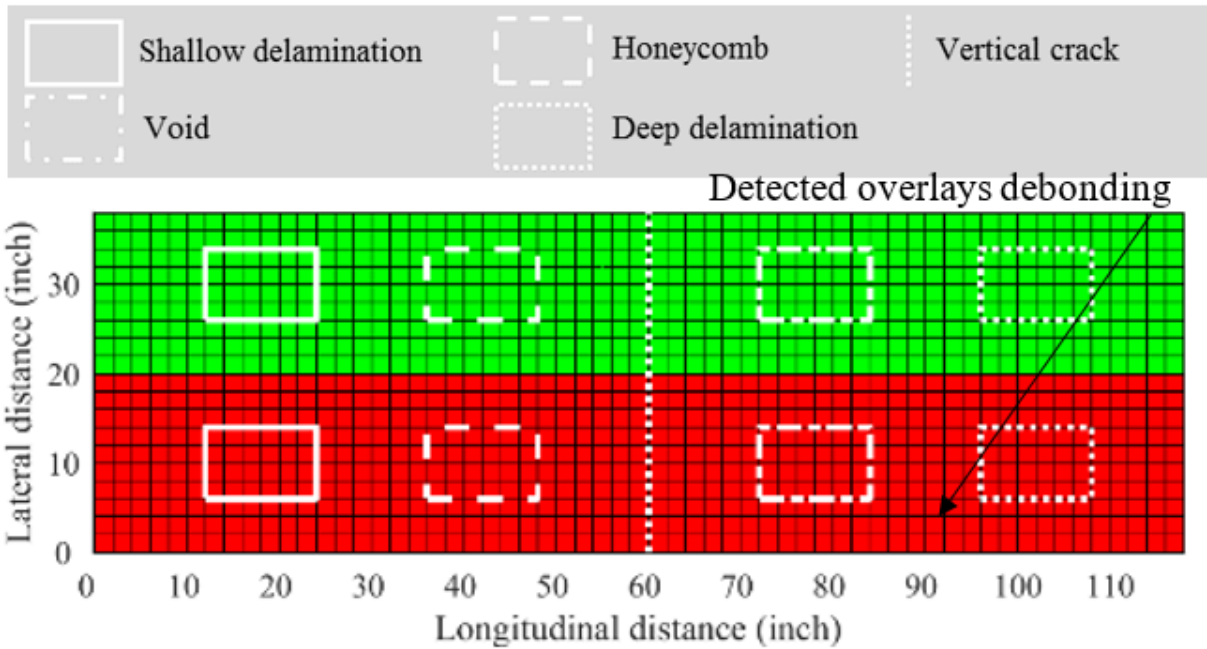
The condition maps based on the sounding method are shown in figure 85-A through figure 85-G. Sounding detected debonding of overlays in all seven specimens but could not detect other defects in the specimens through the bonded overlays. Sounding found unexpected debonded in the top middle of specimen S4AS, as shown in figure 85-C.

The debonding was identified in the condition maps for the USW and IE methods, as shown in figure 86 and figure 89, respectively. This debonding was caused by the cutting saw not cutting through the top middle edge of the overlay in specimen S4AS, and the surrounding asphalt debonded when the specimen was moved and torn off from the edge.



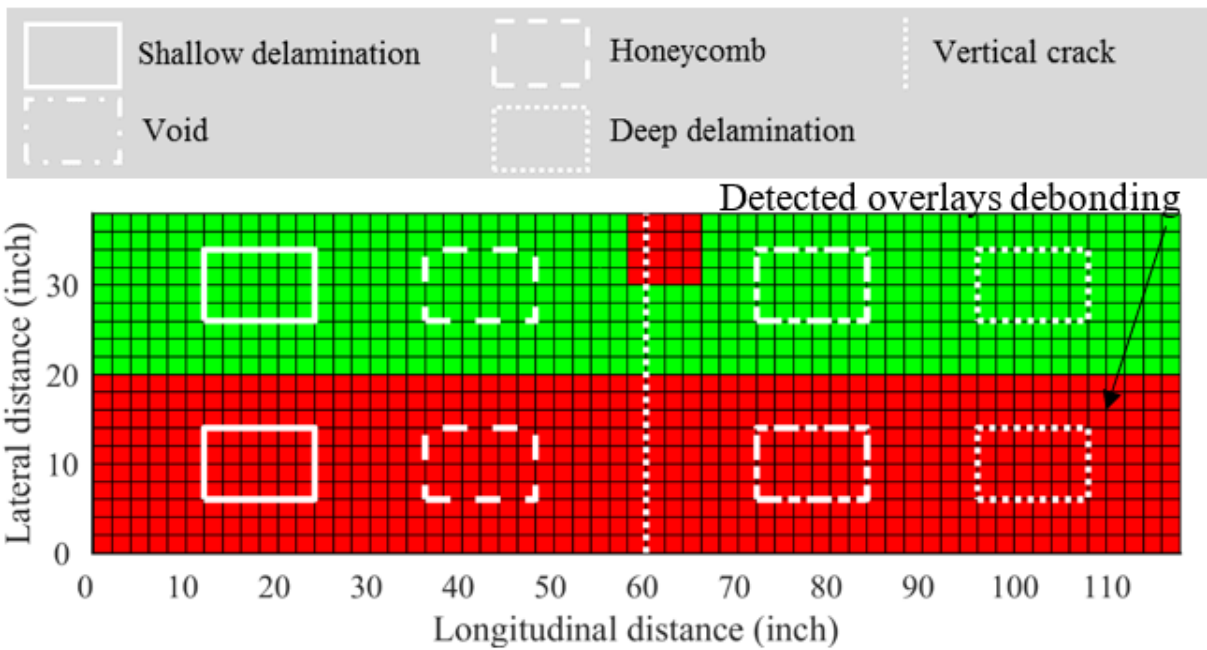
Source: FHWA.

A. S1E.



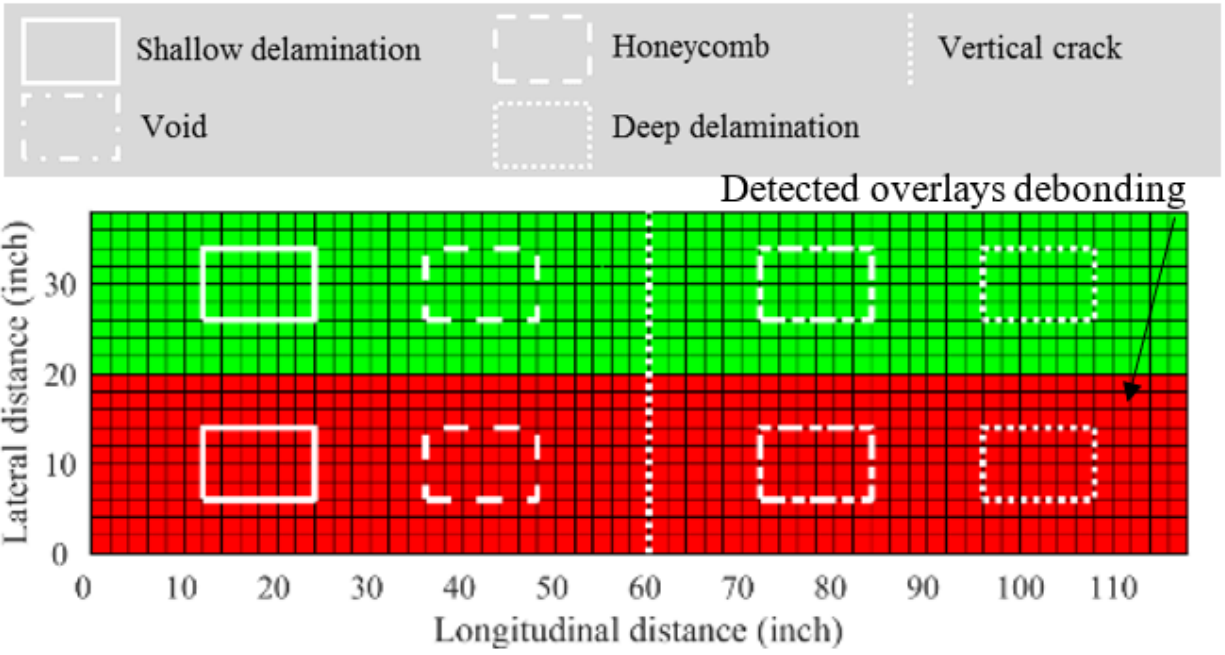
Source: FHWA.

B. S3L.



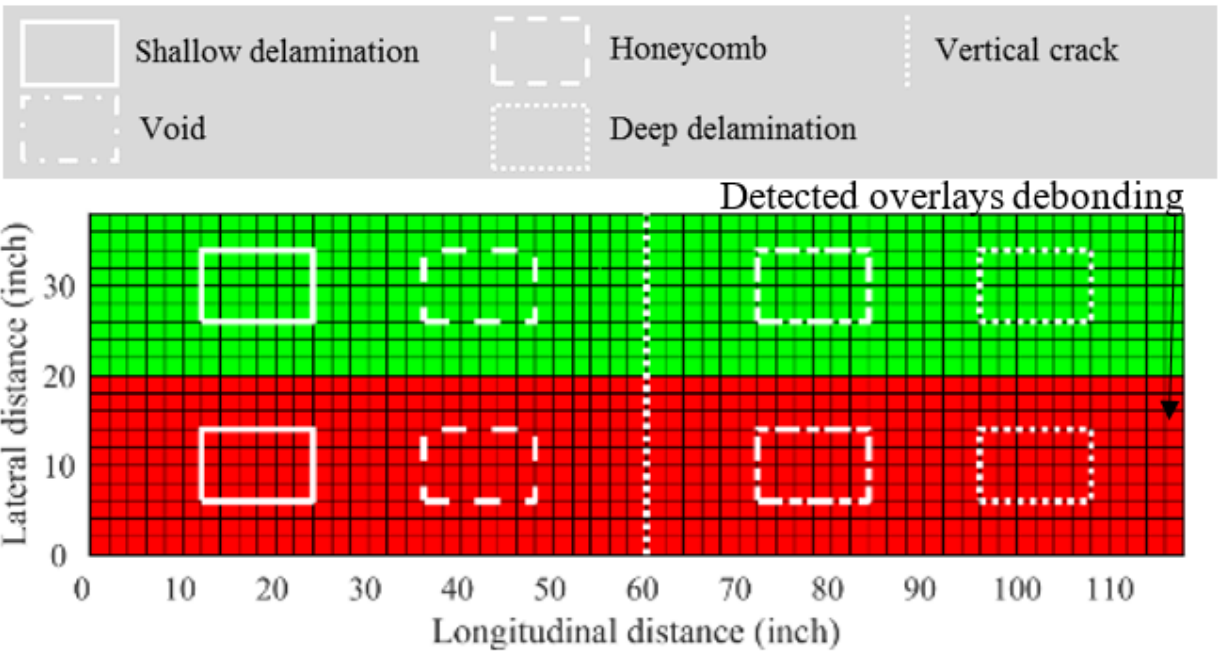
Source: FHWA.

C. S4AS.



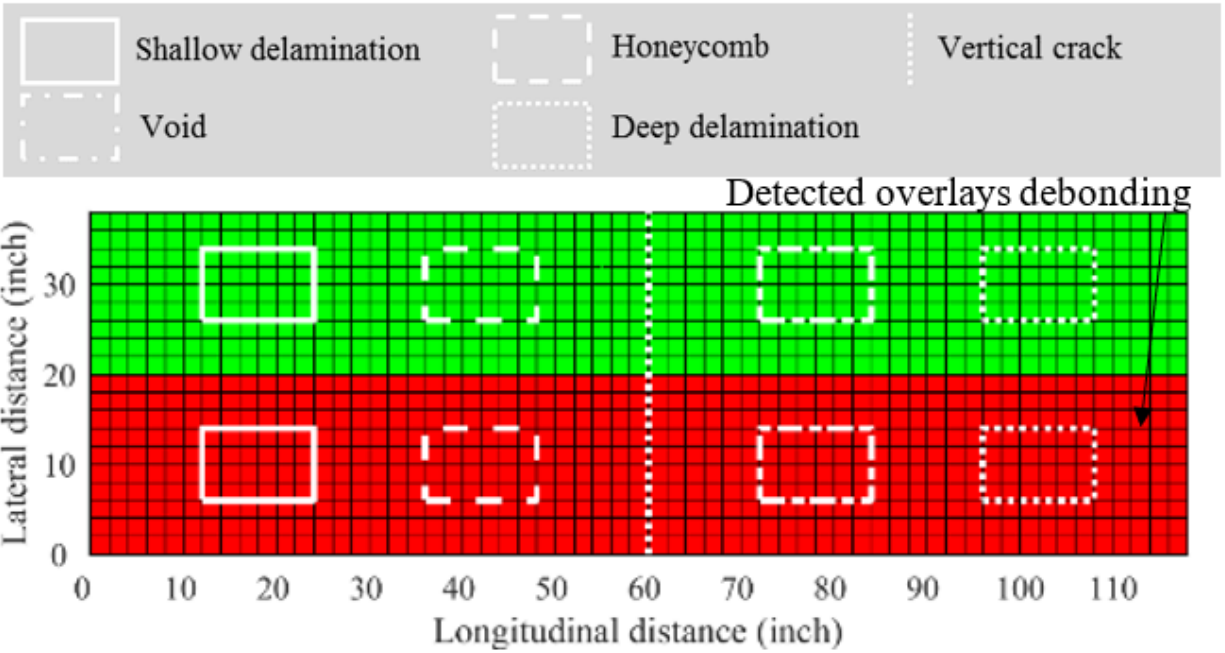
Source: FHWA.

D. S5AL.



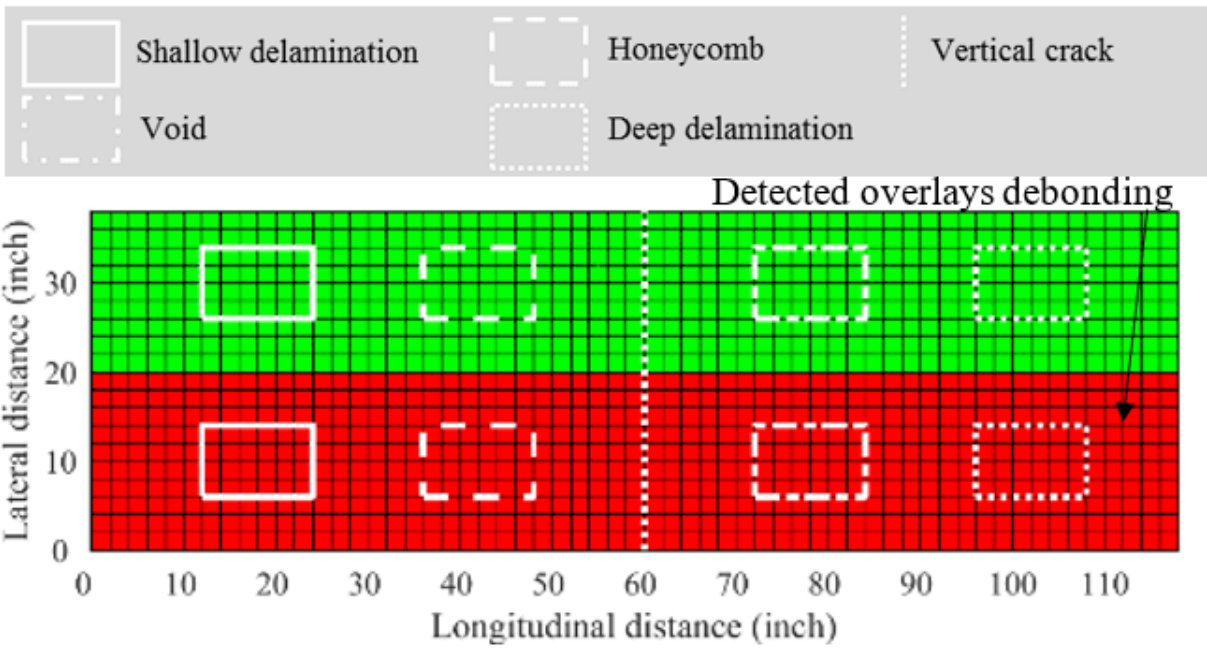
Source: FHWA.

E. S6S.



Source: FHWA.

F. S7A.



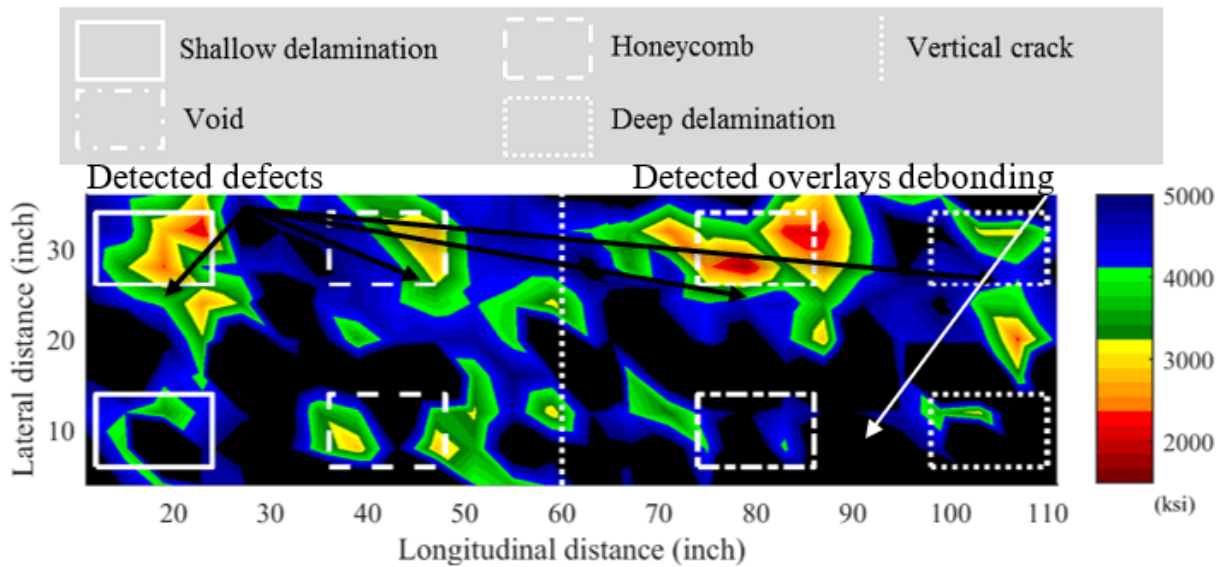
Source: FHWA.

G. S8P.

**Figure 85. Graphs. NDE condition maps from the sounding method.**

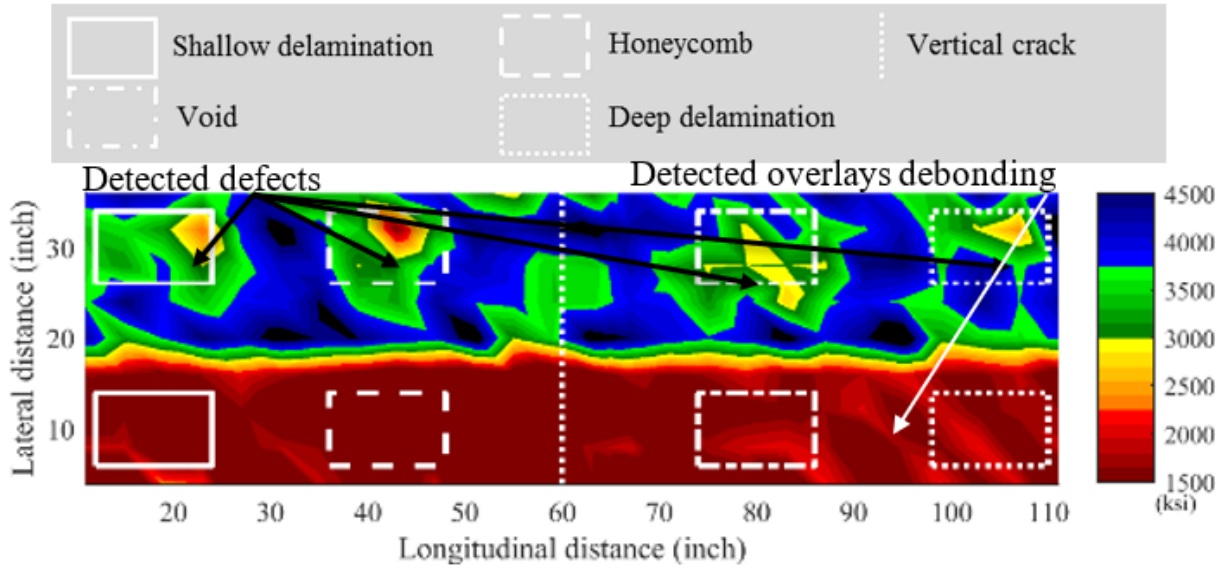
## USW CONDITION MAPS

The condition maps of specimens S1E, S3L, S6S, and S8P based on the USW method are shown in figure 86-A through figure 86-D. For the debonded halves of the specimens, the USW method detected overlay debonding in terms of higher moduli than bonded areas in specimens S1E and S8P and lower moduli than bonded areas in specimens S3L and S6S. Underlying defects could not be detected because the stress waves were trapped in the debonded overlays. For the bonded halves of the specimens, the USW method detected shallow and deep delaminations for specimens S1E, S3L, S6S, and S8P and honeycombing and voids for specimens S1E, S3L, and S8P.



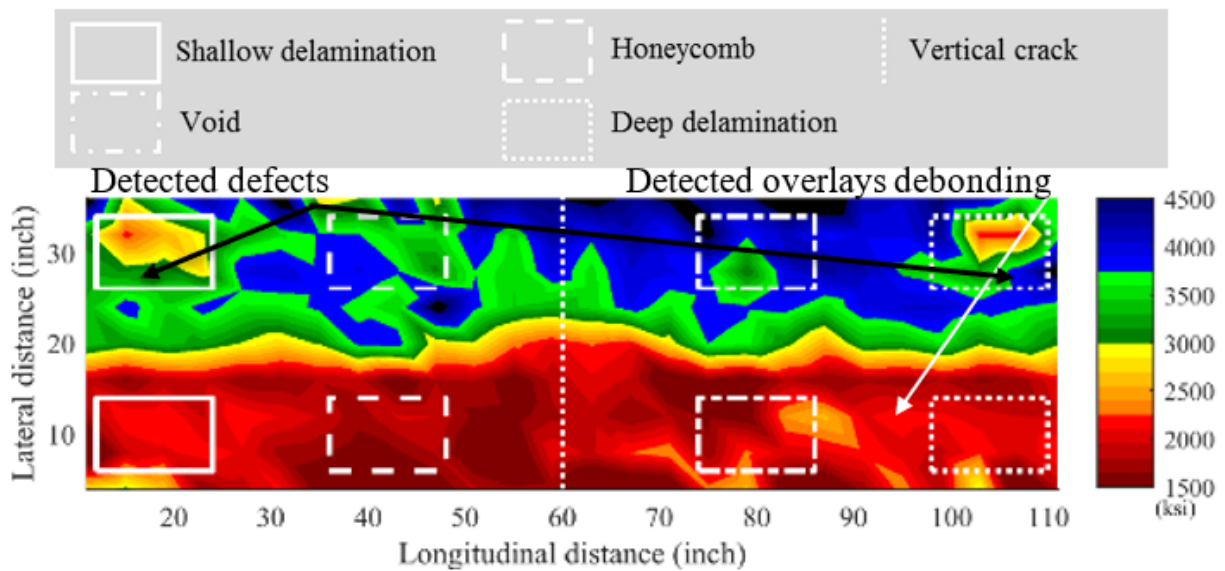
Source: FHWA.

A. S1E.



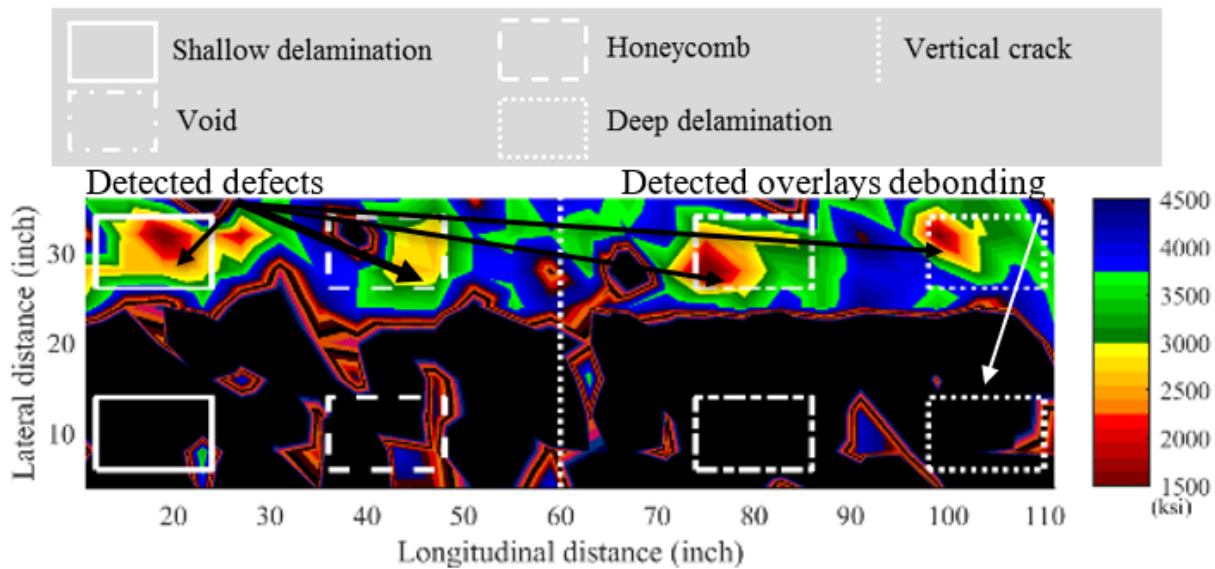
Source: FHWA.

B. S3L.



Source: FHWA.

C. S6S.



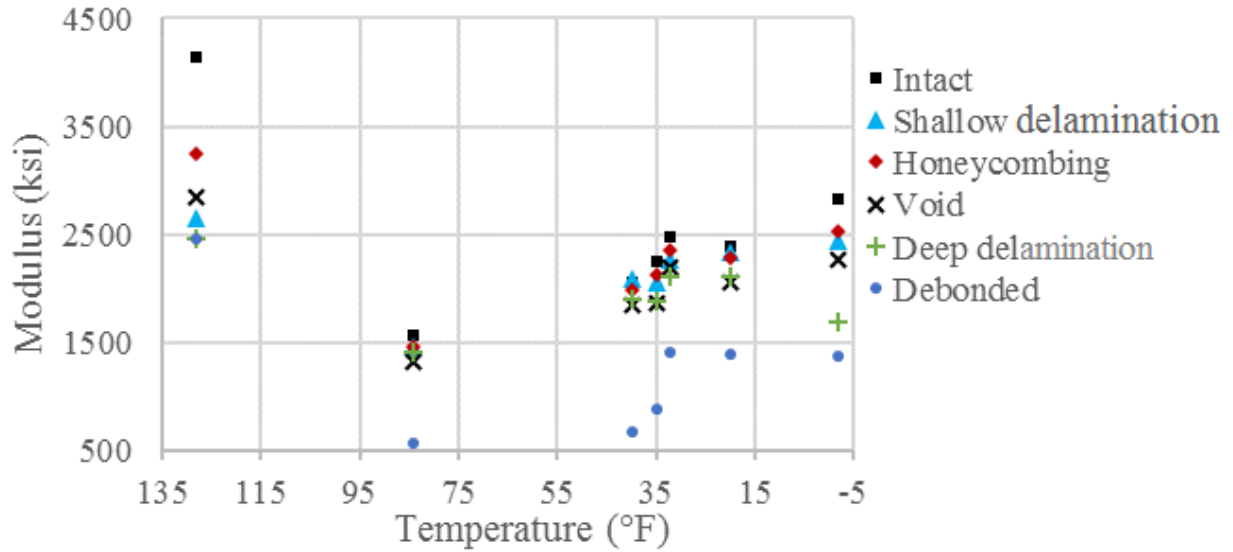
Source: FHWA.

D. S8P.

**Figure 86. Graphs. NDE condition maps of four specimens for the USW method.**

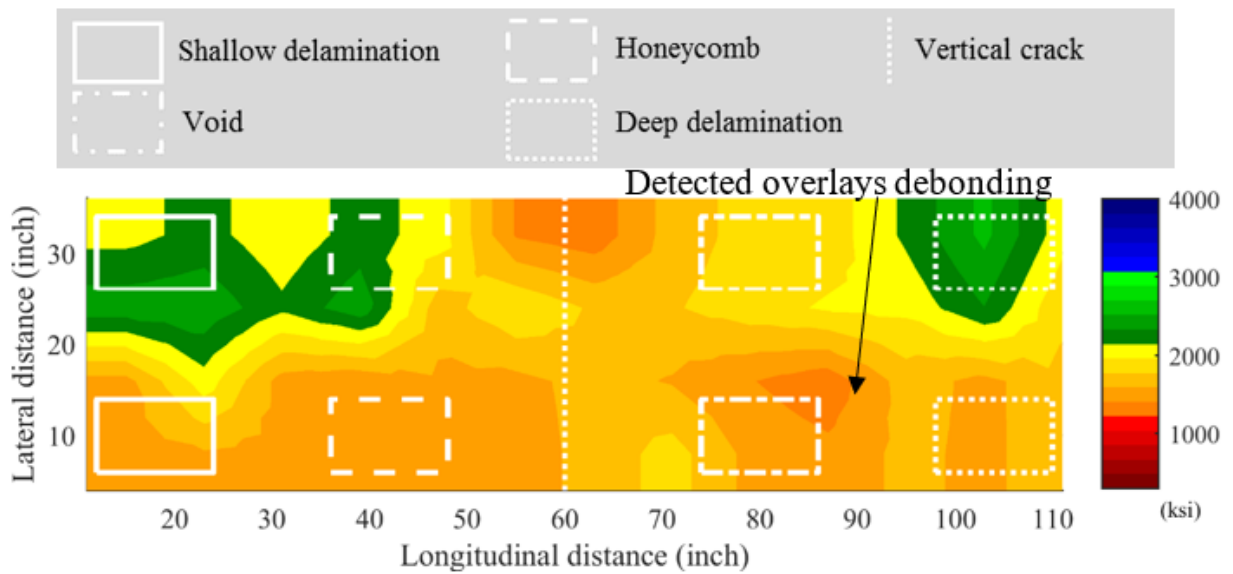
The modulus of asphalt pavement is sensitive to temperature, so specimen S7A was studied to determine the effects of temperature above the intact, shallow delamination, honeycombing, void, deep delamination, and debonded areas.<sup>(52-54)</sup> Tests were conducted at seven temperatures: 128 and 84°F in outdoor conditions, and 40, 35, 32, 20, and -2°F in the temperature chamber. The variation of moduli with temperature is shown in figure 87. The moduli were unreasonably high at 128°F, and as the temperature decreased to 84°F, the tests on top of the debonded overlay showed much lower measurements than those at lower temperatures. The moduli increased as the temperature decreased from 84°F to the lower values in the temperature chamber. The most significant variation was observed from 35 to 32°F for all test locations. The intact area had the highest modulus and the debonded area had the lowest. There were no consistent trends for other defects.

The temperature chamber was set to 32°F for detailed USW scanning of specimens S4AS, S5AL, and S7A with asphalt overlays. The condition maps of specimens S4AS, S5AL, and S7A based on the USW method are shown in figure 88-A through figure 88-C. The USW method distinguished areas with overlay bonding and debonding (i.e., higher modulus versus lower modulus) but could not detect defects in the specimens through the bonded and debonded asphalt overlays. A lower temperature was not beneficial in detecting more defects, and 84°F or below was sufficient to distinguish debonded areas from bonded areas.



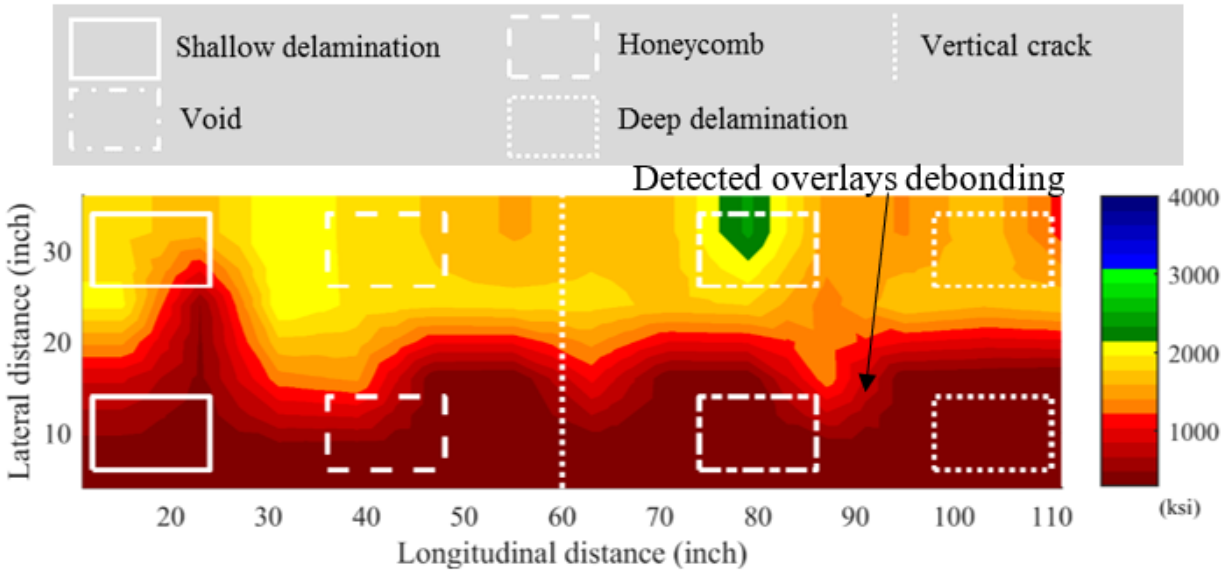
Source: FHWA.

**Figure 87. Graph. Modulus versus temperature with the USW method on specimen S7A.**



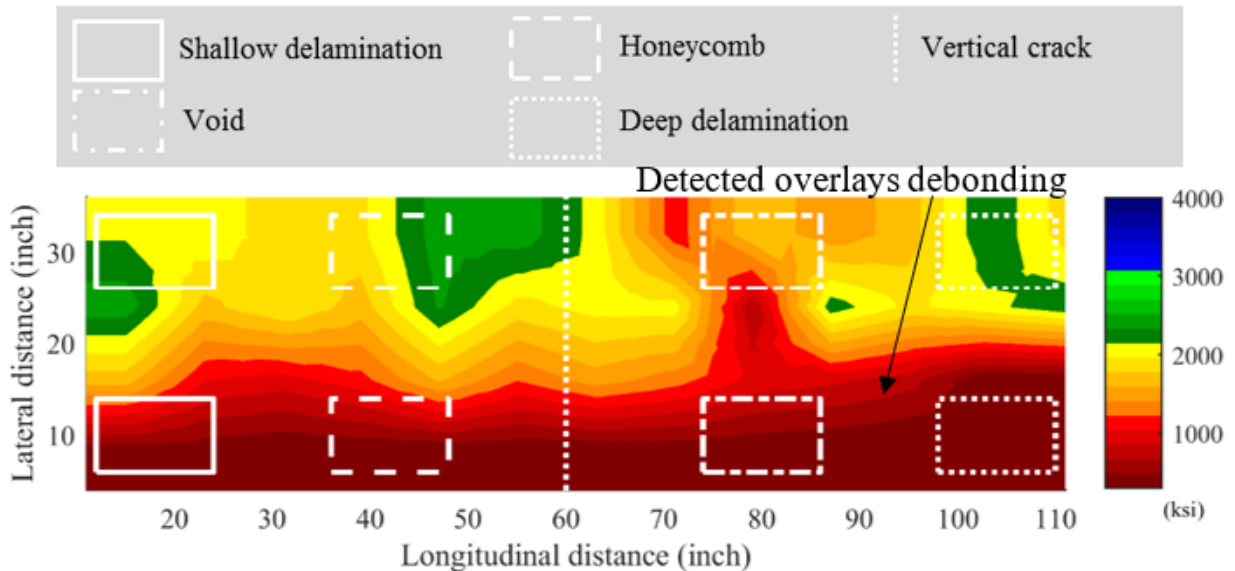
Source: FHWA.

A. S4AS.



Source: FHWA.

B. S5AL.



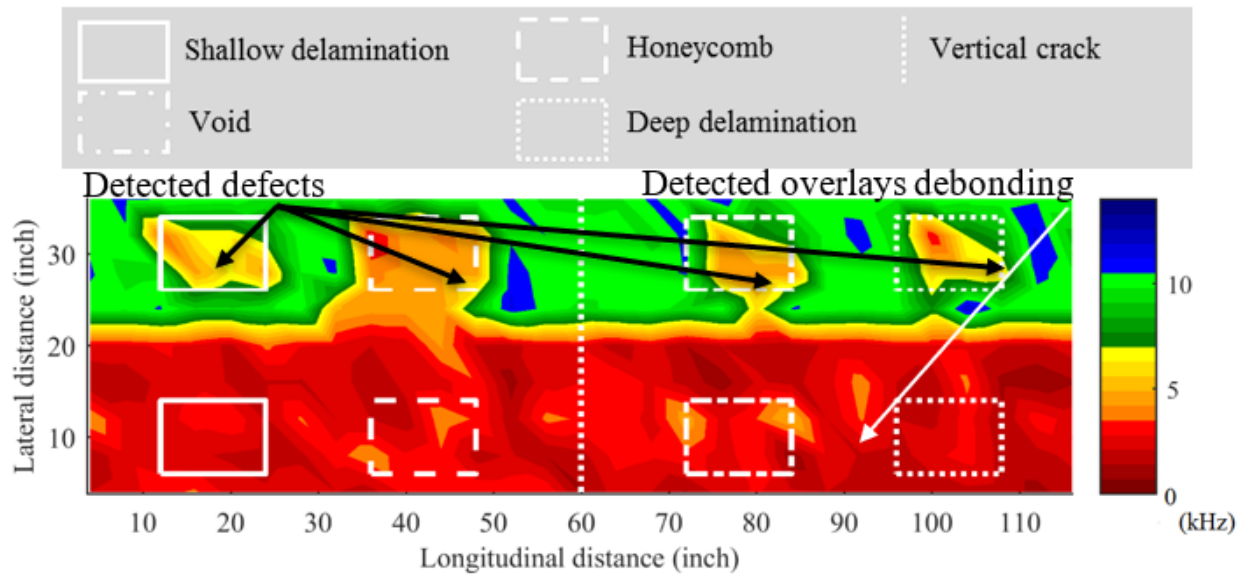
Source: FHWA.

C. S7A.

Figure 88. Graphs. NDE condition maps of three specimens with the USW method.

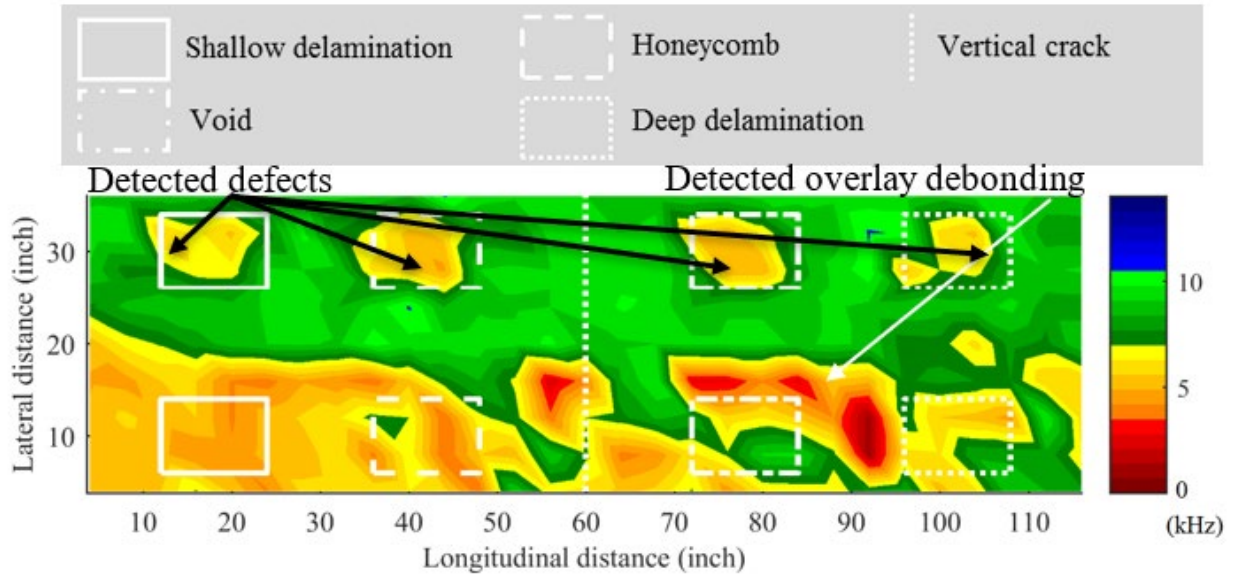
## IE CONDITION MAPS

The condition maps of specimens S1E, S3L, S6S, and S8P based on the IE method are shown in figure 89-A through figure 89-D. For the bonded halves of specimens S1E, S3L, S6S, and S8P, the IE method detected debonding, shallow and deep delaminations, honeycombing, and voids. Areas with detected defects showed lower frequencies than intact areas because the dominant flexural mode with the width-to-depth ratios of the defects was greater than 1.<sup>(47)</sup> Intact areas in the bonded halves had frequencies of the thickness mode of about 10, 9.1, 7.8, and 8.5 kHz for specimens S1E, S3L, S6S, and S8P, respectively. Stress waves for the debonded halves of specimens S1E, S3L, S6S, and S8P were completely reflected at the interface. No underlying defects in the specimens could be detected, but overlay debonding was detected.



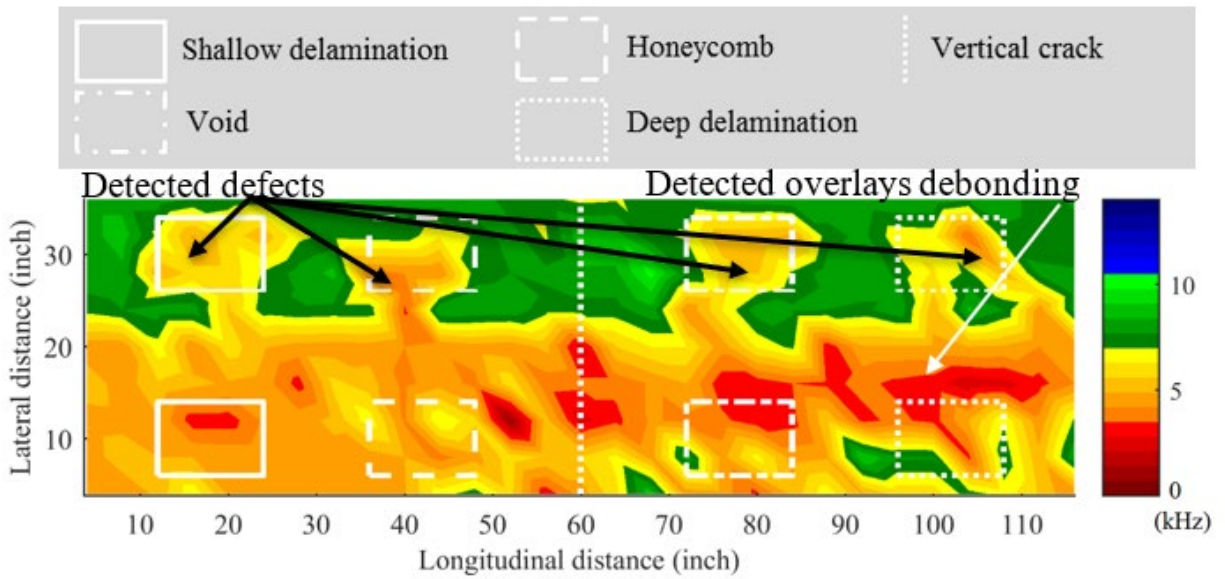
Source: FHWA.

A. S1E.



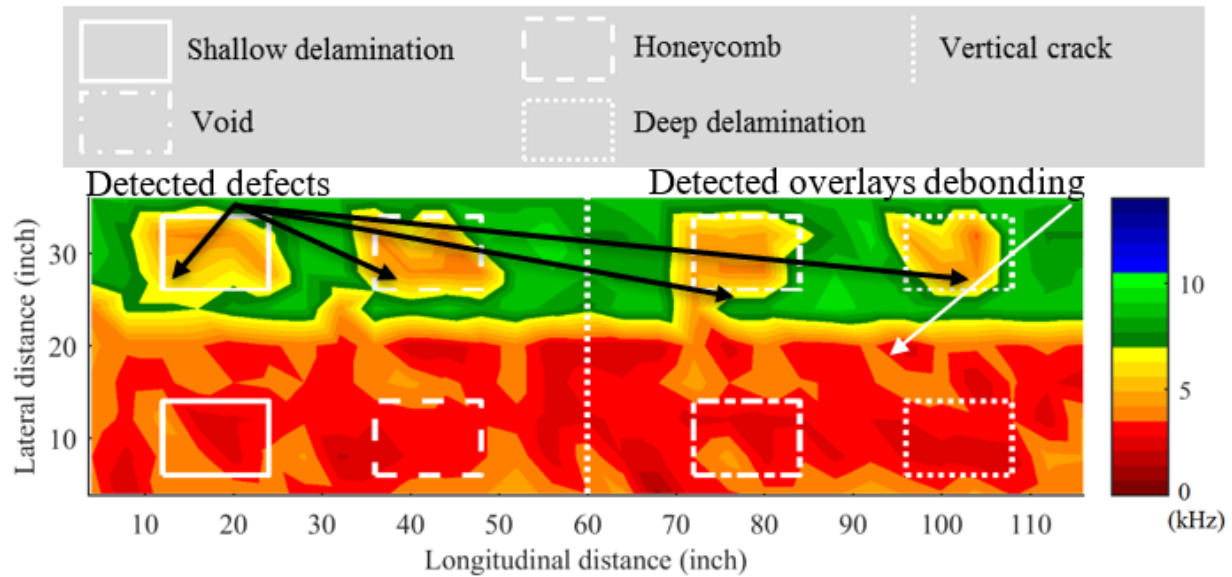
Source: FHWA.

B. S3L.



Source: FHWA.

C. S6S.



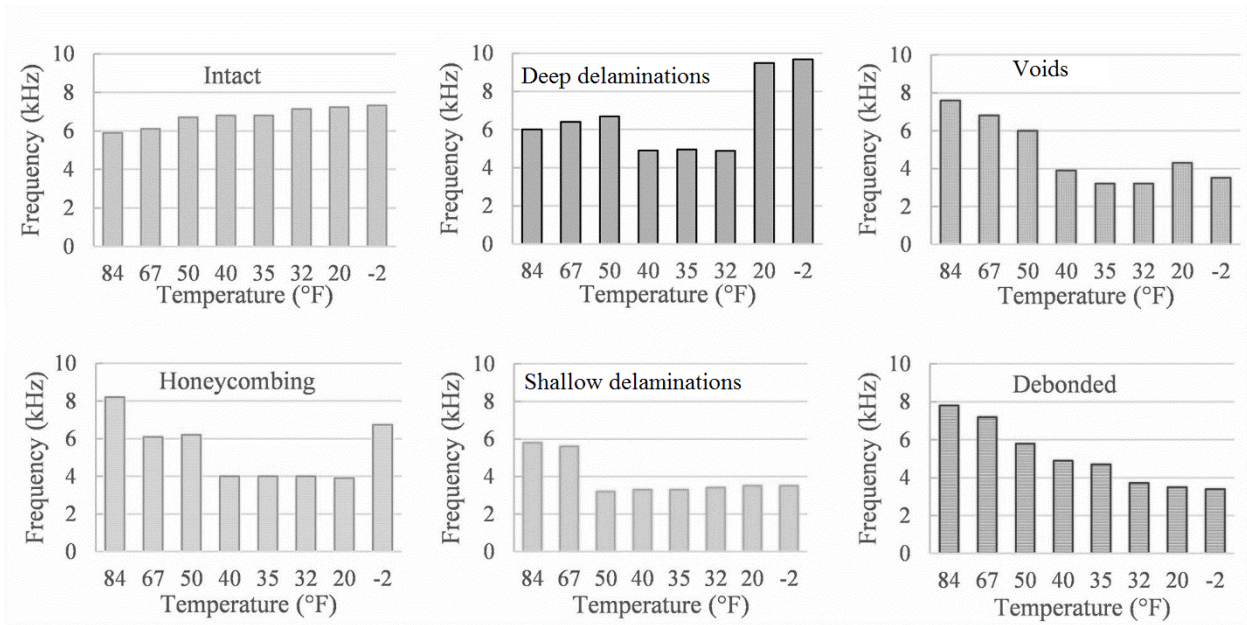
Source: FHWA.

D. S8P.

**Figure 89. Graphs. NDE condition maps of four specimens with the IE method.**

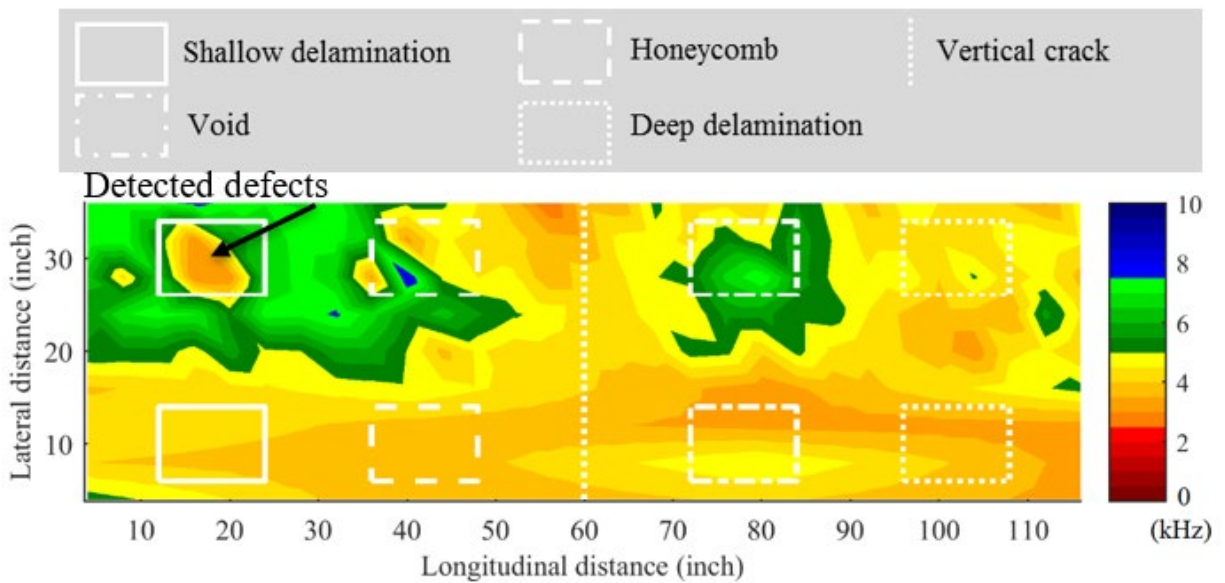
When the IE method is used on asphalt pavements, it should be in cold weather (i.e., 32°F or below).<sup>(54)</sup> To ascertain the temperature threshold, specimen S7A was tested at different temperatures above the intact, shallow delamination, honeycombing, void, deep delamination, and debonding areas. Tests were conducted at eight temperatures in the temperature chamber: 84, 67, 50, 40, 35, 32, 20, and -2°F. The variation of dominant frequency with temperature is shown in figure 90. As the temperature decreased from 84 to -2°F, the dominant frequencies stabilized at 32°F and below. At 32°F and below, both the intact and deep delamination areas showed the frequencies of the thickness mode, and areas with other defects showed the frequencies of the flexural mode. Honeycombing areas showed the frequency of the thickness mode at -2°F.

Based on the findings in figure 90, 32°F or below was sufficient for the IE method to clearly show defects using the dominant frequencies. Thus, the chamber temperature was set to 32°F for detailed IE scanning of specimens S4AS, S5AL, and S7A with asphalt overlays. The condition maps of specimens S4AS, S5AL, and S7A based on the dominant frequencies measured by the IE method are shown in figure 91-A through figure 91-C. The IE method detected shallow delamination and debonding in specimens S4AS and S5AL but could not detect deep delaminations, honeycombing, and voids in the bonded halves of specimens S4AS and S5AL because the waterproof membranes significantly reduced the propagation of waves into the underlying specimens. The IE method detected debonding, shallow and deep delaminations, honeycombing, and voids in specimen S7A because sufficient waves propagated into the underlying specimen without a waterproof membrane underneath the asphalt overlay.



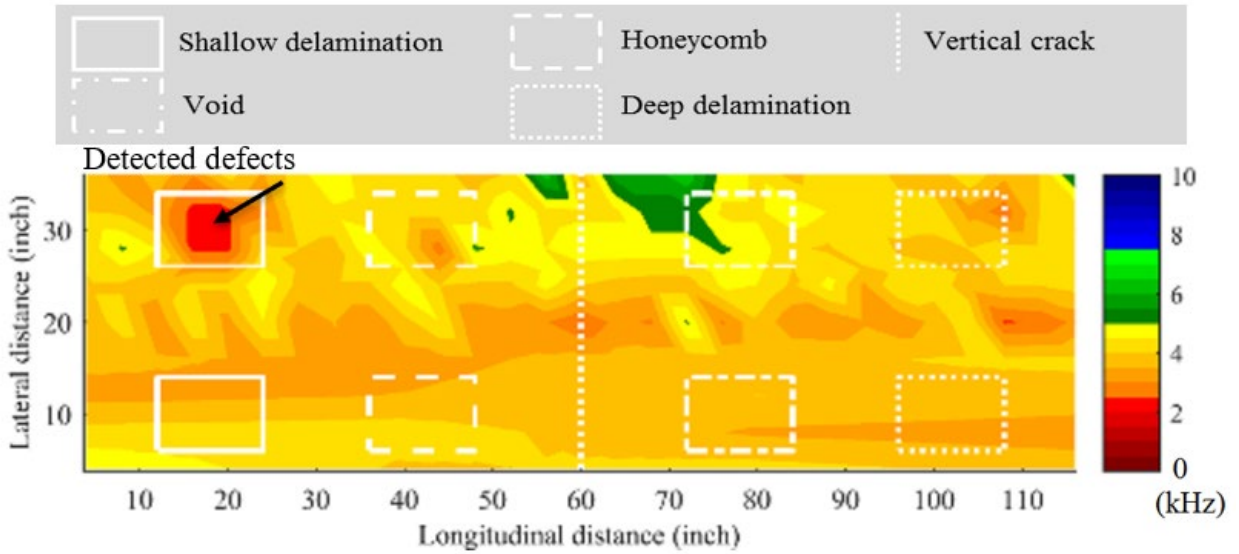
Source: FHWA.

**Figure 90. Graphs. Dominant frequency versus temperature using the IE method on specimen S7A.**



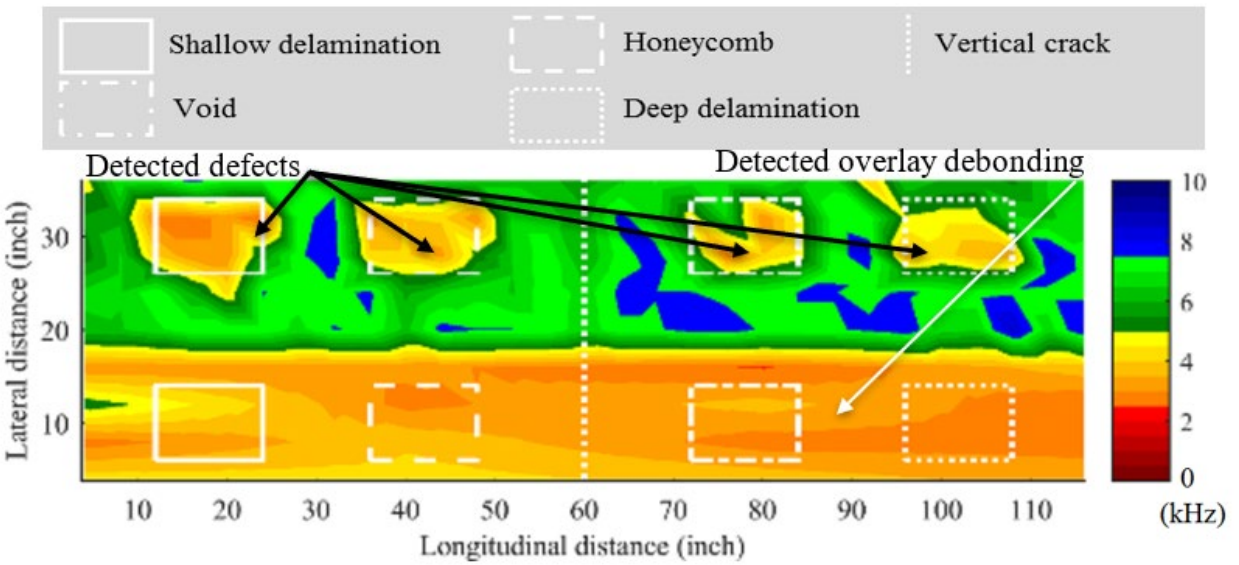
Source: FHWA.

A. S4AS.



Source: FHWA.

B. S5AL.



Source: FHWA.

C. S7A.

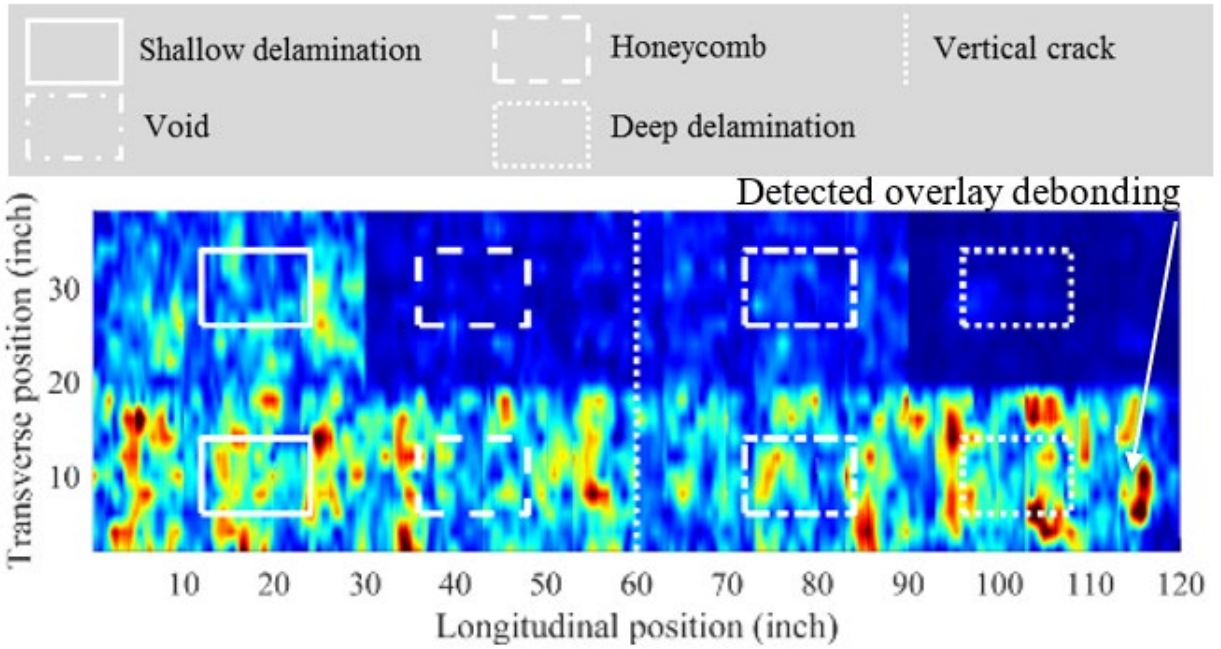
**Figure 91. Graphs. NDE condition maps of three specimens with the IE method.**

## UT C- AND B-SCANS

C-scans with UT-MIRA, B-scans in bonded and debonded areas with UT-MIRA, C-scans with EyeCon, and B-scans in bonded and debonded areas with UT-EyeCon are shown in figure 92 through figure 97, respectively. Specimens S1E, S3L, S6S, and S8P were scanned using the UT method.

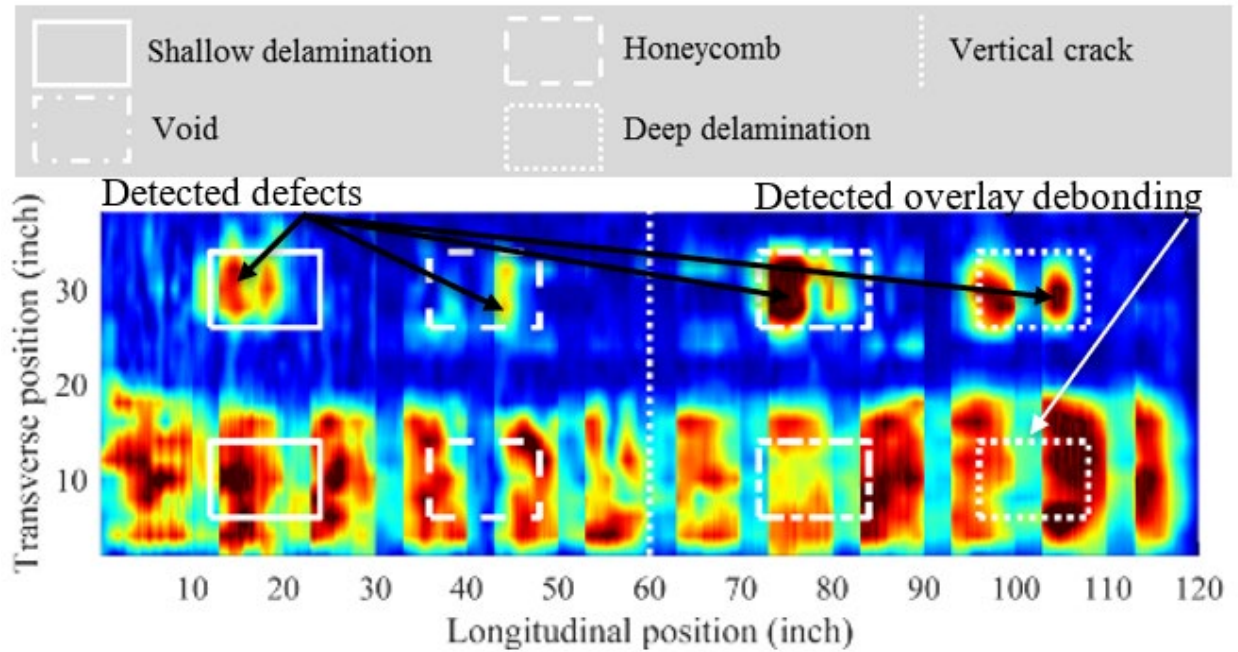
For the bonded areas of specimens S1E, S3L, S6S, and S8P, the UT method could not detect any defects in specimen S1E, but detected shallow and deep delaminations, honeycombing, and voids in specimen S3L, and shallow and deep delaminations and voids in specimens S6S and S8P. The latex and silica fume-modified concrete overlays for specimens S3L and S6S were more homogeneous and had properties closer to the underlying specimens than did the epoxy and polyester polymer overlays for specimens S1E and S8P. More waves propagated into the underlying specimens, and more defects were detected in the bonded halves of specimens S3L and S6S. The polyester polymer overlay in specimen S8P was homogeneous but less so than the latex and silica fume-modified concrete overlays in specimens S3L and S6S. As such, images of defects in specimen S8P were not as clear as those in specimens S3L and S6S.

The epoxy overlay in specimen S1E was not homogeneous because it consisted of two separate layers of epoxy and two separate layers of aggregate, which created sizeable air gaps among the aggregate. The aggregate and air gaps scattered USWs and they could not reach the defects in the bonded halves of specimen S1E. The UT method could not detect defects in the underlying specimen. For the debonded halves of specimens S1E, S3L, S6S, and S8P, USWs were completely reflected at the interface. No underlying defects in the specimens were detected, as shown in figure 94 and figure 97, but debonding was detected, as shown in figure 92, figure 94, figure 95, and figure 97.



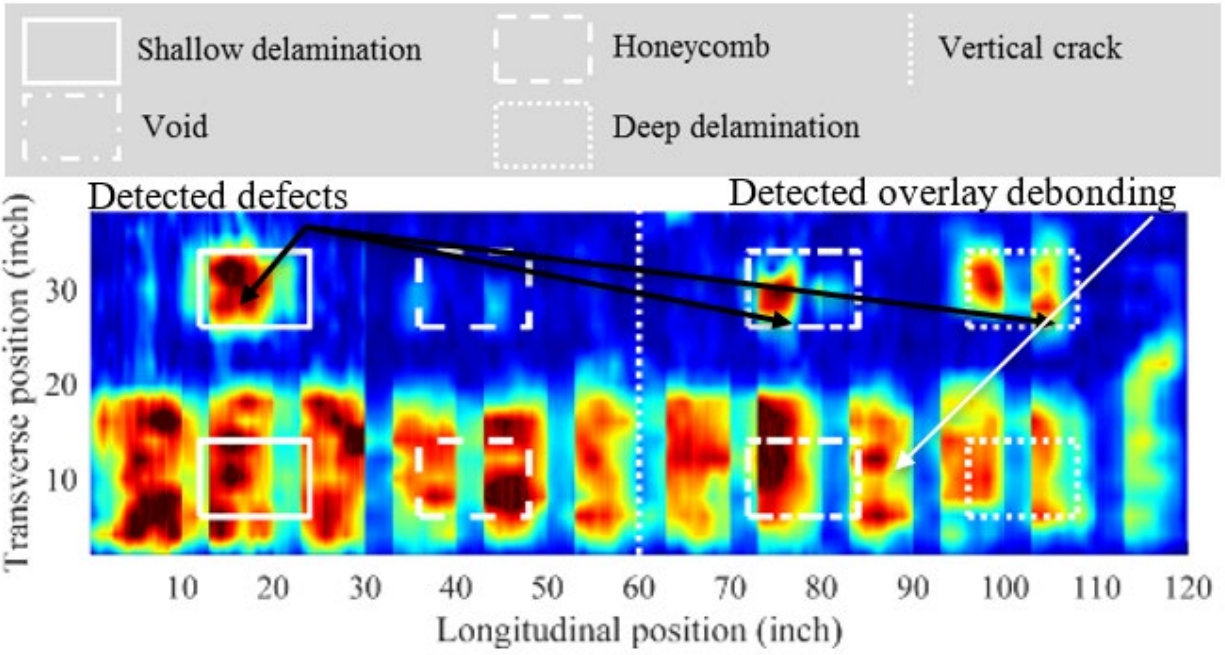
Source: FHWA.

A. S1E.



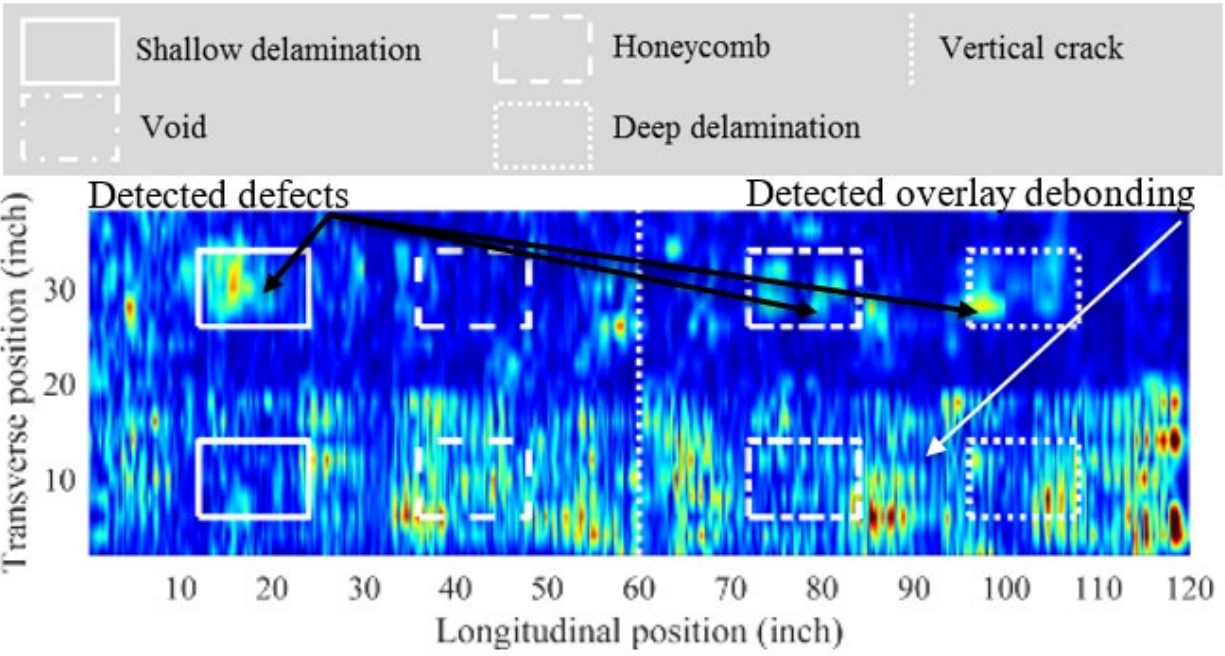
Source: FHWA.

B. S3L.



Source: FHWA.

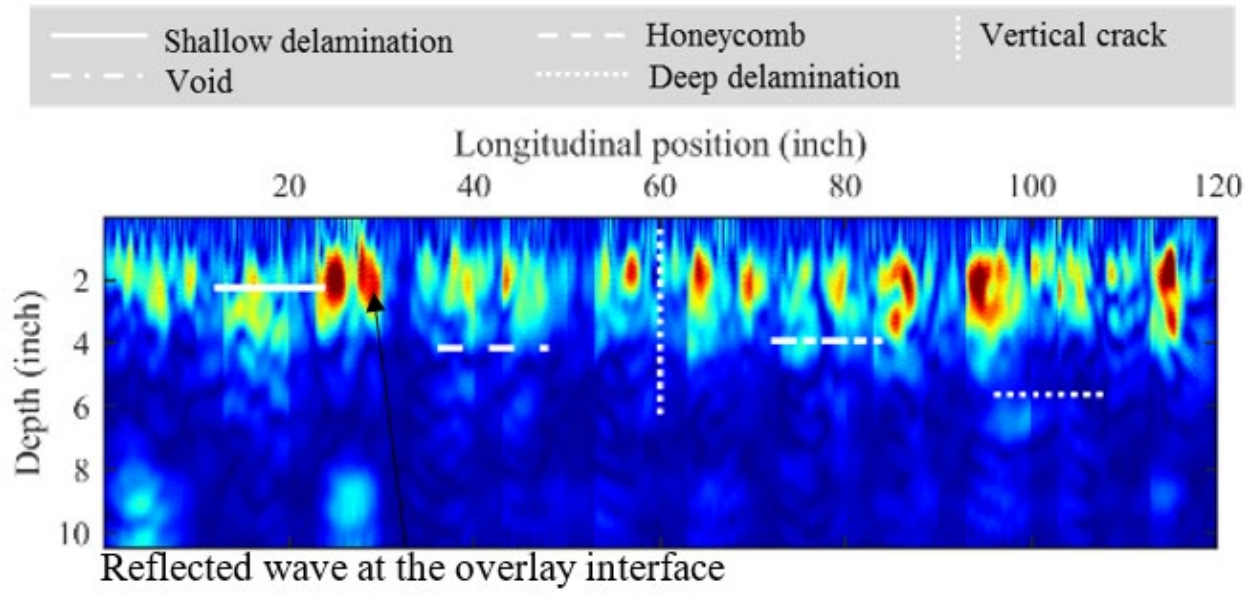
C. S6S.



Source: FHWA.

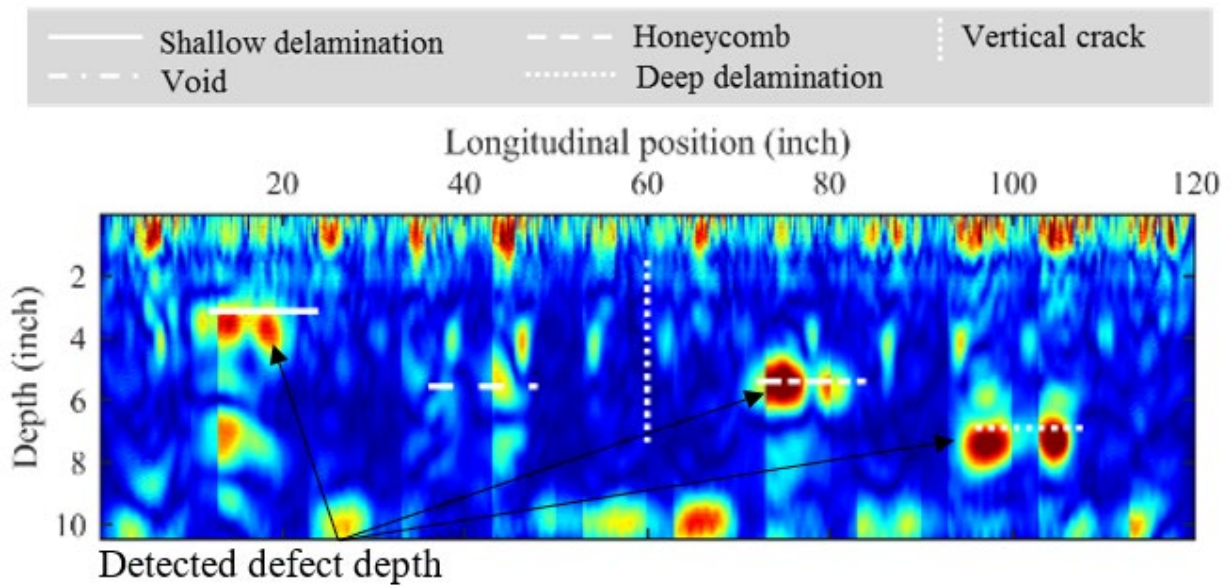
D. S8P.

Figure 92. Graphs. NDE C-scans four specimens with UT-MIRA.



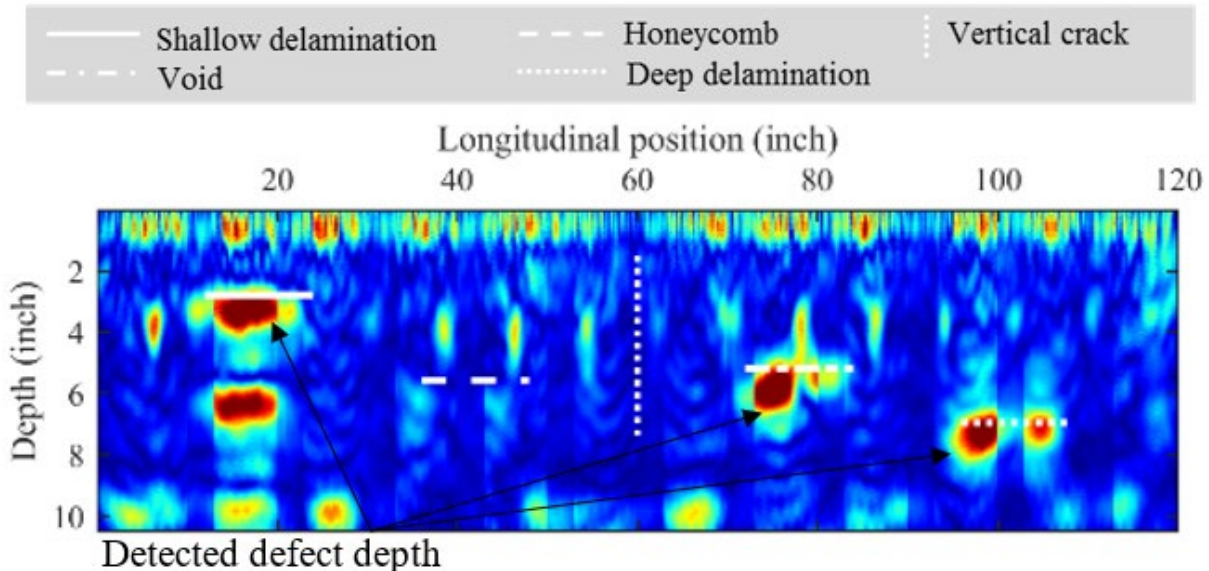
Source: FHWA.

A. S1E.



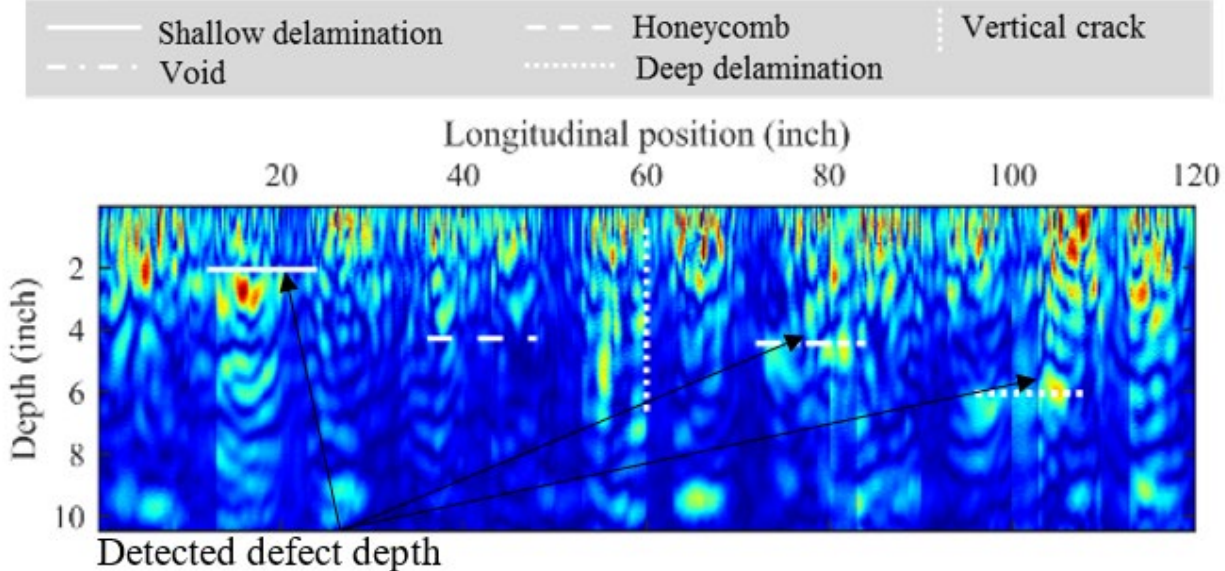
Source: FHWA.

B. S3L.



Source: FHWA.

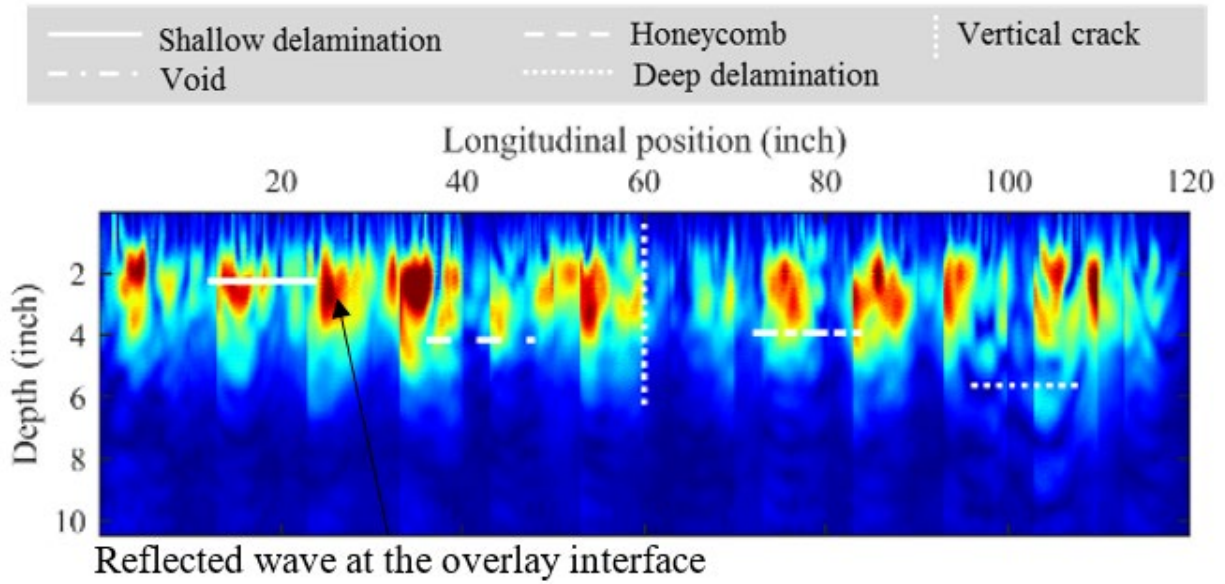
C. S6S.



Source: FHWA.

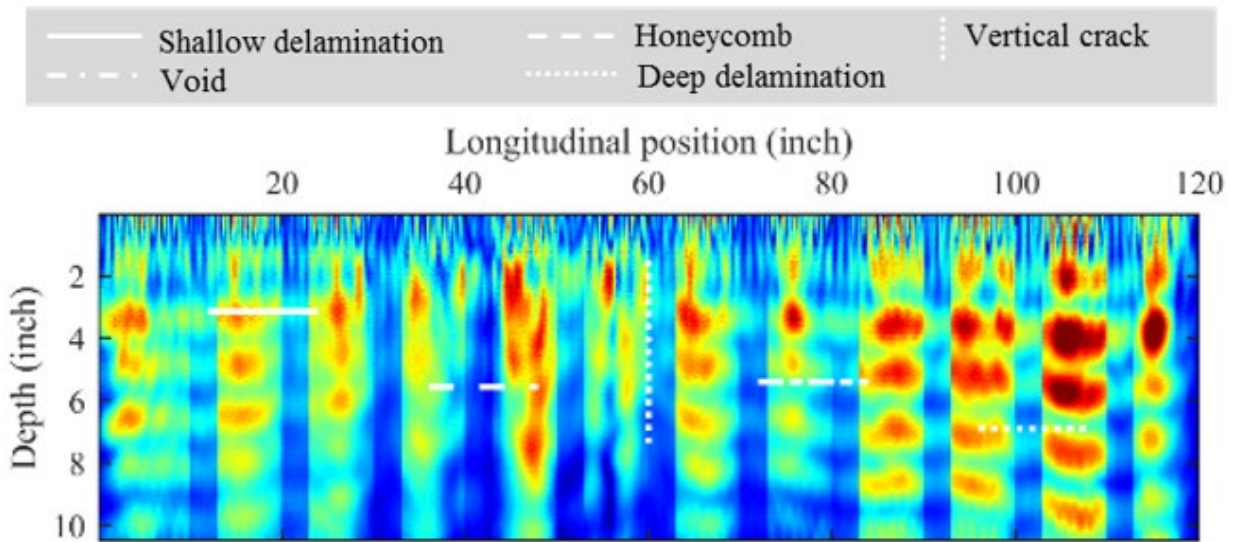
D. S8P.

Figure 93. Graphs. NDE B-scans in bonded area of four specimens with UT-MIRA.



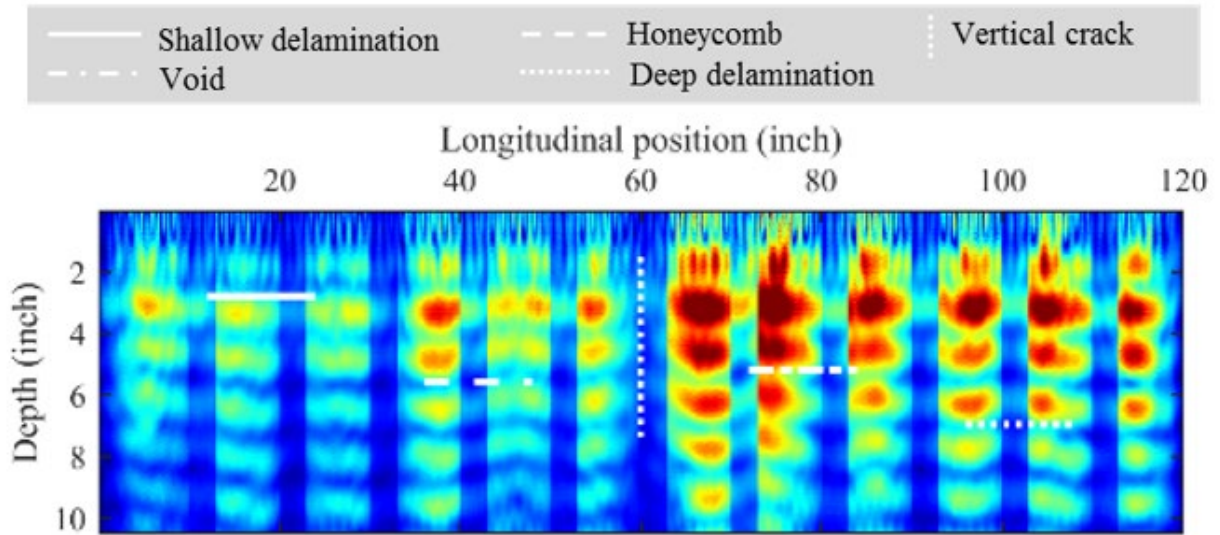
Source: FHWA.  
 Note: No defects detected.

A. S1E.



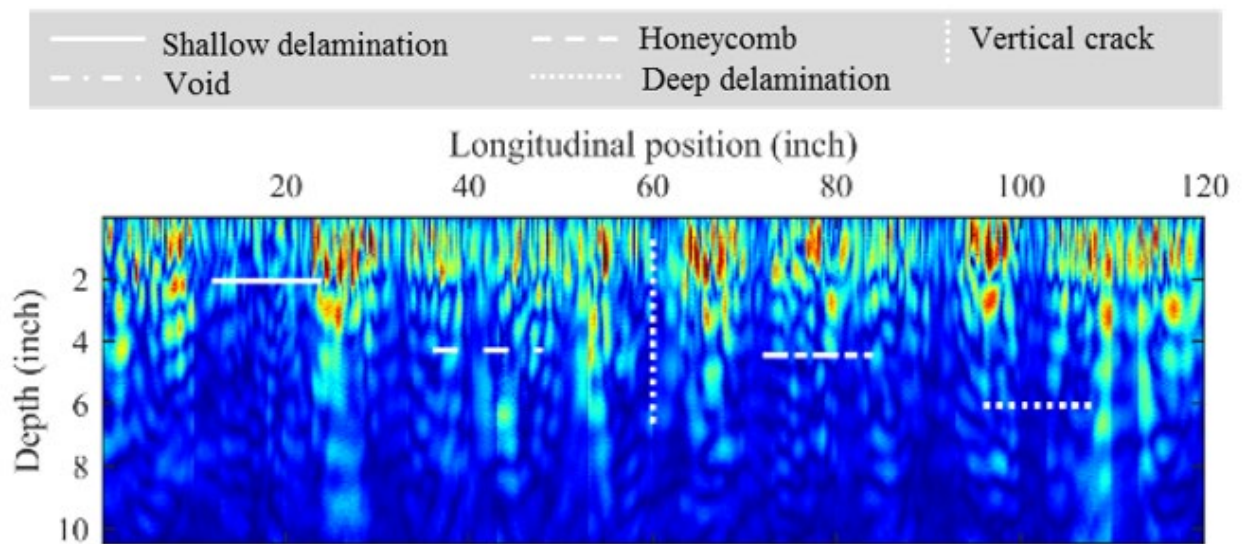
Source: FHWA.  
 Note: No defects detected.

B. S3L.



Source: FHWA.  
 Note: No defects detected.

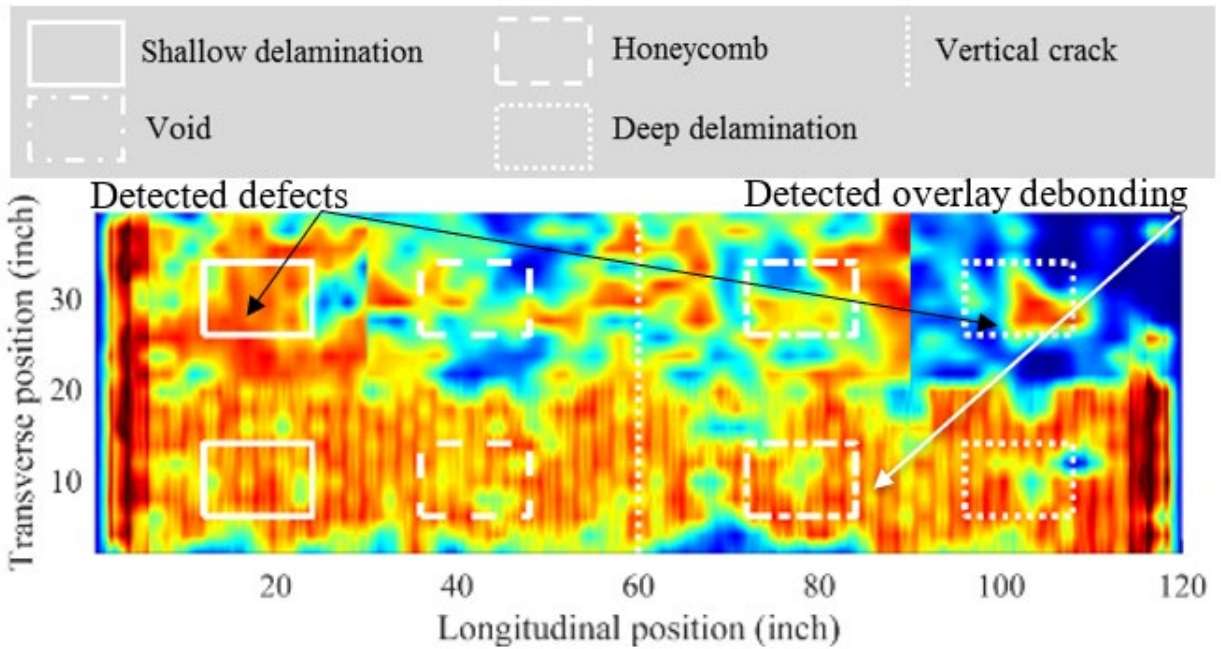
C. S6L.



Source: FHWA.  
 Note: No defects detected.

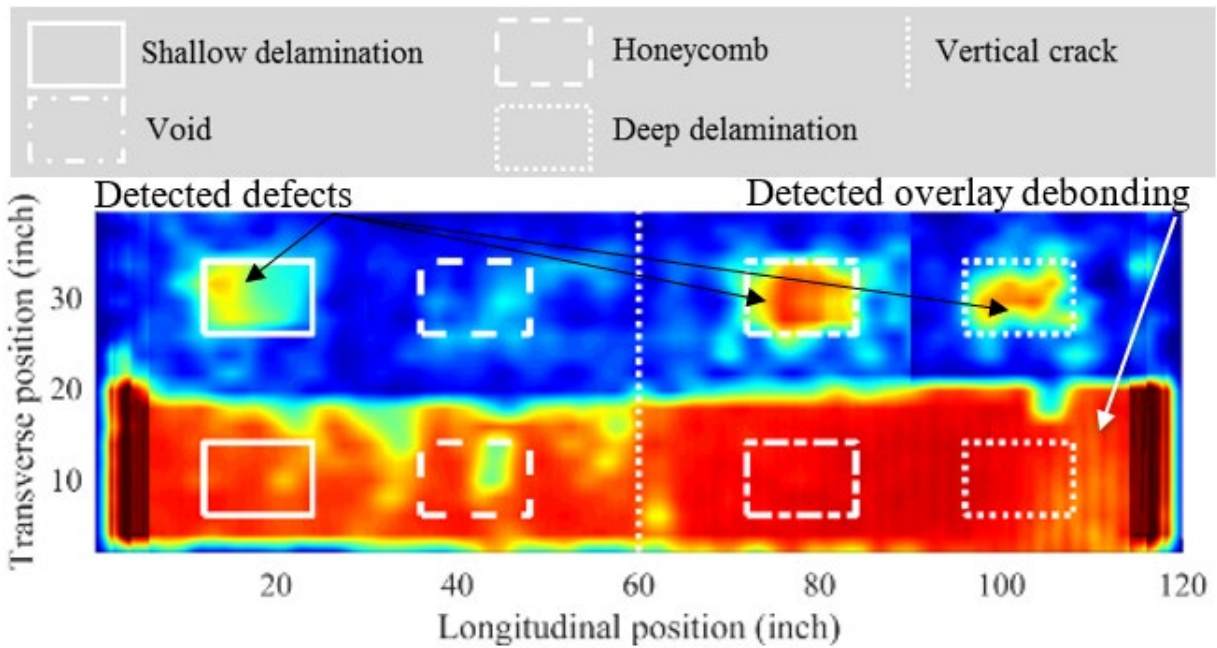
D. S8P.

**Figure 94. Graphs. NDE B-scans in debonded area of four specimens with UT-MIRA.**



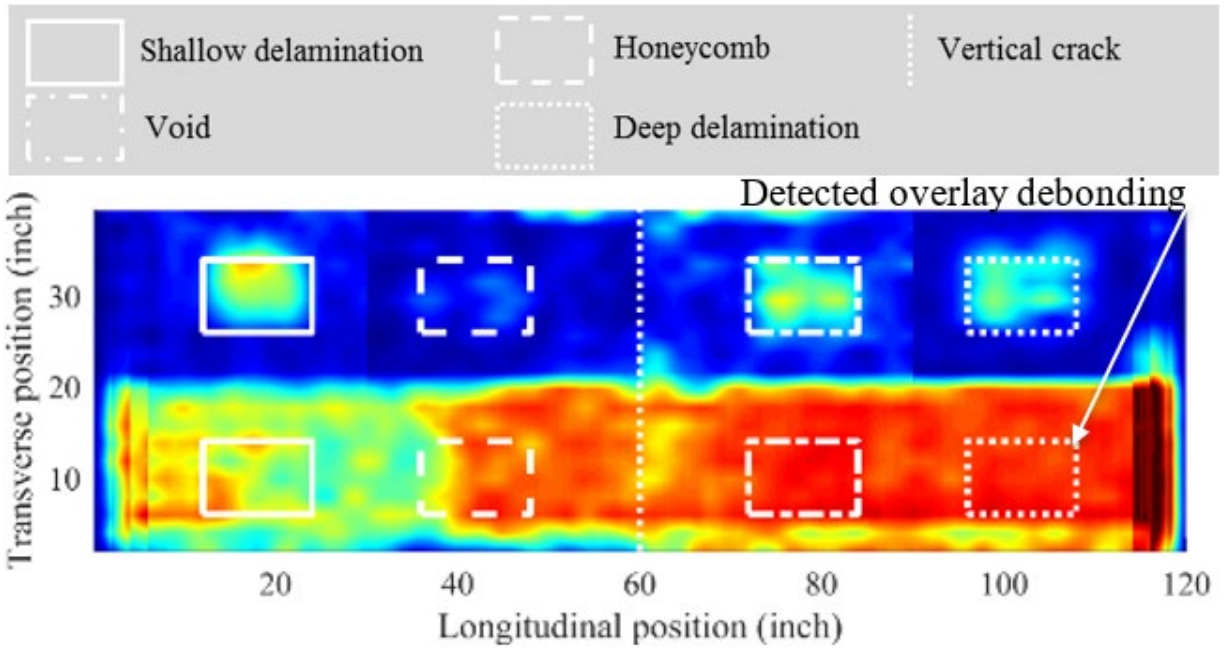
Source: FHWA.

A. S1E.



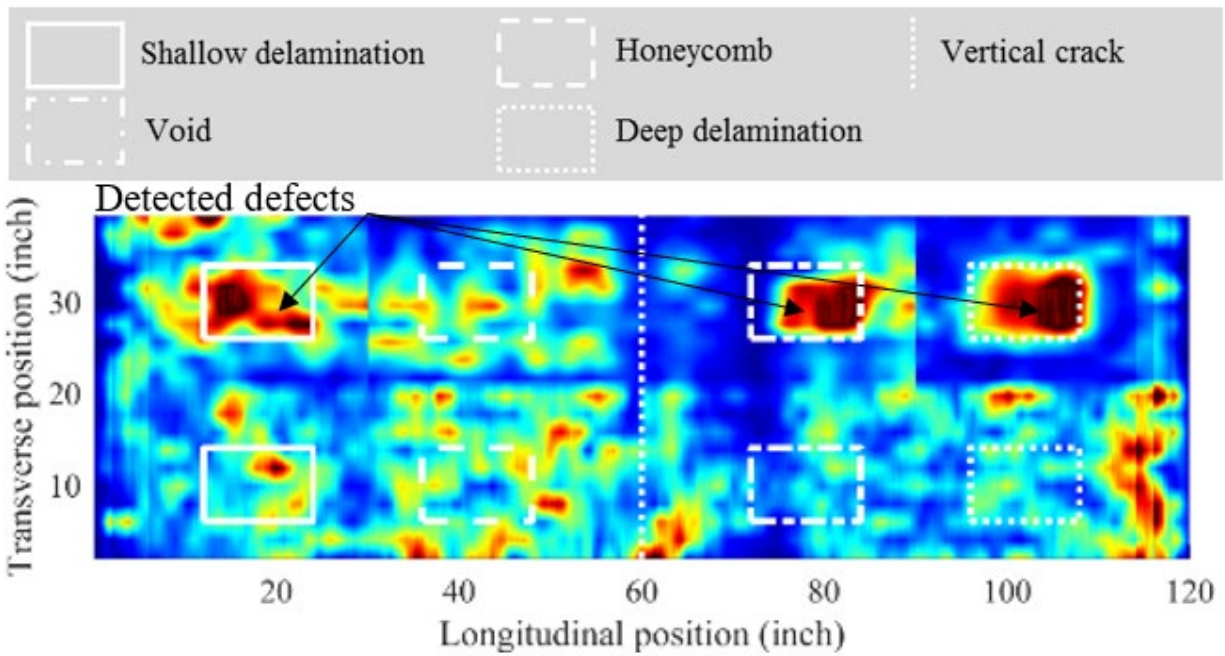
Source: FHWA.

B. S3L.



Source: FHWA.

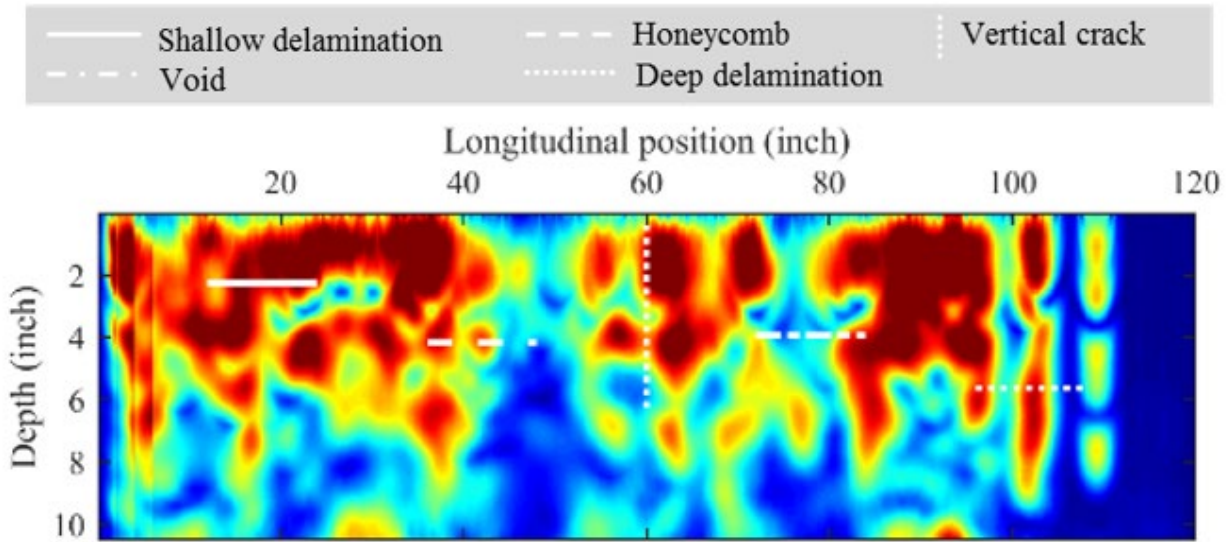
C. S6S.



Source: FHWA.

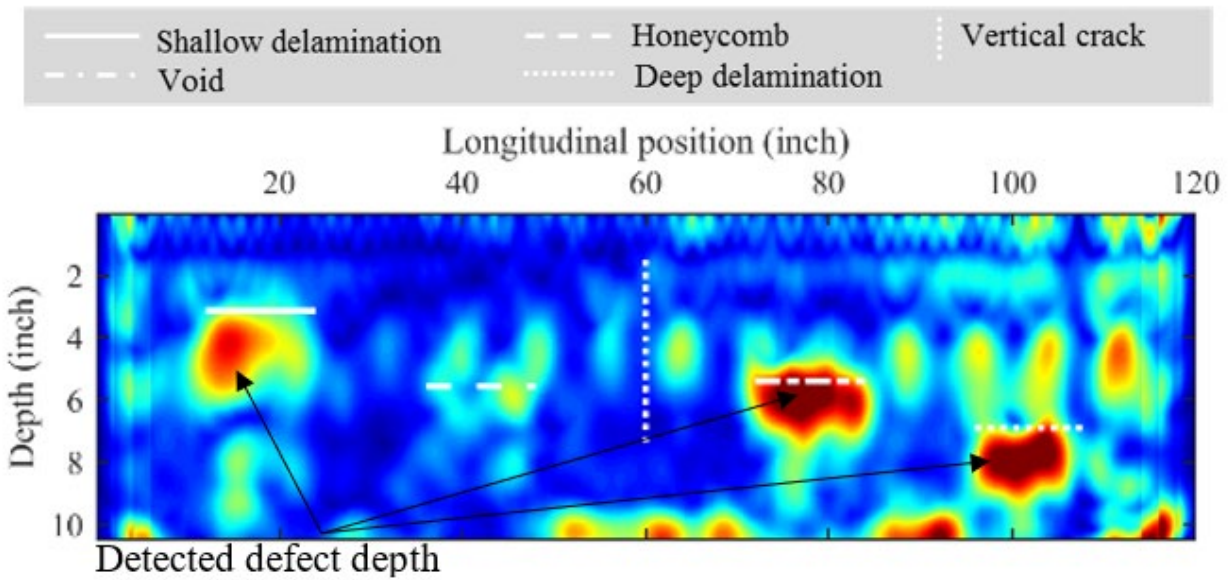
D. S8P.

**Figure 95. Graphs. NDE C-scans of four specimens with UT-EyeCon.**



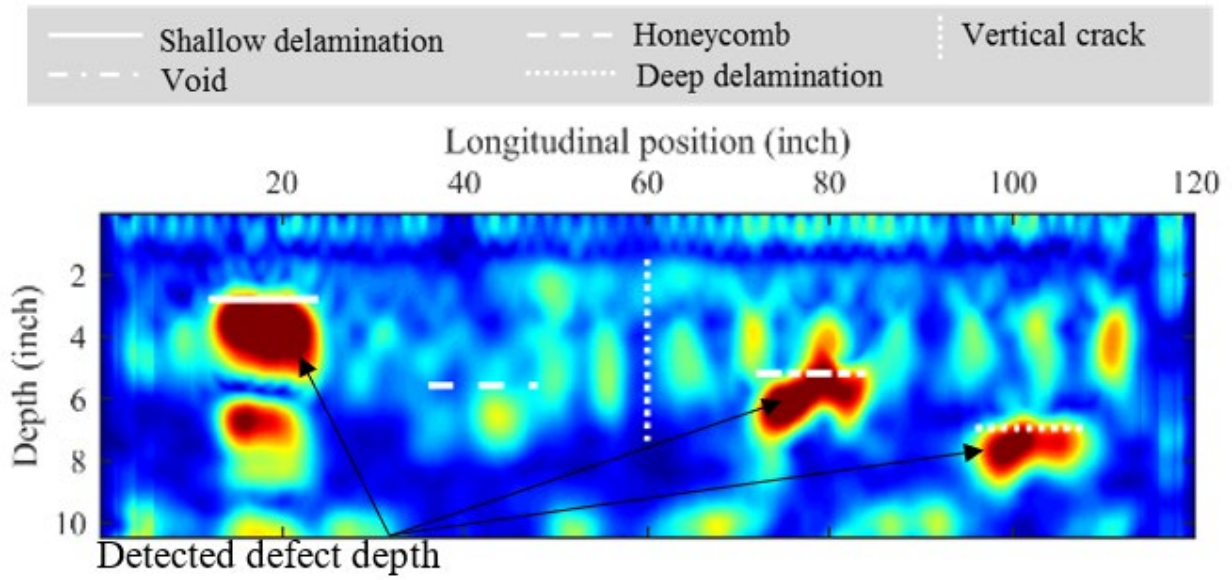
Source: FHWA.  
 Note: No defects detected.

A. S1E.



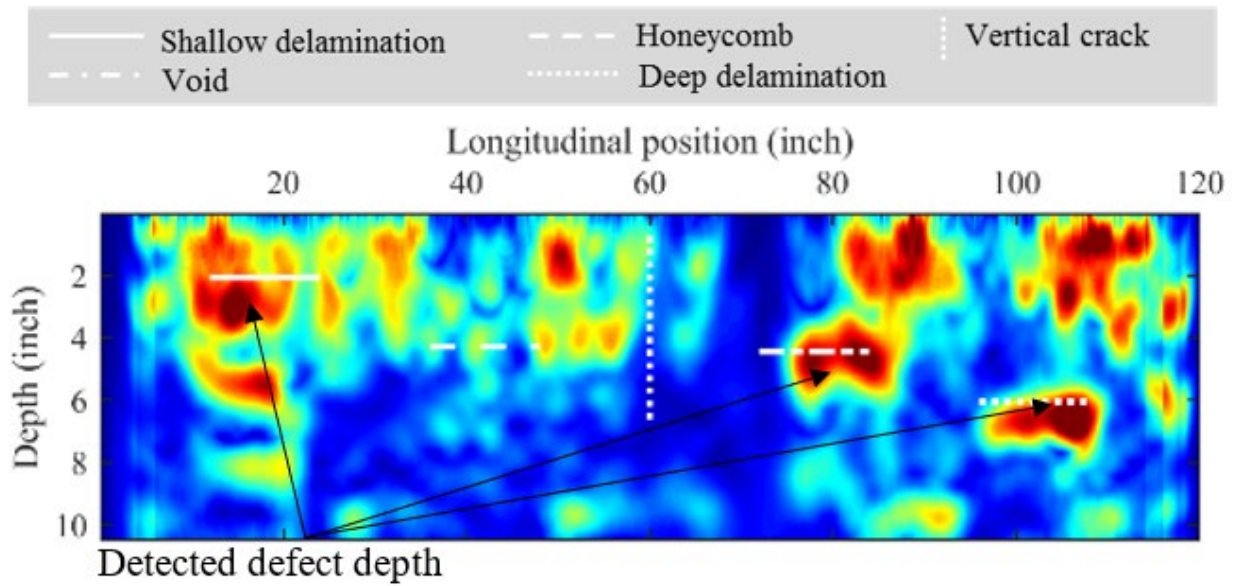
Source: FHWA.

B. S3L.



Source: FHWA.

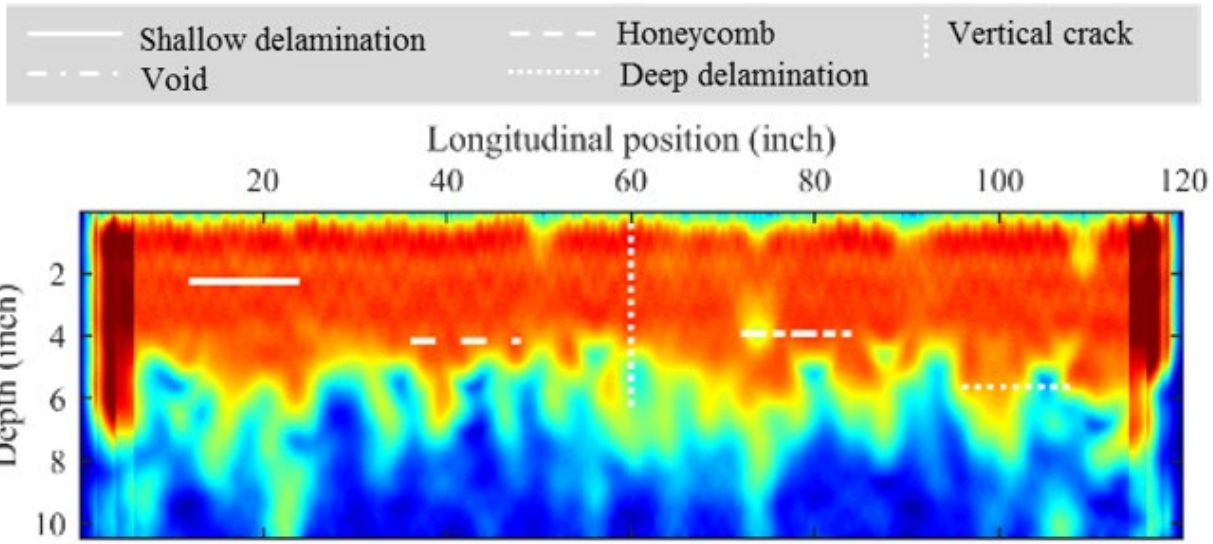
C. S6S.



Source: FHWA.

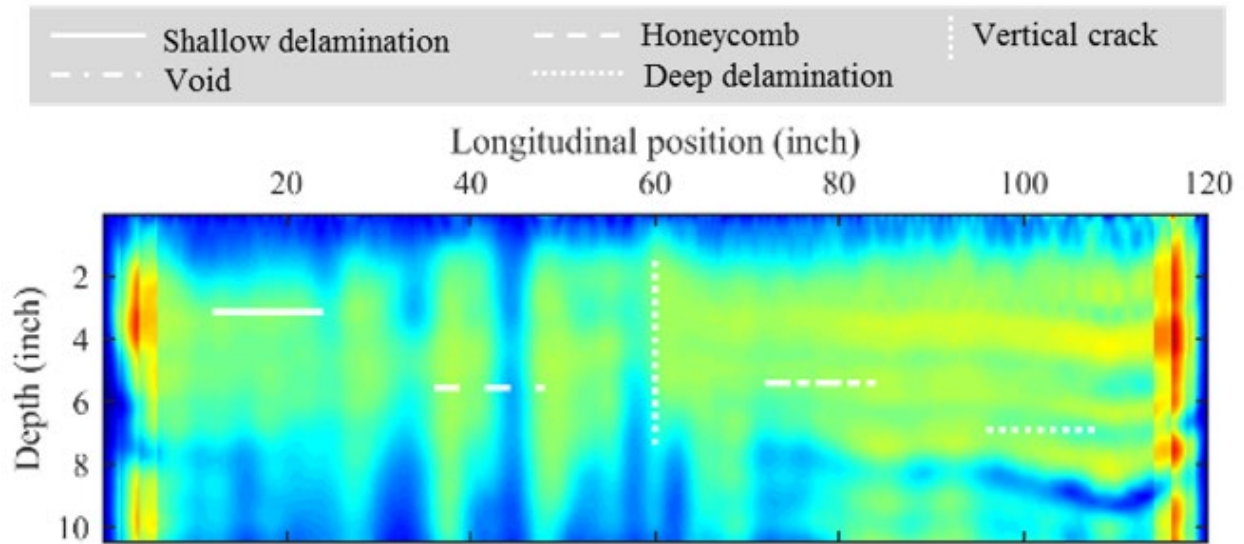
D. S8P.

Figure 96. Graphs. NDE B-scans in bonded area of four specimens with UT-EyeCon.



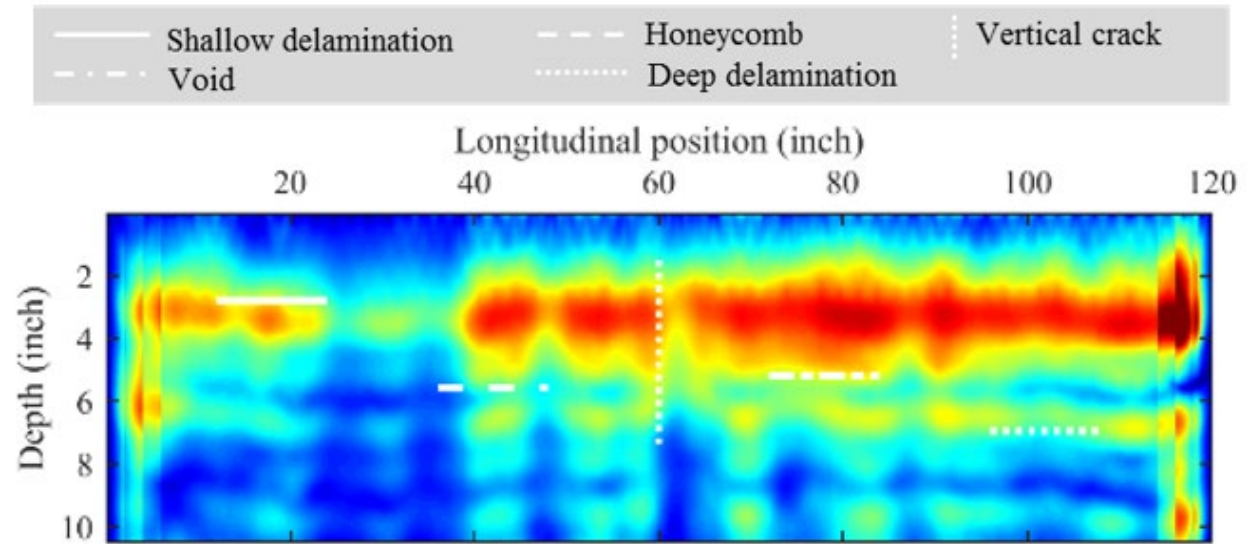
Source: FHWA.  
 Note: No defects detected.

A. S1E.



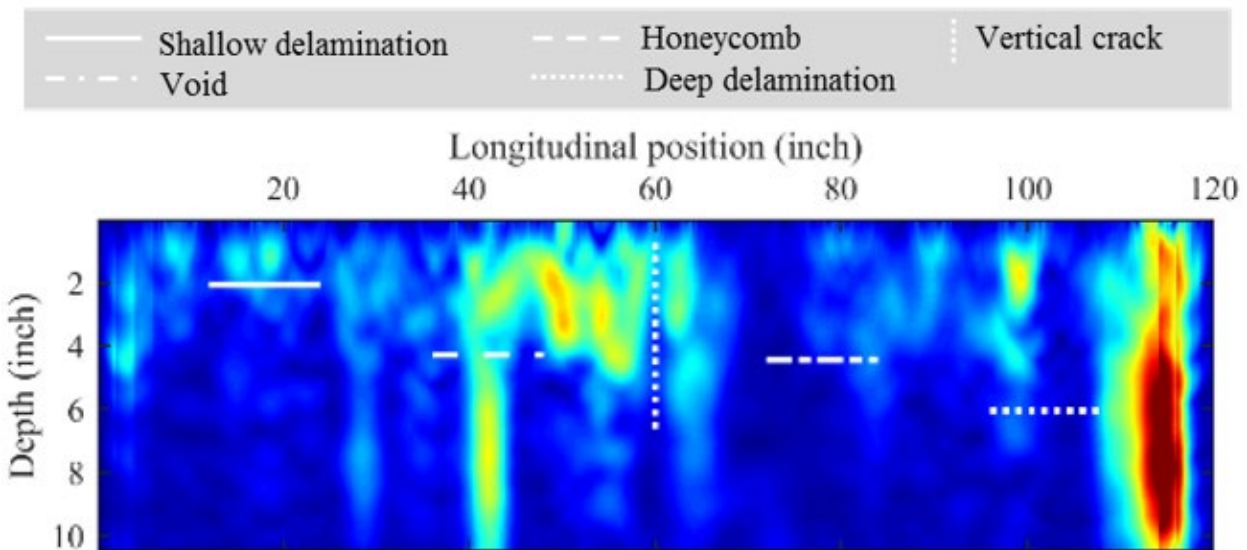
Source: FHWA.  
 Note: No defects detected.

B. S3L.



Source: FHWA.  
Note: No defects detected.

C. S6S.



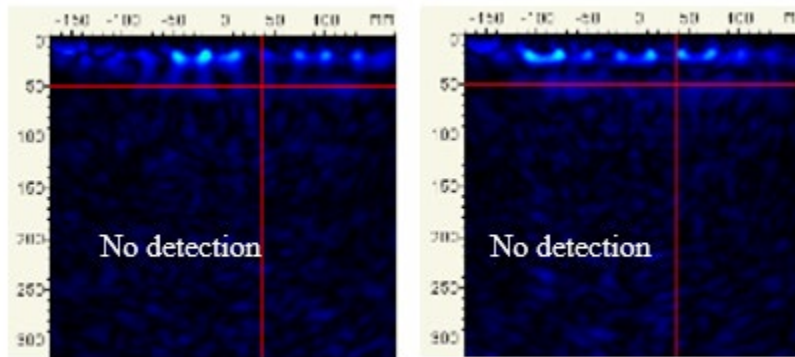
Source: FHWA.  
Note: No defects detected.

D. S8P.

**Figure 97. Graphs. NDE B-scans in debonded area of four specimens with UT-EyeCon.**

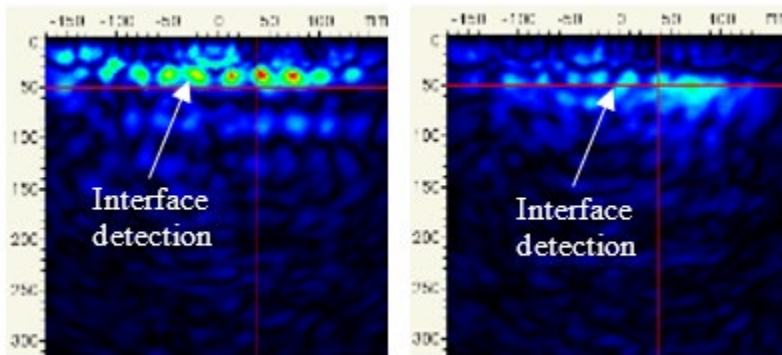
The shear-wave velocity of asphalt pavement is sensitive to temperature, so the UT-MIRA method was used to test specimen S7A above the intact and debonded areas.<sup>(54)</sup> Tests were conducted at seven temperatures: 128 and 84°F in outdoor conditions, and 40, 35, 32, 20, and -2°F in the temperature chamber. The B-scans from the intact and debonded areas look similar, as shown in figure 98-A through figure 98-N. At 128°F, the highly nonlinear and viscoelastic

asphalt pavements dissipate a large amount of ultrasonic stress waves, and the overlay–specimen interface could not be imaged for both debonded and bonded areas. At 84°F, the interface was visible. As the temperature decreased to 40, 35, 32, 20, and –2°F, more waves reached the interface and were reflected and the interface became clearer; meanwhile, the multiple reflection became stronger. Although low temperatures can turn asphalt into a more linear and elastic material, it was still difficult for ultrasonic stress waves to propagate into the underlying specimen in the bonded half. The UT method could not detect defects in the bonded half.



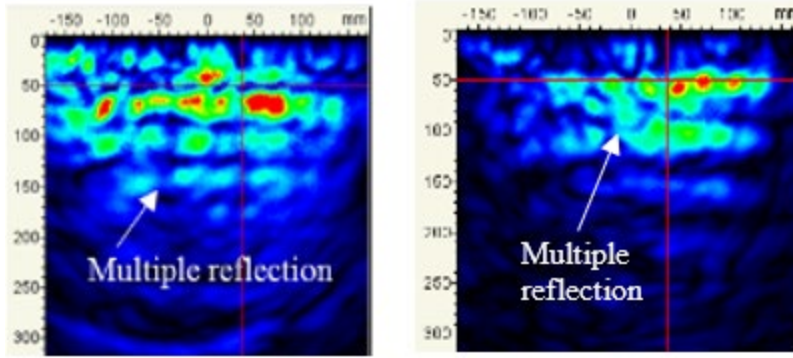
Source: FHWA.  
1 mm = 0.04 inch.

A. Debonded versus intact areas (128°F).



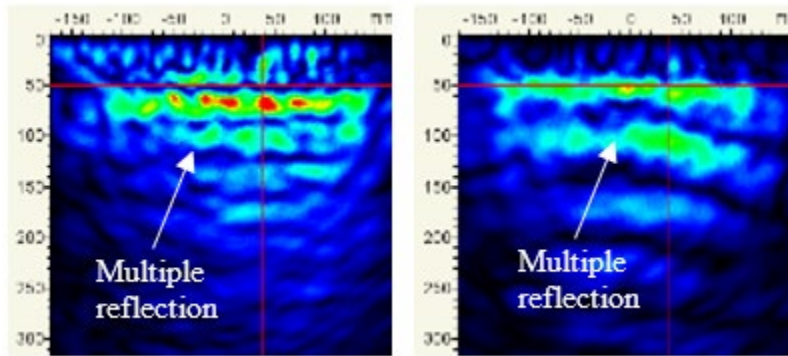
Source: FHWA.  
1 mm = 0.04 inch.

B. Debonded versus intact areas (84°F).



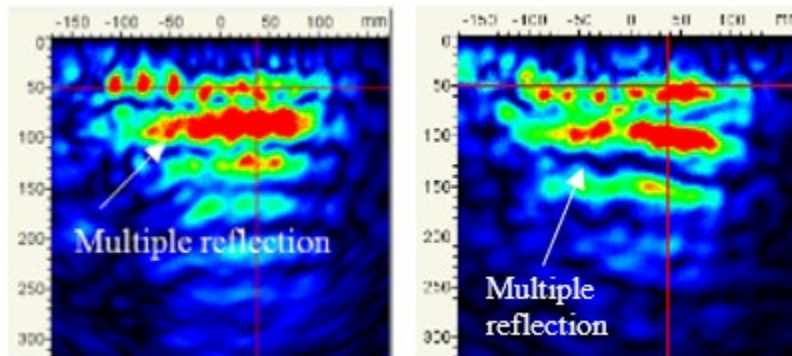
Source: FHWA.  
1 mm = 0.04 inch.

C. Debonded versus intact areas (40°F).



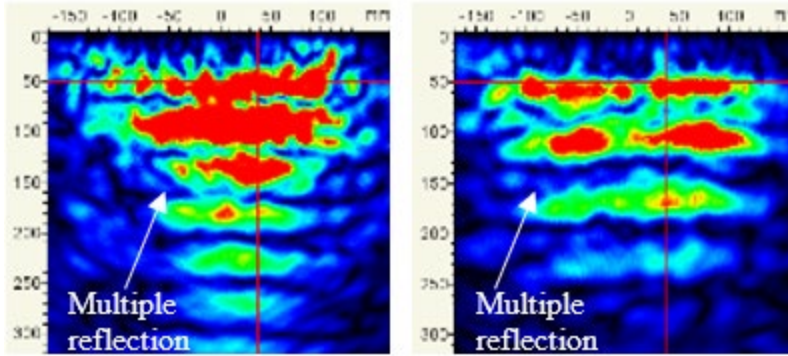
Source: FHWA.  
1 mm = 0.04 inch.

D. Debonded versus intact areas (35°F).



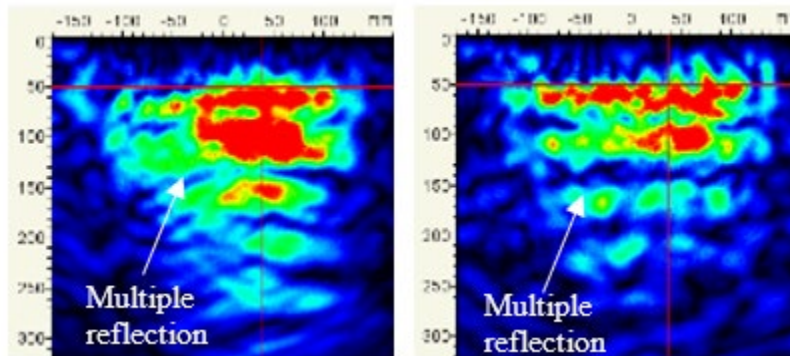
Source: FHWA.  
1 mm = 0.04 inch.

E. Debonded versus intact areas (32°F).



Source: FHWA.  
1 mm = 0.04 inch.

F. Debonded versus intact areas (20°F).

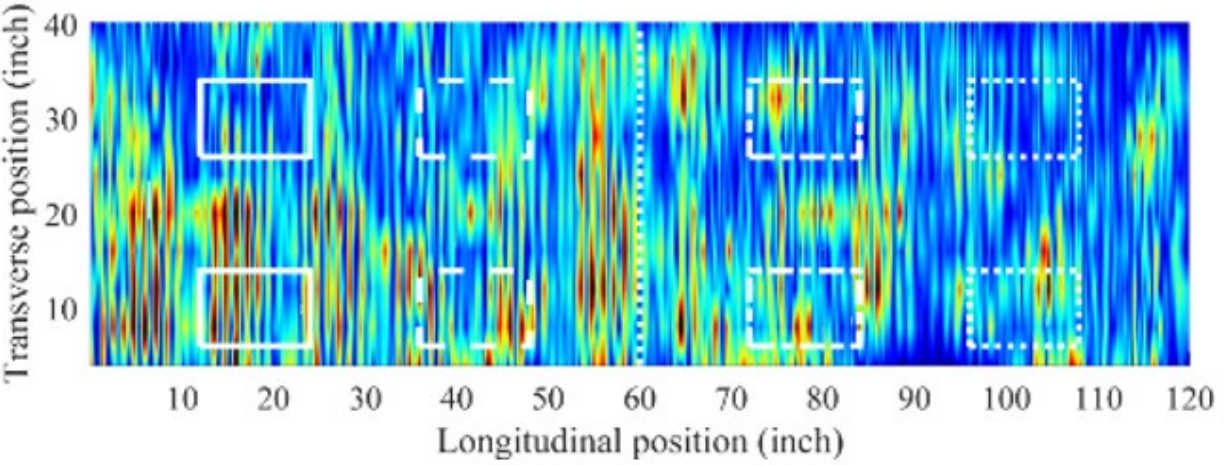
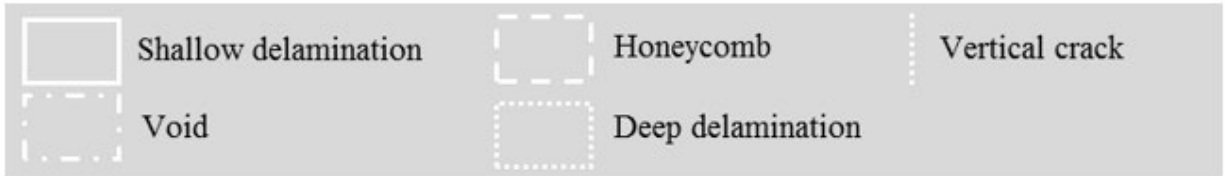


Source: FHWA.  
1 mm = 0.04 inch.

G. Debonded versus intact areas (-2°F).

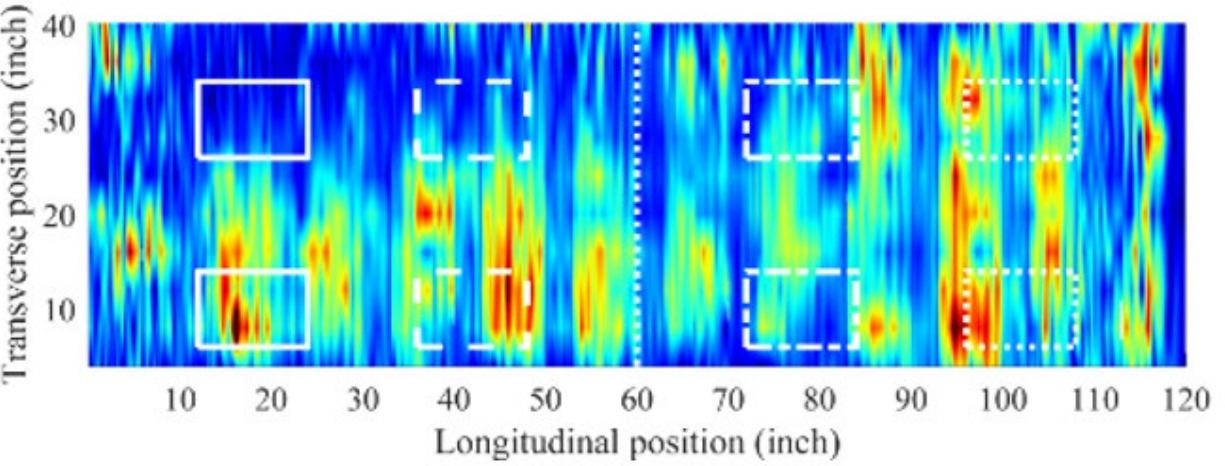
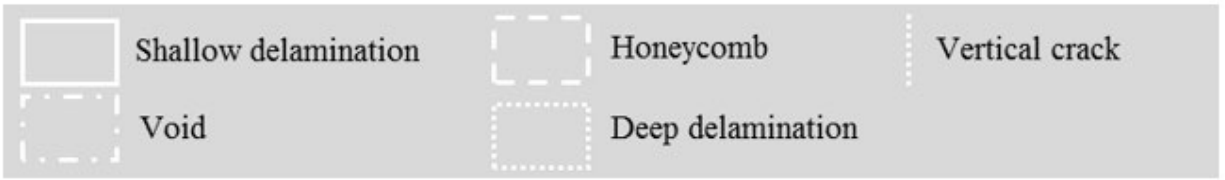
**Figure 98. Graphs. NDE B-scans of the debonded and intact areas of specimen S7A.**

Although the B-scans of specimen S7A indicated the UT method was not promising, specimens S4AS, S5AL, and S7A with asphalt overlays were still scanned using UT-MIRA, along with the USW and IE methods, in the temperature chamber at about 32°F. UT-EyeCon was not used to scan specimens S4AS, S5AL, and S7A because scanning with 2-by-2-inch grids is time-consuming and labor-intensive. Also, the UT-EyeCon mounted on the robotic arm only operated at room temperature (i.e., 68 to 77°F). C-scans and B-scans of specimens S4AS, S5AL, and S7A using the UT method are shown in figure 99 through figure 101, respectively. The UT method detected the asphalt overlay–specimen interface but could not to distinguish overlay bonding and debonding or detect underlying defects.



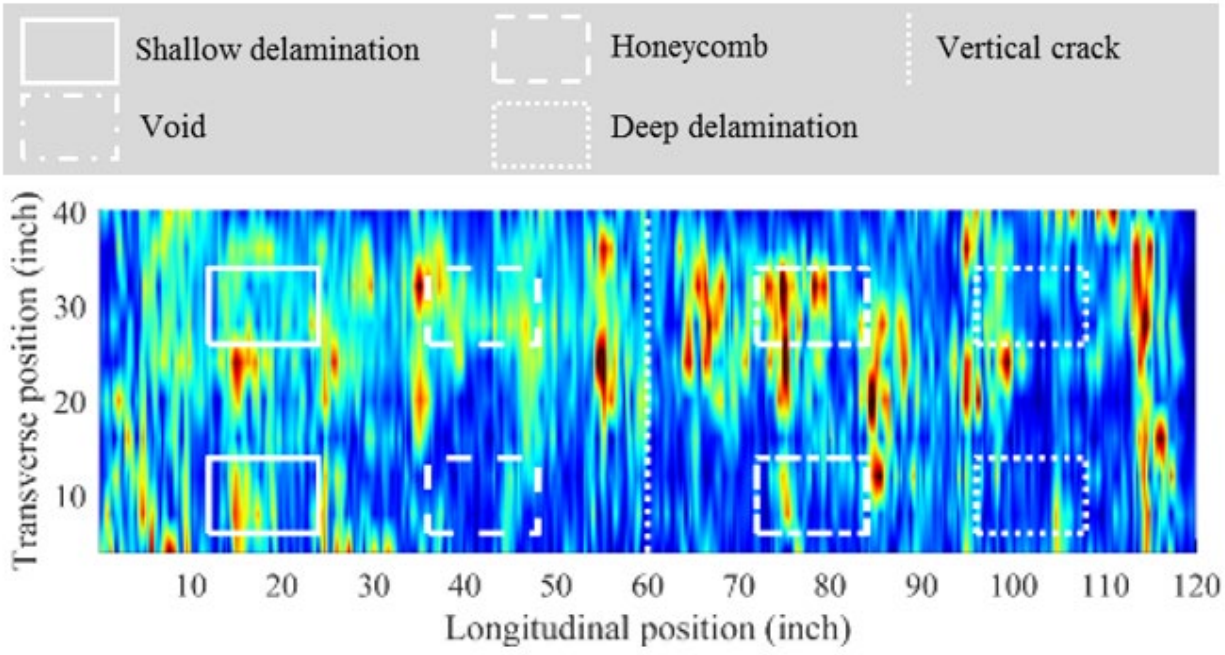
Source: FHWA.  
 Note: No defects detected.

A. S4AS.



Source: FHWA.  
 Note: No defects detected.

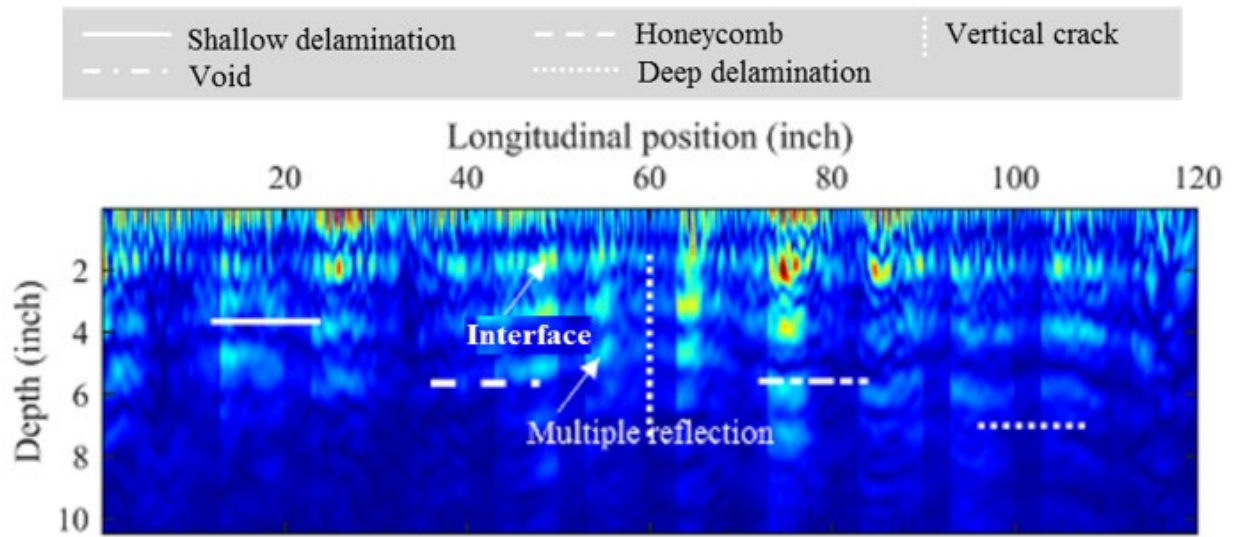
B. S5AL.



Source: FHWA.  
 Note: No defects detected.

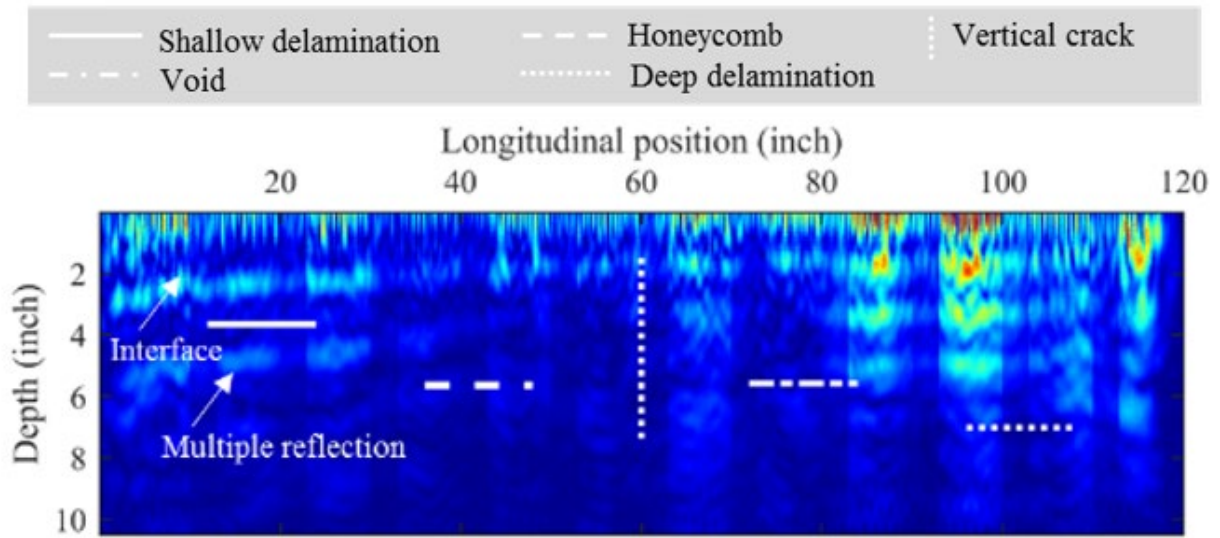
C. S7A.

**Figure 99. Graphs. NDE C-scans of three specimens with UT-MIRA.**



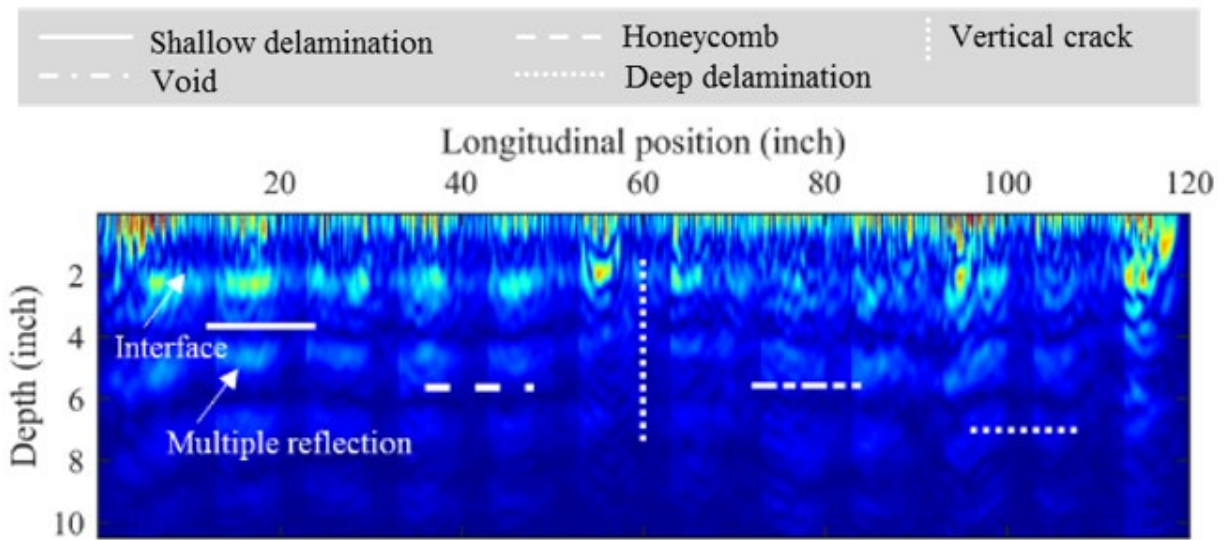
Source: FHWA.

A. S4AS.



Source: FHWA.

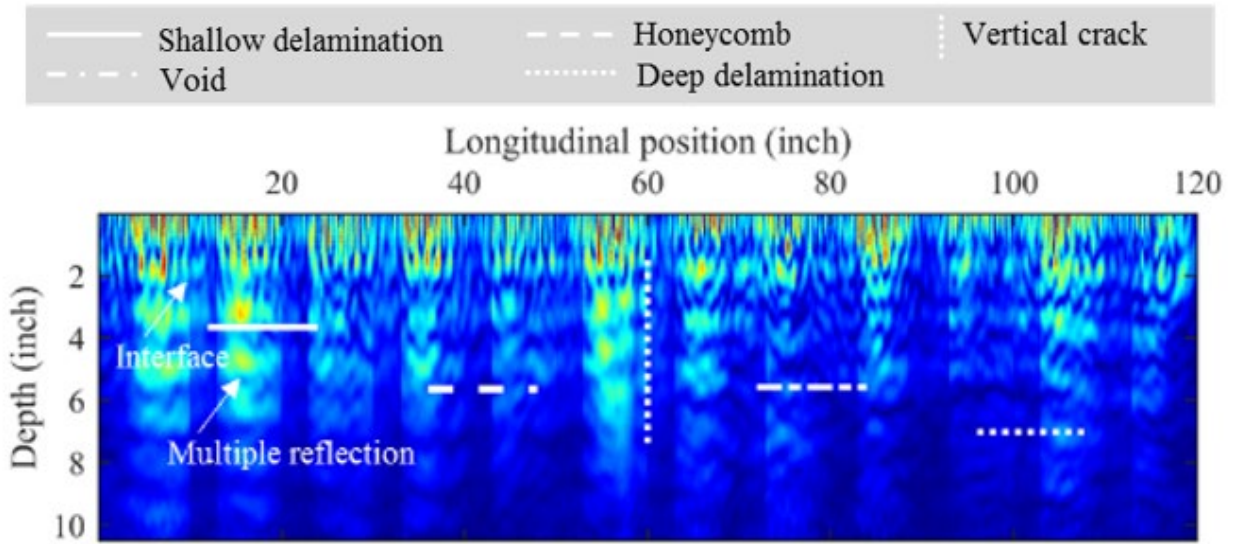
B. S5AL.



Source: FHWA.

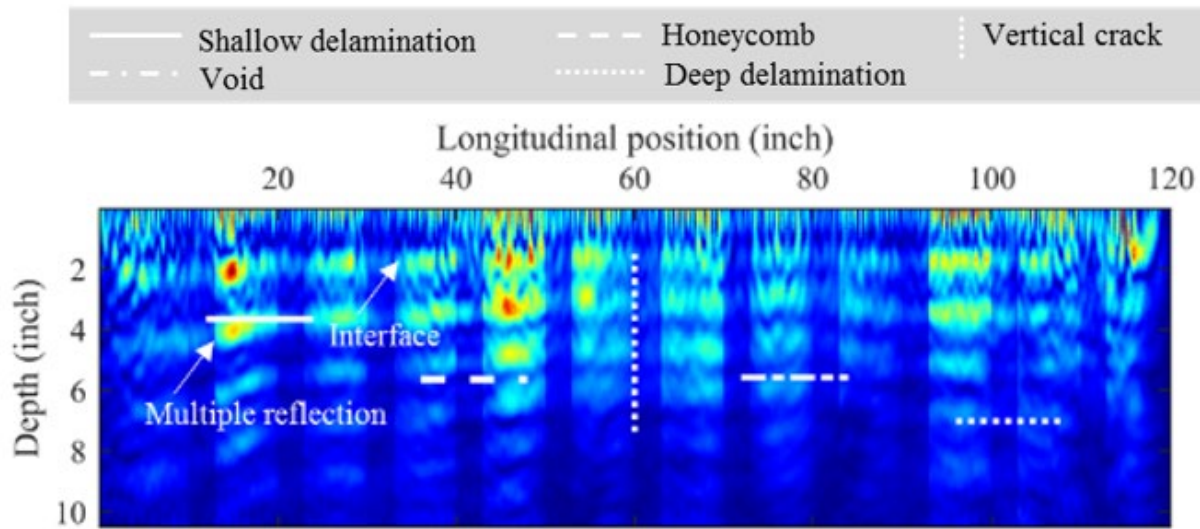
C. S7A.

Figure 100. Graphs. NDE B-scans in bonded area of three specimens with UT-MIRA.



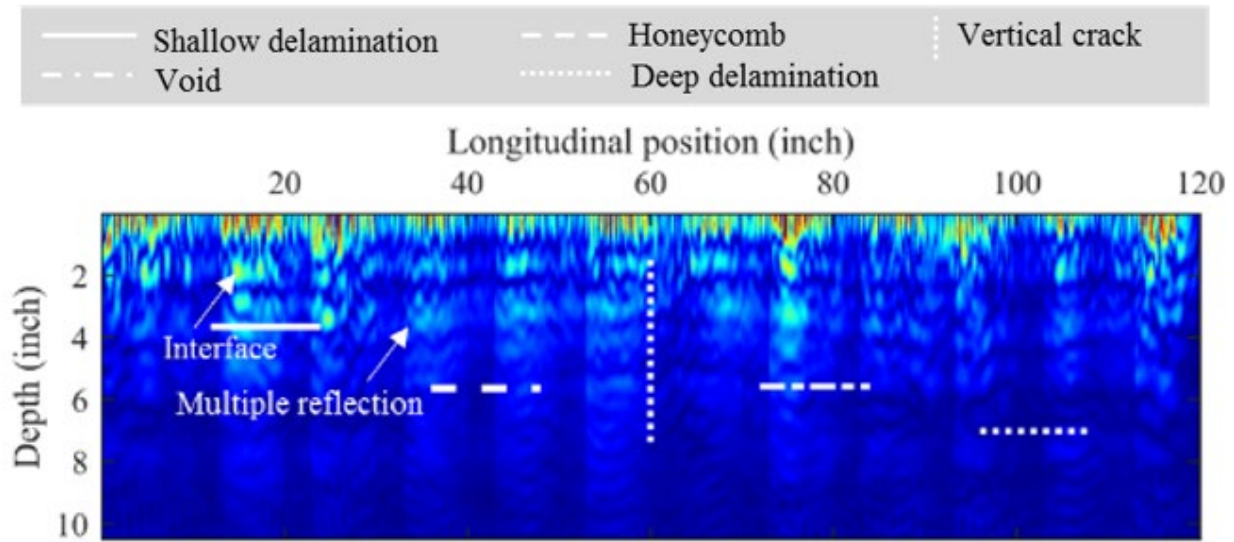
Source: FHWA.

A. S4AS.



Source: FHWA.

B. S5AL.



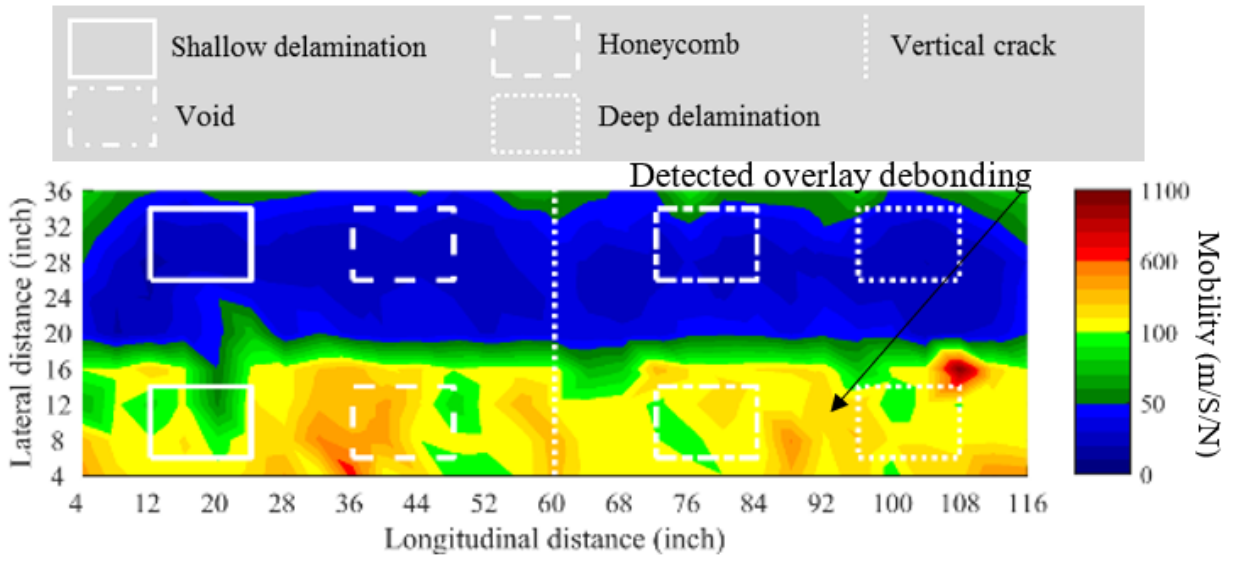
Source: FHWA.

C. S7A.

**Figure 101. Graphs. NDE B-scans in debonded area of three specimens with UT-MIRA.**

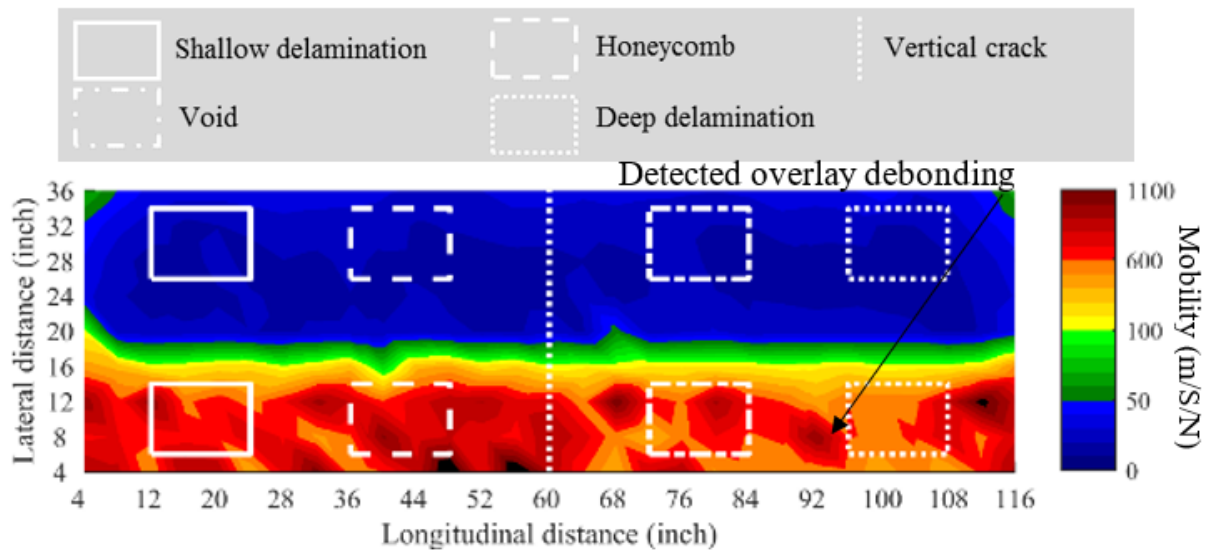
### IR CONDITION MAPS

The condition maps of all seven specimens based on the IR method are shown in figure 102-A through figure 102-G. The IR method detected overlay debonding in terms of lower mobility compared to intact areas in the specimens. The IR method could not detect defects in the underlying specimens in both bonded and debonded areas due to larger depth-to-size ratios compared to specimens without overlays.



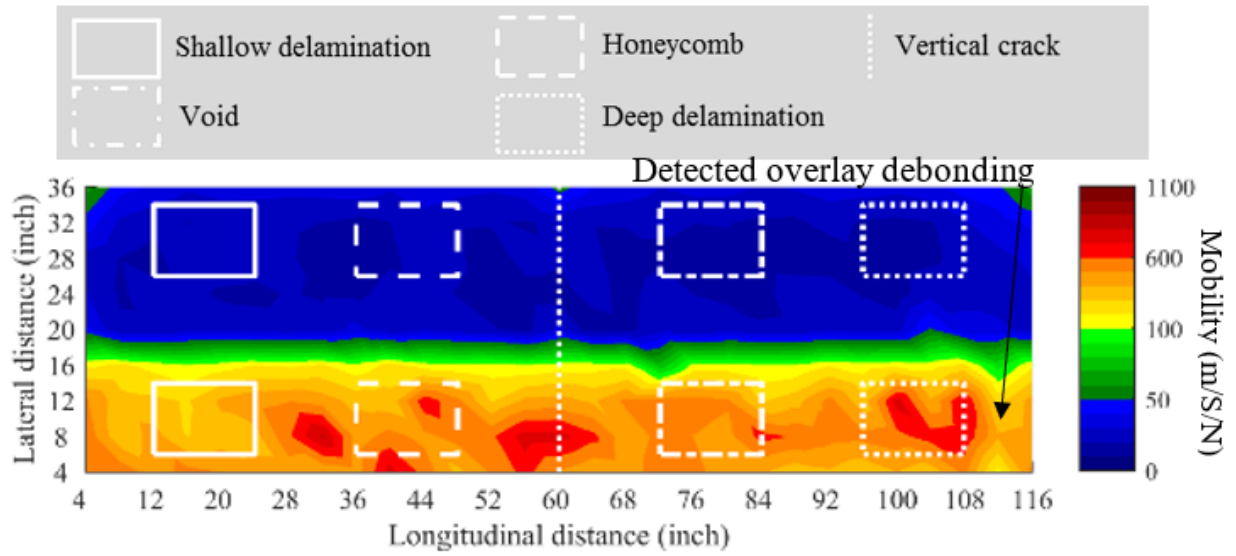
Source: FHWA.  
 1 m/S/N = 0.74 ft/s/lb ft.

A. S1E.



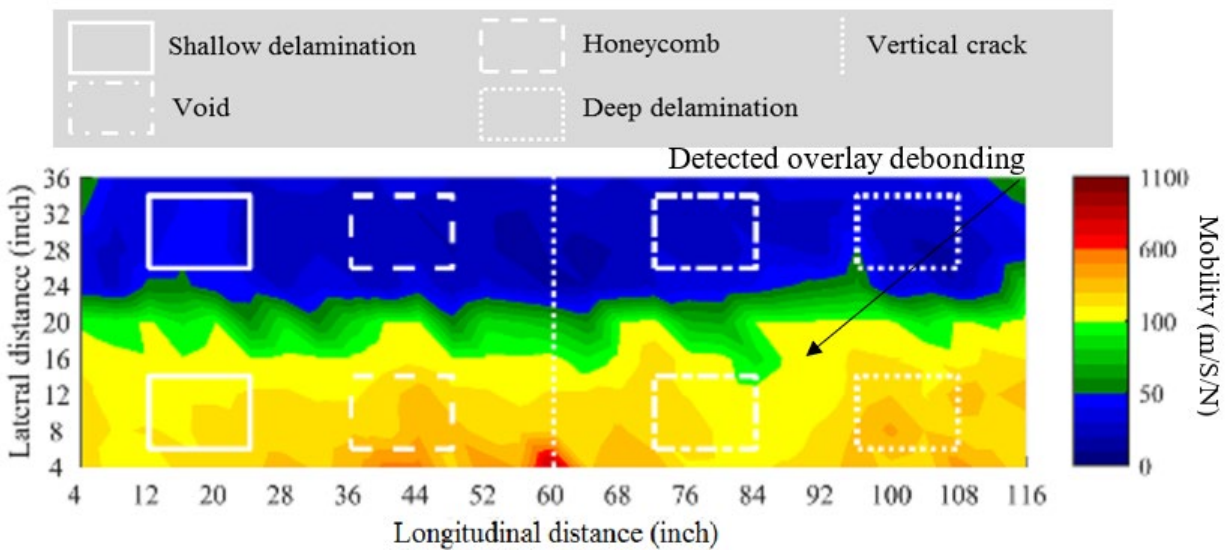
Source: FHWA.  
 1 m/S/N = 0.74 ft/s/lb ft.

B. S3L.



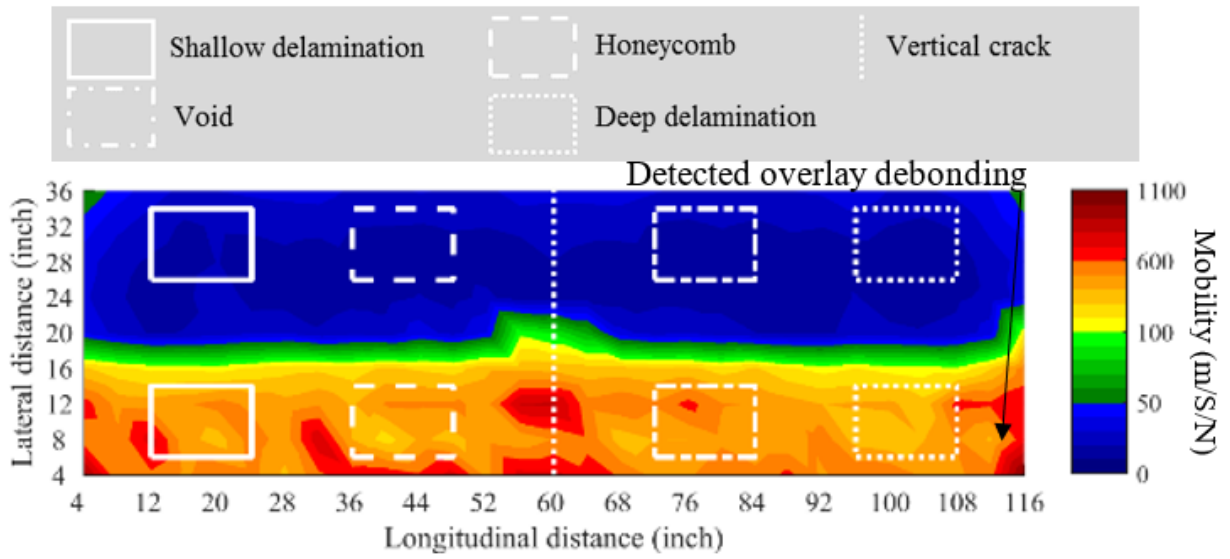
Source: FHWA.  
 1 m/S/N = 0.74 ft/s/lb ft.

C. S4AS.



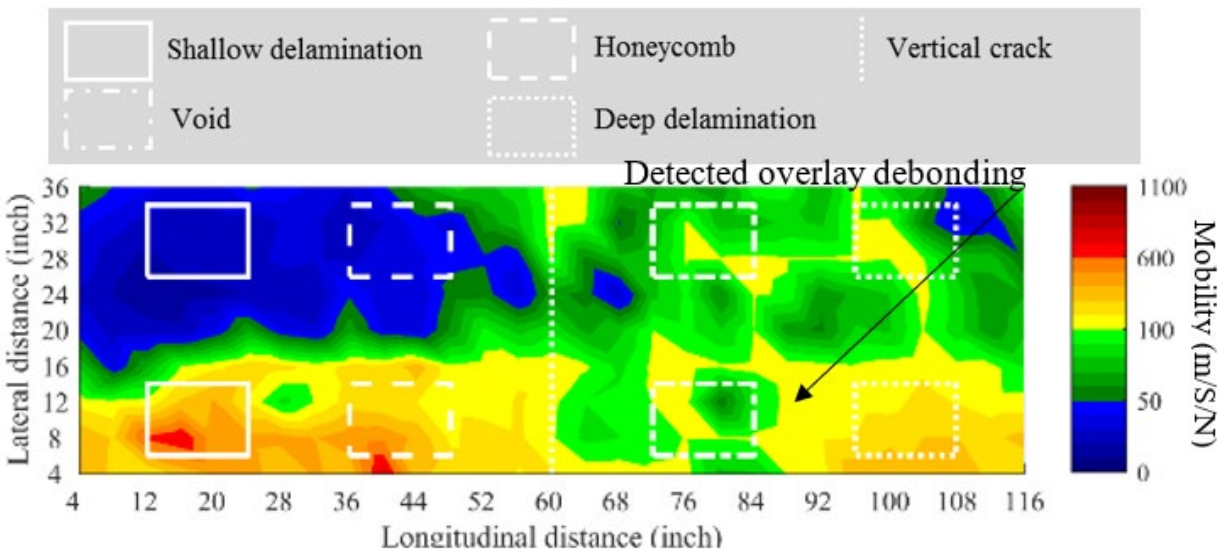
Source: FHWA.  
 1 m/S/N = 0.74 ft/s/lb ft.

D. S5AL.



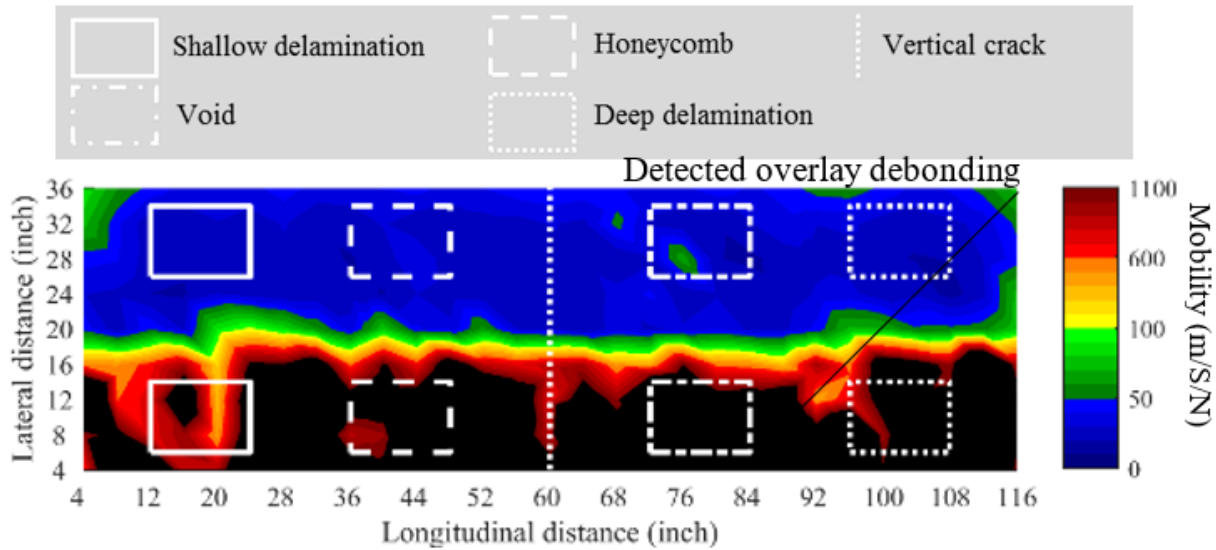
Source: FHWA.  
 1 m/S/N = 0.74 ft/s/lb ft.

E. S6S.



Source: FHWA.  
 1 m/S/N = 0.74 ft/s/lb ft.

F. S7A.



Source: FHWA.  
 1 m/S/N = 0.74 ft/s/lb ft.

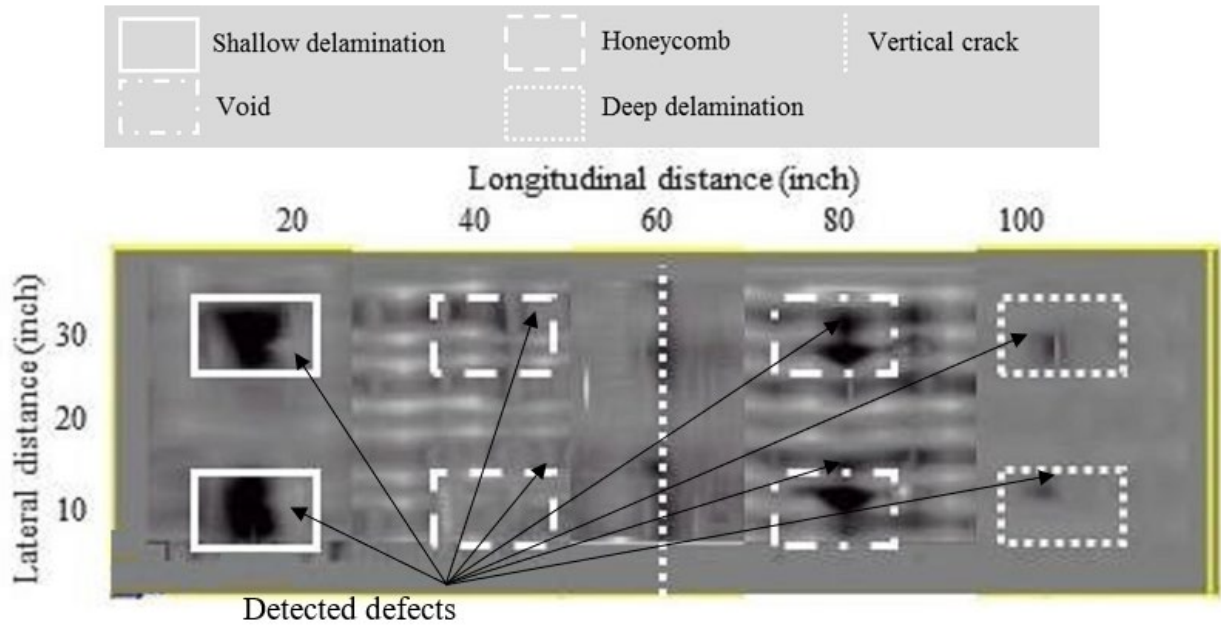
G. S8P.

**Figure 102. Graphs. NDE condition maps with IR.**

### **GPR C-SCANS, B-SCANS, AND DETERIORATION MAPS**

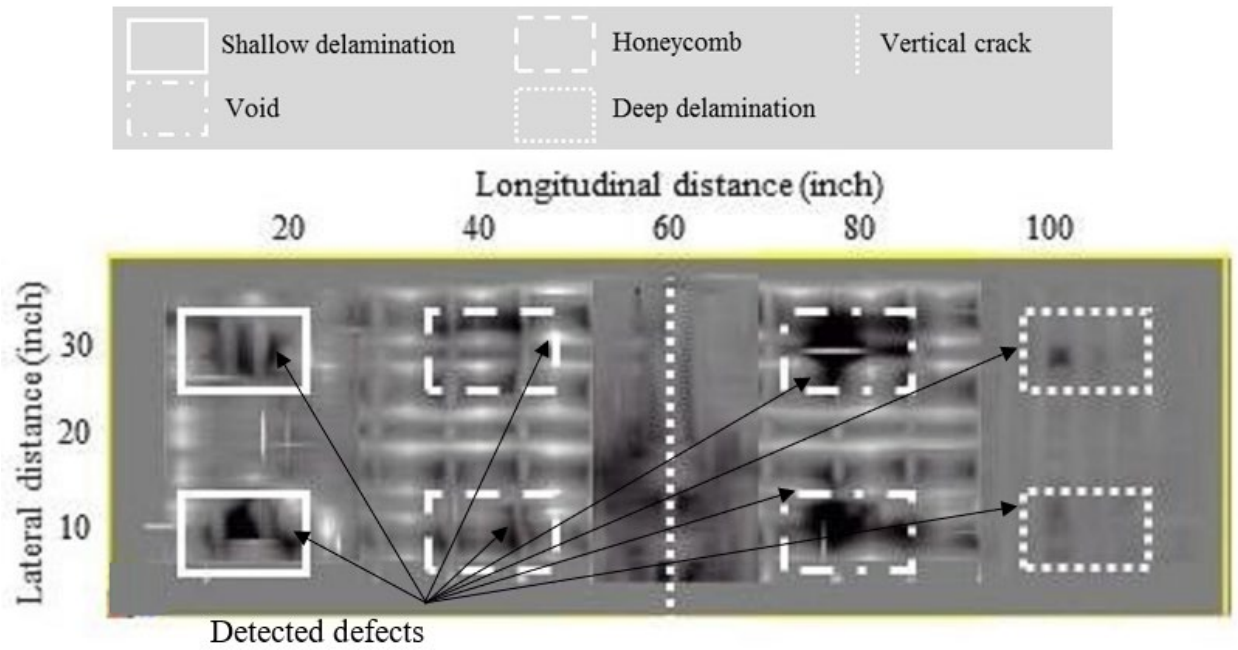
The C-scans, B-scans, and deterioration maps based on the GPR method are shown in figure 103 through figure 106. The C- and B-scans indicated the GPR method detected shallow and deep delaminations, honeycombing, voids, the top layer rebar, and the thickness of the underlying specimens in both bonded and debonded areas for all seven specimens. Additionally, GPR B-scans detected the overlay–specimen interface in specimens S4AS, S5AL, S6S, and S7A because of the different  $\epsilon_r$  of the overlay and the materials of the underlying specimens. Overlay thickness was estimated with the appropriate selection of the  $\epsilon_r$  of the overlay material. Vertical cracks and overlay debonding could not be detected by GPR C- and B-scans. The overlay–specimen interface could not be detected by GPR B-scans in specimens S1E and S8P due to the small overlay thicknesses or in specimen S3L due to similar  $\epsilon_r$  between the overlay and the specimen.

The amplitudes of the signals reflected by the top layer of rebar were used to construct the deterioration maps of the specimens based on the corrosive environment after the accelerated corrosion, as shown in figure 106-A through figure 106-G. The deterioration maps imaged the elevated chloride content environment in specimens S1E, S3L, S4AS, S5AL, and S7A. Since defects in the specimens were created artificially and not induced by the corrosive environment, the condition maps based on the GPR method could not detect any defects except the elevated chloride content environment. When reflected EM waves from the rebar below areas with shallow delaminations were superimposed with reflected EM waves from shallow delaminations, the resulting total reflection was stronger than the rebar without the overlying delamination.



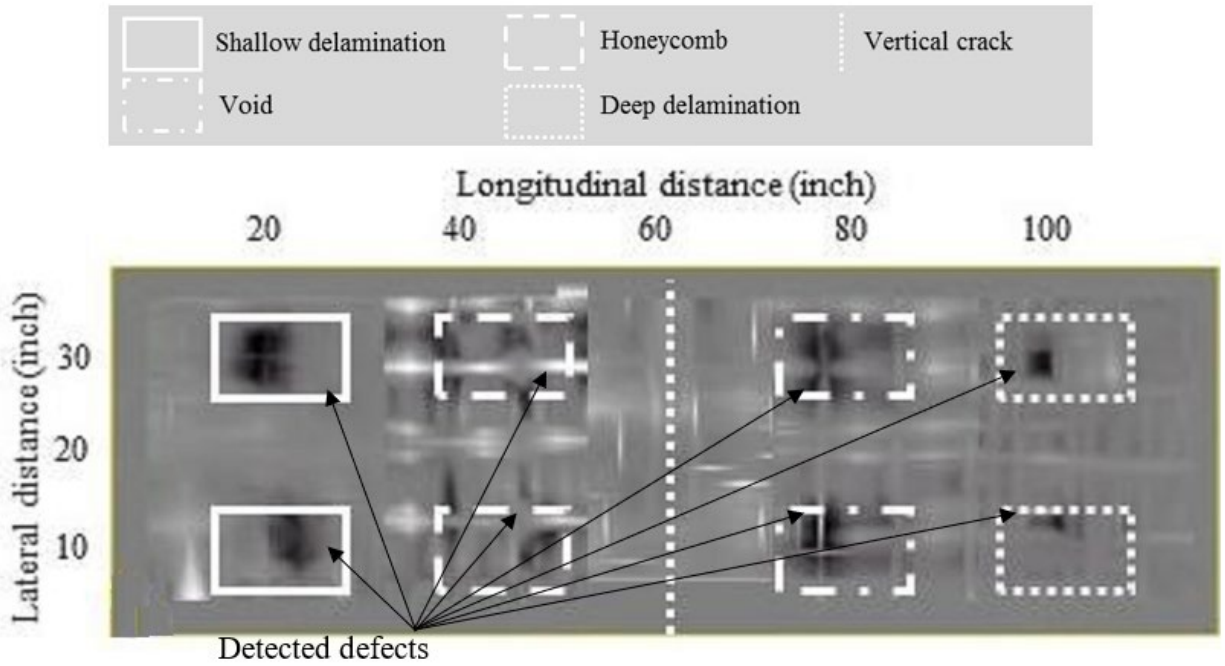
Source: FHWA.

A. S1E.



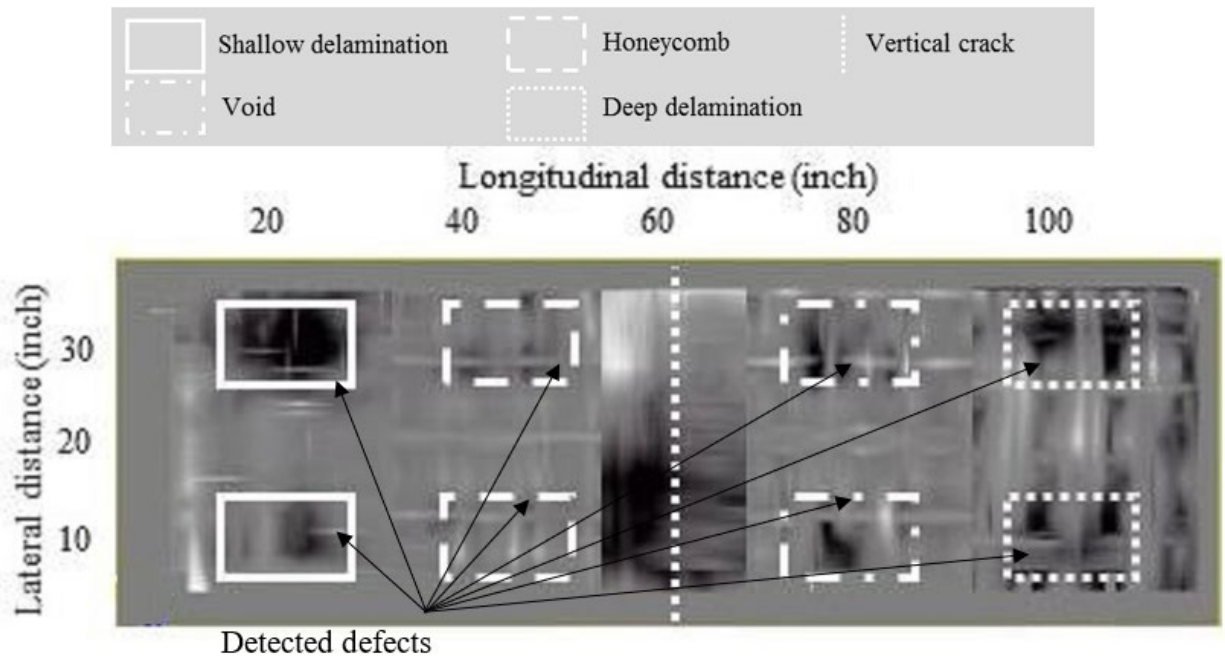
Source: FHWA.

B. S3L.



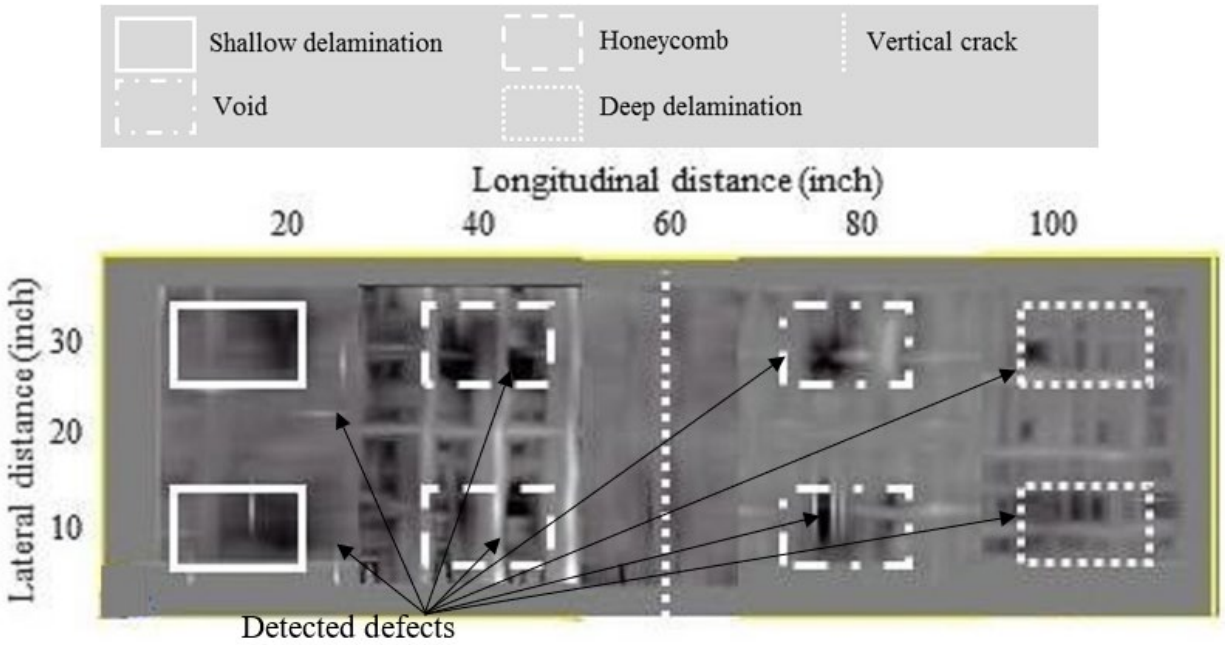
Source: FHWA.

C. S4AS.



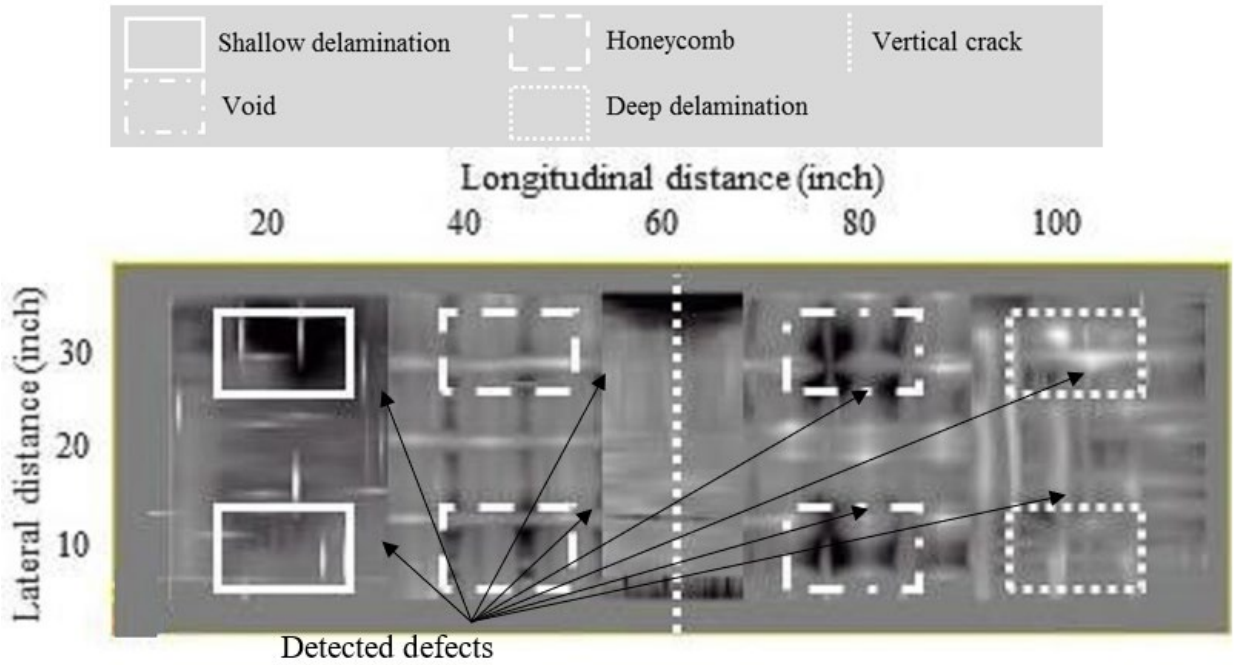
Source: FHWA.

D. S5AL.



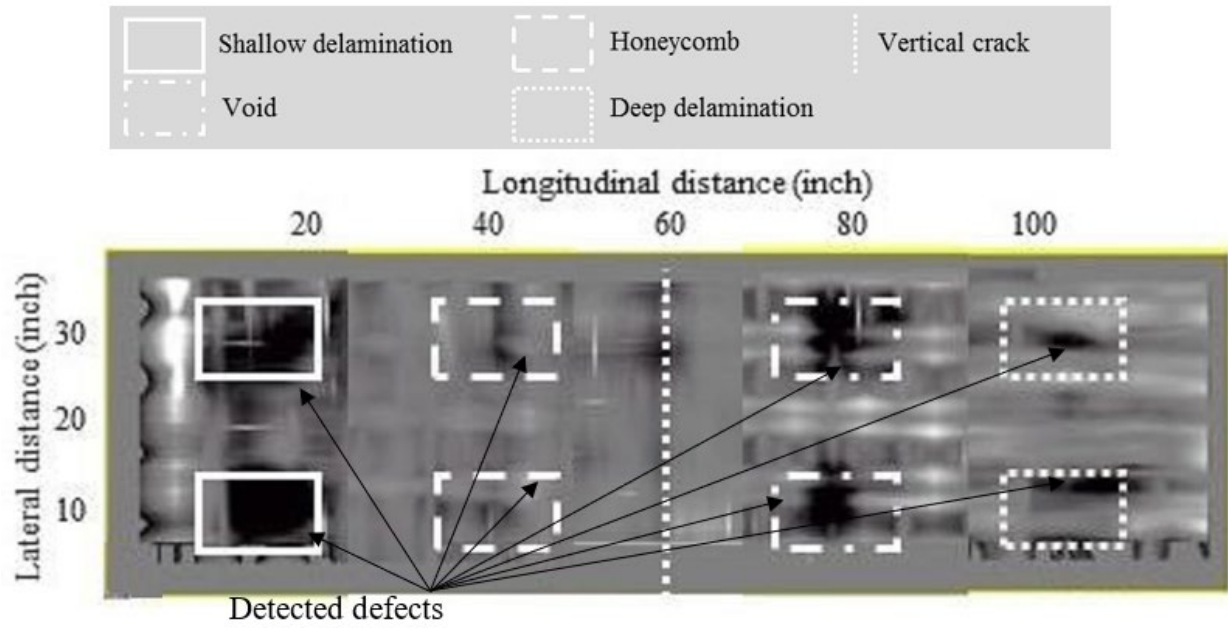
Source: FHWA.

E. S6S.



Source: FHWA.

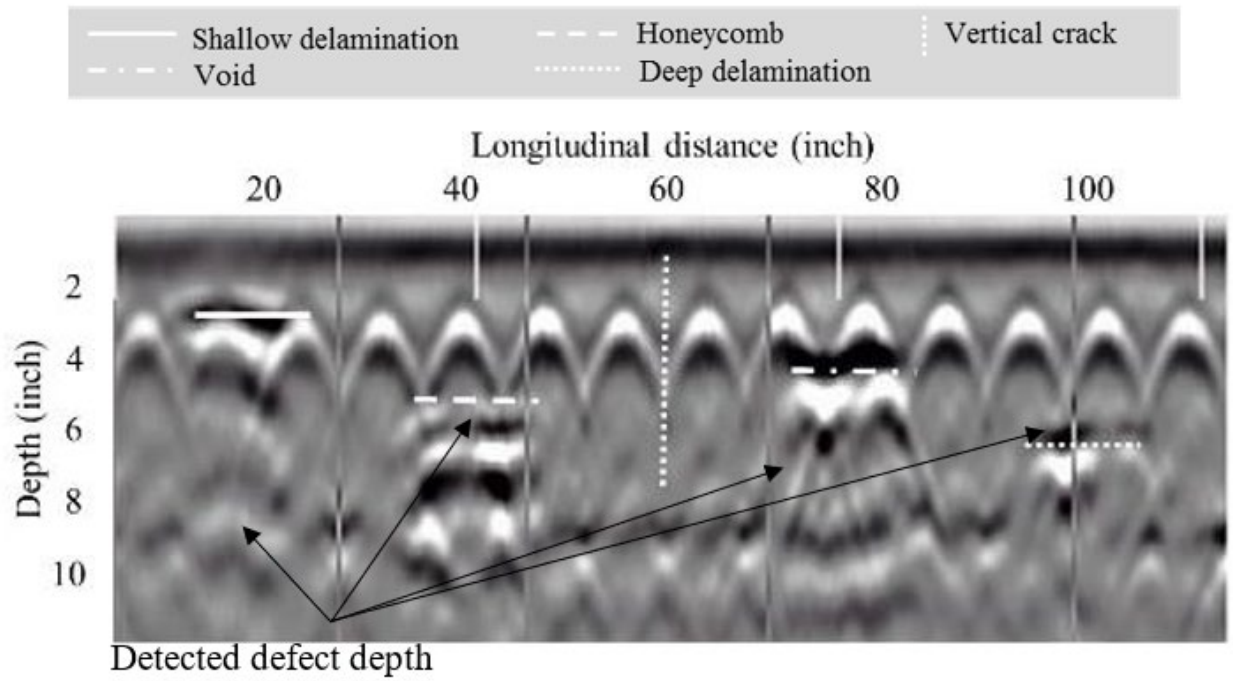
F. S7A.



Source: FHWA.

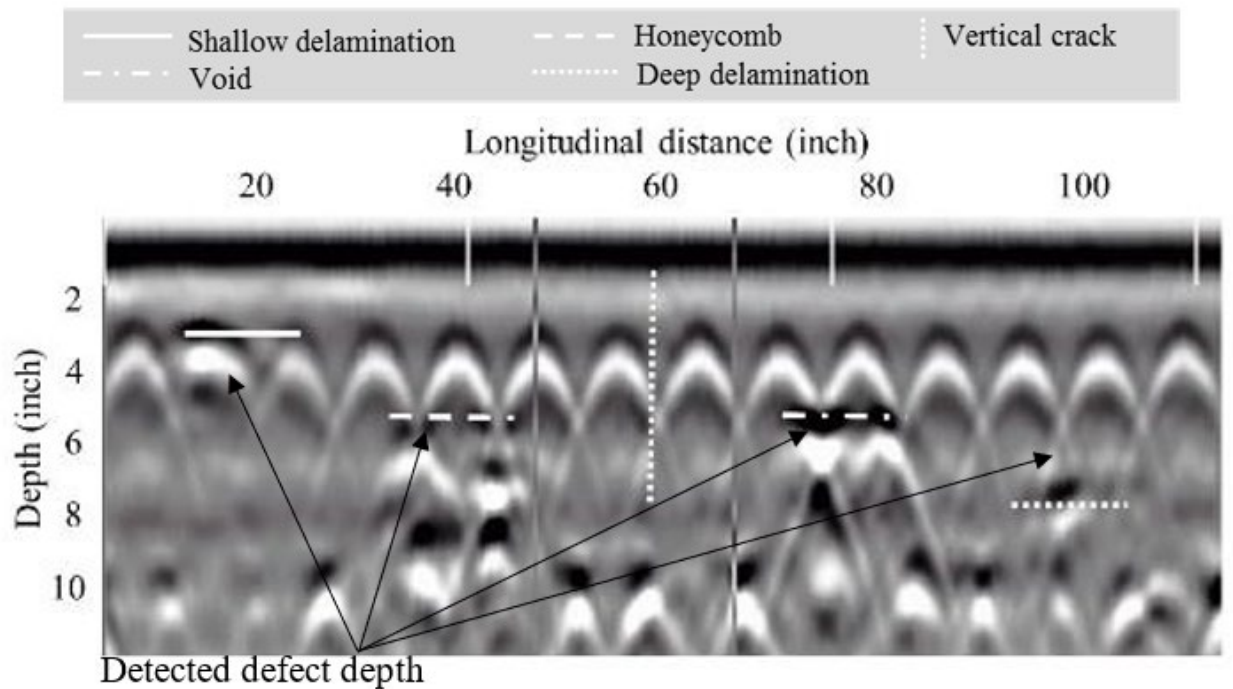
G. S8P.

**Figure 103. Graphs. NDE C-scans with the GPR method.**



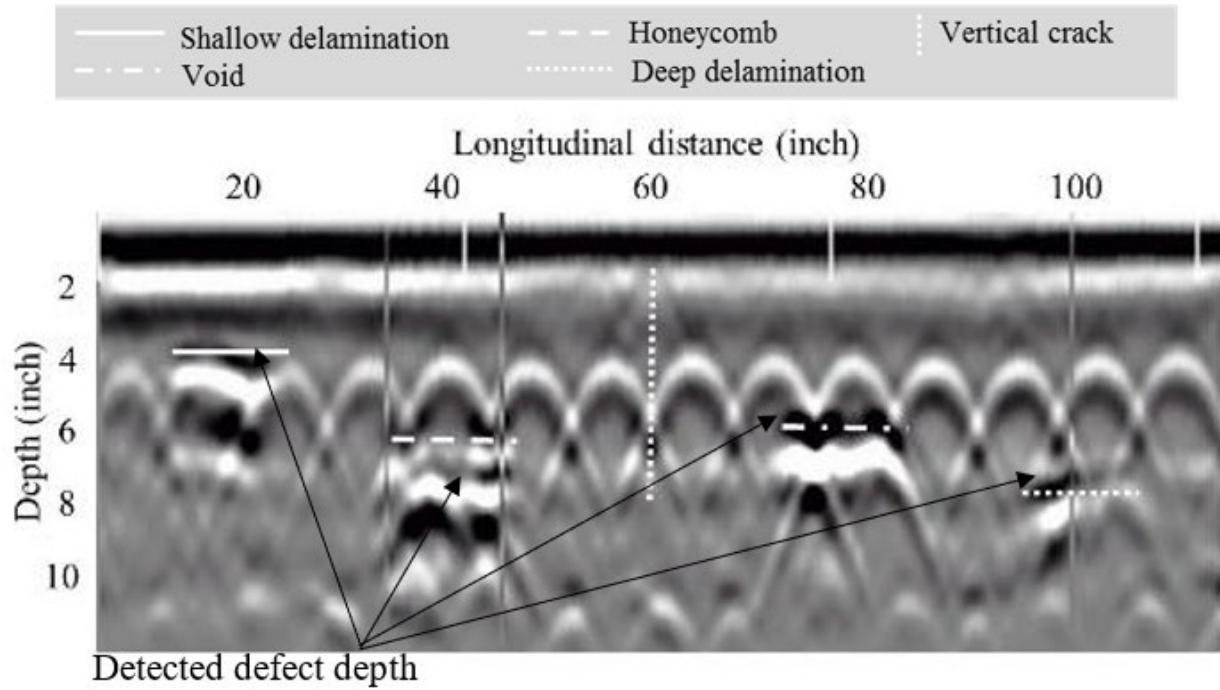
Source: FHWA.

A. S1E.



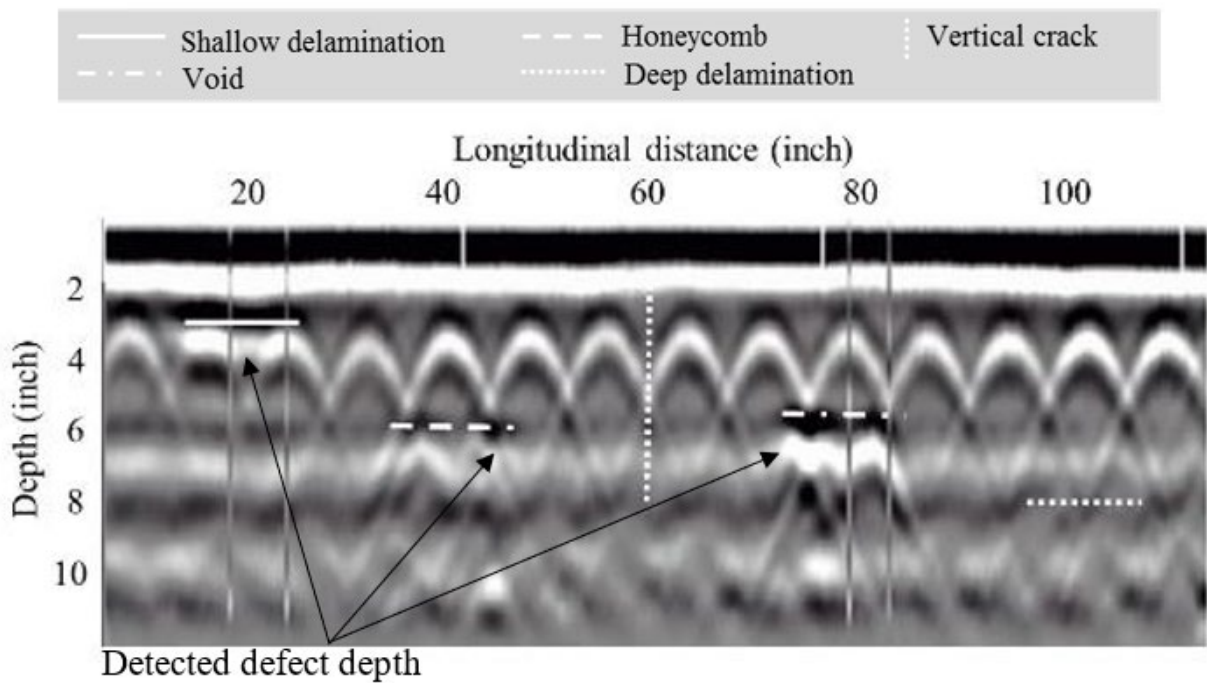
Source: FHWA.

B. S3L.



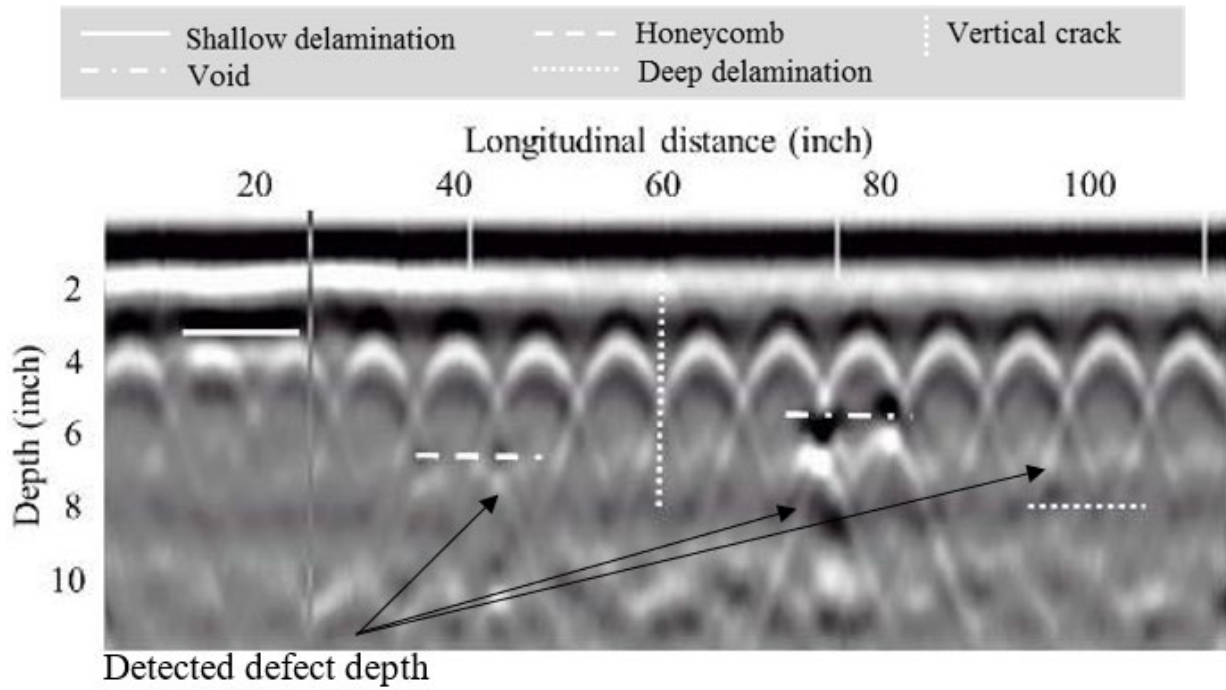
Source: FHWA.

C. S4AS.



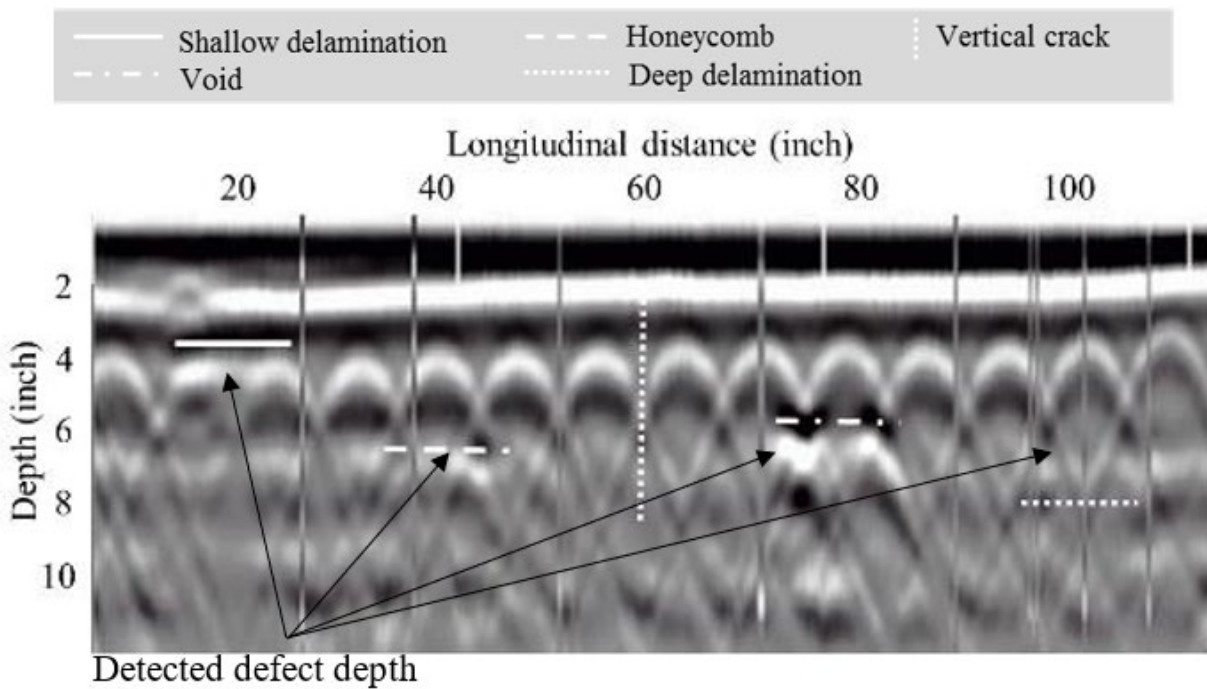
Source: FHWA.

D. S5AL.



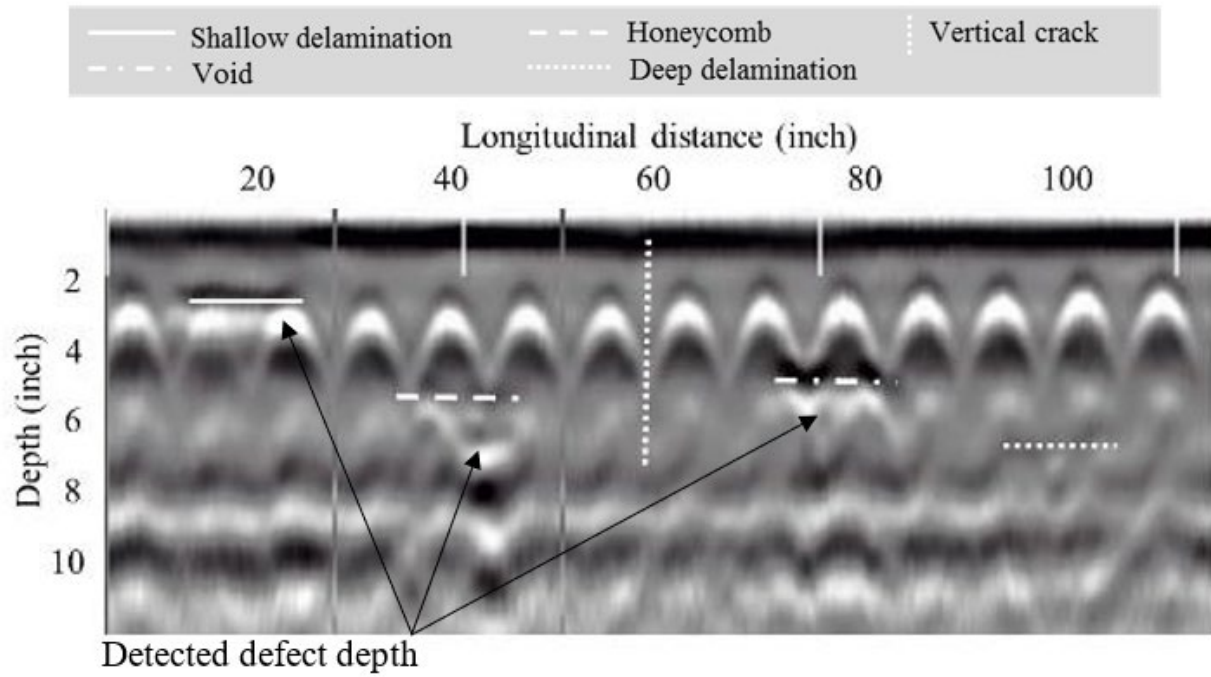
Source: FHWA.

E. S6S.



Source: FHWA.

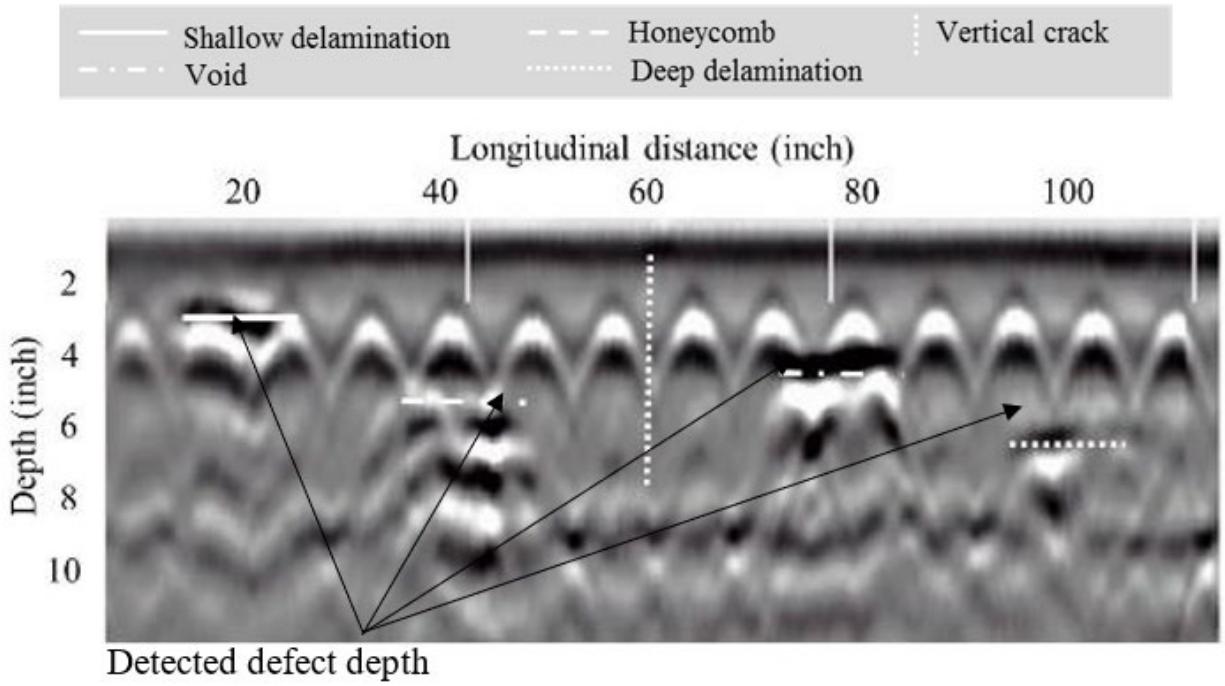
F. S7A.



Source: FHWA.

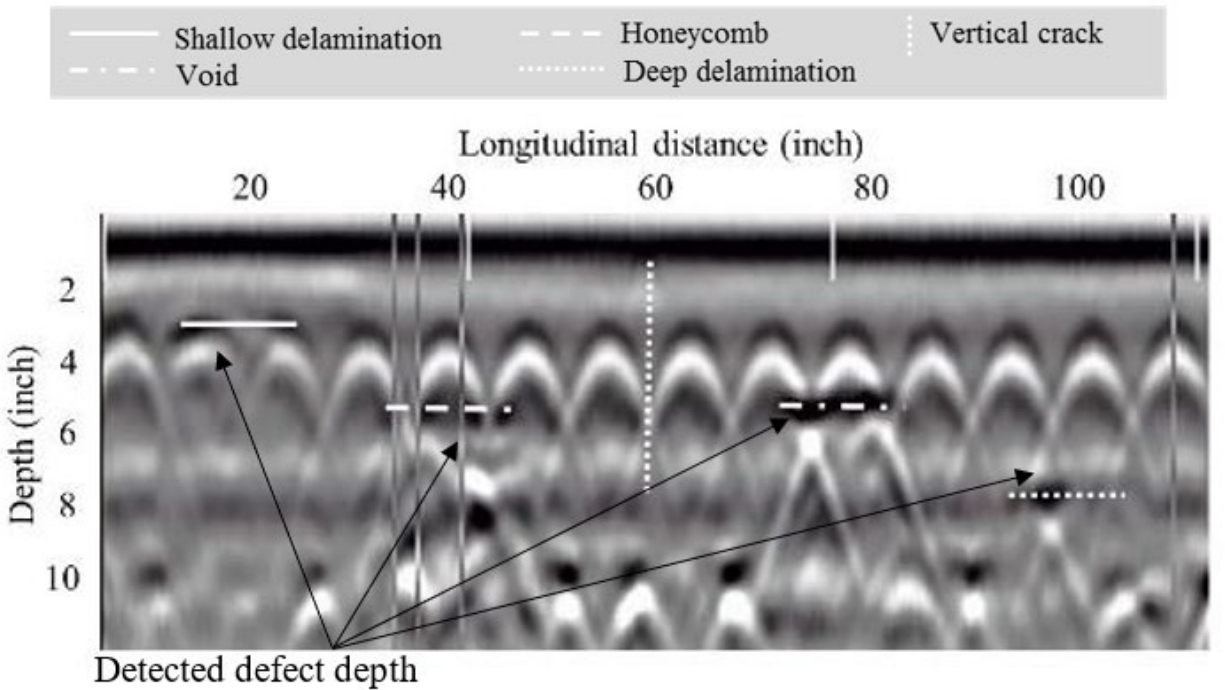
G. S8P.

**Figure 104. Graphs. NDE B-scans in bonded areas with the GPR method.**



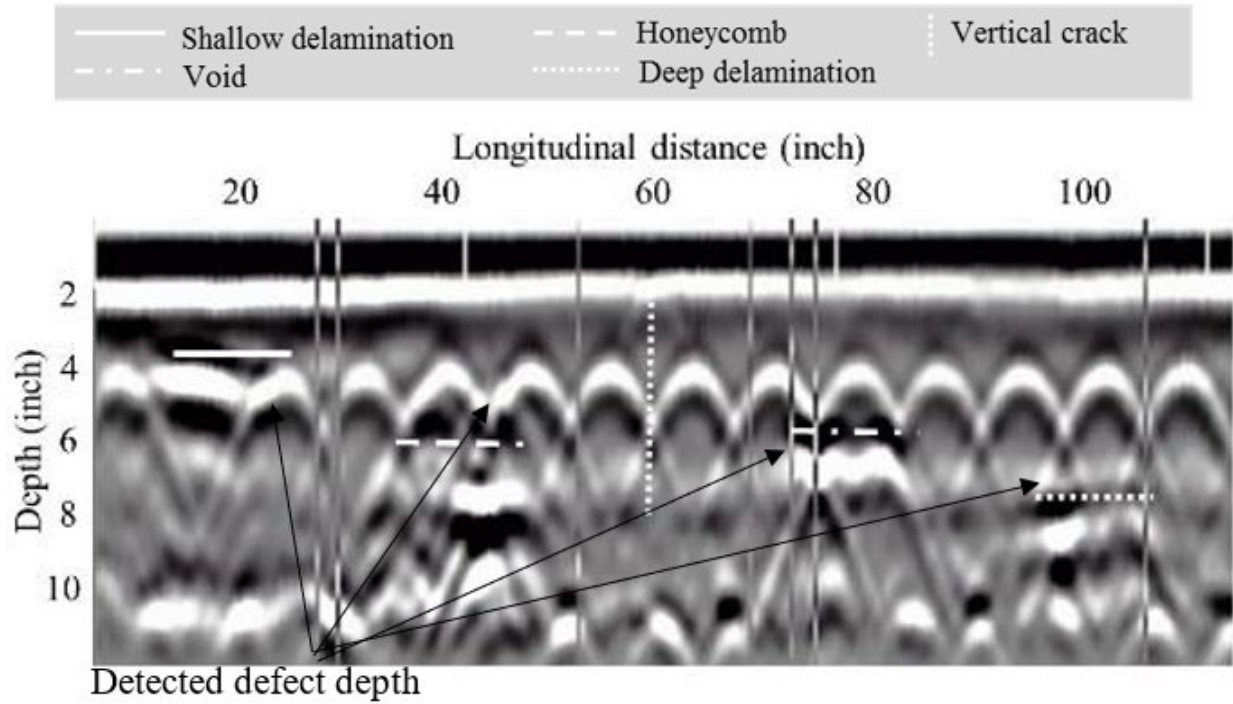
Source: FHWA.

A. S1E.



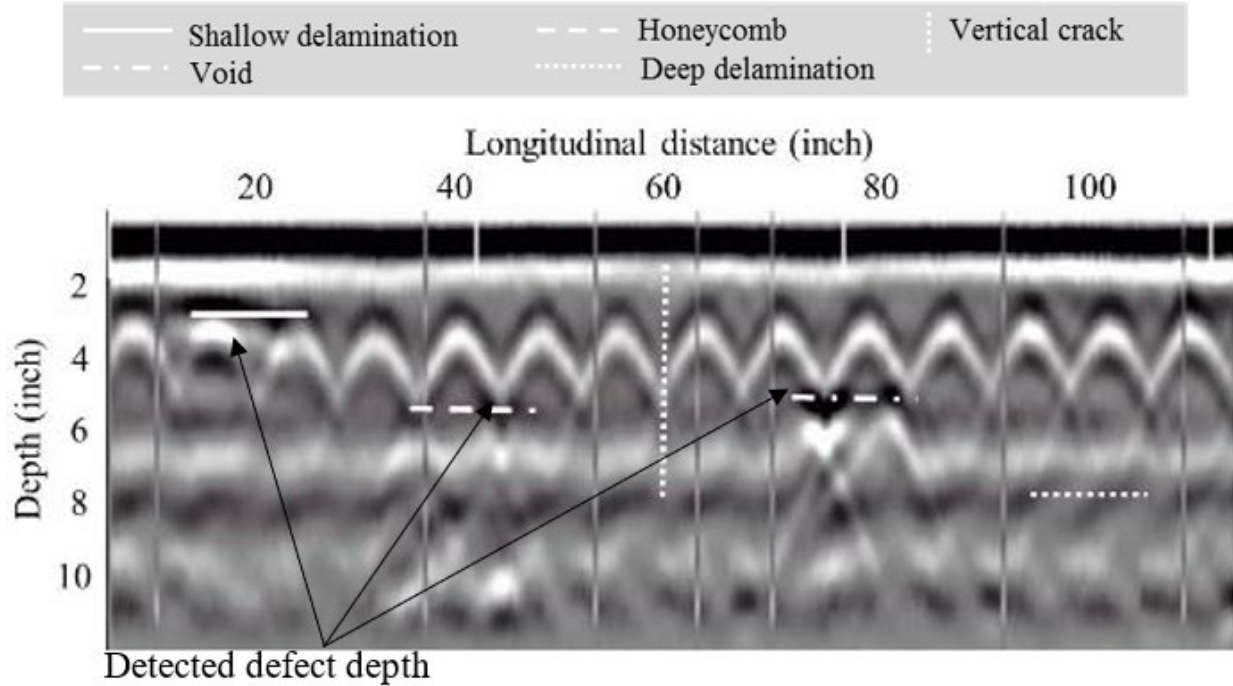
Source: FHWA.

B. S3L.



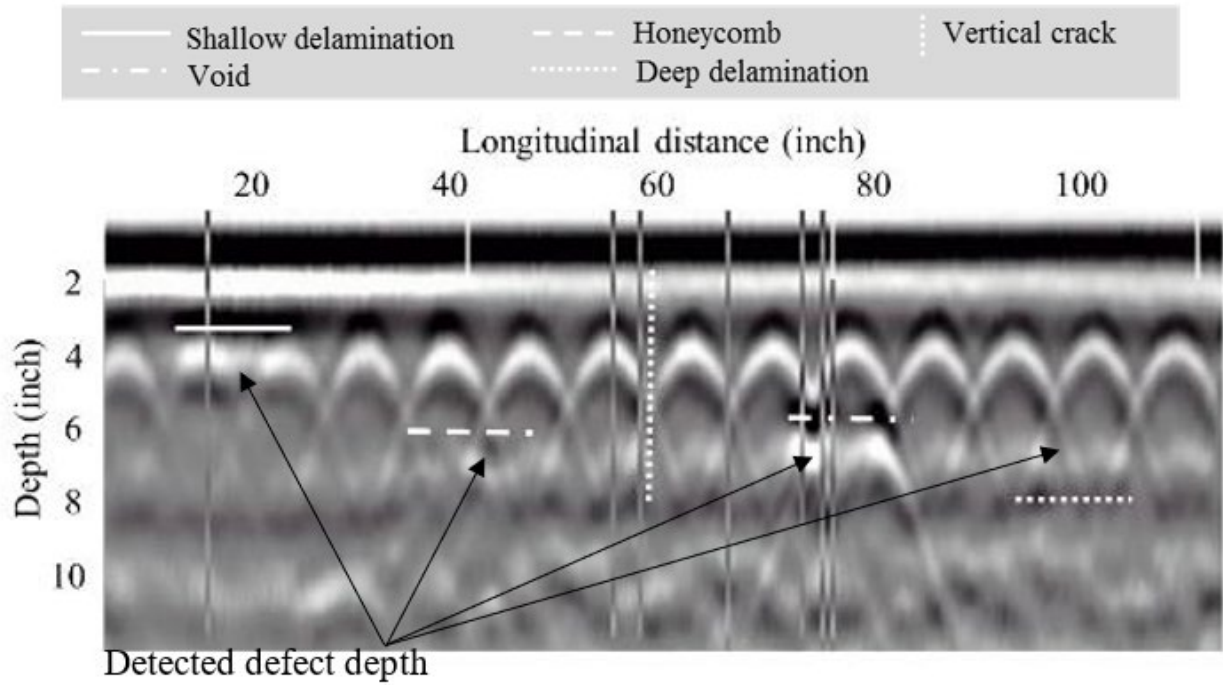
Source: FHWA.

C. S4AS.



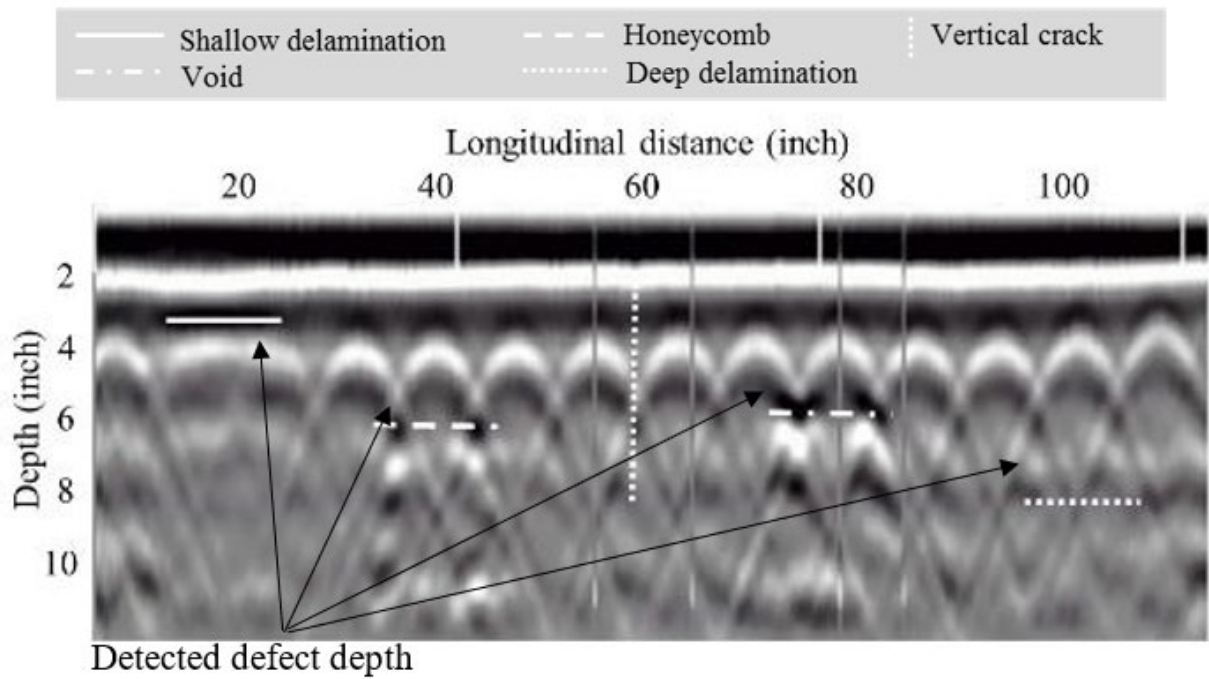
Source: FHWA.

D. S5AL.



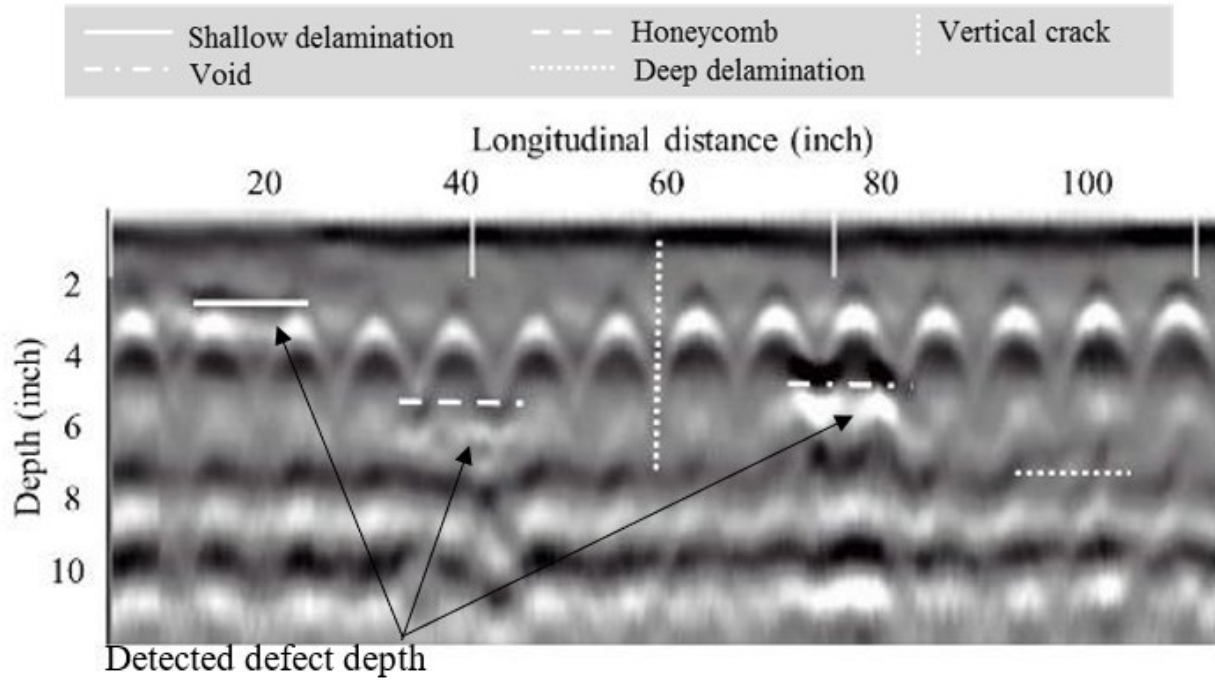
Source: FHWA.

E. S6S.



Source: FHWA.

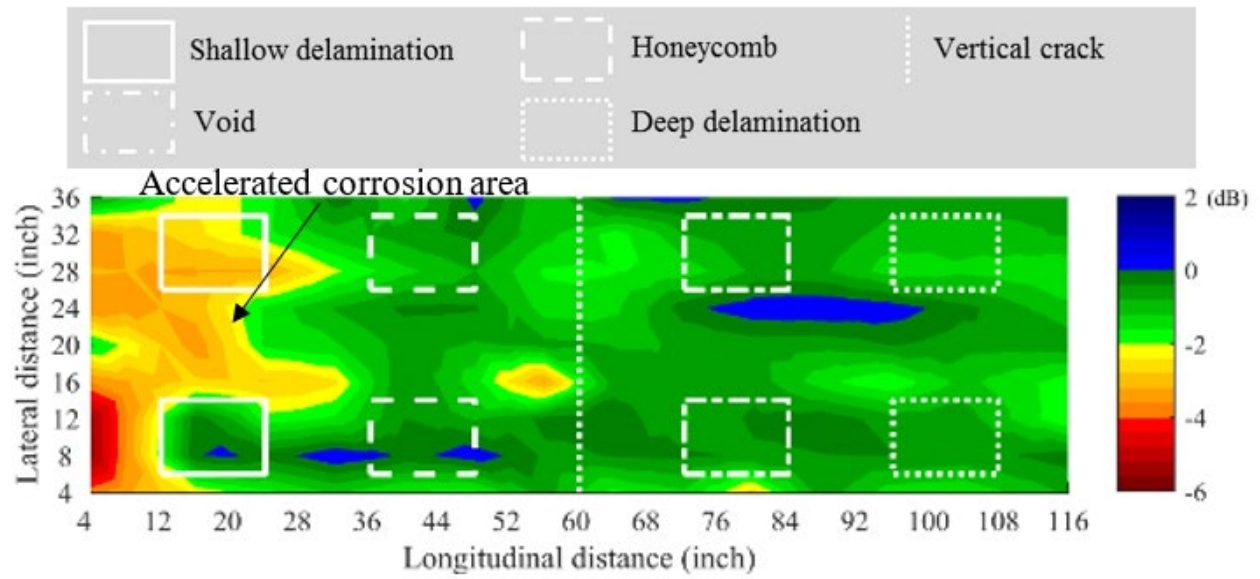
F. S7A.



Source: FHWA.

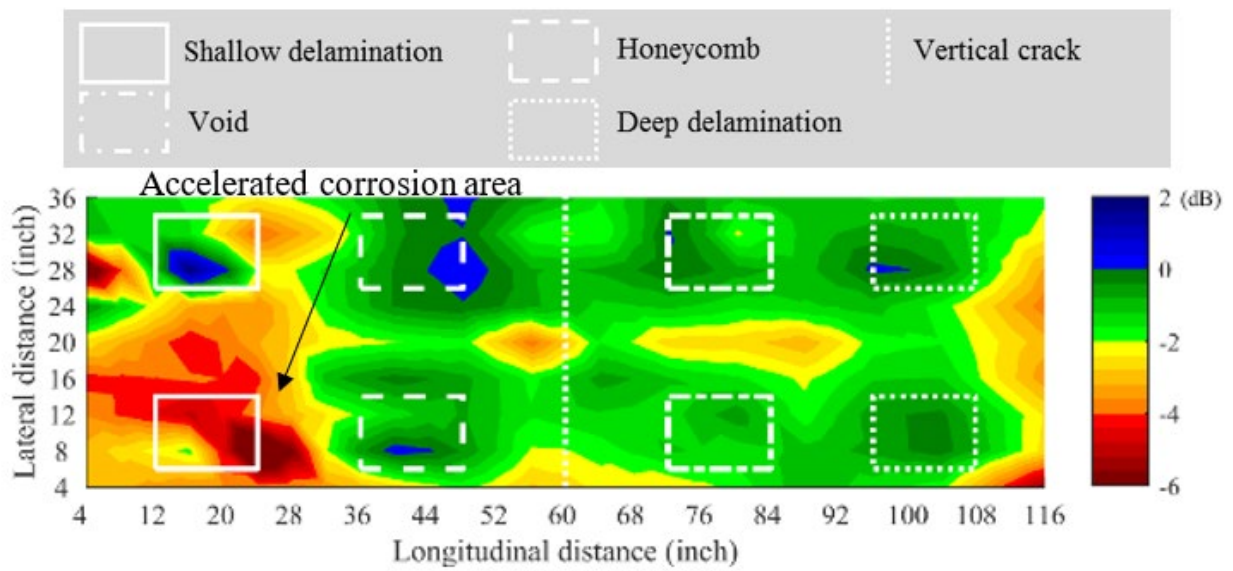
G. S8P.

**Figure 105. Graphs. NDE B-scans in debonded areas with the GPR method.**



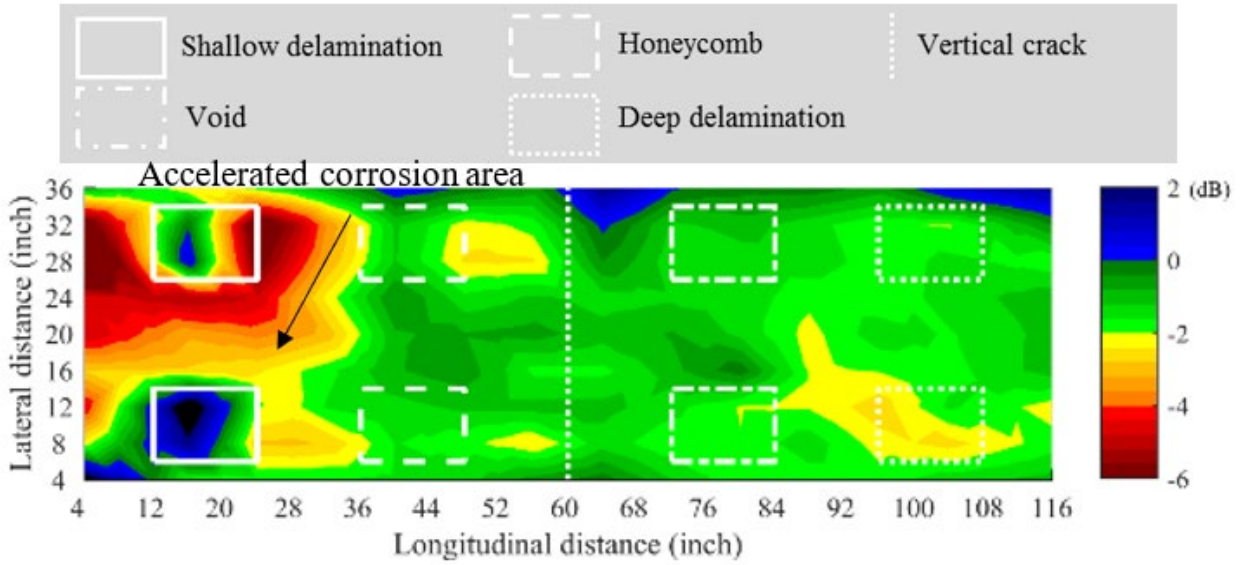
Source: FHWA.

A. S1E.



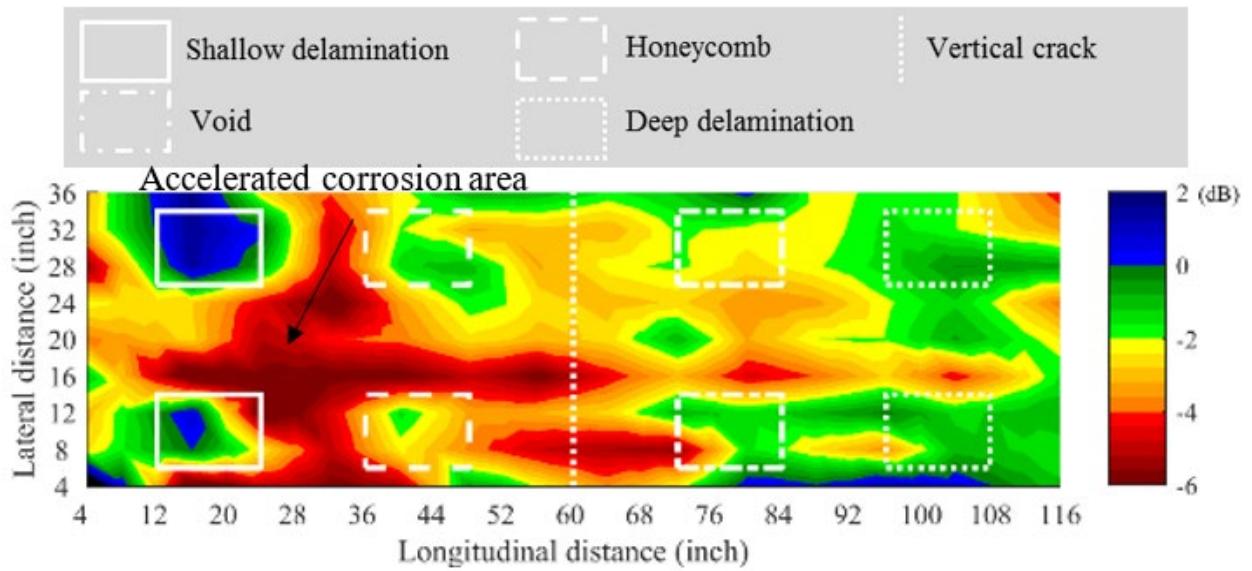
Source: FHWA.

B. S3L.



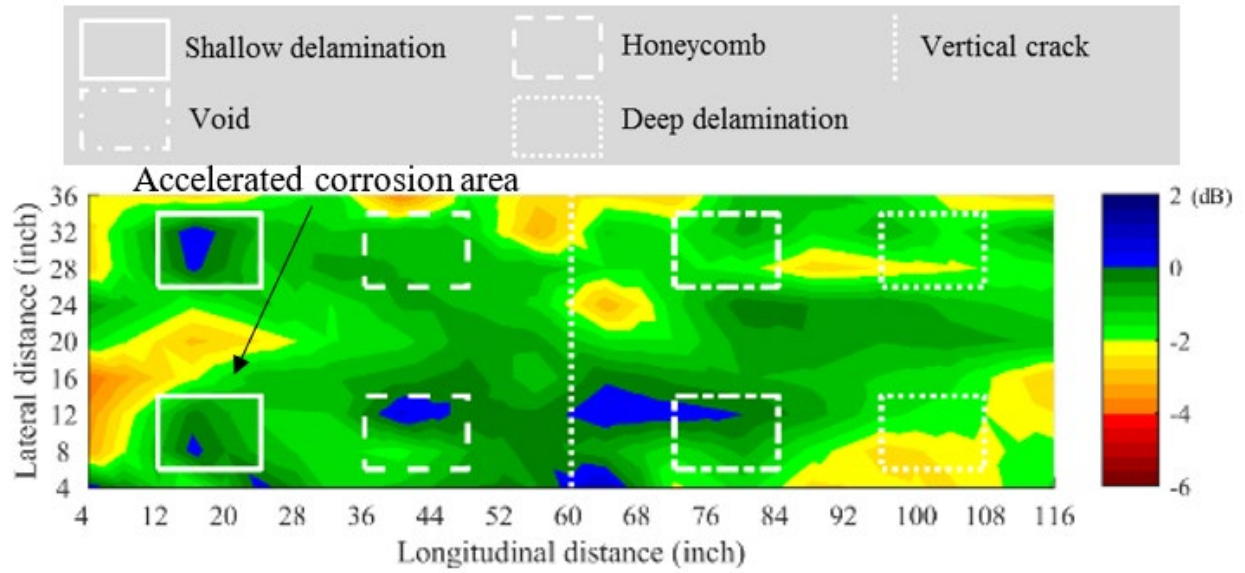
Source: FHWA.

C. S4AS.



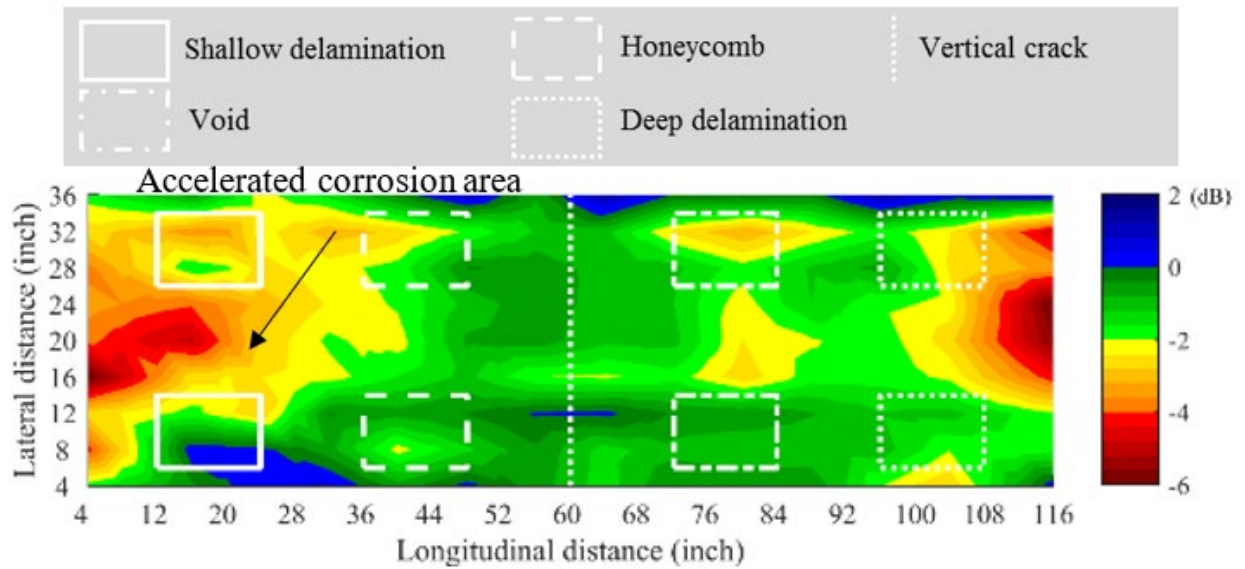
Source: FHWA.

D. S5AL.



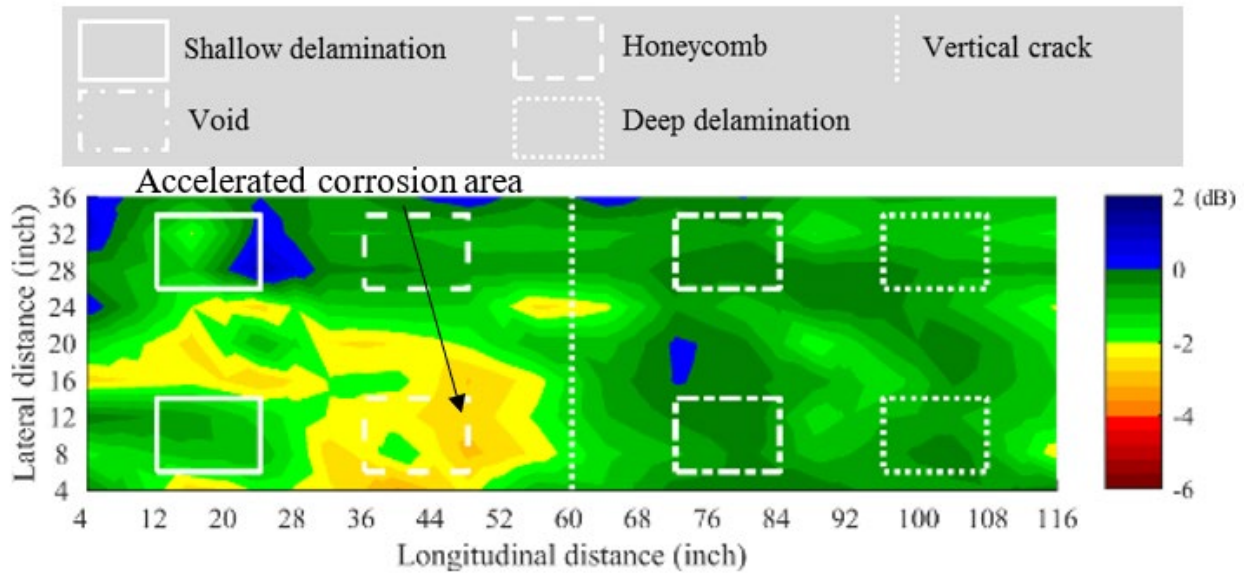
Source: FHWA.

E. S6S.



Source: FHWA.

F. S7A.



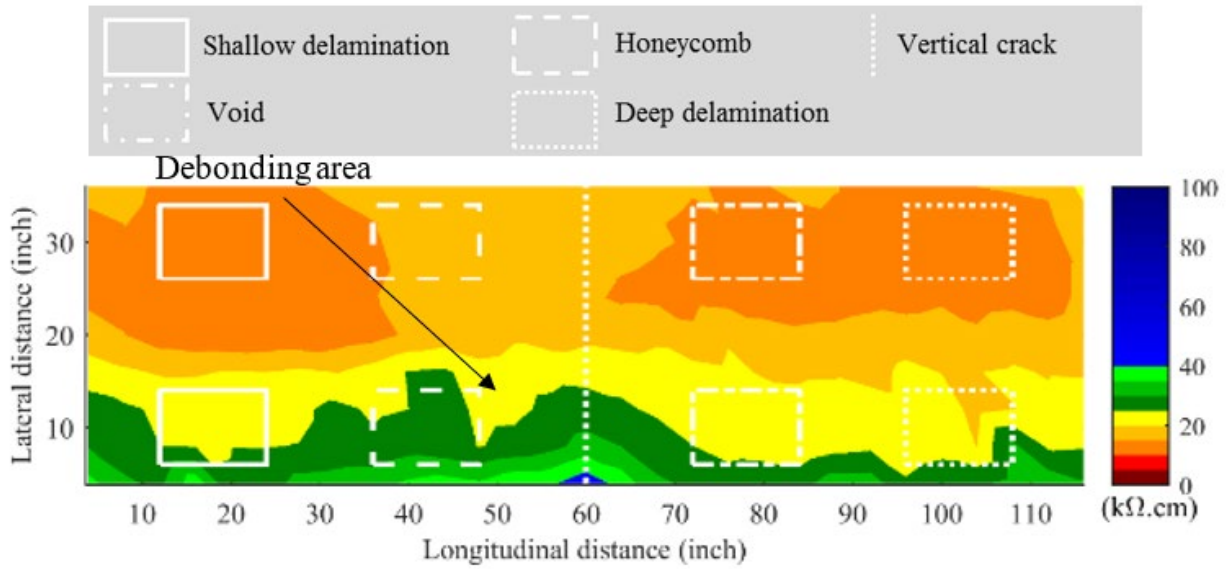
Source: FHWA.

G. S8P.

**Figure 106. Graphs. NDE condition maps with the GPR method.**

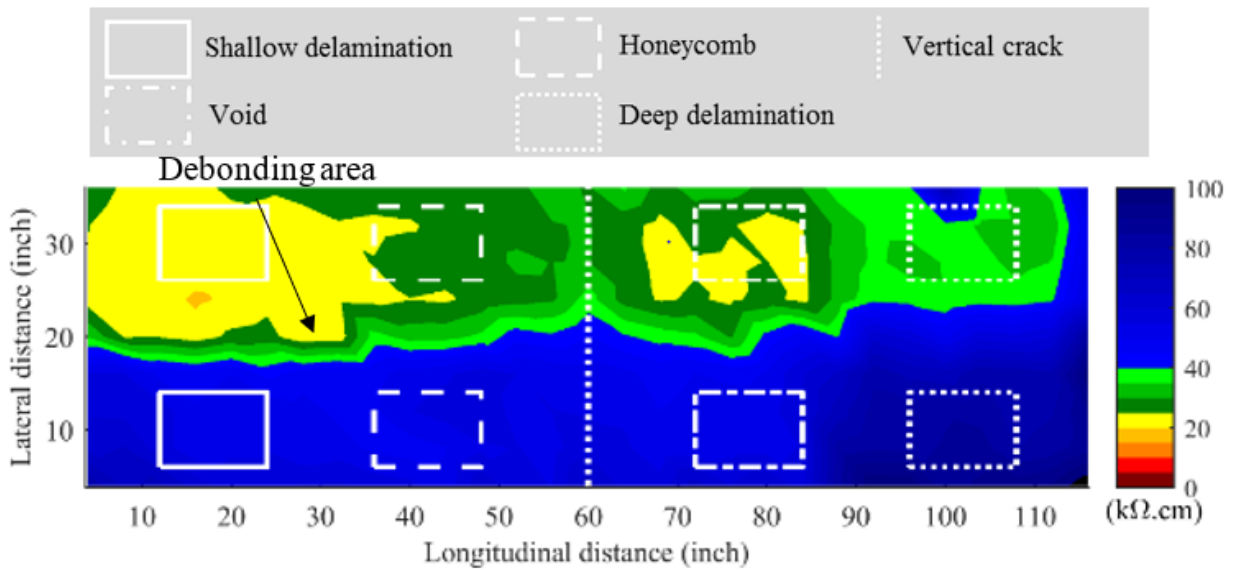
### ER CONDITION MAPS

The condition maps based on the ER method are shown in figure 107-A and figure 107-B. The ER method was ineffective on specimens S1E, S8P, S4AS, S5AL, and S7A with asphalt overlays because of the high resistivity of the overlay materials. The ER method detected debonding in specimens S3L and S6S because of the increased resistivity caused by the air gap in the debonding area but could not detect the elevated chloride content environment in the underlying specimens.



Source: FHWA.  
 Note: No defects detected.

A. S3L.



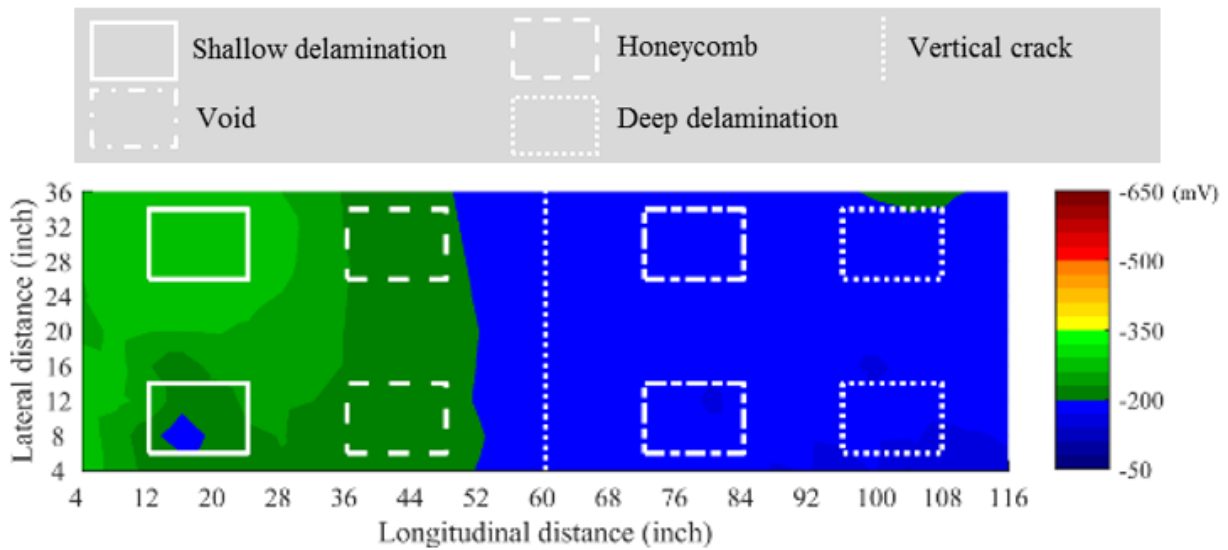
Source: FHWA.

B. S6S.

**Figure 107. Graphs. NDE condition maps with the ER method.**

## HCP CONDITION MAPS

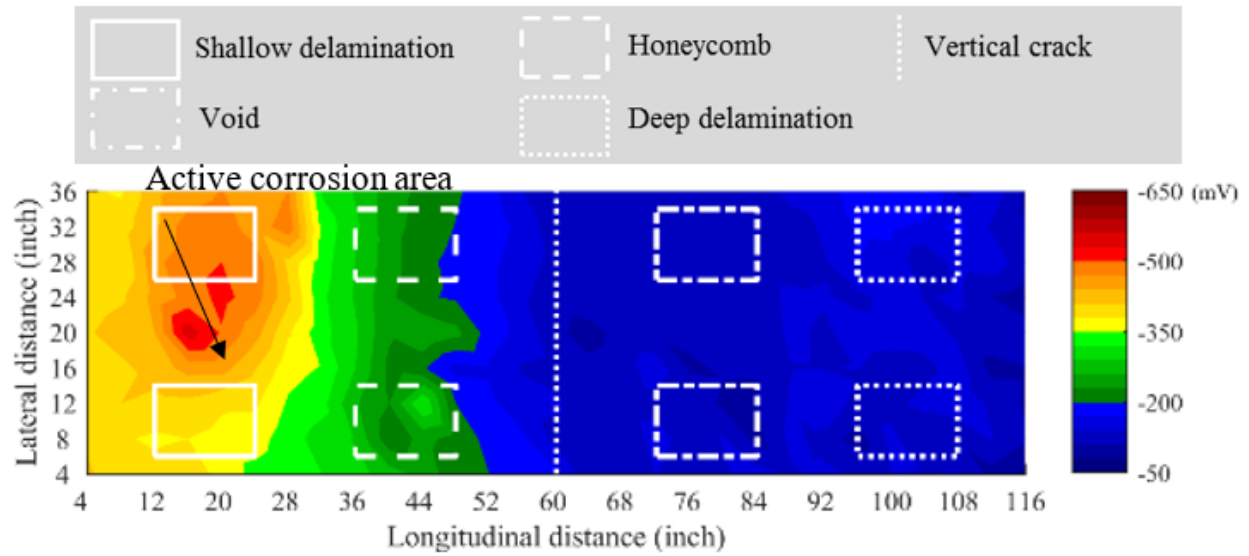
The condition maps based on the HCP method are shown in figure 108-A through figure 108-G. The HCP method detected differences in the electric potentials between the top layer of rebar in different areas. According to ASTM C876-15, potential less than  $-350$  mV means a 90-percent probability of corrosion, and active corrosion was detected in specimens S3L and S8P based on this criterion.<sup>(50)</sup> Although the areas with active corrosion in overlays had lower potential compared to intact areas, the HCP method could not detect active corrosion per ASTM C876-15. Areas with active corrosion for overlays had lower potential than the other two (i.e., latex and polyester polymer) because of the higher electric insulation of the overlay materials.



Source: FHWA.

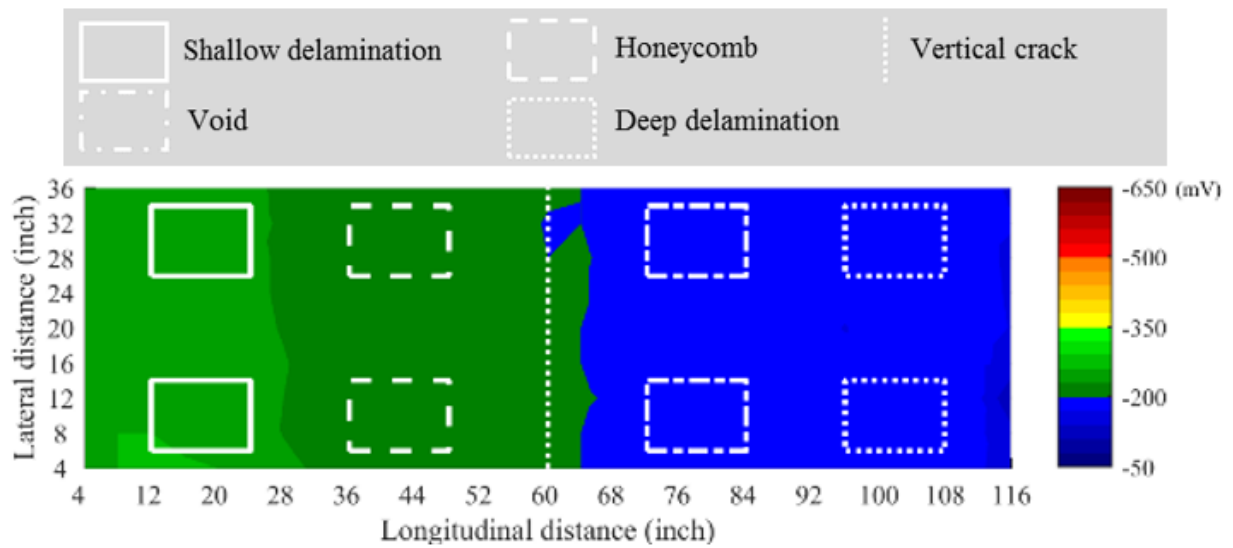
Note: No active corrosion detected.

A. S1E.



Source: FHWA.

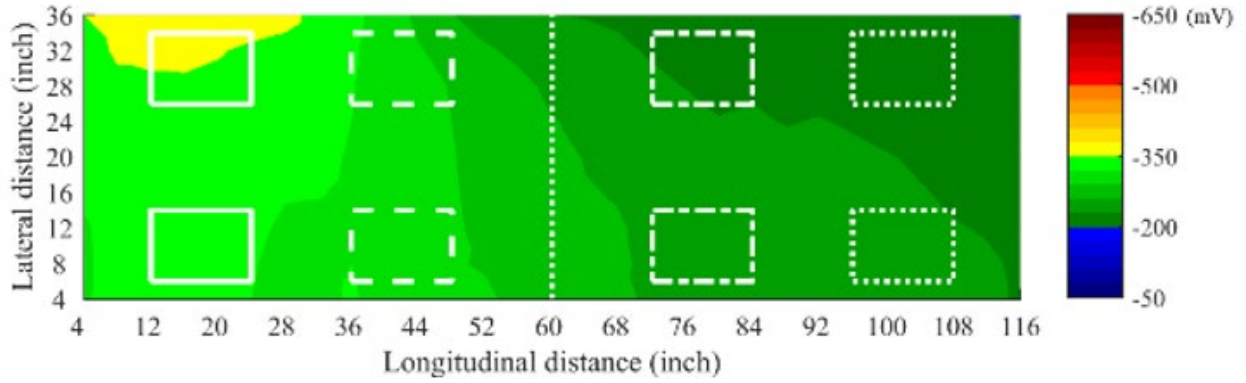
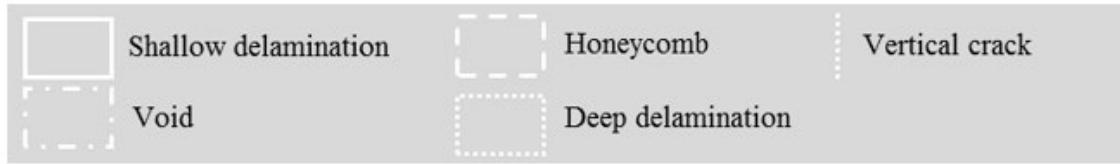
### B. S3L.



Source: FHWA.

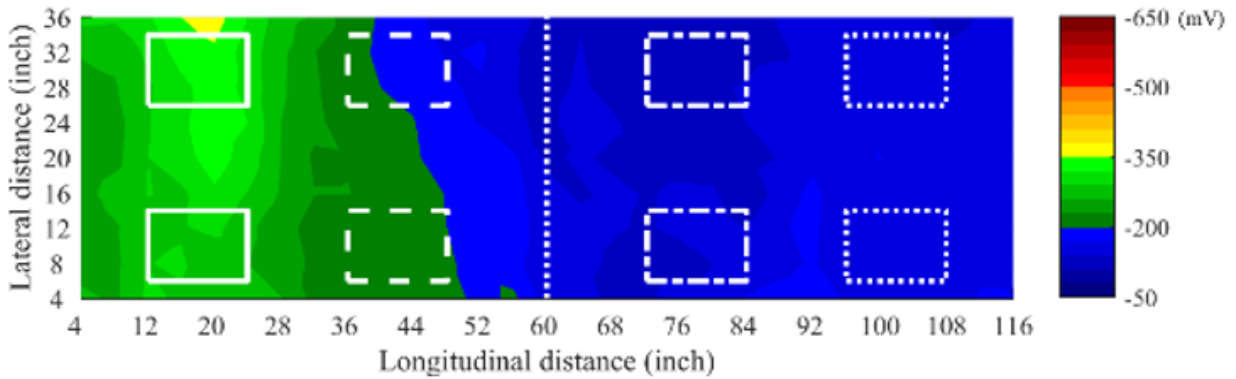
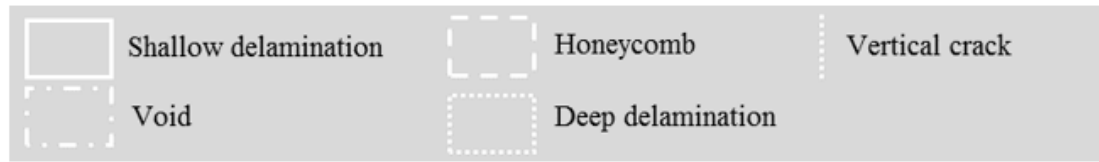
Note: No active corrosion detected.

### C. S4AS.



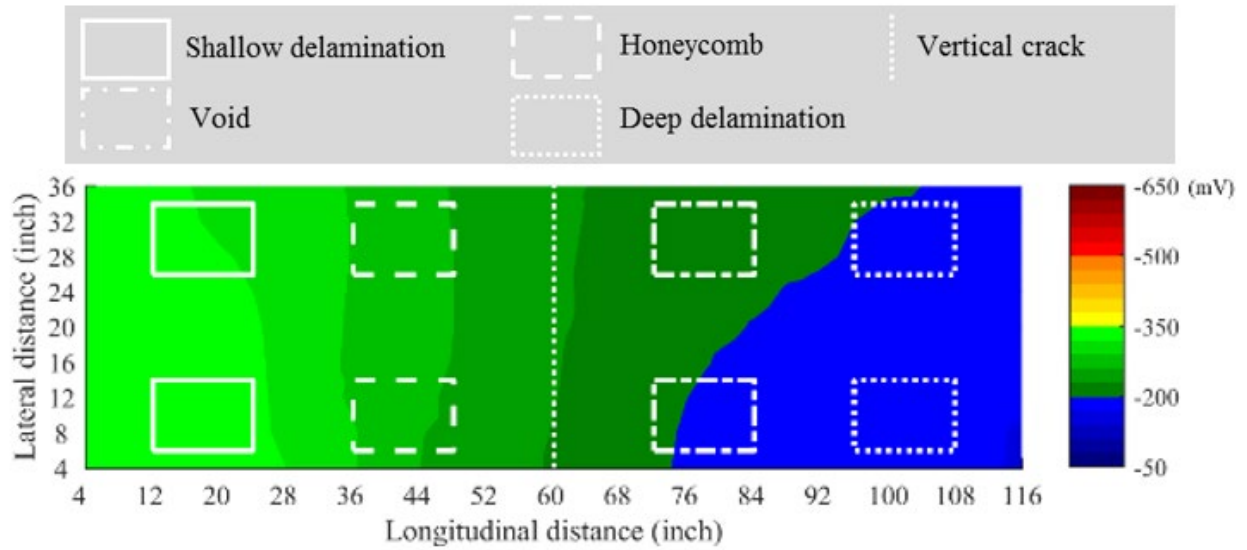
Source: FHWA.  
 Note: No active corrosion detected.

D. S5AL.



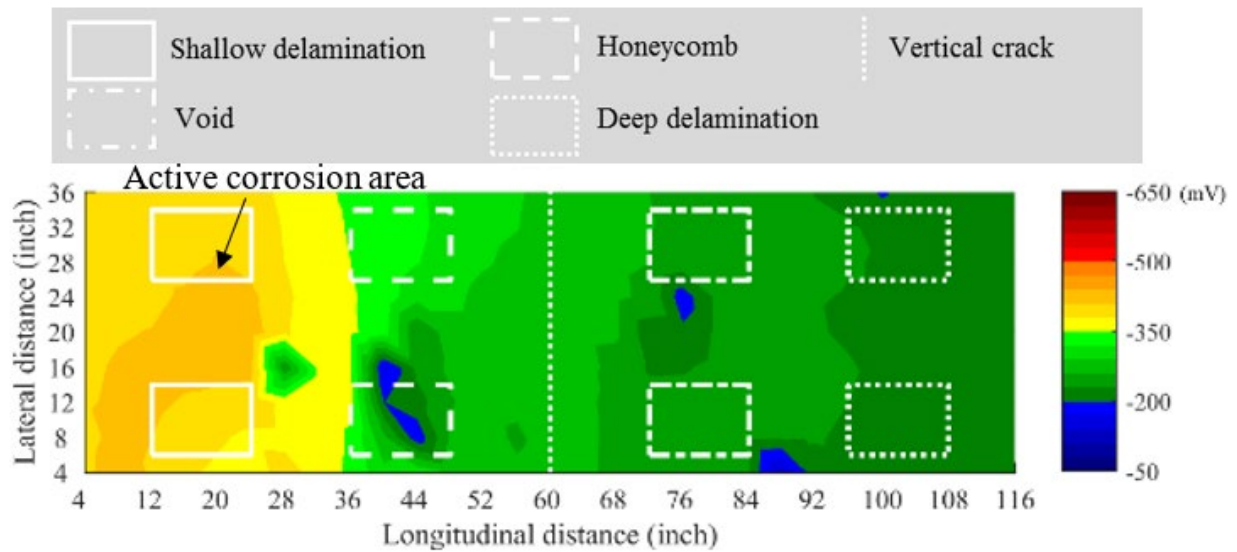
Source: FHWA.  
 Note: No active corrosion detected.

E. S6S.



Source: FHWA.  
 Note: No active corrosion detected.

F. S7A.



Source: FHWA.

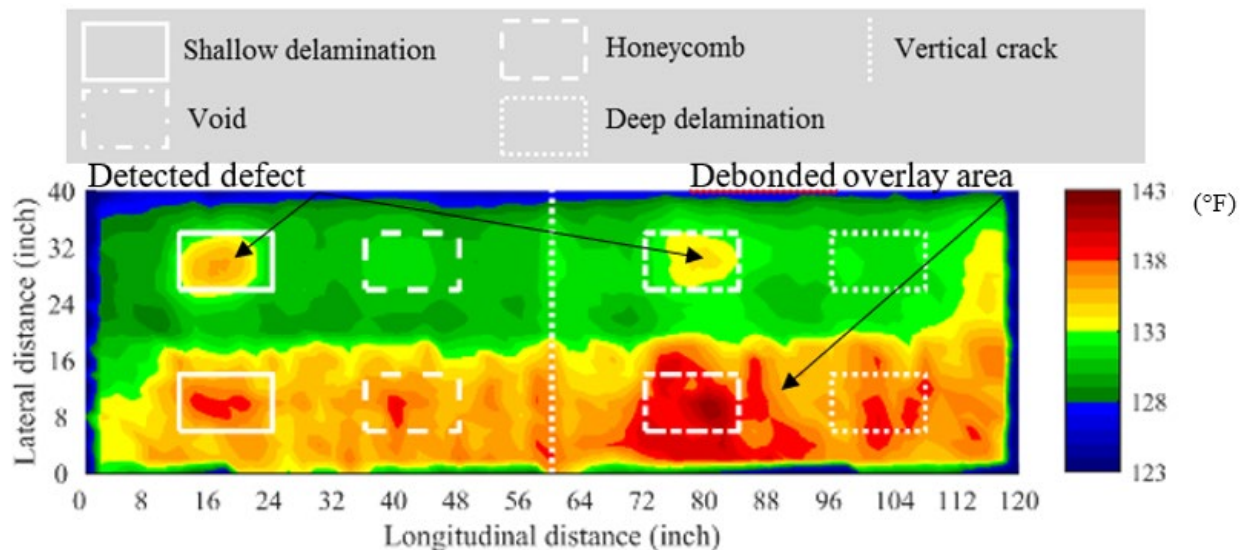
G. S8P.

Figure 108. Graphs. NDE condition maps with HCP.

## IRT CONDITION MAPS

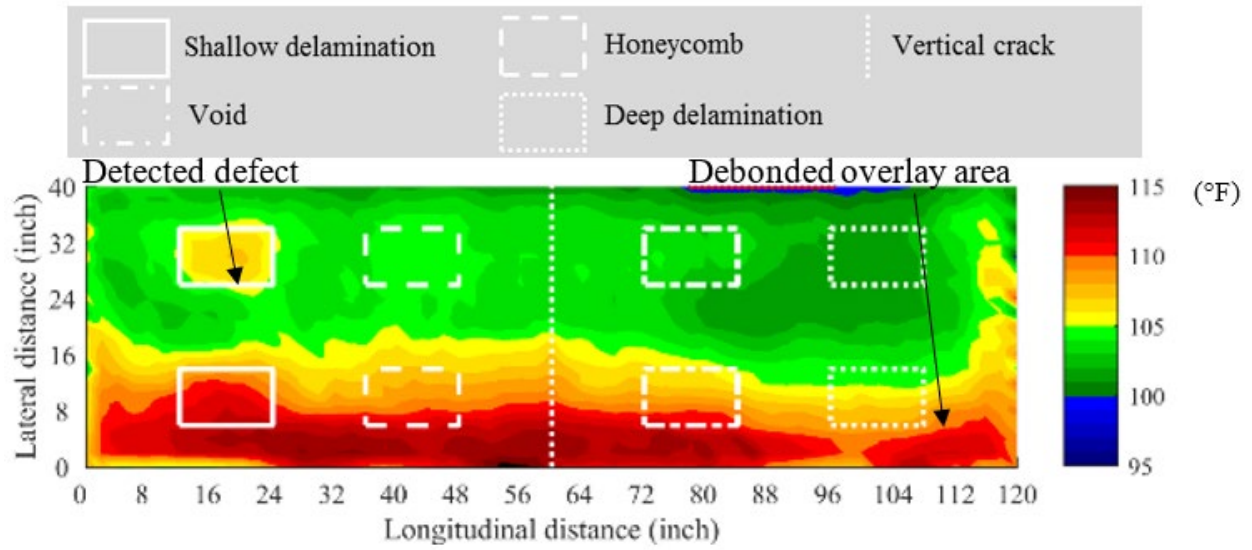
The condition maps of all seven specimens based on the IRT method are shown in figure 109 and figure 110. ASTM D4788-03 suggests testing using the IRT method should be conducted after a specimen was exposed to direct sunlight for a minimum of 3 hr, and that a minimum temperature difference of 33°F be used to differentiate intact areas from those with defects.<sup>(51)</sup> Since the specimens were relatively small compared to a full-scale concrete bridge deck, surface temperatures of the specimens were significantly affected by the boundary condition. Under this circumstance, the temperature difference was increased to 2°F to detect defects. Figure 109-A through Figure 109-G show the results of tests using the IRT method with the surface temperature encountered at 3:00 p.m. The IRT method detected the debonded overlay in all seven specimens with higher temperatures compared to those of the bonded areas. For the defects in bonded areas, the IRT method detected shallow delaminations in specimens S1E, S3L, S4AS, S7A, and S8P and voids in specimens S1E and S8P. The IRT method could not detect honeycombing, deep delaminations, or vertical cracks in bonded areas. For debonded areas, shallow delaminations and voids were detected in specimens S1E and S8P.

The condition maps for the temperature differences between 3:00 p.m. and 11:00 a.m. for all seven specimens are shown in figure 110-A through figure 110-G. The bonded and debonded areas were indistinguishable. For specimens S1E and S8P, bonded areas had greater temperature increases than debonded areas. For specimens S3L, S4AS, S5AL and S6S, bonded areas had lower temperature increases than debonded areas. For specimen S7A, bonded and debonded areas had similar temperature increases. For bonded areas, shallow delaminations were detected in specimens S1E, S3L, S6S, S7A, and S8P, and voids were detected in specimens S1E and S8P. No honeycombing, deep delaminations, or vertical cracks were detected. For debonded areas, shallow delaminations were detected for specimens S6S, S7A, and S8P, but no other defects were detected.



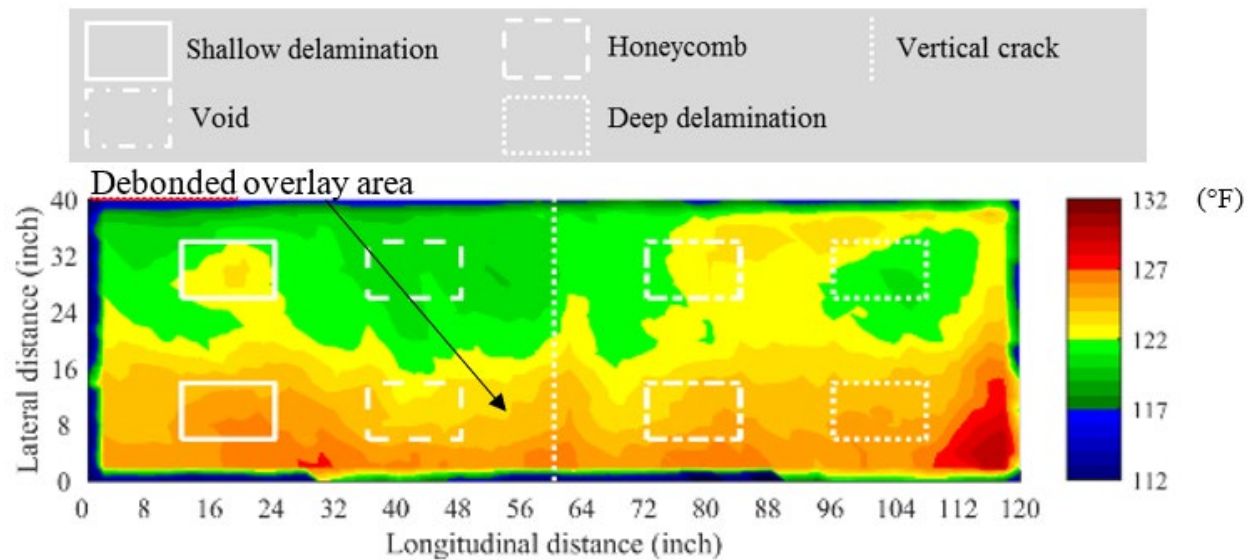
Source: FHWA.

A. S1E.



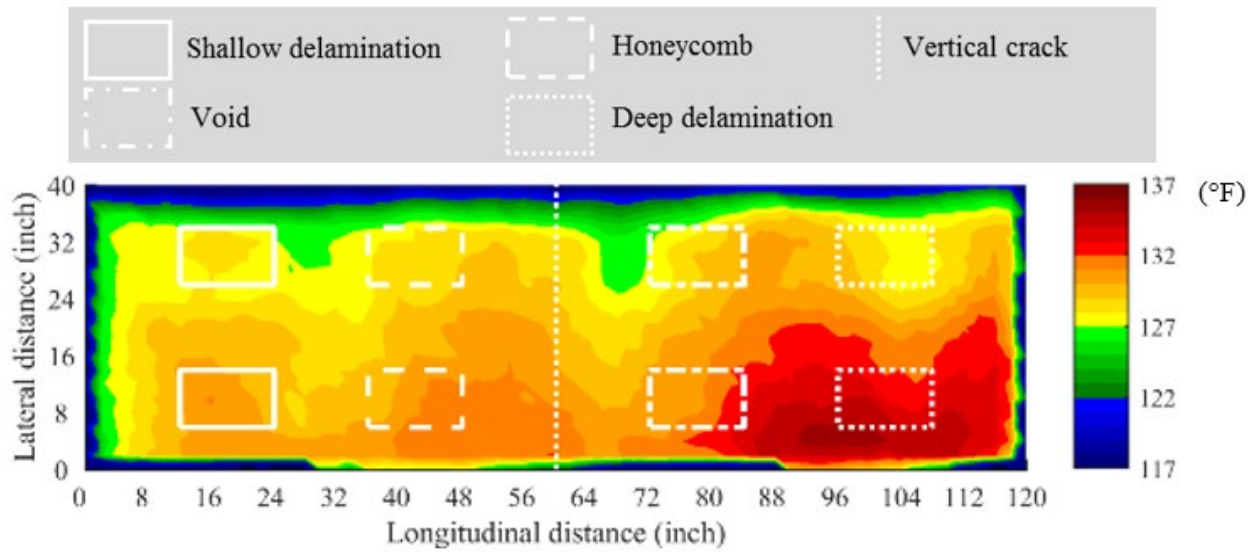
Source: FHWA.

B. S3L.



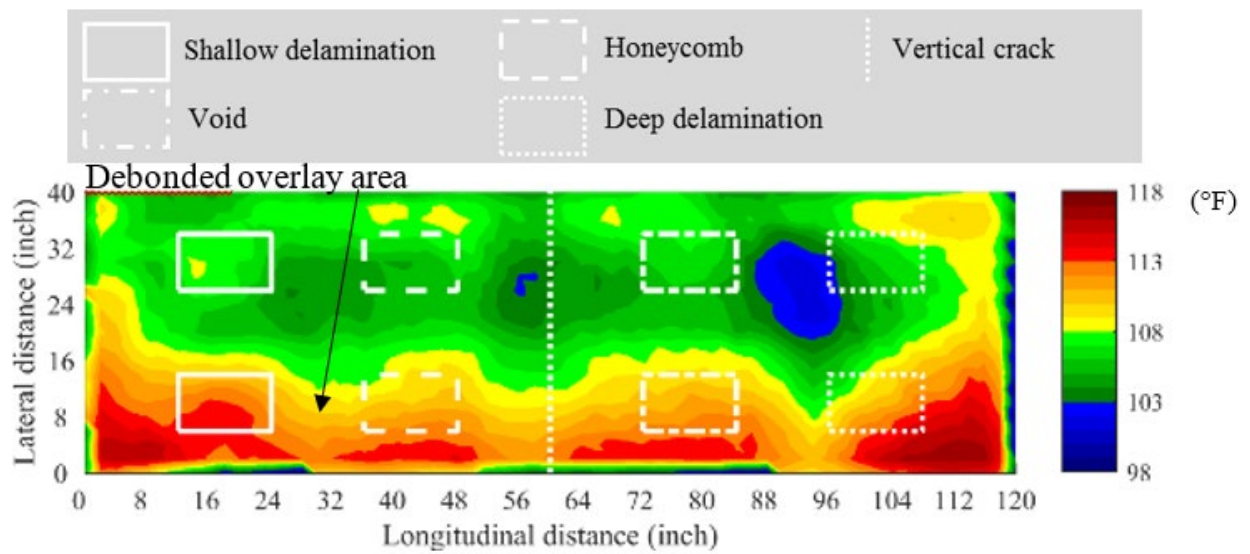
Source: FHWA.

C. S4AS.



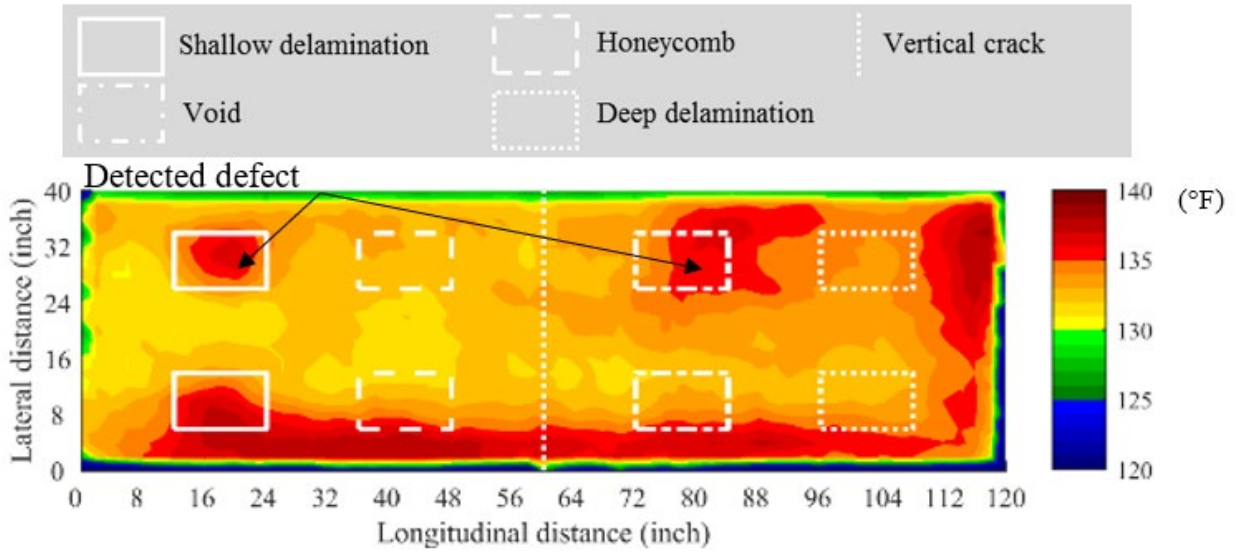
Source: FHWA.  
 Note: No defects detected.

D. S5AL.



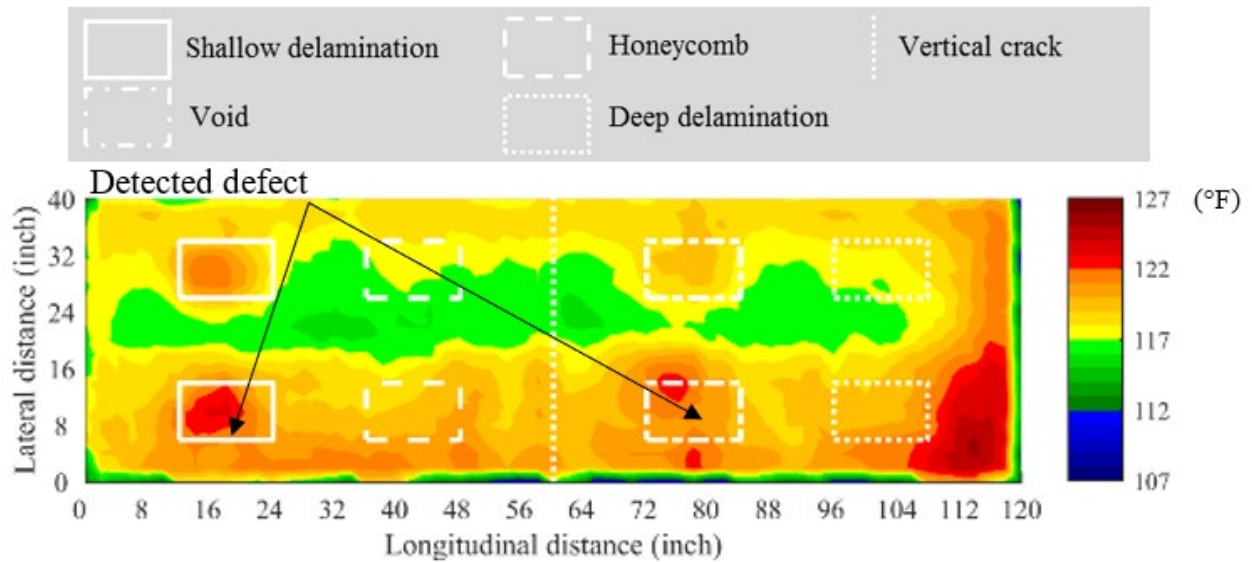
Source: FHWA.

E. S6S.



Source: FHWA.

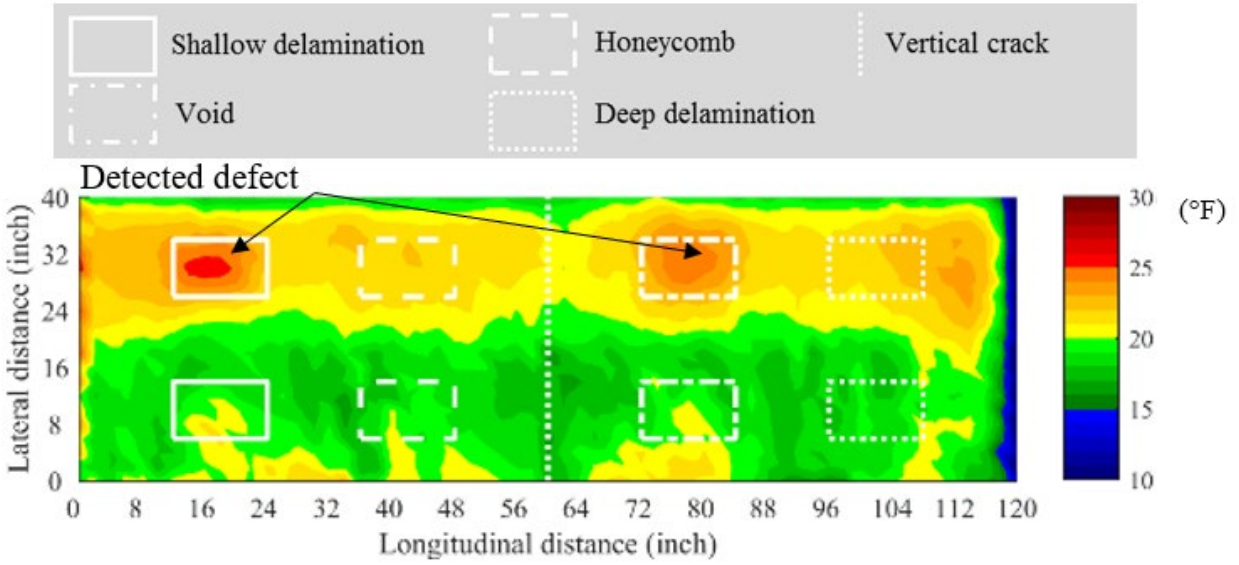
F. S7A.



Source: FHWA.

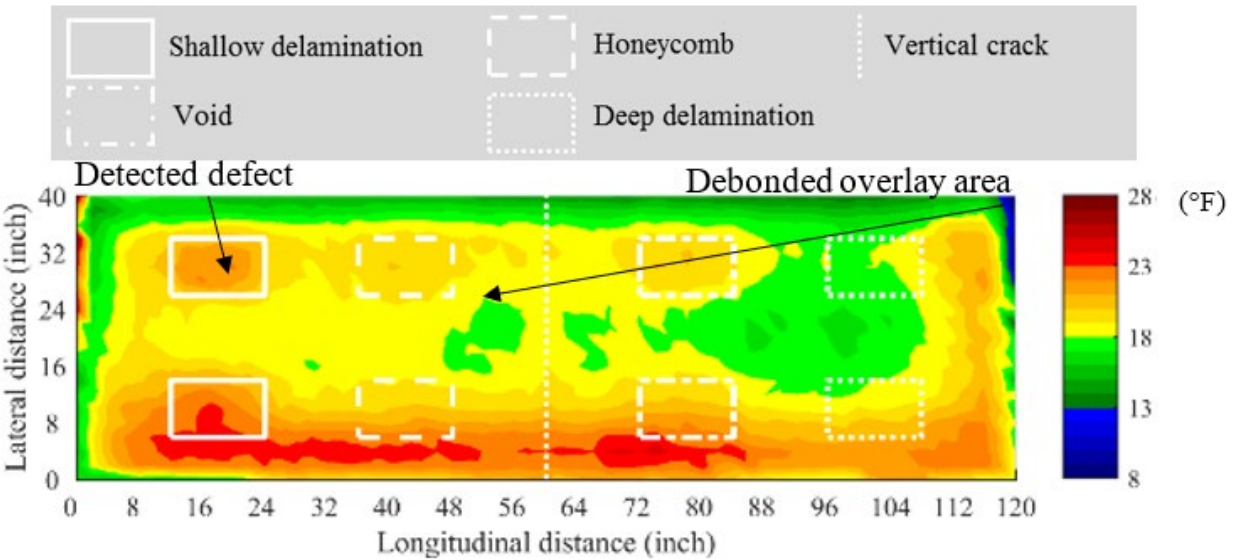
G. S8P.

**Figure 109. Graphs. NDE using the IRT method (temperature at 3:00 p.m.).**



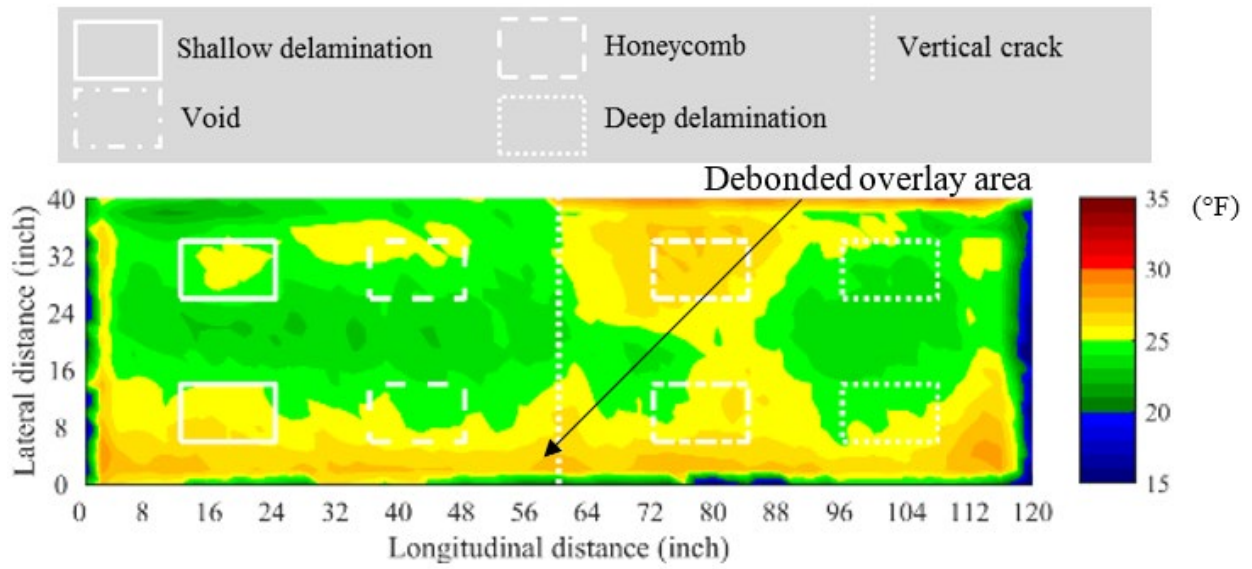
Source: FHWA.

A. S1E.



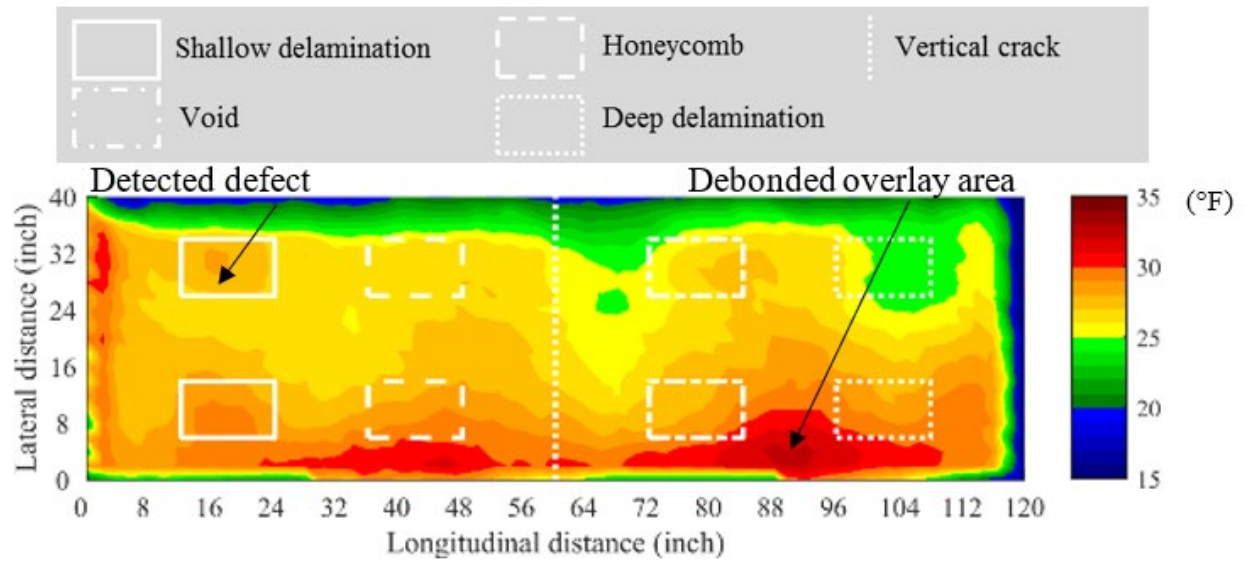
Source: FHWA.

B. S3L.



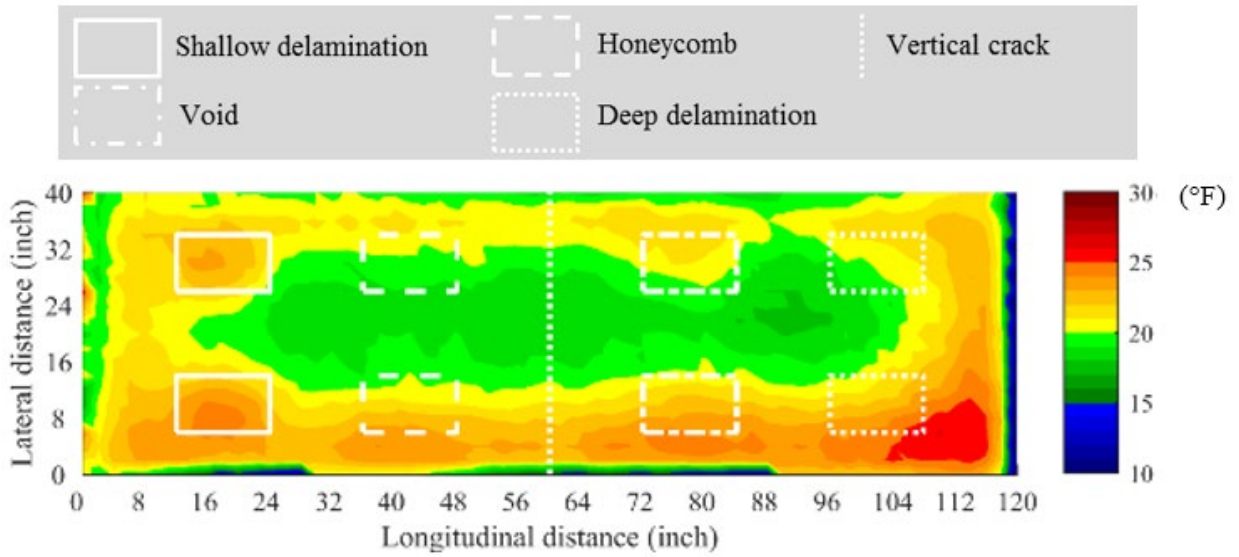
Source: FHWA.

C. S4AS.



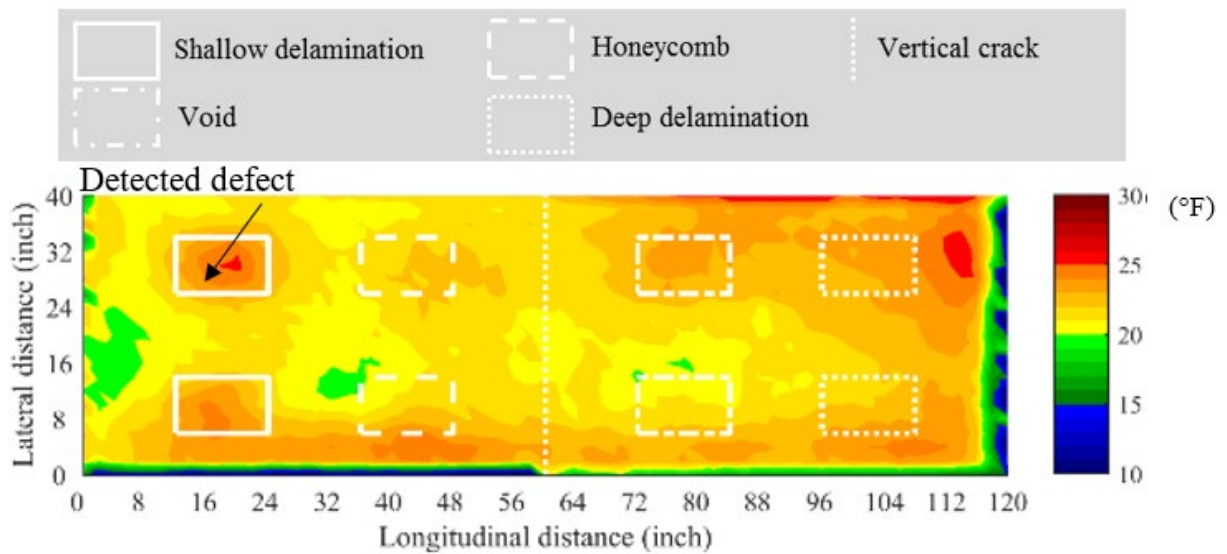
Source: FHWA.

D. S5AL.



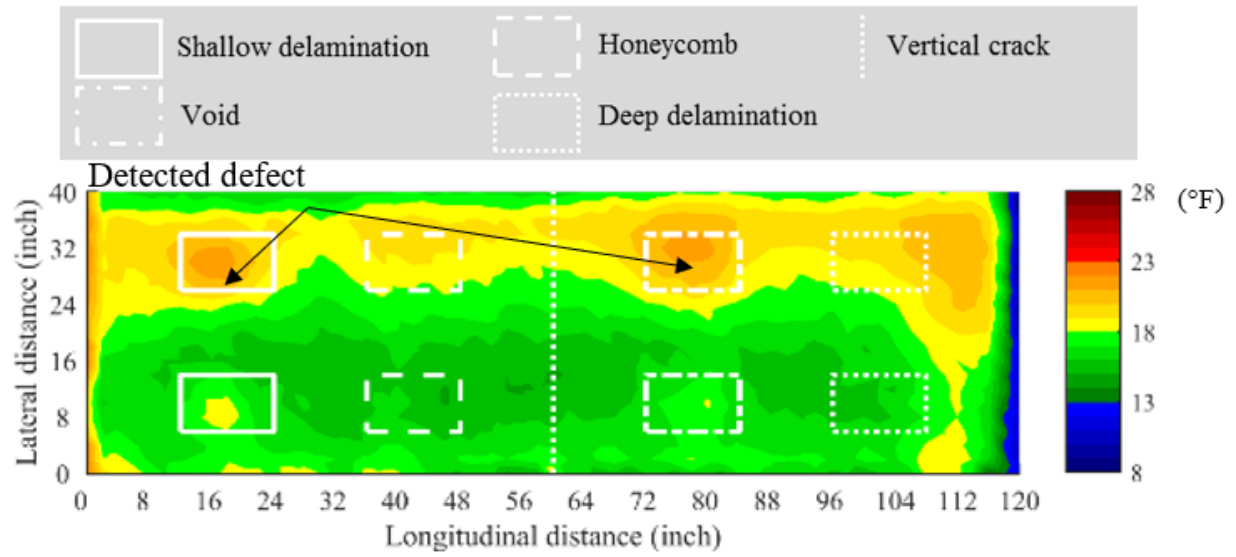
Source: FHWA.  
Note: No defects detected.

E. S6S.



Source: FHWA.

F. S7A.



Source: FHWA.

G. S8P.

**Figure 110. Graphs. NDE using the IRT method (temperature difference from 3:00 to 11:00 a.m.).**

## CHAPTER 10. SUMMARY

This chapter presents the results of seven concrete bridge deck specimens with overlays obtained using nine NDE technologies. The results are summarized in table 10 through table 16 and as follows:

- The sounding method detected debonding in all seven types of overlays but could not detect defects in any of the underlying specimens.
- The USW method detected debonding in terms of higher moduli for epoxy and polyester polymer overlays and lower moduli for latex and silica fume-modified concrete and asphalt overlays compared to the moduli in bonded areas. Lower and higher moduli are not the real moduli of the material but only the apparent moduli obtained from testing. For bonded overlays, the stress waves propagated into the underlying specimens. The USW method detected shallow and deep delaminations in underlying specimens with epoxy, LMC, silica fume-modified concrete, and polyester polymer overlays. The USW method detected honeycombing and voids for epoxy, LMC, and polyester polymer overlays. The USW method could not detect defects in the underlying specimens through the bonded asphalt overlays even though the asphalt overlays became more linear and elastic at low temperatures (i.e., 32°F or below).
- The IE method detected debonding, shallow and deep delaminations, honeycombing, and voids in the underlying specimens with bonded epoxy, LMC, silica fume-modified concrete, polyester polymer, and asphalt without a waterproof membrane overlays. Tests using the IE method for asphalt overlays should be conducted in colder weather with temperatures of 32°F or lower. This temperature threshold was suggested based on a particular type of hot-mix asphalt commonly used in Virginia, and it could vary with different asphalt mixtures (e.g., containing steel slag or warm-mix asphalt). Although tests using the IE method were conducted at low temperatures for asphalt with a sheet membrane overlay and asphalt with a liquid membrane overlay, the IE method detected overlay debonding and shallow delaminations in the underlying specimens in bonded areas but could not detect other defects.
- The UT method detected shallow and deep delaminations and voids in the underlying specimens with bonded polyester polymer and latex and silica fume-modified concrete overlays. It was challenging for the UT method to clearly detect honeycombing because honeycombing has a wave impedance very close to that of intact concrete and the reflections from honeycombing were too weak to detect. For epoxy overlays, the UT method could not detect any defects in the underlying specimens under bonded areas. USWs were completely reflected in debonded areas of epoxy, latex and silica fume-modified concrete, and polyester polymer overlays. Overlay debonding was clearly detected, but the presence of any underlying defects in the specimens could not be detected. Although asphalt overlays became more linear and elastic at low temperatures (i.e., 32°F or below), the UT method could not detect any defects in bonded areas or distinguish between overlay bonding and debonding.

- The IR method detected debonding in all seven types of overlays but could not detect defects in any specimens because of the small size-to-depth ratios of the artificial defects.
- C- and B-scans with the GPR method detected shallow delaminations, voids, honeycombing, and deep delaminations in both bonded and debonded areas of the seven specimens. GPR B-scans detected the overlay–specimen interface for all three asphalt overlays and the silica fume-modified concrete overlay. The GPR could not detect overlay debonding or vertical cracks in any of the seven specimens. The condition maps based on the GPR method constructed by reflection from the upper rebar mat quantified the elevated chloride content environment in all specimens except those with silica fume-modified concrete and polyester polymer overlays. The condition maps based on the GPR method could not detect shallow delaminations because they were simulated by air gaps between two pieces of transparent thermoplastic and were not induced by corrosion.
- The ER method detected debonding in latex and silica fume-modified concrete overlays. Bonded areas had higher resistivity measurements compared to those of debonded areas because of the significant increased resistivity caused by air gaps in debonded areas. The ER method could not detect the elevated chloride content environment in underlying specimens. The ER method was ineffective for epoxy, polyester polymer, and asphalt overlays due to the high resistivity of the overlay materials.
- The HCP method detected active corrosion of rebar in underlying specimens with LMC and polyester overlays in both bonded and debonded areas. Even though areas with active corrosion had lower potentials compared to intact areas, the HCP method could not detect active corrosion in the other inspected overlays because of the electric insulation of the overlay materials.
- The IRT method detected debonding in all seven types of overlays, shallow delaminations in bonded areas in all specimens except asphalt overlays with liquid membranes, and voids in bonded area in specimens with thin overlays (e.g., epoxy and polyester polymer overlays). In debonded areas, the IRT method detected shallow delaminations in specimens with epoxy, polyester polymer, and asphalt without a waterproof membrane overlays, as well as voids in specimens with epoxy and polyester polymer overlays. The IRT method could not detect honeycombing or deep delaminations in any specimens.

**Table 10. NDE technologies for concrete bridge decks with epoxy overlays (S1E).**

Method	Defect							
	Overlay Debonding	Shallow Delamination	Honeycombing	Void	Deep Delamination	Vertical Crack	Active Rebar Corrosion	Concrete Corrosion Environment
Sounding	Yes	No	No	No	No	No	No	No
USW	Yes	Yes	Yes	Yes	Yes	No	No	No
IE	Yes	Yes	Yes	Yes	Yes	No	No	No
UT-MIRA	Yes	No	No	No	No	No	No	No
UT-EyeCon	Yes	No	No	No	No	No	No	No
IR	Yes	No	No	No	No	No	No	No
GPR	No	Yes*	Yes*	Yes*	Yes*	No	No	Yes*
ER	No	No	No	No	No	No	No	No
HCP	No	No	No	No	No	No	No	No
IRT	Yes	Yes*	No	Yes*	No	No	No	No

\*NDE method detected defects in a specimen through the bonded and debonded overlay.

**Table 11. NDE technologies for concrete bridge decks with LMC overlays (S3L).**

Method	Defect							Concrete Corrosion Environment
	Overlay Debonding	Shallow Delamination	Honeycombing	Void	Deep Delamination	Vertical Crack	Active Rebar Corrosion	
Sounding	Yes	No	No	No	No	No	No	No
USW	Yes	Yes	Yes	Yes	Yes	No	No	No
IE	Yes	Yes	Yes	Yes	Yes	No	No	No
UT-MIRA	Yes	Yes	Yes	Yes	Yes	No	No	No
UT-EyeCon	Yes	Yes	Yes	Yes	Yes	No	No	No
IR	Yes	No	No	No	No	No	No	No
GPR	No	Yes*	Yes*	Yes*	Yes*	No	No	Yes*
ER	Yes	No	No	No	No	No	No	No
HCP	No	No	No	No	No	No	Yes	No
IRT	Yes	Yes	No	No	No	No	No	No

\*NDE method detected defects in a specimen through the bonded and debonded overlay.

**Table 12. NDE technologies for concrete bridge decks with sheet membrane asphalt overlays (S4AS).**

Method	Defect							
	Overlay Debonding	Shallow Delamination	Honeycombing	Void	Deep Delamination	Vertical Crack	Active Rebar Corrosion	Concrete Corrosion Environment
Sounding	Yes	No	No	No	No	No	No	No
USW	Yes	No	No	No	No	No	No	No
IE	Yes	No	No	No	No	No	No	No
UT	No	No	No	No	No	No	No	No
IR	Yes	No	No	No	No	No	No	No
GPR	No	Yes*	Yes*	Yes*	Yes*	No	No	Yes*
ER	No	No	No	No	No	No	No	No
HCP	No	No	No	No	No	No	No	No
IRT	Yes	Yes	No	No	No	No	No	No

\*NDE method detected defects in a specimen through the bonded and debonded overlay.

**Table 13. NDE technologies for concrete bridge decks with liquid membrane asphalt overlays (S5AL).**

Method	Defect							
	Overlay Debonding	Shallow Delamination	Honeycombing	Void	Deep Delamination	Vertical Crack	Active Rebar Corrosion	Concrete Corrosion Environment
Sounding	Yes	No	No	No	No	No	No	No
USW	Yes	No	No	No	No	No	No	No
IE	Yes	No	No	No	No	No	No	No
UT	No	No	No	No	No	No	No	No
IR	Yes	No	No	No	No	No	No	No
GPR	No	Yes*	Yes*	Yes*	Yes*	No	No	Yes*
ER	No	No	No	No	No	No	No	No
HCP	No	No	No	No	No	No	No	No
IRT	Yes	No	No	No	No	No	No	No

\*NDE method detected defects in a specimen through the bonded and debonded overlay.

**Table 14. NDE technologies for concrete bridge decks with silica fume-modified overlays (S6S).**

Method	Defect							Concrete Corrosion Environment
	Overlay Debonding	Shallow Delamination	Honeycombing	Void	Deep Delamination	Vertical Crack	Active Rebar Corrosion	
Sounding	Yes	No	No	No	No	No	No	No
USW	Yes	Yes	No	No	Yes	No	No	No
IE	Yes	Yes	Yes	Yes	Yes	No	No	No
UT-MIRA	Yes	Yes	Yes	Yes	Yes	No	No	No
UT-EyeCon	Yes	Yes	Yes	Yes	Yes	No	No	No
IR	Yes	No	No	No	No	No	No	No
GPR	No	Yes*	Yes*	Yes*	Yes*	No	No	No
ER	Yes	No	No	No	No	No	No	No
HCP	No	No	No	No	No	No	No	No
IRT	Yes	Yes	No	No	No	No	No	No

\*NDE method detected defects in a specimen through the bonded and debonded overlay.

**Table 15. NDE technologies for concrete bridge decks with asphalt without waterproof membrane overlays (S7A).**

Method	Defect							
	Overlay Debonding	Shallow Delamination	Honeycombing	Void	Deep Delamination	Vertical Crack	Active Rebar Corrosion	Concrete Corrosion Environment
Sounding	Yes	No	No	No	No	No	No	No
USW	Yes	No	No	No	No	No	No	No
IE*	Yes	Yes	Yes	Yes	Yes	No	No	No
UT-MIRA	No	No	No	No	No	No	No	No
IR	Yes	No	No	No	No	No	No	No
GPR	No	Yes*	Yes*	Yes*	Yes*	No	No	Yes*
ER	No	No	No	No	No	No	No	No
HCP	No	No	No	No	No	No	No	No
IRT	Yes	Yes*	No	No	No	No	No	No

\*NDE method detected defects in a specimen through the bonded and debonded overlay.

‡NDE method only worked in cold weather (i.e., 32°F or below).

**Table 16. NDE technologies for concrete bridge decks with PPC overlays (S8P).**

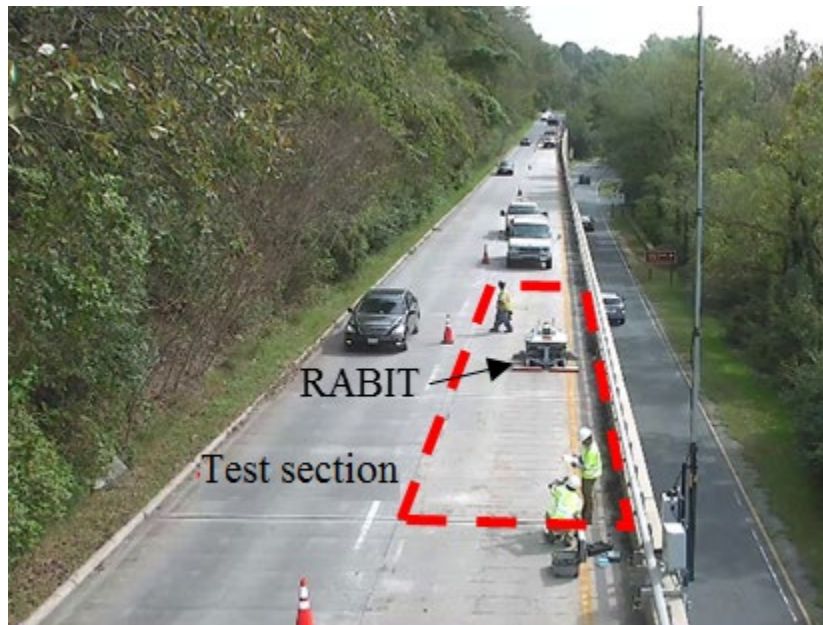
Method	Defects							
	Overlay Debonding	Shallow Delamination	Honeycombing	Void	Deep Delamination	Vertical Crack	Active Rebar Corrosion	Concrete Corrosion Environment
Sounding	Yes	No	No	No	No	No	No	No
USW	Yes	Yes	Yes	Yes	Yes	No	No	No
IE	Yes	Yes	Yes	Yes	Yes	No	No	No
UT	Yes	Yes	No	Yes	Yes	No	No	No
UT-EyeCon	Yes	Yes	No	Yes	Yes	No	No	No
IR	Yes	No	No	No	No	No	No	No
GPR	No	Yes*	Yes*	Yes*	Yes*	No	No	No
ER	No	No	No	No	No	No	No	No
HCP	No	No	No	No	No	No	Yes	No
IRT	Yes	Yes*	No	Yes*	No	No	No	No

\*NDE method detected defects in a specimen through the bonded and debonded overlay.

## CHAPTER 11. FIELD VALIDATION

### CLARA BARTON PARKWAY CANTILEVER STRUCTURE

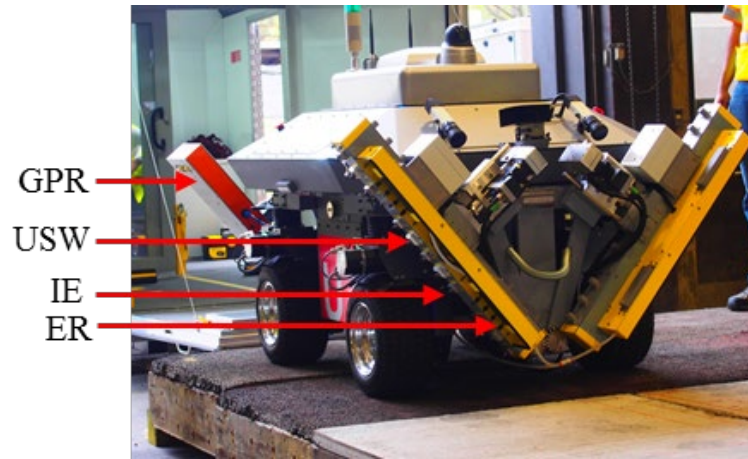
The Clara Barton Parkway cantilever structure was built in the 1950s, and the overlay was placed in 1995 with 4- to 6-inch lightweight fiber RC after removing deteriorated concrete from the cantilever surface, as shown in figure 111. The concrete of the cantilever structure had a specified minimum compressive strength of 3,000 psi, and the overlay concrete had a specified minimum compressive strength of 4,000 psi. A 10 ft wide and 100 ft long section of the Clara Barton Parkway cantilever structure was tested with the RABIT™ bridge deck assessment tool, as shown in figure 111.



Source: FHWA.

**Figure 111. Photo. Test section of the Clara Barton Parkway cantilever structure.**

RABIT used four NDE technologies: IE, USW, GPR, and ER, as shown in figure 112. RABIT moved every 2 ft in the longitudinal direction and required two passes to cover the entire section.



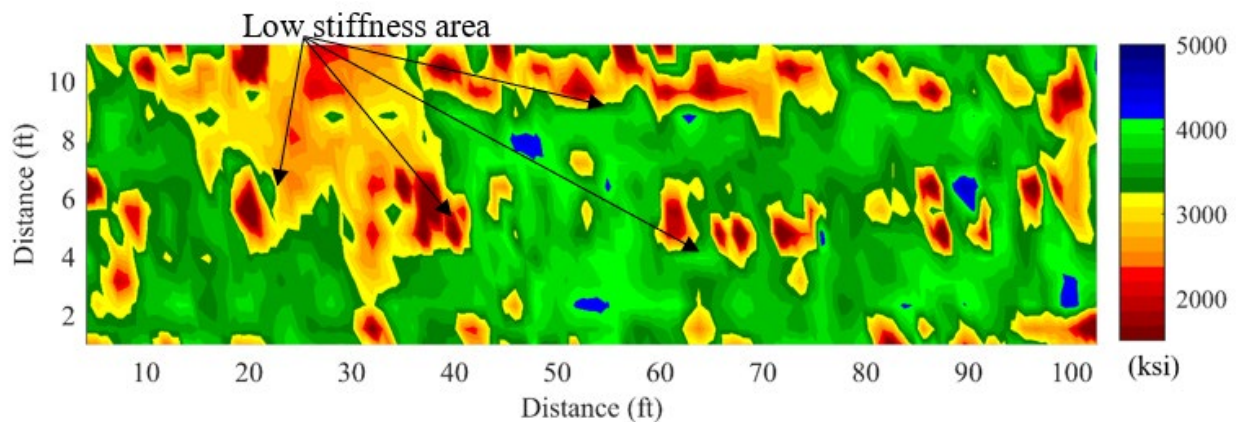
Source: FHWA.

**Figure 112. Photo. RABIT.**

Data were automatically processed by the RABIT software, and four NDE condition maps were generated for the four techniques, as shown in figure 113 through figure 116.

The USW method employed the dispersion phenomenon of surface waves (i.e., phase velocity as a function of frequency or wavelength) to obtain an apparent modulus from each measurement location. An area with lower moduli compared to other areas indicated a defect (e.g., delamination or void).

The condition map based on the moduli measured with the USW method is shown in figure 116. The USW method detected a large area of delamination from 15 to 40 ft in the longitudinal direction.

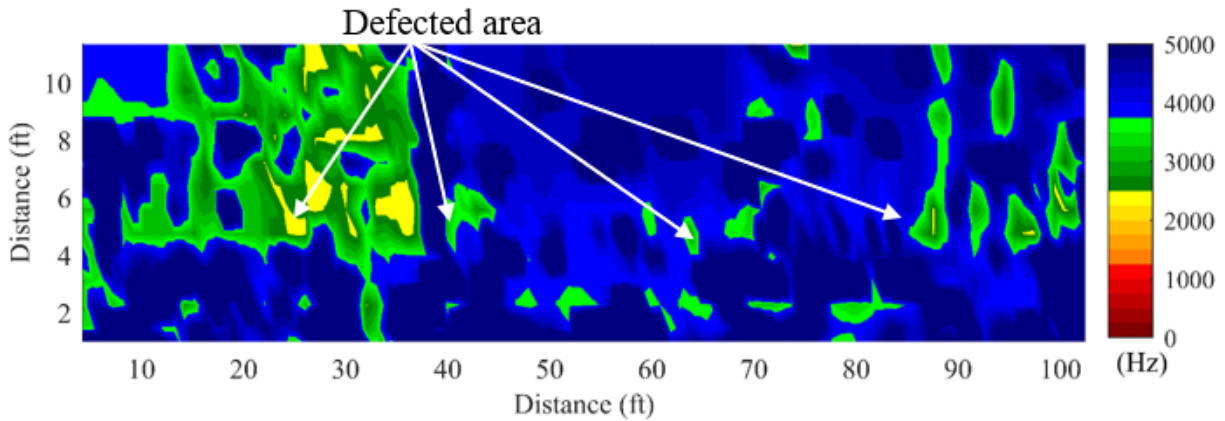


Source: FHWA.

**Figure 113. Graph. NDE condition map with the USW method.**

The IE method is based on the transient resonances caused by multiple reflections of stress waves between the top surface of a concrete bridge deck and a reflector (i.e., defect). Areas with defects have different dominant frequencies of their transient resonance than those of intact areas. The condition map based on the dominant frequencies measured by the IE method is

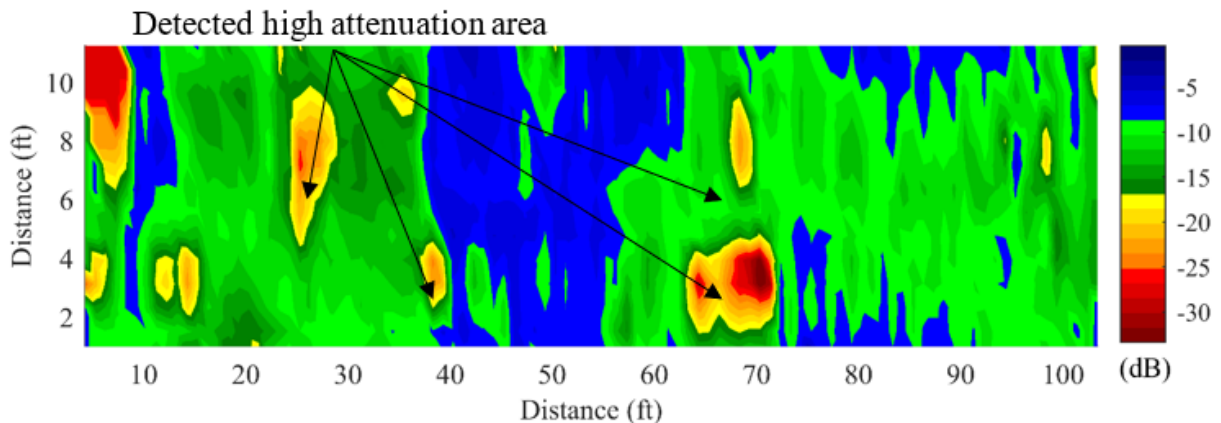
shown in figure 117. The IE method detected a large area of delamination from 15 to 40 ft in the longitudinal direction. The area with detected delamination showed lower frequencies than intact areas. Intact areas had the frequency of the thickness mode at about 7 kHz, while areas with delamination had the dominant flexural mode with a frequency at about 3 kHz.



Source: FHWA.

**Figure 114. Graph. NDE condition map with the IE method.**

The GPR method transmitted EM waves into the concrete and recorded reflected EM waves when the  $\epsilon_r$  of reflectors (e.g., rebar, delamination) differed from those of concrete. The GPR method measured the attenuation of EM waves reflected from the top layer rebar and presented the results in a condition map to quantify the severity of the corrosive environment. The condition map using the GPR method based on the attenuation of the reflected waves from the top layer rebar is shown in figure 118. The condition map using the GPR method detected the high attenuation areas with elevated chloride contents from 0 to 40 ft and from 60 to 100 ft in the longitudinal direction.

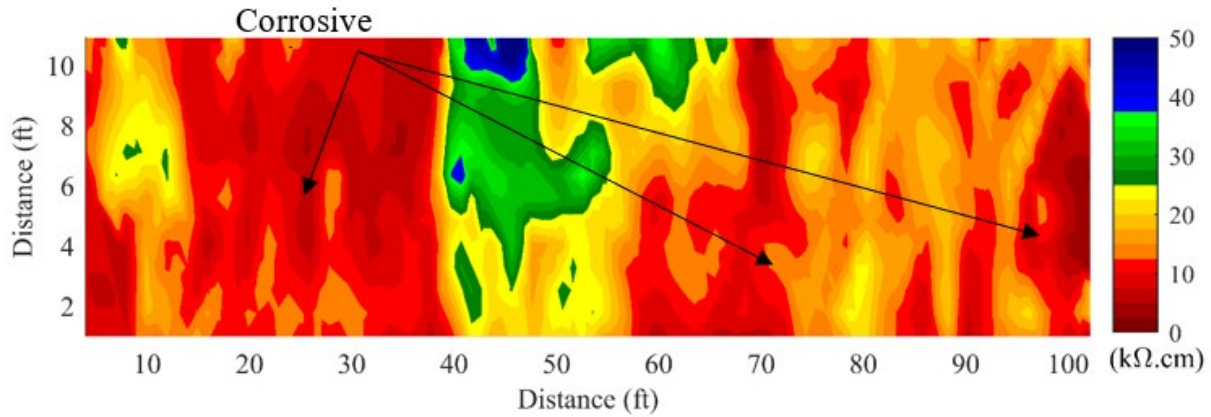


Source: FHWA.

**Figure 115. Graph. NDE condition map with the GPR method.**

The ER method measured concrete resistivity using a Wenner probe with current applied between the outer electrodes and potential measured between the two inner probes. The resistivity was used to characterize concrete's susceptibility to corrosion by characterizing its

corrosive environment because the elevated chloride content of a corrosive environment in the concrete decreases the ER of concrete. Figure 119 shows the condition map based on the resistivity measured by the ER method. The ER method detected low resistivity areas with elevated chloride contents from 0 to 40 ft and from 50 to 100 ft in the longitudinal direction.



Source: FHWA.

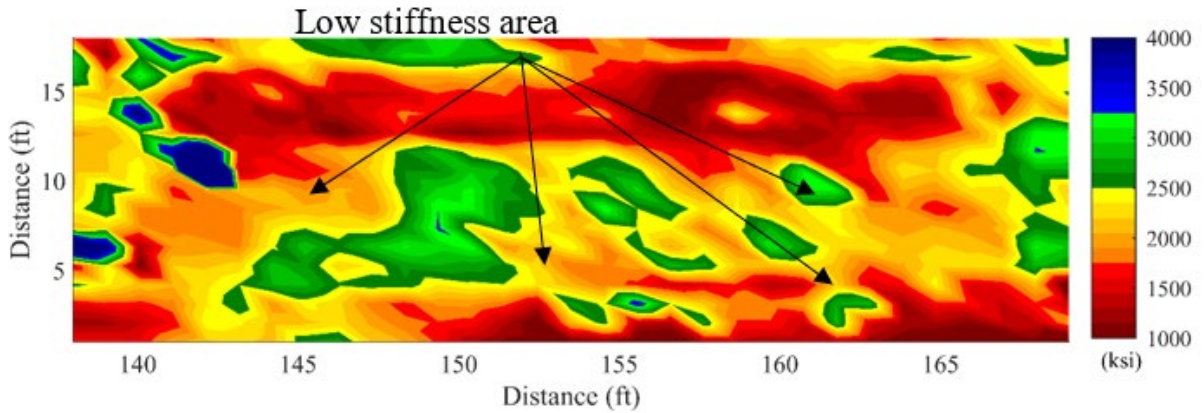
**Figure 116. Graph. NDE condition map with the ER method.**

Comparing the four condition maps shown in figure 116 through figure 119 indicates the following: delamination areas detected by the USW method agree with those of the IE method, and the USW and IE methods detected delamination in the concrete bridge deck through the overlay; areas with corrosive environments detected by the GPR method agree with those of the ER method, and the GPR and ER methods measured corrosive environments in overlays and concrete bridge decks; and areas with corrosive environments are much larger than areas with delamination.

## ARLINGTON MEMORIAL BRIDGE

The Arlington Memorial Bridge crosses the Potomac River connecting Washington, DC, with Virginia. The Arlington Memorial Bridge is 2,138 ft long and consists of 9 arches. The concrete bridge deck has a thickness of 1 ft with an asphalt overlay and two reinforcing steel layers.

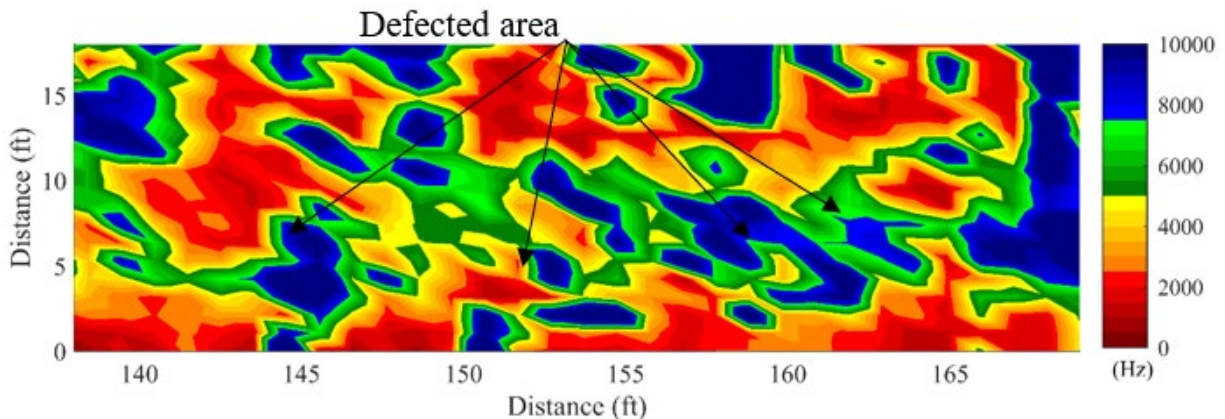
A study was conducted to determine the performance of the IE, USW, and UT methods NDE technologies on concrete bridge decks with asphalt overlays. The condition maps based on the moduli measured with the USW method are shown in figure 117. Areas with lower moduli compared to other areas indicated debonding. The USW method detected two large areas of debonding: one from 141 to 165 ft in the longitudinal direction and from 12 to 16 ft in the transverse direction, and the other from 150 to 170 ft in the longitudinal direction and from 0 to 4 ft in the transverse direction.



Source: FHWA.

**Figure 117. Graph. NDE condition map with the USW method.**

The condition map based on the dominant frequencies measured by the IE method is shown in figure 118. Areas with lower frequencies compared to other areas indicate debonding. The IE method detected two large areas of debonding: one on the top of the condition map from 141 to 167 ft in the longitudinal direction and from 12 to 16 ft in the transverse direction, and the other along the bottom of the condition map. Intact areas had the frequency of the thickness mode at about 10 kHz, while areas with debonding had the dominant flexural mode with frequencies around 2 kHz.



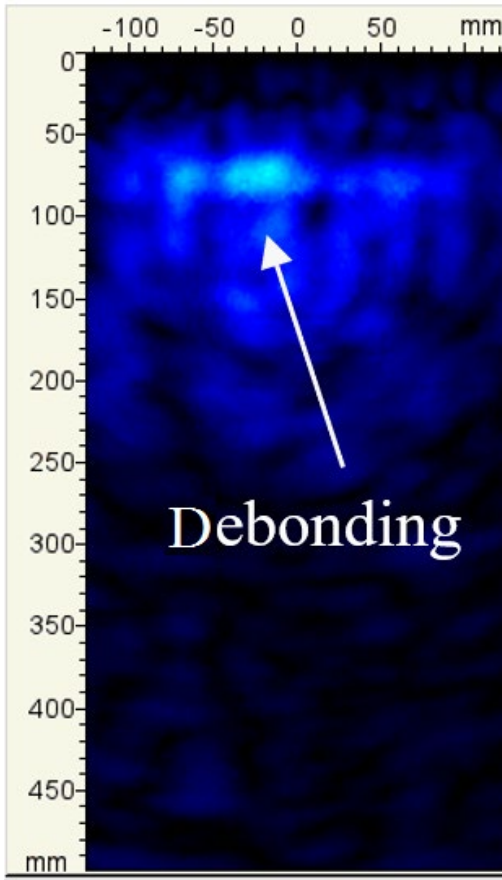
Source: FHWA.

**Figure 118. Graph. NDE condition map with the IE method.**

Comparing the two condition maps in figure 117 and figure 118 indicates areas with debonding detected by the USW method agree with those of the IE method; the USW, IE, and UT methods detected debonding; and the USW, IE, and UT methods could not detect any defects in the underlying concrete bridge deck through the asphalt overlay.

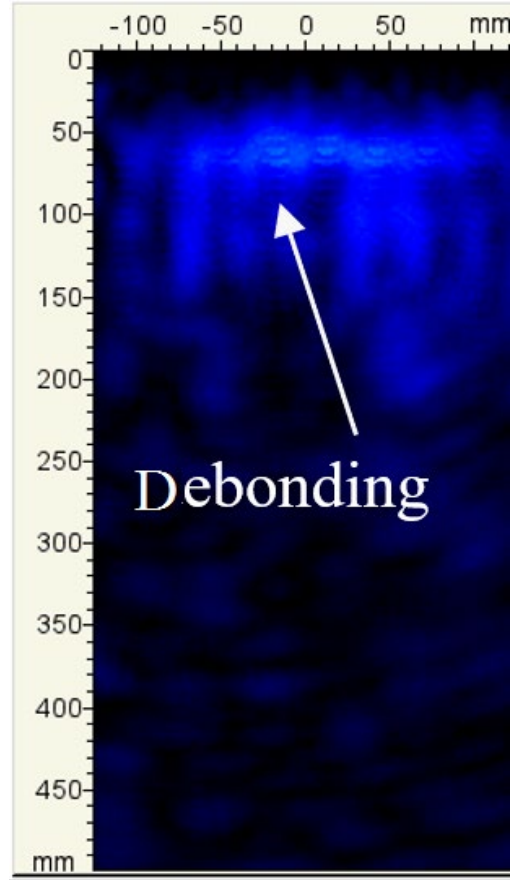
Testing using the UT-UT-MIRA method was conducted at a spacing of 11.8 inches. The panoramic B-, C-, and D-scan could not be created because the spacing was beyond the up limit for merging individual B-scan data with UT-MIRA. From the condition maps from the USW and IE methods, some individual B-scans from debonded and intact areas were selected and shown in

figure 119. Debonded areas had stronger reflections from the interface, whereas intact areas had weaker reflection, as shown in figure 119-A and figure 119-B versus figure 119-C and figure 119-D. Although some wave energy propagated into the underlying concrete bridge deck in intact areas, the UT method could not image any objects in the concrete bridge deck.



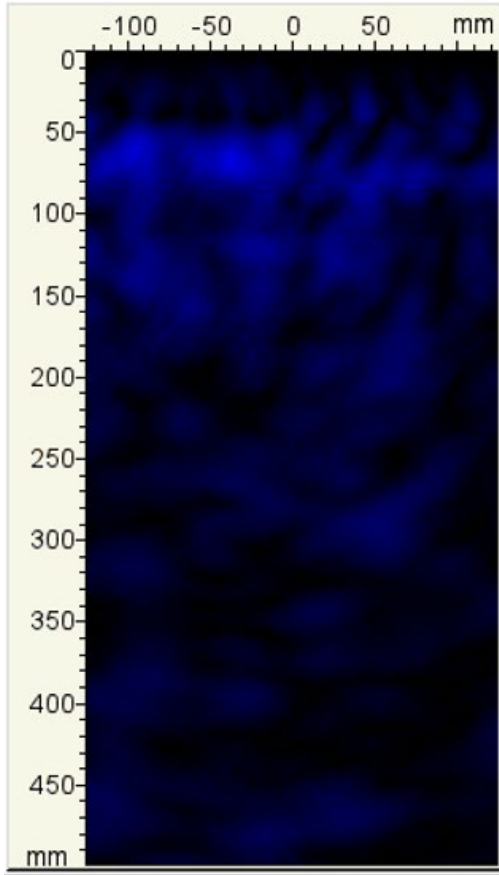
Source: FHWA.  
1 mm = 0.04 inch.

A. Debonded area.



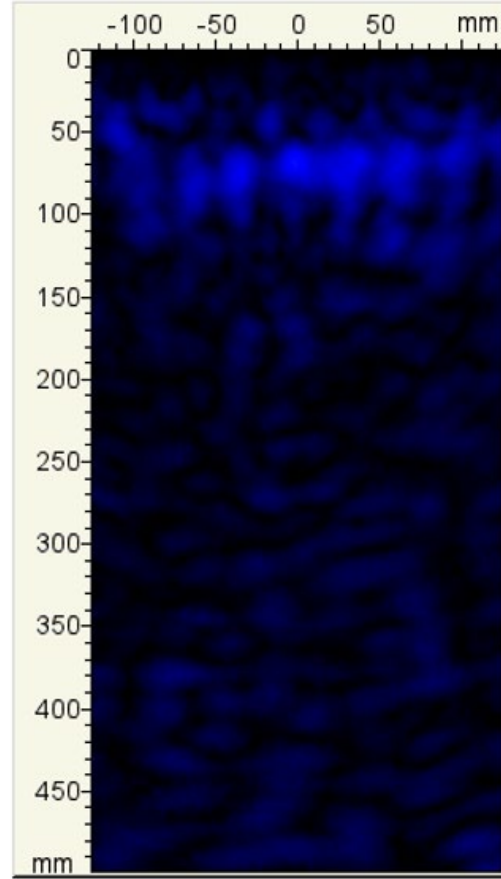
Source: FHWA.  
1 mm = 0.04 inch.

B. Debonded area.



Source: FHWA.  
1 mm = 0.04 inch.

C. Intact area.



Source: FHWA.  
1 mm = 0.04 inch.

D. Intact area.

**Figure 119. Graphs. NDE B-scans of the debonded and intact areas.**



## REFERENCES

1. Sprinkel, M 2000. Evaluation of Latex-Modified and Silica Fume Concrete Overlays Placed on Six Bridges in Virginia. Charlottesville, VA: Virginia Transportation Research Council.
2. Delatte, N.J., Fowler, D.W., McCullough, B.F., and Gräter, S.F. 1998. “Investigating Performance of Bonded Concrete Overlays.” *Journal of Performance of Constructed Facilities*, 12(2): 62–70.
3. Delatte, N.J., Chen, S., Davidson, J., Sehdev, A., Amer, N., and Endfinger, M. 2001. *Design and Quality Control of Concrete Overlays*. Tuscaloosa, AL: University Transportation Center for Alabama.
4. Li, M., Anderson, N.L., Sneed, L.H., and Kang, X. 2016. “An Assessment of Concrete over Asphalt Pavement Using both the Ultrasonic Surface Wave and Impact Echo Techniques.” *Journal of Environmental and Engineering Geophysics*, 21(4): 137–149.
5. Davis, A.G., Hertlein, B.H., Lim, M.K., and Michols, K. 1996. “Impact-Echo and Impulse Response Stress-Wave Methods: Advantages and Limitations for the Evaluation of Highway Pavement Concrete Overlays.” *Proceedings of SPIE 2946, Nondestructive Evaluation of Bridges and Highways, Scottsdale, AZ, November 13, 1996*. Bellingham, WA: Society of Photo-Optical Instrumentation Engineers.
6. Gucunski, N., Romero, F., Kruschwitz, S., Feldmann, R., Abu-Hawash, A., and Dunn, M. 2010. “Multiple Complementary Nondestructive Evaluation Technologies for Condition Assessment of Concrete Bridge Decks.” *Transportation Research Record* 2201: 34–44.
7. Sansalone, M.J. and Carino, N.J. 1989. “Detecting Delaminations in Concrete Slabs with and without Overlays Using the Impact-Echo Method.” *ACI Materials Journal* 86(2): 175–184.
8. Sansalone M.J. 1993. “Detecting Delaminations in Concrete Bridge Decks with and without Asphalt Overlays Using an Automated Impact-Echo Field System.” *Proceedings of the British Institute of Non-Destructive Testing International Conference, NDT in Civil Engineering, Liverpool, England, April 14–16, 1993*. Northampton, England: British Institute of Non-Destructive Testing: 807–819.
9. Gucunski, N., Imani, A., Romero, F., Nazarian, S., Yuan, D., Wiggerhauser, H., and Shokouhi, P. et al. 2012. *Nondestructive Testing to Identify Concrete Bridge Deck Deterioration*, SHRP 2 Report S2-R06A-RR-1. Washington, DC: Transportation Research Board.
10. dos Reis, H.L.M. and Baright, M.D. 1999. *Inspection of Concrete Bridge Decks with Asphalt Overlays — a Comparison of Nondestructive Evaluation Methods*. Thompson, D.O. and Chimenti D.E. (eds), Review of Progress in Quantitative Nondestructive Evaluation, Vol. 18 A, 2137–2144. Boston, MA: Springer.

11. Maser, K.R. 2009. "Integration of Ground Penetrating Radar and Infrared Thermography for Bridge Deck Condition Evaluation." *Proceedings of NDTCE '09, June 30–July 3, 2009, Nantes, France*. Paris, France: Non-Destructive Testing in Civil Engineering.
12. Wibowo, H., Wood, R., and Sritharan, S. 2016. "Delamination Assessment of an Ultra-High Performance Concrete Deck Overlay Using Infrared Imaging." *Proceedings of the First International Interactive Symposium on UHPC, Des Moines, IA, July 18–20, 2016*. Des Moines, IA: Ultra-High Performance Concrete.
13. Russell, H.G. 2012. *NCHRP Synthesis 425: Waterproofing Membranes for Concrete Bridge Decks*. Washington, DC: Transportation Research Board.
14. EAPA. 2013. *Asphalt Pavements on Bridge Decks*. Brussels, Belgium: European Asphalt Pavement Association.
15. Lane, S. 2016. *FHWA LTBP Summary—Current Information on the Use of Overlays and Sealers*, Report No. FHWA-HRT-16-079. Washington, DC: Federal Highway Administration.
16. AASHTO. 2010. *AASHTO LRFD Bridge Construction Specifications*. Third Edition. Washington, DC: American Association of State Highway and Transportation Officials.
17. TDOT. 2015. *Tennessee Department of Transportation Standard Specifications for Road and Bridge Construction*. Nashville, TN: Tennessee Department of Transportation.
18. Sprinkel, M., Sellars, A.R., and Weyers, R.E. 1993. *Rapid Concrete Bridge Deck Protection, Repair and Rehabilitation*, SHRP-S-344, NRC, Washington, DC.
19. Wade, D.M., Fowler, D.W. and McCullough, B.F. 1995. *Concrete Bond Characteristics for a Bonded Concrete Overlay on IH-10 in El Paso*. Research Report 2911-2, Austin, TX: University of Texas at Austin Center for Transportation Research.
20. Delatte, N.J. 1996. *High Early Strength Bonded Concrete Overlay Designs and Construction Methods for Rehabilitation of CRCP*. Ph.D. Dissertation, Austin, TX: University of Texas at Austin.
21. Sprinkel, M. 2000. *Evaluation of Latex-Modified and Silica Fume Concrete Overlays Placed on Six Bridge in Virginia*, Report No. 01-R3. Charlottesville, VA: Virginia Transportation Research Council.
22. Sprinkel, M. 1998. *Very-early-strength Latex-Modified Concrete Overlay*, Report No. VTRC99-TAR3. Charlottesville, VA: Virginia Transportation Research Council.
23. Luo, S. 2002. *Evaluations of Concrete Overlays for Bridge Deck Applications*. M.S. thesis, Morgantown, WV: West Virginia University.

24. Harries, K.A., McCabe, M., Sweriduk, M. 2013. *Structural Evaluation of Slab Rehabilitation by the Method of Hydrodemolition and Latex Modified Overlay*, Report No. FHWA-PA-2013-006-PIT WO 01, Harrisburg, PA: Pennsylvania Department of Transportation.
25. ACI. 1993. ACI 548.4-93, *Standard Specification for Latex-Modified Concrete (LMC) Overlays*. Farmington Hills, MI: American Concrete Institute.
26. West Virginia Division of Highways. 2010. *Standard Specifications Roads and Bridges: Section 679*, Charleston, WV: West Virginia Division of Highways.
27. Gama, N. 1999. *Durability of Epoxy Polymer Concrete Overlays for Bridge Decks*. Montreal, Québec, Canada: McGill University Department of Civil Engineering and Applied Mechanics.
28. Sprinkel, M. 1983. *Evaluation of the Construction and Performance of Polymer Concrete Overlays on Five Bridges*, Interim Report No. 1. Charlottesville, VA: Virginia Transportation Research Council.
29. Sprinkel, M. 1990. *Premixed Polymer Concrete Overlays*, Report No. 9615. Charlottesville, VA: Virginia Transportation Research Council.
30. Young, L.M., Durham, S., and Liu, R. 2014. *Performance of Thin Bonded Epoxy Overlays on Asphalt and Concrete Bridge Deck Surfaces*, Report No. CDOT-2014-2, Denver, CO: Colorado Department of Transportation.
31. ASTM. 2013. D4788-13, *Standard Test Method for Detecting Delamination in Bridge Decks Using Infrared Thermography*. West Conshohocken, PA: ASTM International.
32. Gucunski, N., Imani, A., Romero, F., Nazarian, S., Yuan D., Wiggerhauser H., and Kutrubes D. 2012. *Nondestructive Testing to Identify Concrete Bridge Deck Deterioration*, SHRP 2 Report No. S2-R06A-RR-1. Washington, DC: Transportation Research Board.
33. Maser, K.R. 2009. *Integration of Ground Penetrating Radar and Infrared Thermography for Bridge Deck Condition Evaluation*. NDTCE 09, Nantes, France: Non-destructive Testing in Civil Engineering.
34. Daniels, D.J. 2004. *Ground Penetrating Radar*. Second Edition, Report No. ISBN 0-86341-360-9. London, England: IEE.
35. Parrillo, R. and Roberts, R. 2006. *Bridge Deck Condition Assessment Using Ground Penetrating Radar*. ECNDT 2006 - Tu.4.2.5.
36. ASTM. 2015. D6087-08, *Standard Test Method for Evaluating Asphalt-Covered Concrete Bridge Decks Using Ground Penetrating Radar*. West Conshohocken, PA: ASTM International.

37. Delatte, N.J. 1996. *High Early Strength Bonded Concrete Overlay Designs and Construction Methods for Rehabilitation of CRCP*. Ph.D. Dissertation. Austin, TX: University of Texas at Austin.
38. Sansalone, M.J., and Carino, N.J. 1989. Detecting Delaminations in Concrete Slabs with and without Overlays Using the Impact-Echo Method, *ACI Materials Journal* 86(2): 175–184.
39. Sansalone, M.J. 1993. “Detecting Delaminations in Concrete Bridge Decks with and without Asphalt Overlays Using an Automated Impact-Echo Field System.” *Proceedings of the British Institute of Non-Destructive Testing International Conference NDT in Civil Engineering, Liverpool, England, April 14–16, 1993*: 807–820.
40. Gowers, K.R. and Millard, S.G. 1999. “Measurement of Concrete Resistivity for Assessment of Corrosion Severity of Steel Using Wenner Technique.” *ACI Materials Journal* 96(5): 536–542.
41. ASTM. 2015. C876-15, *Standard Test Method for Corrosion Potentials of Uncoated Reinforcing Steel in Concrete*. West Conshohocken, PA: ASTM International.
42. Baumann, K. 2008. “Practical Example of Interpretation of Half Cell Measurements on R.C. Structures.” *Proceedings of the 12th International Conference on Structural Faults and Repair, Edinburgh, Scotland*.
43. Langenberg, K.J., Berger, M., Kreutter, Th., K. Mayer, K., and Schmitz V. 1986. “Synthetic Aperture Focusing Technique Signal Processing.” *NDT&E International* 19(3): 177–189.
44. Shokouhi, P., Wolf, J., and Wiggenhauser, H. 2013. “Detection of Delamination in Concrete Bridge Decks by Joint Amplitude and Phase Analysis of Ultrasonic Array Measurements.” *Journal of Bridge Engineering* 19(3): 04013005-1–04013005-11.
45. Washer, G., Dawson, J., Ruiz-Fabian, P., Sultan, A., and Trial, M. 2016. *Field Testing of Hand-Held Infrared Thermography*, Phase II, TPF-5(247) Final Report, Volume 2.
46. Sansalone, M. and Street, W. 1997. *Impact Echo: Nondestructive Evaluation of Concrete and Masonry*. Ithaca, NY: Bulbrier Press.
47. Kee, S. H., and Gucunski, N. 2016. “Interpretation of Flexural Vibration Modes from Impact-Echo Testing.” *Journal of Infrastructure Systems* 22(3): 1–10.
48. Layssi, H., Ghods, P., Alizadeh, R., and Salehi, M. 2015. “Electrical Resistivity of Concrete.” *Concrete International* 37(5): 41–46.
49. Azarsa, P., and Gupta, R. 2017. “Electrical Resistivity of Concrete for Durability Evaluation: A Review.” *Advances in Materials Science and Engineering*: 1–31.

50. Morales, M. 2015. *Experimental Investigation of the Effects of Embedded Rebar, Cracks, Chloride Ingress and Corrosion on Electrical Resistivity Measurements of Reinforced Concrete*, Master thesis. Corvallis, OR: Oregon State University.
51. ASTM. 2015. C876-15, *Standard Test Method for Half-Cell Potentials of Uncoated Reinforcing Steel in Concrete*. West Conshohocken, PA: ASTM International.
52. ASTM. 2013. D4788-03, *Standard Test Method for Detecting Delaminations in Bridge Decks Using Infrared Thermography*. West Conshohocken, PA: ASTM International.
53. Nazarian, S., Tandon, V., and Yuan, D. 2005. “Mechanistic Quality Management of Hot Mix Asphalt Layers with Seismic Methods.” *Journal of ASTM International* 2: 1–12.
54. Celaya, M., and S. Nazarian. 2006. “Seismic Testing to Determine Quality of Hot-Mix Asphalt.” *Transportation Research Record* 1946: 113–22.





